# DYNAMICAL EFFECTS IN MAGNETIC NANOSTRUCTURES: A DETAILED ANGULAR-DEPENDENT DYNAMIC STUDY OF MODEL SYSTEMS WITH COMPETING ANISOTROPIES, REORIENTATION TRANSITIONS, OR REVERSAL CHANGES.

JOSÉ LUIS FERNÁNDEZ CUÑADO

A DISSERTATION SUBMITTED TO THE FACULTY OF SCIENCE
IN PARTIAL FULFILLMENT OF THE REQUIREMENTS
FOR THE DEGREE OF

DOCTOR OF PHILOSOPHY

DOCTORATE PROGRAM IN DEPARTMENT OF CONDENSED MATTER PHYSICS
UNIVERSIDAD AUTÓNOMA DE MADRID
MADRID, SPAIN

Thesis supervisor: JULIO CAMARERO DE DIEGO

JUNIO 2017

**DYNAMICAL EFFECTS IN MAGNETIC NANOSTRUCTURES: A DETAILED ANGULAR-DEPENDENT DYNAMIC STUDY OF MODEL SYSTEMS WITH COMPETING ANISOTROPIES, REORIENTATION TRANSITIONS, OR REVERSAL CHANGES.**

by **José Luis Fernández Cuñado**

a dissertation submitted to the Faculty of Science of the Universidad Autónoma de Madrid in partial fulfillment of the requirements for the degree of

**DOCTOR OF PHILOSOPHY**

# DYNAMICAL EFFECTS IN MAGNETIC NANOSTRUCTURES: A DETAILED ANGULAR-DEPENDENT DYNAMIC STUDY OF MODEL SYSTEMS WITH COMPETING ANISOTROPIES, REORIENTATION TRANSITIONS, OR REVERSAL CHANGES.

by **José Luis Fernández Cuñado**

*Universidad Autónoma de Madrid*
*(Departamento de Física de la Materia Condensada, Instituto de Ciencia de Materiales Nicolás Cabrera and IFIMAC)*

*Instituto Madrileño de Estudios Avanzados de Nanociencia - IMDEA Nanociencia*
*(Nanomagnetism and Critical Materials)*



Examination Committee Members:

1. Dr. Juan José de Miguel Llorente
2. Dr. Alberto Bollero
3. Dr. Stefania Pizzini
4. Dr. Josep Nogués
5. Dr. Juan de la Figuera Bayón

# Abstract

The studies on dynamics of magnetic properties constitute an important issue in Nanomagnetism today, from both fundamental and technological points of view. The use of magnetic materials in a very large number of applications ranging from compass needles to electrical motors, smart devices and personal computers has triggered the search for materials with particular static and dynamic properties. For instance, magnetization reversal features (i.e., relevant mechanism, reversal times, reversal fields) determine how the magnetization preserves its state in powerful permanent magnet applications, based on nanograin ferromagnetic structures consolidated in bulk systems, as well as how the information can be read and written in spintronic devices, based on multilayered thin film nanoarchitectures (low dimensionality). The complete understanding of these magnetic nanostructures requires, in addition, probing the dynamic properties with experimental techniques combining capabilities to identify all dynamic parameters. Current and future technologies require hence basic understanding and control of dynamic processes in this context.

This thesis provides systematic studies on the dynamics of magnetic properties in model magnetic nanostructures, illustrating how critical they are at the nanoscale. Both technical and scientific advances are presented in the different chapters of the manuscript. Unique vectorial-resolved magnetometers based in the magneto-optic Kerr effect have been developed to investigate in detail the angular dependence of the dynamical properties over nine decades of applied magnetic field sweep rate, from $10^{-4}$ T/s to $10^{+4}$ T/s, and in a broad temperature range, from 5 K to 500 K. These magnetometers are named drv-MOKE and TRISTAN instruments, respectively.

The magnetic nanostructures investigated in this thesis range from the simplest magnetic symmetry system (ferromagnetic films with well-defined uniaxial magnetic anisotropy) to more complex magnetic heterostructures with competing magnetic anisotropies (biaxial+uniaxial; ferromagnetic/antiferromagnetic exchange coupled bilayers) with spin reorientation transitions, driven either intrinsically (originated from a different temperature-dependent behavior of competing anisotropies or by a phase transition such as metal-insulator Verwey transition) or extrinsically (via field cooling procedure). In general, the angular-dependent dynamics of relevant magnetic parameters (transition fields, remanences, effective magnetic symmetries) as well as magnetization reversal mechanisms are addressed in the framework of thermal and non-thermal activated processes, where temperature and applied field rate are used to control dynamic behavior. As a general conclusion, the key that control the dynamic magnetic properties is the dynamic effective magnetic symmetry.

Several important scientific highlights are presented in the manuscript: i) The emergence of Stoner-Wohlfarth astroid in ferromagnetic thin films at dynamic regime,

where nucleative processes govern the magnetization reversal; ii)The symmetry-breaking effects in systems with competing anisotropies with different temperature evolution, as found in Fe(100) thin films with tailored magnetic symmetry; iii) Unexpected spin reorientation in magnetite $Fe_3O_4(001)$ films at the Verwey transition; iv) Revisiting of the field-dependent exchange coupling effects in ferromagnetic/antiferromagnetic $Co/MnF_2(111)$ bilayers. v) The experimental data are discussed in the framework of the Stoner-Wohlfarth model (suitable for single-domain reversal mechanisms as well as for extended systems with nucleative-like reversal mechanisms) and the pinning and Cowburn models (more suitable for systems where domain wall propagation is the dominant reversal mechanism). Remarkably, the basic clues on the frontier of application of the models are also given. The results provide new fundamental insights within nanomagnetism opening additional avenues to develop future advanced magnetic devices based on (dynamic) effective symmetry-tailored magnetic nanostructures.

# Resumen

El estudio de la dinámica de las propiedades magnéticas es una cuestión muy relevante en el nanomagnetismo hoy en día, tanto desde el punto de vista fundamental como tecnológico. El uso de materiales magnéticos en muchísimas aplicaciones desde las agujas de las brújulas a los motores eléctricos, teléfonos móviles y ordenadores personales, ha impulsado la investigación de materiales con propiedades particulares tanto en su comportamiento estático como dinámico. Por ejemplo, las características de la inversión de imanación (es decir, los mecanismos relevantes, tiempos y campos de inversión) determinan cómo la magnetización preserva su estado en aplicaciones para imanes permanentes potentes, basados en estructuras magnéticas nanogranulares, consolidadas en sistemas macroscópicos (volumen grande), así como la manera en que la información se lee y escribe con dispositivos de espintrónica, basados en nanoarquitectura de multicapas de láminas delgadas (baja dimensionalidad). El entendimiento completo de estas nanoestructuras magnéticas require, además, indagar en las propiedades dinámicas mediante el uso de técnicas experimentales que combinan la capacidad de identificar todos los parámetros dinámicos. Las tecnologías presentes y futuras requieren por tanto una comprensión a nivel fundamental y el control de los procesos dinámicos en este contexto.

Esta tesis proporciona un estudio sistemático de la dinámica de las propiedades magnéticas de nanoestructuras tipo, ilustrando cuán críticas son en la nanoescala. Avances tanto técnicos como científicos se presentan en los distintos capítulos del manuscrito. Se han desarrollado magnetómetros vectoriales únicos en su clase, basados en el efecto Kerr magneto-óptico, para investigar en detalle la dependencia angular de las propiedades dinámicas sobre un rango de variación de rampa magnética de hasta nueve décadas, desde $10^{-4}$ T/s hasta $10^{+4}$ T/s, en un amplio rango de temperaturas desde 5 K hasta 500 K. Estos magnetómetros se han llamado drv-MOKE y TRISTAN respectivamente.

Las nanoestructuras magnéticas investigadas en esta tesis abarcan desde el sistema con simetría magnética más simple (láminas ferromagnéticas con anisotropía magnética uniaxial bien definida) hasta las heteroestructuras magnéticas más complejas con competición de anisotropías (biaxial-uniaxial; bicapas con acoplo de canje de material ferromagnético/antiferromagnético) con reorientación de spin, inducidos o bien intrínsecamente (originados a partir de comportamientos diferentes de las dependencias con la temperatura de cada anisotropía que está compitiendo o mediante transiciones de fase, como es el caso en las transiciones Verwey, de metal a aislante), o extrínsecamente (a través de procesos de Field Cooling). En general la dependencia angular y dinámica de las magnitudes magnéticas relevantes (campos de transición, remanencias, simetrías magnéticas efectivas) así como los mecanismos de inversión de

imanación se abordan en el marco de los procesos tanto térmicamente activados como no, donde la temperatura y el rango de variación del campo aplicado son usados para controlar el comportamiento. Como conclusión general, la clave para el control del comportamiento magnético en dinámica es la anisotropía magnética dinámica efectiva.

En este manuscrito se presentan muchos resultados científicos importantes, tales como: i) la aparición del astroide de Stoner-Wohlfarth en láminas ferromagnéticas delgadas en el régimen dinámico, donde los procesos nucleativos gobiernan la inversión de imanación; ii) efectos de ruptura de simetría en sistemas con competición de anisotropías de evolución distinta con la temperatura, como se encuentra por ejemplo en láminas delgadas de Fe(100) con anisotropía magnética inducida a propósito; iii) transiciones de reorientación de spin inesperadas en láminas delgadas de magnetita, $Fe_3O_4(001)$ , a la temperatura de Verwey; iv) revisión de los efectos de acoplamiento de canje dependientes del campo en bicapas ferro/antiferro de $Co/MnF_2(111)$; v) los datos experimentales se discuten en el marco de los modelos teóricos de Stoner-Wohlfarth (adecuado para los sistemas cuya inversión de imanación se rige por mecanismos tipo monodominio, y también para los extendidos que se rigen por procesos de inversión de tipo nucleativo) y los de "pinning" y de Cowburn (más adecuados para sistemas en los que los fenómenos propagativos de paredes de dominio constituyen el mecanismo dominante en la inversión de imanación). Cabe remarcar que se aportan una serie de pautas básicas con las que se pueden enfrentar problemas que serían de otro modo imposibles de conciliar. Los resultados proveeen nuevas prospecciones dentro del nanomagnetismo, abriendo vías para el desarrollo futuro de dispositivos magnéticos basados en nanoestructuras cuya dinámica y simetrías magnéticas se diseñan ex profeso para cada aplicación.

*I dedicate this thesis with very special affection to Cristina and to our little kid David. Cristina has been very concerned and sacrificed during this period, in special in the last lap of the race. In the last month when proximity of deadline made thesis full-time demanding, David was able to get on with "missing daddy", his sweet little voice saying: "Mom, dad is working upstairs in the loft.".*

*I also dedicate this thesis to our missing friend Dr. Juanjo Hinarejos.*

*José Luis F. Cuñado*
*Universidad Autónoma de Madrid*
*$25^{th}$ June 2017*

# Acknowledgements

I want to acknowledge Doctor Julio Camarero, Professor Rodolfo Miranda and our missing friend Doctor Juanjo Hinarejos. All of them encouraged me to do a thesis, and told me the same words of support: *"age is not a drawback for this"*. To Julio for being my thesis supervisor, a good friend and companion in the scientific adventures, and for having managed to obtain financial support for me during these years. To Professor Rodolfo Miranda, for being a good friend as well, and a pillar that has supported my stay in the institutions, both UAM and IMDEA. To Juanjo Hinarejos, who talked to Julio about me, and who taught me all the things I know about vacuum, as well as many in materials and instrumentation. I want to acknowledge also to Daniel Farías for letting me collaborate with him at the molecular beam diffraction instruments in those times when I was still working for a private company. I'm also very grateful to Dr. Alberto Bollero, for letting me collaborate in Nanopyme project and for sharing friendship and nice times, including my first "cross of the puddle".

I'm very grateful to all my teachers during my degree in physics, in special to Prf. Luis Robledo, Prf. Félix Ynduráin and Prf. Enrique Álvarez, and during the Master in Condnesed Matter Physics. The mention of them all must be taken for granted.

I wish to acknowledge to my classmates of the Master Degree, in special to Dr. Juan Pedro Cascales, Dra. Ana Moreno, Dra. Cristina Blanco, Dr. José Jaime Ruth and Diego González (soon to become Dr.). We spent nice time together, and we shared discussions in physics and computing, as well as "paellas", guitars and golf sticks.

I'm very grateful to all the scientist with whom I have had collaborations or talks. I have obtained very important part of my knowledge from them. In particular, I wish to acknowledge to Dr. Hermann Suderow, Prf. Sebastian Vieira and Dra. Isabel Guillamn, at LBTUAM, for low temperature physics knowledge that they have transmitted to me, to Dr. José Gabriel Rodríguez (LBTUAM also) for his support on instrumentation, to Dr. Jesús Álvarez, who taught me electronics and has also given me ideas on data analysis, and to Dr. José Vicente Álvarez, who has discussed some issues on magnetism with me. I have had collaborations with Dr. Juanjo de Miguel, so here is my acknowledge as well. I wish to thank people at IMDEA Nanoscience, specially to Dr. Paolo Perna, Dr. Fran Terán, Dra. Cristina Navío, Dra. Teresa Gonález, Dr. Roberto Otero, among others.

I wish to thank to UAM research support services, SEGAINVEX and to the technical staff at UAM Condensed Matter Department, specially to Santiago Márquez, Andrés Buendía and José Luis Romera. Their work has been critical for the realization of the new set-up TRISTAN.

I wish to acknowledge as well to all the scientists and institutions of Spain and out

of Spain that have helped me during collaborations. In special to IOFFE Institute at St. Petersburg, in particular to Prf. Nikolai S. Sokolov, Dr. Sergey Gastev, Dr. Sergey Suturin and Dr. Vladimir Fedorov, among others; to UNIMORE University in Italy, in particular to Prf. Luca Pascuali; to people from CNRS and Néel Institute, including Prf. Jean Marc Tonnerre, Prf. Nikola Jaouen (at SOLEIL Synchrotron facility), Prf. J. Vogel, and many others; to people from IFW at Dresden, Prf. Volker Neu and Prf. Rudolf Schafer; to people from Nanompyme project, including personal from IMA. I want to also acknowledge people from ESRF beamline BM25, Prf. Germán Castro and Prf. Juan Rubio, people from ID8, Flora Yaku, and many others at ESRF. I do not forget my college Dr. Iulian Preda, I met him in module 3 at UAM, and he was the person who showed me the inside of ESRF for the first time. I mention also here to Prf. Juan de la Figuera and extend to people from Rocasolano and CSIC institutes.

The full list of acknowledgement is much longer than this, but it would take several pages to list them all. Just here I include a general acknowledgment to the Universidad Autónoma de Madrid as Institution, as well as to IMDEA Nanociencia, including people from administration, who have been very kind at helping me in any administrative task required thus far.

I wish to specially acknowledge to Prf. Nikolai Sokolov and Prf. Luca Pascuali for their support on this work for the International Mention.

Finally I kindly acknowledge to all the members of the Tribunal in the thesis defense, and in particular to Prf. Stefania Piccini for traveling to Spain for the occasion.

# Table of Contents

# Abbreviations

This is not exhaustive list, but only the most frequently used abbreviations, acronyms and symbols.

Table 1: Abbreviations and symbols

| Acronym/Abbreviation | Description |
|---|---|
| AFM | Antiferromagnetic/Antiferromagnet |
| AFM | Atomic Force Microscopy |
| APB | Anti-Phase Boundary |
| CW | Cowburn Model |
| DAQ | Data acquisition systems |
| drv-MOKE | Dynamical Range Vectorial Magneto-optical Kerr effect |
| DW | Domain Wall |
| DWM | Domain Wall Motion |
| $\epsilon$ | Angle of polarization of light |
| $\epsilon_\alpha$ | Domain Wall pinning energy |
| EB | Exchange Bias |
| FC | Field Cooling |
| FM | Ferromagnetic/Ferromagnet |
| FMR | Ferromagnetic Resonance |
| GMR | Giant Magnetoresistance |
| GP-IB | General-Purpose Instrumentation Bus |
| $\lambda/2$ | Half-wave retarder plate |
| MOKE | Magneto-optical Kerr effect |
| MFT | Mean Field Theory |
| $H_C$ | Coercive Field |
| $H_D$ | Departure point |
| $H_E$ | Exchange Bias Field |
| $H_K$ | Anisotropy Field |
| $H_M$ | Meeting point |
| $H_S$ | Switching Field |
| HTR | Heater |
| IEEE 488.2 | Actual standard protocol for GP-IB control |
| IR-PLD | Infrared Pulsed Laser Deposition |
| $I_\Delta$ | Polarization rotation signal |
| $I_\Sigma$ | Reflectivity signal |

| Acronym/Abbreviation | Description |
|---|---|
| $K_i$ | Anisotropy Constant |
| $M_D$ | Magnetization at departure point |
| $M_M$ | Magnetization at meeting point |
| $M_R$ | Remnant Magnetization or Remanence |
| $M_S$ | Saturation Magnetization |
| PID | Proportional-Integral-Derivative instrument control |
| PLD | Pulsed Laser Deposition |
| PVC<br>Polyvinyl Chloride | |
| SEGAINVEX | General Research Support Service |
| SOC | Spin Orbit Coupling |
| SPLEEM | Spin-Polarized Low Energy Electron Microscopy |
| SQUID | Superconducting Quantum Interference Device (magnetometer) |
| SW | Stohner-Wohlfarth |
| SWT | Spin Wave Theory |
| TEV | Total Electron Yields |
| THERMOKE | On-purpose control software for TRISTAN |
| TP | Twin Photodiodes |
| VLV | Electrovalve Control for He Flow |
| v-MOKE | Vectorial Magneto-optical Kerr effect |
| VSM | Variable Sample Magnetometer |
| XAS | X-Ray Absortion Spectroscopy |
| XMCD | X-Ray Magnetic Circular Dichroism |
| XRD | X-Ray Diffraction |
| XRMR | X-Ray Magnetic Resonance |
| $\parallel$ | Parallel component (subscript) |
| $\perp$ | Perpendicular component (subscript) |
| XYZ | Used to refer 3 translational axes in opto-mechanic devices. |

# Notes

Along this thesis, some general rules will be used that deserve initial mentioning.

Error bars in plots are generally omitted, on the ground that they are quantified in a global way, stated in the chapter dedicated to instrumentation, and to favor more clear views of the angular plots. When error bars are large enough as to make data unreliable, either data are discarded or, if some comments should be done on them, error bars are explicitly shown in the corresponding graphs.

Concerning units, since the magnetometry carried out with vMOKE does not account for absolute values of magnetization, this is expressed as a normalized magnitude, i.e., $M/M_S$. As a consequence, $M$ will in general be dimensionless. As far as magnetic field is concerned, a voltage signal is used to drive a current amplifier that supplies the current to the electromagnet coils. A calibration curve that relates the voltage signal with the total magnetic flux (obtained with a hall sensor), allows to directly transform voltage into values of $\mu_0 H_{EXT}$ given in Tesla. As far as the normalization value is concerned, it corresponds to a voltage value measured in an oscilloscope, since $M$ appears just as that, and has no resemblance with any real magnitude because no calibration is possible with this technique. This is why in general, normalizing $M_S$ values are not indicated in graphs or in text. The equations for energy in theoretical models involve terms proportional to trigonometric dimensionless functions, with the anisotropy $K$ as the proportional constant, and Zeeman terms as $\mu_0 M H_{EXT}$ (Zeeman energy term). As $M$ is not known in absolute terms, expressions for energy are divided by $M$, so we are really using $E/M$. This fact does not alter minimization process, and has the advantage that both field values and anisotropy constants are then given directly in Tesla. Values of $K$ or $H$ inserted in simulation software are then directly given in this unit. This is why in general, throughout this thesis, we very rarely (if ever) have issues concerning units, since we mostly use normalized (dimensionless) magnetization values, and field/anisotropy values always in mT.

For the anisotropy constants nomenclature, it is usually found in the literature the symbol $K_1$ for cubic anisotropy, or in-plane biaxial anisotropy, and both $K_1$ or $K_U$ for uniaxial. Here we have preferred to use $K_1$ for uniaxial, $K_2$ for biaxial when they are present together in a system, and only in some special cases when pure uniaxial system is dealt with, $K_U$. This has the drawback of causing some confusion when writing general expressions for anisotropy as expansion of direction cosines, where each term is indexed as $K_1$, $K_2$ and successive (for instance in cubic anisotropy), however those

expressions are not deeply analyze, as to create a great problem. On the other hand is more in accordance with the nomenclature used in simulation software.

Another note on nomenclature affects magnetization. In general, magnetization is written as $M$ without any subindex, and it is equivalent to $M_S$ when no confusion may appear. In general, $M$ refers to the maximum magnetization a system can have at zero temperature. Once we are out of that temperature, $M$ refers to $M(T)$ as the maximum magnetization it can have for that temperature. It is also called saturation magnetization, $M_S$, to emphasize this character of "maximum value". The subtlety arrives when the external field applied is not enough to make all the magnetic moments of a system fully align with the external field direction. In that case, $M_S$ fails to be equal to $M$. It is important to note that in vectorial analysis, parallel component of $M$, $M_{\parallel}$ refers to the component parallel to the external field. In that sense, sometimes we use sample saturation concept in terms of "$M$ fully aligned with the external field direction". This means $M_{\parallel} = M_S$ and $M_{\parallel} = 0$.

The maximum fields used in this thesis ranges up to around 200 mT, and the frequency used to drive the field sweep is usually 4 Hz, with either triangular or sinusoidal shape. This values must be understood as default, not specified explicitly in text or graphs unless different values are used or they are part of the free parameters used in the investigations. This is the case in field induced effects or dynamical studies, where the frequency or field rates are explicitly specified.

If only one unique system/sample is used in a chapter, its description will not appear in graphs.

Polarization rotation angle is represented in this thesis with the symbol $\epsilon$, and this same letter is used to represent the angle between magnetic domain orientations at both sides of a domain wall. In this last case, $\epsilon$ usually has a subscript indicating the angle, such as $\epsilon_{180^\circ}$. The context allows to clearly difference both meanings.

In the context of domain wall motion as reversal mechanism in magnetism, it is customary to use the terms "domain wall angle", or "DW angle" to refer to the difference in angle between the magnetization directions of the domains at each side of the wall. Do not confuse this with the direction that the wall itself has. In addition, another particular way of speaking in this context is to refer to the magnetization direction inside a magnetic domain as simply the domain orientation. The DW angle is then the difference in angle between domain orientations at both sides of the DW. We always use this way of speaking in this thesis.

# 1 Introduction

## 1.1 Motivation

Understanding magnetization reversal process is critical in the development of technological applications based on magnetism [1, 2]. From permanent magnets [3] used in compass needles, electrical motors, support devices and passive sensors, where static (constant) magnetization is exploited, to magnetization reversal-dependent applications such as spin valves and GMR [4], used in magnetic disk storage, reading heads and the promising race track memory [5], spontaneous and field-induced reversal of the magnetization at static and dynamic regimes must be finely controlled to obtain the adequate properties. In addition, critical temperature of order-disorder magnetic transition establishes practical limit conditions for the magnetic behavior, which is a very important issue for practical purposes [6, 7].

Examples of how technological applications have pushed the research on these concerns are magnetic storage and spintronics (figure 1.1), two of the most spread technologies at hand. In magnetic storage devices, where each bit of information is stored in a small magnetic region, two mutually opposed properties must be tuned: rapid change of the magnetization state at moderate external fields demands low coercivity, while durable and immune to undesired external influences demands high coercivity. Compromise solution must be taken [4, 5] . Spintronics (for example spin valves) exploits the resistance dependence that magnetic nanostructures have on the relative magnetic orientation between FM layers (reading heads) and/or between FM and current (sensing) [8], i.e. transport properties are governed by magnetic orientation. Coercivity and magnetic orientation are (among others) tightly linked to magnetic symmetry, i.e., to magnetic anisotropy [6, 7], making it necessary to grant a high level of control on it to obtain the desired magnetic and transport behavior. These are just examples of the general statement that specific settings of magnetic properties require a deep understanding of magnetization reversal process and magnetic symmetry.

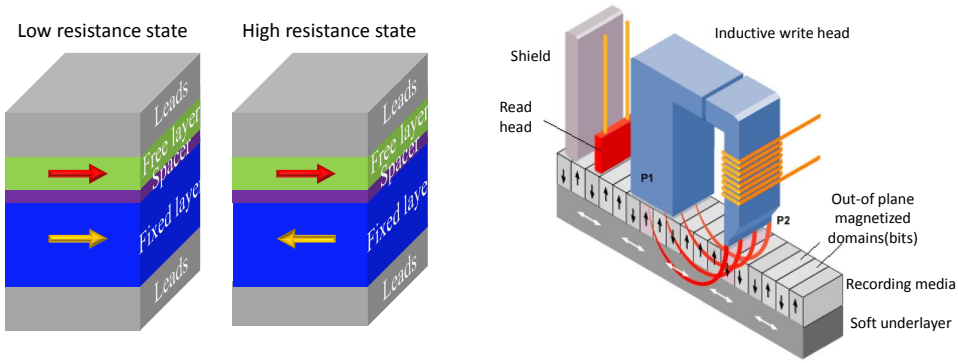


Figure 1.1: Two examples of magnetic devices that exploit control of magnetic parameters such as magnetization and coercive field, as well as a high control on magnetic anisotropy. On the left, schematic fundamentals of a spin valve, where a combination of pinned and free magnetic layers allows to control current flow by setting the magnetization direction of the free layer. On the right, schematics of disk storage technology (adapted from Computer Desktop Encyclopedia).

The reversal process can take place through many different mechanisms that depend on size, dimensionality and shape, as well as on physical properties such as exchange interaction and magnetic anisotropy [9, 10, 11]. It becomes more complex to interpret as the dimensionality increases, from zero-dimensional (nanoparticles) to two-dimensional (thin films). The exchange interaction, magnetic anisotropy and magnetostatics (dipole interaction) are among the most important physical parameters involved [7]. First, exchange interaction favors uniform magnetization configurations. Second, magnetic anisotropy favors the orientation of the magnetization vector along certain preferred directions. And third, magnetostatics favors configurations giving null average magnetic moment, in contrast with anisotropy and exchange. In addition to these intrinsic parameters, the reversal depends on extrinsic parameters such as temperature, applied field angle, and applied field sweep rate. Thermal activation plays an important role as a source of temperature-dependent behavior and as a time-scale mechanism responsible for dynamical effects.

In general, reversal process includes reversible (rotation) and irreversible (switching) magnetic transitions. Models for collective reversal provide good agreement between experiment and theory in the case of small particles [12], both in uniform reversal modes [9], as shown for nanoparticles [13], or in non-uniform ones, as in nanowires [14] and extended systems [15, 16]. For microscopic objects and extended thin films, reversible and irreversible magnetization transitions represent different reversal processes, and they are often a manifestation of the magnetic symmetry of the system [17]. While reversible transitions are related to rotation processes, irreversible ones are related to nucleation of reversed magnetic domains and subsequent propagation of their magnetic domain walls, under the field pressure [18]. In addition, reversal mechanism is quite sensible to the angle direction of the external field with respect

to magnetic symmetry directions, establishing different angular dependent evolutions of magnetic properties for different reversal mechanisms.

For the investigation of reversal process hysteresis loop is the "universal currency", since it encodes nearly all the important magnetic parameters, such as critical fields, remanence and saturation [6], and the accurate determination of magnetic symmetry and reversal process mechanism will demand full angular range vectorial magnetometry [19, 20]. In figure 1.2, left plot, representative vectorial hysteresis loop is presented as an example, while on right plot, an example of angular evolution of critical fields obtained from vectorial loop's analysis is shown, for an extended model system Fe/MgO. It will be shown along this thesis that the particular evolution of magnetic parameters with angle (curve shape and behavior around high symmetry directions) turns out to be a fingerprint of the different reversal mechanisms.

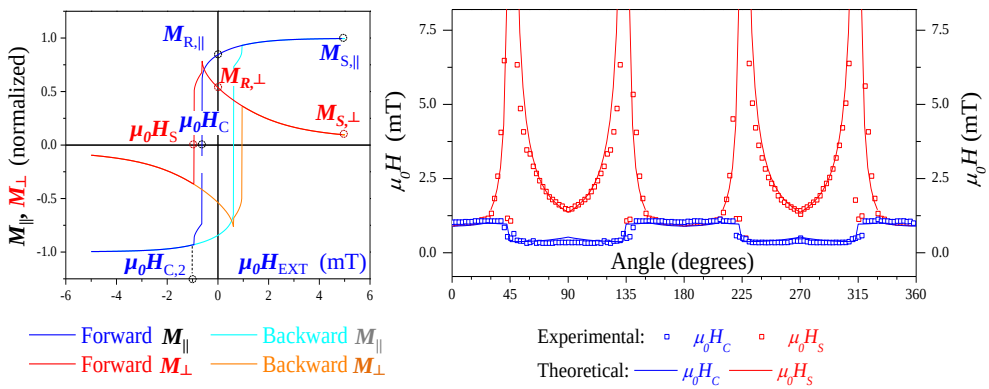


Figure 1.2: Example (arbitrary biaxial system) of vectorial hysteresis model loop is depicted in left plot, showing reversible and irreversible pathways, and magnetic parameters that can be extracted from it. Example of angular evolution of transition fields are depicted on the right (blue and red symbols for), corresponding to uniaxial-biaxial Fe/MgO model system at RT. Magnetic symmetry can be spot by looking at the periodicity, while the reversal process mechanism can be deduce by the good agreement with theoretical Cowburn pinning model (blue and red lines in the left plot).

Theoretical models to study reversal processes comprises microscopic semi-classical, and quantum mechanical descriptions, as well as phenomenological approaches. While phenomenological approaches relays on a few energetic considerations, microscopic description aims at explaining such considerations and the extent of their validity. Predicting from a microscopic framework all the magnetic properties such as saturation magnetization and anisotropy constants is a very complex program. Phenomenological models on the other hand accounts quite well for many of the experimental facts observed, and in particular help to interpret the results, by introducing some experimental parameters on them. Comparison between experimental data and data expected from phenomenological models (examples used in this thesis are Stohner-

Wohlfarth model and pinning models [9, 16, 21]) allows to satisfactory investigate the reversal mechanism.

In addition, the phenomenological models must be complement with a non zero-temperature panorama. At finite temperatures, thermal effects provide dynamical aspects and correspondingly, temperature-dependent evolution of magnetic parameters. On the one hand, thermal energy modifies the energy landscape that governs the reversal, leading to temperature-driven effects. On the other hand, as switching attempt mechanism of spin (related to quantum fluctuations) is involved in the microscopic description of the magnetization reversal, characteristic time will play a fundamental role in combination with the measurement time scale (field sweep rate). This aspects constitute the link between temperature dependence and dynamics or field rate dependence in the reversal process, and both are like heads and tails of the same coin [22]. They are naturally enclosed in the general term of dynamical effects and/or thermal activated effects.

## 1.2 Program of this thesis

For all the aforementioned general aspects, this thesis is devoted to the understanding of reversal processes from a dynamical stand point, by probing temperature/field rate dependent angular evolutions of magnetic properties. It is ascribed to ordered systems, and in particular, we deal with ferromagnetic (FM) and ferromagnetic/ antiferromagnetic (FM/AFM) thin films. This general framework will be assumed hereafter.

Various model magnetic nanostructures (described later) have been used for this program. A new instrument has been developed on purpose, capable of performing full angular range vectorial acquisition of hysteresis loops under controlled temperature and field rate conditions, ranging from 4K to 450K in temperature, and up to 9 decades in the field rate. With this instrument, detailed studies have been faced on thermal-activated effects in different systems with competing anisotropies, exchange bias, or spin reorientation transition, both at quasi-static and dynamic regimes.

The program of this thesis is first to present preliminary material as tools for the understanding of the investigation process. This material is collected later in this introduction chapter. Then we go into the main chapters. The general layout of the theis is described in the following, while a diagram of the different magnetic systems probed are depicted in figure 1.3.

The introduction covers the following basic aspects in brief, leaving for appendixes additional material in order not to make the introduction too thick. First, magnetic anisotropy is introduced in section 1.3, mentioning the different origins, and establishing the basic classification diagram. Second, a basic overview on hysteresis in magnetism is given in section 1.4, where the magnetic parameters and vectorial components are briefly explained. Third, reversal processes are discussed in section 1.5, where the different processes that will be faced during the thesis are introduced. Fourth, theoretical models are introduced in section 1.6. And finally, an introduction to vectorial MOKE magnetometry, or v-MOKE is given in section 1.7, as preliminary material for the chapter where the new setup is described. All the introduction will take some pages but the expert reader could easily step over it and proceed directly

to the main chapters.

In chapter 2 details on the new instrumental setup TRISTAN for variable temperature full angular range v-MOKE technique are given, with emphasis in what is new on the technique and how practical problems have been solved. With this brand new instrument we get access to many dynamical effects not accessible up to today.

In chapters 3 and 4 we discuss the first case of figure 1.3, where dynamical effects arise from the time-scale, i.e., from the different field sweep rates, ranging over 9 decades. The system studied is uniaxial $Co/Si(111)$ extended thin film, where reversal process would be expected to be multi-domain propagative-like. As the field rate is increased, however, this extended system develops a nucleative-like behavior which can be assimilated to coherent-rotative reversal processes. We also explore cases where even for extended systems at quasi-static regimes, nucleative processes can be observed. Theoretical models are used to determine the nature of the reversal.

Next chapter 5 is devoted to temperature-driven spin reorientation effects, and is divided into three sections, described in the following.

In section 5.1 we qualitatively review the assumption of temperature-dependent spin reorientation, at the so called Verwey transition, around 125 K, in magnetite ($Fe_3O_4$), for system epitaxially grown on $SrTiO_3(001)$. The reported anisotropy axes orientations for similar systems are here rotated by 45°. The different orientation must be associated with the substrate and the growth technique.

In section 5.2 competing anisotropies and temperature-driven symmetry breaking effects are studied for collinear uniaxial-biaxial $Fe/MgO(001)$ model system, where the intrinsically magnetocrystalline/magnetoelastic anisotropy of iron competes with growth-induced dipolar anisotropy. We emphasize in the important role that the different temperature evolutions of each anisotropy contribution play in the total temperature-dependent effective anisotropy. The importance of variable temperature full angular range vectorial magnetometry is demonstrated as a crucial tool to disentangle magnetic anisotropy contributions, that would otherwise remain hidden. We also largely exploit the different theoretical models, Stoner-Wohlfarth and Pinning/Cowburn models in a new combined method that allows to quantify the temperature evolution of anisotropy constants.

In section 5.3, a puzzling bilayer exchange biased system consisting on polycrystalline Co grown on $MnF_2$ (trigonal antiferromagnetic) is addressed. While standard negative exchange bias is seen below $MnF_2$ Néel temperature (around 67 K) upon cooling under the presence of an external field, unprecedented positive exchange bias is reported above that temperature, upon asymmetric field sweep. Here we discuss thermal-activation effects including the pinning of the antiferromagnetic moments at the interface, and puzzling field-cooling induced effects on magnetic symmetry.

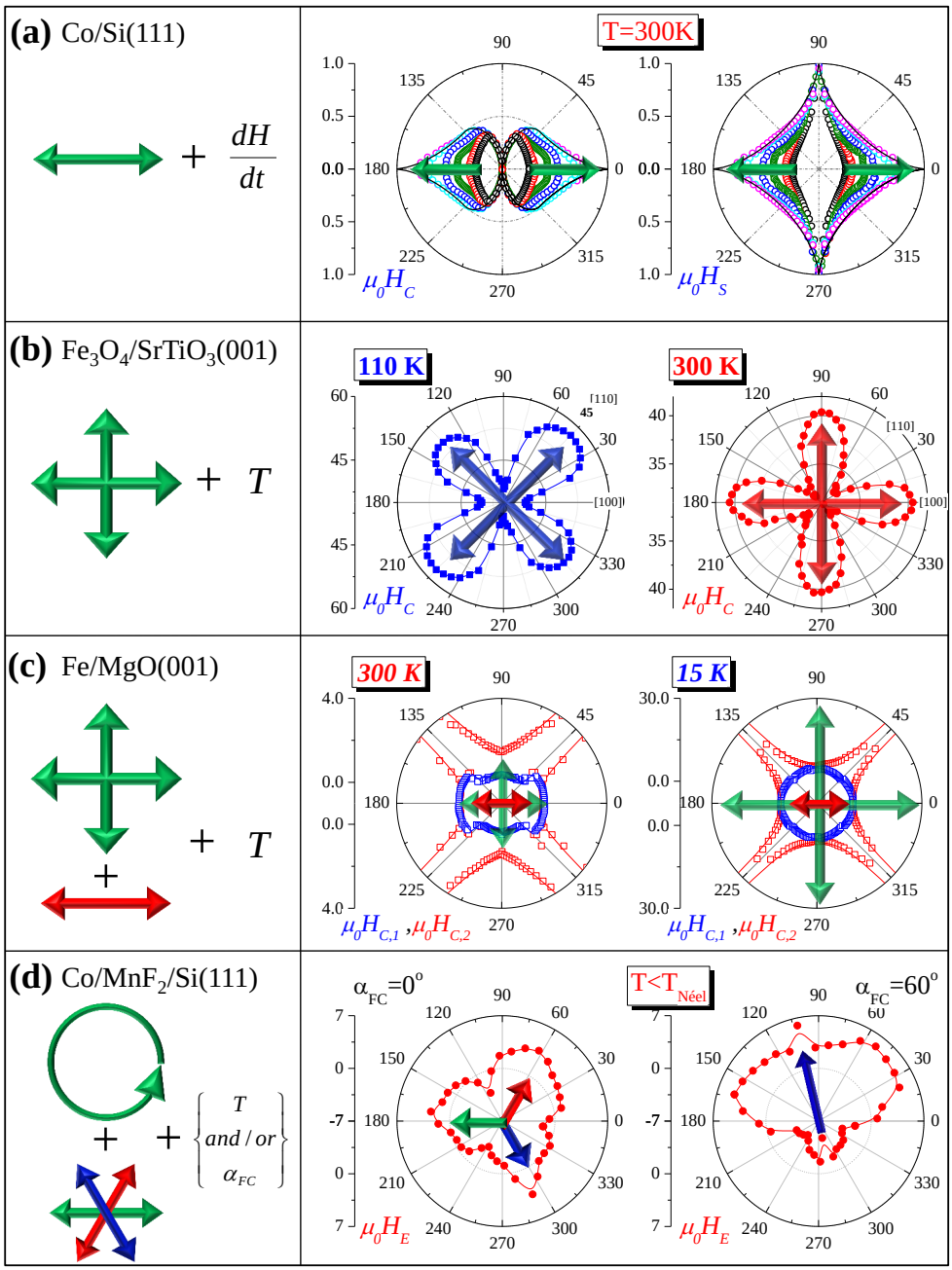


Figure 1.3: Summary of the systems probed in this thesis. Frames on the left are schemes of the magnetic anisotropies explored and free parameters used in the studies, while frames on the right are the corresponding representative examples of the vectorial angular evolution of magnetic properties observed.

## 1.3 Magnetic anisotropy

Anisotropy is the characteristic that certain systems have of giving different values for the same physical property when measured from different directions. It is a natural property in crystals due to the presence of a periodic lattice, a consequence of the orientations of atomic orbitals. In the context of magnetism this is called magnetic anisotropy, and refers to the tendency that magnetic moments have to line up on preferential directions, called anisotropy axes. Magnetic anisotropy constitutes an angular dependent energy contribution to the total internal magnetic energy.

Anisotropy energy is described by even functions of the angle (usually explained as time-reversal symmetry). Depending on the order of the anisotropy symmetry, it can be classified as two-fold (or uniaxial), four-fold (or biaxial), six-fold (or trigonal) and so on. Exchange Anisotropy is an special case, referred as one-fold, where there is no inversion symmetry, and is also called unidirectional.

Magnetic anisotropy is responsible of hysteresis (and coercivity) upon reversal of the magnetization, and its symmetry will manifest in the particular angular evolution of magnetic parameters. Hence hysteresis is a natural way to investigate magnetic anisotropy. Anisotropy has strong influence on the directions that magnetic moments adopt during reversal of the magnetization. While at high magnetic fields (saturation condition), magnetization is expected to line up close to the external field direction, as Zeeman energy term (interaction between magnetization and external field) becomes larger in comparison with anisotropy and/or magnetostatics, at low (and zero) fields, magnetic moments will reorient according to the various energy minima directions provided by the anisotropy magnetic symmetry. Regions with different anisotropy direction orientations may occur (called magnetic-domains) if their formation provides reduction of magnetostatic energy. Low field conditions happen naturally during the reversal of the magnetization, so magnetic-domains are in general present in reversal process. More on this aspects will be explained in later sections 1.5 and 1.6.

### 1.3.1 Origins of the magnetic anisotropy

Magnetic anisotropy can be classified from its origins in two contributions, those arising from spin-orbit coupling (SOC) effects, and contributions coming from dipolar interactions. Magnetocrystalline and magnetolastic anisotropies belongs to the first type, and shape anisotropy to the second.

The orbitals of the atoms in a crystal adopt specific orientations when binding is formed. As the orbital moment is tightly fixed to the crystal lattice, it can barely reorient under external field. The electron spin, however, is weakly coupled to the orbital moment, giving an energy contribution that depends on the relative orientation of the magnetization and the crystal axes. This is the origin of the magnetocrystalline anisotropy. In general, at the boundaries/interfaces of any material, symmetry breaking of crystal lattice promotes many physical effects such as dangling bonds, charge transfer/redistribution, relaxations and stress, forcing the orbitals not to follow necessarily the same bulk geometry. This reorientation originates the so called magnetoelastic anisotropy. It was introduced by Néel, and contributes decisively in systems dominated by surface properties.

Shape anisotropy is a consequence of dipolar interaction appearing due to finite

size of material, such as the interaction between magnetization and the stray field that it creates outside, or due to the interaction between different regions of a micro or nano-structured (surface or grains), such as crests in a rigged surface or steps in terrace structures. In thin films, dipolar interactions are responsible for the anisotropy to lay down into surface in-plane directions in systems where bulk anisotropy presents out of plane directions. As dipolar effects can enter in competition with surface magnetoelastic effects, there can be cases where the same thin film presents both in-plane anisotropy and out-of-plane one, depending on thickness and/or temperature [23].

It was suggested [24, 25, 26] that the effective magnetocrystalline anisotropy in low dimensionality systems could be separated into two terms, the volume $K_V$ and the surface $K_S$ contributions, that can be expressed as $K_{eff}$=$K_V$+$K_S$S/V. In the case of thin films, this phenomenological formula reduces to $K_{eff}$=$K_V$+2$K_S$/t, where t is the film thickness. However this last separation is not accepted by all authors, see for instance *A critical remark on magnetic surface anisotropy* at section 2.1.4 in [27], where arguments have been given that the surface term should be constant with t, while the 1/t term would come from other effects such as the relative increase of the bulk with thickness. It is important to mention here that, as surface/interface effects can be originated both by magnetoelastic effects (Néel theory) and dipolar effects, the separability of them from those of the bulk, in experiments, will depend on their dependencies on temperature and/or thickness.

It is then concluded that in low dimensionality systems, such as thin films, nanoparticles and in general, nanostructures where the boundaries become large with respect to bulky materials, the effective magnetic anisotropy has various contributions and in general do not necessarily present the same characteristics as that of the bulk material. Intermixed effects make it difficult then to investigate magnetic anisotropy in low dimensionality systems, and the complexity on the subject keeps even today many open questions. Bulk magnetic anisotropy is discussed in many relevant books and review articles [28, 29, 30, 31, 32, 33], while references devoted to thin films and nanostructures can be found in references [33, 34, 35, 36, 37, 38, 39, 40, 41, 42, 43, 44, 45, 46, 47, 48, 49, 50, 51]

In figure 1.4, the different magnetic anisotropies are classified according to their origins, in three categories, after the arrows emerging from the box to the left. From the box to the right, additional arrows represent the classification according to surface/interface effects and dimensionality.

### 1.3.2 Anisotropy energy

Magnetic anisotropy energy is described through power expansions of some direction-dependent functional. The constants associated to each term in the expansion are called the anisotropy constants. The structure of this expansion depends on the symmetry of the crystal.

It is customary to express anisotropy energy in a generalized way as

$$E_{ani} = Kf(\theta, \phi) \tag{1.1}$$

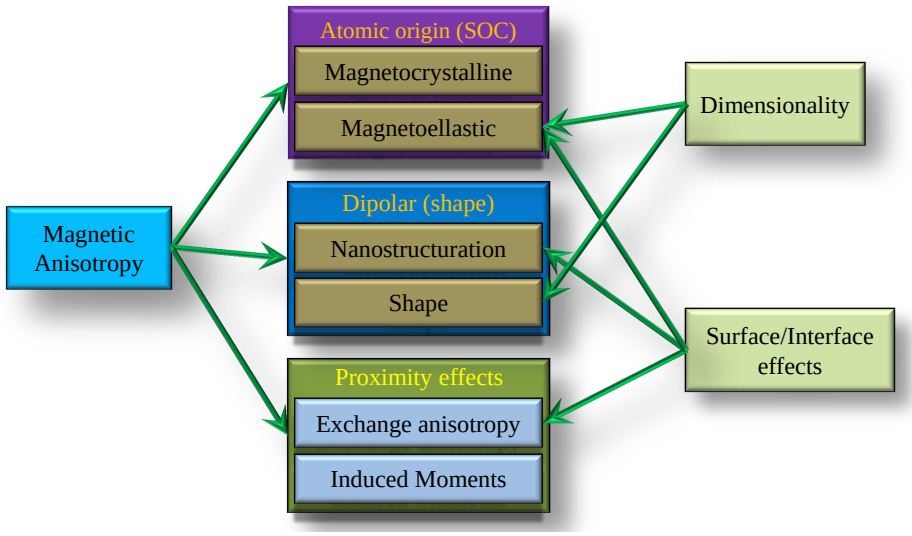


Figure 1.4: Classification of magnetic anisotropies. The three categories based on the origins are represented in the central boxes. Dimensionality and surface effects are linked to the corresponding physical aspects that they influence.

where $\theta$ and $\phi$ describe the relative direction of the magnetization vector with respect to the anisotropy axes, and $f$ is a dimensionless function. $f$ can be expressed with any set of functions complying with the crystal symmetry.

This functional in turn can also be expanded in an expansion series of functions of the direction cosines. For instance, in theoretical studies of cubic systems it can be written as [52, 53]:

$$F_A(\alpha) = K_1 s + K_2 p + K_3 s^2 + ... \tag{1.2}$$

where s=$\alpha_1{}^2\alpha_2{}^2 + \alpha_2{}^2\alpha_3{}^2 + \alpha_3{}^2\alpha_2{}^2$ and p=$\alpha_1{}^2\alpha_2{}^2\alpha_3{}^2$.

Note here that $K$ in equation 1.1 has been separated into $K_1$, $K_2$, called the first, second and so on anisotropy constants.

Supplemental material on the subject can be found in appendix A. For the scope of this thesis, when phenomenological models are used, expressions 1.1 will be enough, using for $f$ squared trigonometric functions of integer multiple of the magnetization angle with respect to one of the (reference) anisotropy axes (the integer multiple ensures the correct symmetry order). This assumption finds a natural justification in the Stohner-Wohlfarth model, but energy terms expressed in this way are also the starting point for other pinning models (see later section 1.6).

### 1.3.3 Temperature dependency

The first approach to temperature dependency of magnetic anisotropy constant in cubic crystals was given by Akulov and Callen-Callen [52, 54] in a classical framework.

They obtained a $10^{th}$ power law for $K_1$ as a function of M(T). After these works, Zener [55] improved the model incorporating a second order anisotropy constant, ending up with a $21^{th}$ power law of M(T) for $K_2$. The standard quantum-mechanical approach was given by Van Vleck [56, 57, 58], who obtained a too slow temperature dependence for $K_1$. By incorporating correlations in the framework of Spin Wave Theory (SWT), Keffer and Oguchi [59, 60] accounted for the $10^{th}$ power for $K_1$ and explained the magnetization behavior at low temperatures more accurately than Mean Field Theory. Expanded material on this can be found in appendix A.

Deviation from this laws when surface effects are present have been extensively explored in recent works, and is still an open question (see for instance [61]).

### 1.3.4 Shape anisotropy

Anisotropy originated by dipolar interaction is generally called shape anisotropy. We differentiate two types, one arising from the global shape of the magnetic object and its aspect ratio (bulk, extended thin films, spherical nanoparticles, ellipsoids) and the other originated by the micro or nanostructuration of the object and/or its interfaces (surface roughness, islands, grains, among others).

Magnetized material creates magnetic field in its outer space (stray field), that interacts with the magnetization (magnetostatic energy) and promotes many effects driven by reduction of energy, such as forcing in-plane anisotropy or promoting the formation of magnetic domains. We call this "global" shape anisotropy.

Micro or nanostructuration of surfaces or interfaces may lead to dipolar interactions as well, which depend on magnetization angle, setting preferential directions (energy minima) for it to sit on. For example, this happens in rigged surfaces or terraces, where dipolar interaction will depend on crests and steps directions, respectively. Effects of these kind can be induced by miscut surfaces or by the so called self-shadowing effects during growth under oblique conditions, among others.

In figure 1.5 a sample collection of effects is depicted. Magnetic anisotropy in the major axis of an ellipsoid nanoparticle is depicted in (a). Magnetic domain structure reducing magnetostic energy is depicted in (b). In (c) and (d) micro or nanostructured objects such as steps, vacancies, terraces and ridges are depicted. In (e) islands grown on a thin film are depicted, that also may lead to complex dipolar interactions in between and single-domain behavior inside them.

Shape anisotropy is more important in low dimensionality systems, and it may superimpose over other magnetic anisotropies. In general, the magnetic effective anisotropy will be a competition between shape and magnetocrystalline/magnetoelastic effects.

As dipolar anisotropy is directly related to the distance between the interacting objects, it is expected to have little dependence on temperature.

### 1.3.5 Exchange anisotropy and exchange bias

Exchange anisotropy is the magnetic preferential direction produced by the exchange interaction of the magnetic moments through an interface between two different magnetically ordered systems in closed contact. It was first reported by Meiklejohn and Bean in 1956 [62] and gives rise to the phenomena called Exchange Bias (EB), because

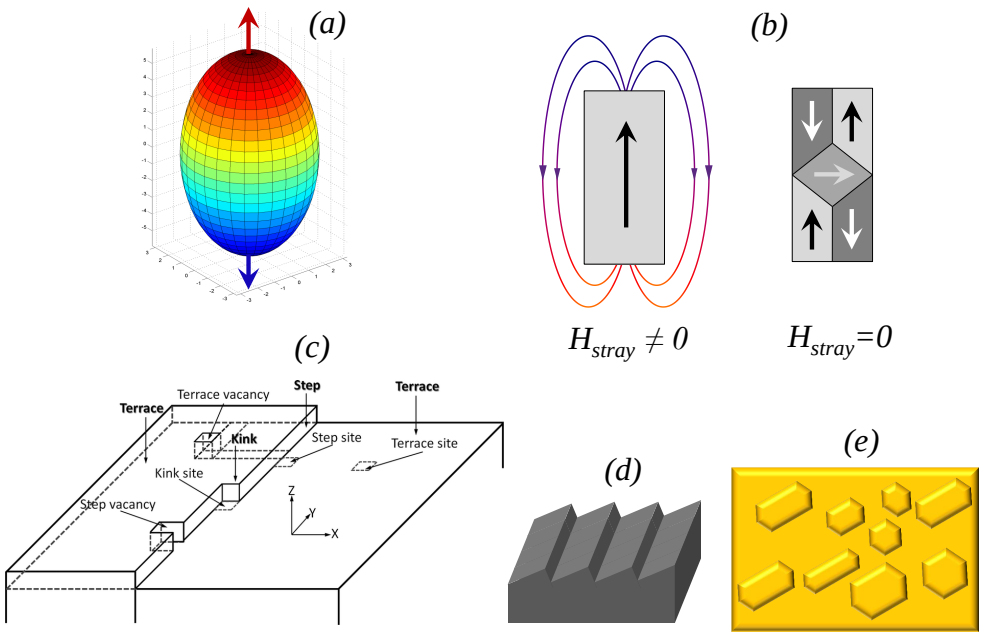


Figure 1.5: Shape anisotropy. (a) Interaction with stray field in an ellipsoid nanoparticle. (b) Magnetic domains promoted to reduce magnetostatic energy. (c) Examples of structure effects that may lead to shape anisotropy. (d) Ridged surface created after oblique angle deposition, where the ridges interact magnetostatically to give an additional surface shape anisotropy. (e) Mixed dipolar interaction landscape of islands gown on thin film.

of its manifestation in hysteresis loops as a shift (or Bias) of the loop. One of the most important exchange anisotropy systems for its technological applications is the ferromagnetic/antiferromagnetic ( FM/AFM) thin film heterosystems.

When such a system is driven to below the AFM's Néel temperature with the FM moments fully oriented in one direction (for instance using Field Cooling process, i.e, cooling under saturating field), the exchange coupling between FM and AFM moments at the interface promotes the same direction for the neighboring AFM moments (either parallel or antiparallel, depending on the sign of the exchange coupling in between), which acts as a seed for the orientations of the rest of the AFM moments upon traversing Néel's temperature ($T_N$). Below that $T_N$ the antiferromagnetic moments in the AFM layer get almost frozen, so that those at the interface act on the FM neighboring moments as if there were an unidirectional effective external field during the reversal of the magnetization. Critical fields are no longer symmetric, and a shift in the hysteresis loops (exchange bias, EB) appears.

Exchange bias phenomena is influenced not only by the orientation of the moments at the interface, but also by its mobility and compensation, the interface roughness and magnetic frustration, strain etc. giving rise to additional features in the reversal

processes and hysteresis loops.

For instance, rotatable AFM moments in the interface increase the energy required to reverse the magnetization of the FM, since those rotatable moments are dragged against the actual AFM fixed configuration, promoting an enhancement of the coercive field. In addition, the cost of dragging those moments is also directional, being more in one direction than in the opposite one, and in addition, they provide additional asymmetric rotative processes during the reversal. The hysteresis loops present asymmetries in the shape (see for instance references [63, 64] among othes. In figure 1.6 the phenomenology is schematically presented.

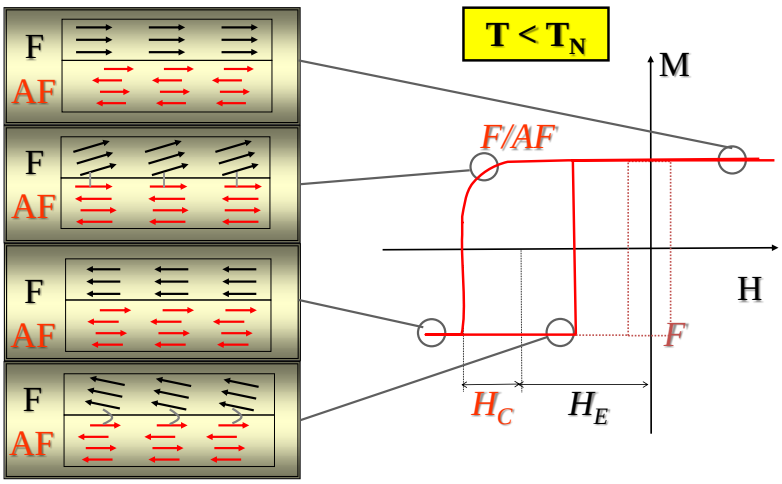


Figure 1.6: Scheme of uncompensated rotatable moments in exchange bias phenomena, with an asymmetric hysteresis loop.

The sign of the exchange bias can be negative or positive, depending on the shift direction of the loop with respect to the direction of the field cooling. While common (standard) exchange bias is negative, field induced[1] exchange bias can be positive or negative, and correlation between coupling type and the sign of the exchange bias has been reported in [65, 66].

## 1.4 Hysteresis

Magnetic hysteresis refers to a difference in the go and return pathways followed by a magnetic parameter in each semi-cycles of an external field that sweeps from initial value to final and back. The result is an hysteresis loop.

Very rich quantitative and qualitative information can be obtained from hysteresis loops such as saturation magnetization, remanence, transition (or critical) fields and

[1]Do not confuse here field induced EB with Field Cooling procedure, this last is intended to keep FM moments fully aligned during cooling down, inducing EB bellow $T_N$, while the former is a more general field effect phenomenology that can happen in many ways even at RT(chapter 5.3)

reversibility of the reversal process among others. When the hysteresis loops are examined as a function of the angle of the external field, effective magnetic symmetries can be mapped. When temperature evolution is explored, we can disentangle the different anisotropy contributions to effective magnetic symmetry.

The main technique used in this thesis to explore hysteresis is vectorial MOKE (Magneto-Optical Kerr effect) magnetometry, referred as v-MOKE for short. Vectorial hysteresis loops have revealed critical in the understanding of magnetic anisotropy.

### 1.4.1 Hysteresis in magnetism

In figure 1.7, example of in-plane vectorial magnetization hysteresis loop for a biaxial system with field applied at 30° is depicted to show the magnetic parameters that can be obtained from it. Component parallel to the external field direction appears in black and perpendicular one in red. Each loop is split into two branches, the forward (from positive field values to negative) and the backward (from negative to positive), depicted in dark ans soft colors respectively.

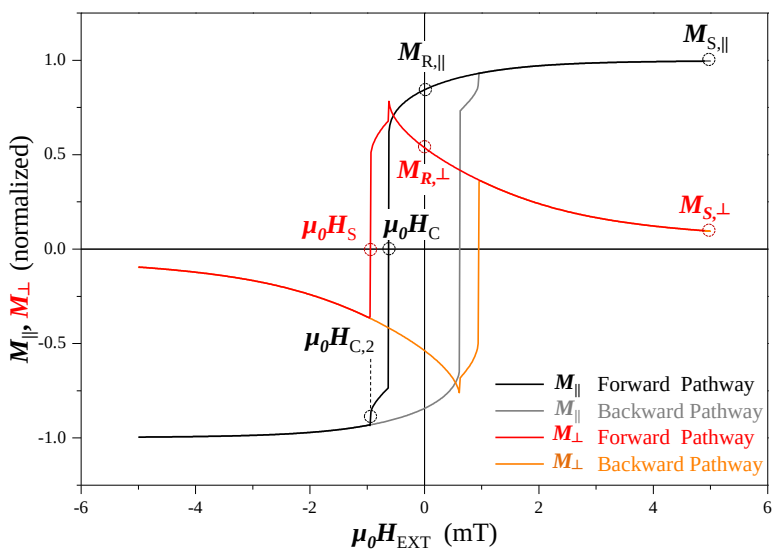


Figure 1.7: Example of vectorial in-plane hysteresis loop with the quantitative parameters that can be obtained from it. Parallel component appears in black-grey, and perpendicular in red-orange, where dark and soft color correspond to forward and backward branches respectively. Transition fields $\mu_0 H_C$ and $\mu_0 H_{C,2}$, remanences $M_{R,\parallel}$ and $M_{R,\perp}$ and saturation $M_{S,\parallel}$ and $M_{S,\perp}$ have definition in both branches (here marked only in the forward branch), in practice the mean modulus value is taken. Note that the loops are composed of rounded regions and abrupt jumps, corresponding to reversible and irreversible processes respectively.

$M_R$ corresponds to the remanence, the magnetization at zero external field, split into parallel $M_{R,\parallel}$ and $M_{R,\perp}$ remanence components. $M_S$ corresponds to the saturation, maximum magnetization value that the system can have (reached when strong external field is applied or at the high symmetry directions called easy axes). It is also split into $M_{S,\parallel}$ and $M_{S,\perp}$ components.

$\mu_0 H_C$ and $\mu_0 H_S$ are the transition fields, coercive field and switching field respectively. Their respective formal definitions are the fields at which the parallel and the perpendicular magnetization components become zero during the reversal. In general, for single jump reversal processes, these formal definitions coincide with the points at which the jumps in both components are happening. However they are not sufficient to define jumps positions when there are multiple jumps during the reversal, as is the case in the figure, where two jumps are present. In this case, the $\mu_0 H_C$ appearing in the figure would be renamed as $\mu_0 H_{C,1}$, using $\mu_0 H_{C,2}$ to define the field at which the second jump occur. It is important to note that the formal definition of $\mu_0 H_C$ in this context should be changed by the field value at which the first jump occurs rather than the zero crossing position, since in some cases, the intermediate region between the two jumps could lay right in the horizontal axes, leading to wrong coercive field for the first jump. In practice, the transition fields can be located by finding peaks in the derivatives of the loop.

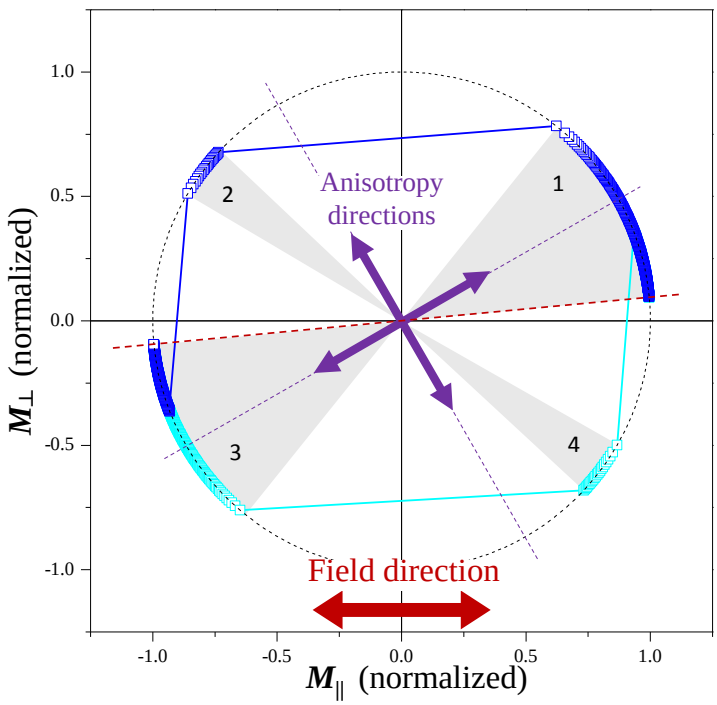


Figure 1.8: Polar plot for the vectorial hysteresis loop exhibited in figure 1.7.

Many subtleties are behind this fact. To further illustrate them, the polar plot for the loops depicted in figure 1.7 is shown in figure 1.8, where $M_{\parallel}$ is in the horizontal axis, and $M_{\perp}$ is in the vertical one (using symbols for more visibility). As can be seen in the figure, the dark blue pathway corresponding to the forward reversal branch presents a first rotative region (shaded region 1), followed by an abrupt jump that happens from the first quadrant to the second, i.e., from the limit of rotative region 1 to the beginning of rotative (shaded) region 2. At this position the magnetization has switched no more than 150° with respect to the initial saturating angle direction, and the perpendicular component of the magnetization is still positive. It can also be viewed in this way: the magnetization has jumped from shaded region 1 to 2 which cannot be considered a full reversal of the magnetization vector, only the parallel component has changed its sign. Nevertheless, this jump is an irreversible transition, the first step in parallel component in figure 1.7. In the second jump, when the magnetization jumps from the shaded region 2 to the shaded region 3, the quadrant where it arrives is the opposite one with respect to the quadrant where the magnetization was at the initial saturation point. So after this second jump the magnetization is considered to have suffered a real switching (close to 180°), and now the perpendicular component has changed its sign. This switching field coincides with $\mu_0 H_S$ of figure 1.7 and generally (but not always) also coincides with $\mu_0 H_{C,2}$. This is why in general the switching field $\mu_0 H_S$ is associated with the moment in which the magnetization truly reverses. Another way of seeing is this: at positive external field, magnetization is inside shaded region 1, and when the field overcomes $\mu_0 H_S$, the magnetization vector will be in shaded region 3, which is the reversed region from 1, although not necessarily in a fully opposite direction with respect to the initial saturating direction: notice that when $\mu_0 H_S$ happens, the magnetization does not jump in this case to the exact opposite direction from the positive saturation direction (marked with the red dashed line, side of the region 1), but it rather jumps to the point signaled with the short green segment, and from there, rotation (dragged by Zeeman interaction) happens until it reaches the red line for the negative saturating direction, i.e., the true opposite direction with respect to positive saturation direction. So switching field is closer to the true reversal of the magnetization. For single step transition, the panorama is more simple, only one $\mu_0 H_C$ is present, and $\mu_0 H_S$ marks the point for the switching. More complex transitions with three or more steps can happen (not explained in this thesis).

### 1.4.2 Hysteresis and anisotropy

Hysteretic behavior is naturally linked to magnetic anisotropy, as already introduced in section 1.3. As anisotropy axes establish preferential directions for the magnetic moments to sit on, reversing the magnetization of a systems necessarily implies overcoming the extra energy provided by anisotropy, so that the position at which magnetization reverses is no longer happening at zero field but at a finite external field which is usually (but not necessarily, see for instance EB phenomena) of opposite sign with respect to the initial saturating field, leading to open loops, i.e., hysteresis loops. A simplistic analogy of hysteresis can be made with spring and dashpot system, where spring action is associated to a (unrealistic) linear response of magnetization to the external field, while the dashpot effect (a viscosity term in the dynamical differential

equations of the problem), is represented here by the anisotropy. This very simplistic analogy shows open loops and field-rate dependence of the coercivity. Some suplementary material about the relation between hysteresis and anisotropy can be found in appendix B, section B.1.

### 1.4.3 Reversibility

Reversibility of reversal process means that the magnetization follows the same pathway back to an initial state as the pathway that it followed from that initial state to the point where the external field is reversed. When looking at an hysteresis loop as a whole, i.e., when the field sweep goes from positive saturating field, to negative and back, the whole process is in general irreversible in the overall (open loops). However, locally the hysteresis loops may present regions where the process is happening in a reversible way. This reversible regions correspond to rounded sections of the pathway present before abrupt jumps, in between, or after them. This processes are rotative, as will be discussed in next section. Additional supplementary material can be found in appendix B, section B.2.

### 1.4.4 Angular dependence vectorial hysteresis

In this thesis we will demonstrate that angular vectorial magnetometry is a valuable tool to investigate magnetic anisotropy. First, vectorial magnetometry supplies accurately all the parameters required to identify transitions (not easy to do with just one component), and second, the angular evolution of the magnetic parameters reproduce the symmetries associated to the effective magnetic anisotropy, revealing the fingerprints of the reversal mechanisms. In general, complementary information taking various vectorial parameters is necessary. This question will be clear when we face the chapter 5.2. More aspects have been added as supplemental material in appendix B, section B.3, while in the main chapters of the thesis, this question will be reinforced in practical investigations.

## 1.5 Reversal processes

Reversal process refers to the way that the magnetization reverses from a saturation state in one direction to its opposite one, and how this takes place in terms of magnetic moments. In bulk homogeneous systems, reversal can take place in different ways depending on magnetic anisotropy, size and shape effects, and boundaries with other materials, among others. Size and shape appears to be critical in low dimensionality systems, such as thin films and nanoparticles. In addition thin films consisting of inhomogeneous multilayers present interface phenomena that can be large with respect to bulk effects, determining features in the reversal that would not be present in the bulk. Facing the study of reversal process necessarily requires to account for many microscopic details. However a phenomenological treatment based in basic microscopic assumptions is also possible, as will be seen in the section 1.6 devoted to theoretical models .

Two different reversal mechanisms are considered. One is single-domain reversal processes, usually referred as "coherent rotation", where the magnetic moments either rotate coherently, and/or switch all at once, keeping always the same parallel alignment in between. This mechanism is also known as "macrospin" behavior, as the whole systems behaves as if there were a single moment with saturation magnetization magnitude. It is a mechanism mainly associated to small particles where multi-domain structures are unfavorable, and was established and satisfactory described by E.C. Stoner and E.P. Wohlfarth in 1947 [9, 67]. For this reason, this reversal mechanism is also referred to as "Stoner-Wohlfarth model" (SW for short).

The other mechanism is multi-domain reversal processes, consisting on the formation (or nucleation) of regions with reversed magnetization in an initially magnetically saturated system, called domains, and subsequent expansion of the domain walls (DW) that separate those domains from their surrounding, under the field pressure, until the whole system's magnetic moments are reversed. The DW is defined as the region over which magnetic moments rotate smoothly to accommodate the magnetization at each sides of the wall. The existence of magnetic domains was first stated by Pierre Weiss in the context of Mean Field Theory. Multi-domains in reversal mechanism were studied by Bloch, Néel and Becker-Kersten [68]. Various models for multi-domain reversal processes have been developed, and in particular in this thesis we use the model developed by Cowburn et al. between 1995 and 1997 [16] [21], based on a description of the domain wall motion as a process in which a pinning energy must be overcome to make propagation possible. The formation of multi-domains is promoted by the reduction in dipolar interaction between the magnetization of the system and the stray (and or internal) field it creates (also known as magnetostatics), it is naturally associated to extended system, and it generally happens at low field values, where Zeeman energy cannot compete with anisotropy and magnetostatics.

Details on both models are given in next section 1.6, and expanded in appendix E.

Both single-domain and multi-domain behaviors present reversible and irreversible transitions during the reversal. The way that transitions happen and the critical fields depend on the directions of the anisotropy axes with respect to the external field direction. In general, reversal (rotative) processes happen at high field regimes, and they manifest as rounded regions in the hysteresis, while at low field regimes, irreversible (abrupt jumps) transitions happen as anisotropy energy becomes more relevant, and are associated to switching of the magnetic moments between directions close to anisotropy axes, either in a single-domain (coherent rotation) or multi-domain way (nucleation and DW propagation).

As the relevance of each mechanism depends also on dynamic effects, different behaviors might appear in the same system when varying temperature and field rates. A very good introduction to the subject of dynamics can be found on O. Fruchart's lectures [22].

### 1.5.1 Coherent rotation

This reversal mechanism describes well the experimental behavior of systems where formation of domain walls are unfavorable and only single-domain can happen. It is in general ascribed to nanoparticles, the context where the theory was initially formulated. It will be shown in chapter 3 that under certain circumstances, extended

systems may behave in a single-particle fashion.

Coherent rotation reversal mechanism is fully understood in the framework of energy balance between anisotropy and Zeeman energies. For practical description, the anisotropy energy will be defined as even functions with the adequate periodicity to reproduce the symmetries of the magnetic anisotropy involved, giving minimum positions at the anisotropy axes, thus promoting alignment of magnetization on the closest minimum. In general, trigonometric functions are used, which encounters its justification after Stoner-Wohlfarth works. On the other hand the Zeeman energy (interaction between magnetization and external field), arises from the scalar product of $M$ and $H$, so that it is a cosine function (one-fold) with energy minimum at field direction, promoting the alignment of magnetization with the external field. The final direction of the magnetization will be the minimum of the total internal energy so defined.

### 1.5.2 Nucleation and domain wall motion

In this kind of reversal mechanism, in the field region where transitions happen, the reduction of dipolar electrostatic energy due to multi-domain structure makes nucleation of small region of reversed moments and subsequent domain wall motion a more favorable process than coherent switching of the magnetization. A multi-domain reversal process is expected then to happen, provided that the energy cost of forming domain walls is balanced by the reduction in the dipolar energy that the system would have in a single-domain state (uniformly magnetized). In addition, DW must have room enough to form, and this depends on the relative dimensions of the system and the DW thickness. DW thickness depends on the magnetic anisotropy, as a $1/K$. If the system is not big enough to support the wall, its formation becomes energetically unfavorable and the reversal process will be single-domain like. For completeness we mention here that the distribution of magnetic moments through the DW can be classified in two types, depending on whether the misaligned moments evolve parallel with the domain wall or perpendicular to it (referred to as Bloch's wall or Néel's wall respectively).

Multi-domain reversals comprises a combination of nucleation processes and expansion of domain walls in a certain proportion. Dominant effect, nucleation or propagation of DW depends on dynamical aspects. While in general at low field rates the process is mainly propagative, i.e., nucleation of a certain amount of reversed domains with subsequent domain wall expansion, at high field rates it is nucleative, where the nucleation happens faster than the time that takes DWs to expand, and hence the system reverses by population of nucleated regions. Models to account for both nucleative and propagative mechanisms have been developed by Néel (nucleative processes) and Bruno (DW motion), each one proposing an activation energy for micro-domains nucleation and DW motion respectively (see for instance summary article by Raquet et al [69])

Domains are easy to create at defects, impurities, boundaries and inhomogeneities. Once a domain is formed, its expansion also depends on defects and inhomogeneities, since they act as pinning centers, with associated energy barrier (due to interaction between DW and defects, having an associated stress field) that must be overcome. The wall is retained here until the field provides the energy required to overcome

it, allowing the domain wall to expand to the next (eventually higher in energy) pinning boundary. First suggestions on pinning effect was given by Vicena, followed by important works from Kronmuller and coworkers (compilation material can be found in book [70]).

Figure 1.9 shows a (naive) example of propagative process where DWs expands after nucleation in defective regions. In sketch (a) two nucleation regions have been depicted, and then the system evolves by domain wall propagation process as in sketches (b) to (f). Small circles are simple representations of pinning centers where domain walls encounter energy barriers for their motion. In figure 1.10, a nucleative reversal is illustrated, where the propagation of the DW have no time enough to cover a certain distance before the external field has provided more energy for additional nucleation of domains.

For simplicity in the previous explanations, we have used the term "reversed domains" in the sense of 180° reorientation, with 180° DW. In general domains are able to nucleate at different angles, depending on the symmetries of the magnetic anisotropy and the angle of the external field. For instance, a two step reversal in biaxial systems corresponds to a sequence of two processes of nucleation and subsequent DW propagation with domains at 90° in both steps.

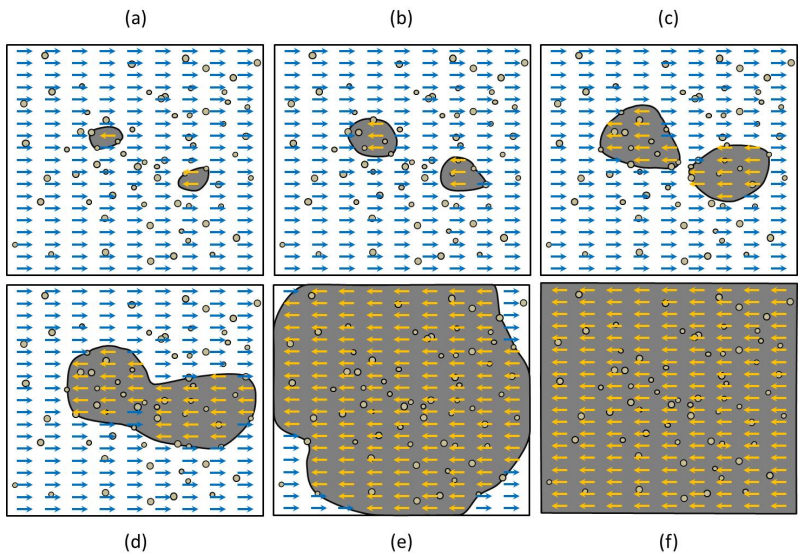


Figure 1.9: Figures (a) to (f) shows a sequence of domain wall expansions after a few magnetic domains have been nucleated. In this sequence, only 2 nucleation regions have been formed at the initial stage, and the system has time enough for the domain wall expansion to happen.

In order to account for nucleation and domain wall propagation processes as reversal mechanism, various phenomenological models have been proposed, for instance, Givord et al. proposed (for uniaxial systems) the model known as starting field

theory [71] that was further improved by Gao and Zhang [72], based on nucleation energy, while Cowburn et al. proposed in 1995 [16] a pinning model for uniaxial-biaxial collinear system for ultrathin Ag/Fe/Ag(1OO) epitaxial films. Haesendonck and coworkers proposed a generalized pinning model for uniaxial-biaxial systems with arbitrary relative orientation between both competing anisotropies [73].

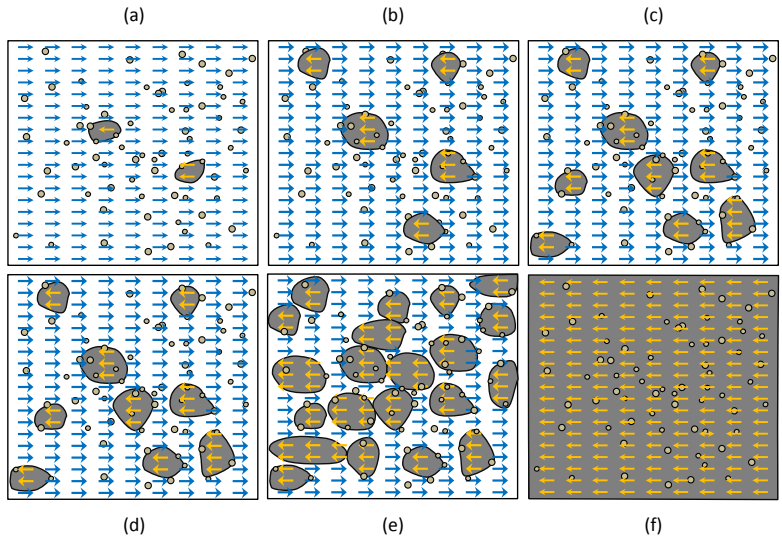


Figure 1.10: Figures (a) to (f) shows a sequence of a nucleative process, where domain walls have no time enough to expand before other domains are nucleated..

### 1.5.3 Thermal activation in reversal processes

As already introduced earlier, the reversal of the magnetization is related to the so called "switching" events. A switching event happens when an energy barrier separating two different magnetization directions falls over. The energy barriers are affected by thermal fluctuations. Spins are constantly undergoing attempts to switch at the so called "attempt rate" (average rate at which a spin tries to reorient). Both macro-spin (coherent rotation) or multi-domain (nucleative and/or propagative) reversal processes depends on this two aspects that establishes dynamical conditions for the reversal.

In the context of macro-spin reversal process, thermally activation energy contributes to overcome a single energy barrier, while in the context of multi-domain reversal, a distribution of energy barriers must be accounted for. Two complementary phenomenological models describe these situations, one is the Néel model [74], and the other one is the Bruno model [75, 76]. Both models introduce thermal activation in the reversal process through a relaxation time parameter. Differential equations for the dynamics of the magnetization vector are solved, with this relax-

ation time defined under certain hypothesis on the micro-domain behavior during the reversal. The functional dependence of the relaxation time will be different depending on whether the process is nucleative or propagative. It is through this relaxation parameter that the dynamical behavior and the temperature enter into play on the reversal processes. A direct overview of both models can be seen in the reference from Raquet et al, [69]. The Néel model corresponds to reversal mechanisms where domain wall motion is favored after some nucleation of micro-domains, and the system evolves during the irreversible transition by a rapid domain wall expansion, while the Bruno model corresponds to mechanism where the micro-domains are rapidly populated, letting very little time to the domain walls to expand, before all the system is covered by reversed micro-domains.

Supplementary material can be found in appendix D, and more details on the phenomenology can be found in O. Fruchart's lectures [22].

## 1.6 Theoretical models

Theoretical models for magnetization reversal mechanisms are very useful to interpret hysteresis loops and the angular evolution of the magnetic parameters, helping in disentangling and quantifying effective magnetic anisotropy. Here we give a brief introduction to two phenomenological theoretical models used in this thesis, already mentioned in previous sections, and the ambit of their applicability is explained. One is the Stohner-Wohlfarth (SW) model for coherent rotation, and the other is the Cowburn (CW) model for DW propagation in collinear uniaxial-biaxial systems. They are easy to implement in a computer, and specific software has been developed on purpose during this thesis to better suit our needs. Extended details on both models together with some description of the developed software can be seen in appendix E, while here we limit to a brief discussion of what each model accounts for.

### 1.6.1 Stoner-Wohlfarth model

The SW model relays on energetic considerations and a minimization process with respect to the final magnetization angle. Energy is expanded in anisotropy energy terms and Zeeman energy, which are functions of the anisotropy constants and its geometry, and of the external field strength and direction, respectively. Magnetization magnitude in SW model is always constant and equal to its saturating value. As a consequence, the magnetization either rotates or switch at critical fields during the reversal.

The model in general explains very well the behavior of single-domain reversal processes, giving a correct view of the angular dependences of the magnetic parameters. In systems where the reversal mechanism is multi-domain, in general the model fails to predict correctly transition fields, especially around easy axes, and other important aspects observed experimentally. However, the reversible parts of hysteresis loops, away from critical fields, are expected to be well explained by SW model, as these regions are mainly dominated by rotative process. This fact will be satisfactory exploited in later chapters. Close to hard axes the model is also expected to work fine, as these angular regions are also governed by rotative processes. For pure anisotropy systems, the symmetries are also well predicted, despite its fail to fit other

parameters. As remanence and saturation are magnetic parameters typically away from critical fields, i.e., in the regions where rotative process governs the reversal, SW model also accounts well for these parameters even in systems where the reversal is not single-domain.

### 1.6.2 Cowburn model

The CW model [16, 21] is based on the assumption that at low fields during the reversal the magnetic moments are aligned with anisotropy directions creating domains, and the reversal takes place by a set of transitions or jumps between single domain states. A jump happens upon expansion of the DW that separates a single domain state from small domains with other magnetization direction nucleated as the field is reversed. The DW is classified by the difference in angle of the magnetic moment's orientation (also called domain orientation) at each sides of it, and we refer to this as "DW angle". The expansion of the DW requires energy (provided by the external field), called depinning energy, that depends on the DW angle. The model considers only a maximum depinning energy for each DW angle, and once this energy is provided by the external field, the DW is considered to expand freely. For a certain anisotropy geometry (Cowburn model was born for collinear biaxial-uniaxial systems) different orientations of the single domains can happen, each one with its corresponding magnetic energy expressed as in the SW model. Upon reversal, jumps happen between domains of different orientations. In general various routes of jumps are compatible in a reversal process, and they compete energetically in between. The more favorable jumps in terms of energy (those that will give lower coercive field value) will happen, establishing the route that will be realized in the reversal. Energy of a jump is calculated by the energy difference of the corresponding single domain states taking part on it. The coercive field of each jump is related to the depinning energy of the associated DW. At certain directions, this depinning energy has a direct relation with coercive field, establishing the phenomenological way to obtain them.

The model does not include nucleation activation energy or time scales for the DW motion, and does not use distributions of depinning energies, but single maximum energy for each DW angle. As this model was developed for uniaxial-biaxial collinear system, only 90° and 180° DWs are considered.

Under these assumptions, CW model allows to directly calculate maximum DW depinning energies, reversal routes, and the corresponding coercive fields, for each angle of the external field. However cannot account neither for remanence, nor for saturation values (see later in section 1.6.4).

Details of the mathematical formulation of the model, and the implementation of software to simulate the angular evolutions of the critical fields are shown in appendix E, section E.2.

### 1.6.3 Resembling models

The CW model reproduces quite well the angular dependence of transition fields and gives the transition route (number of steps), but does not draw the complete hysteresis loops, since it only computes coercive fields.

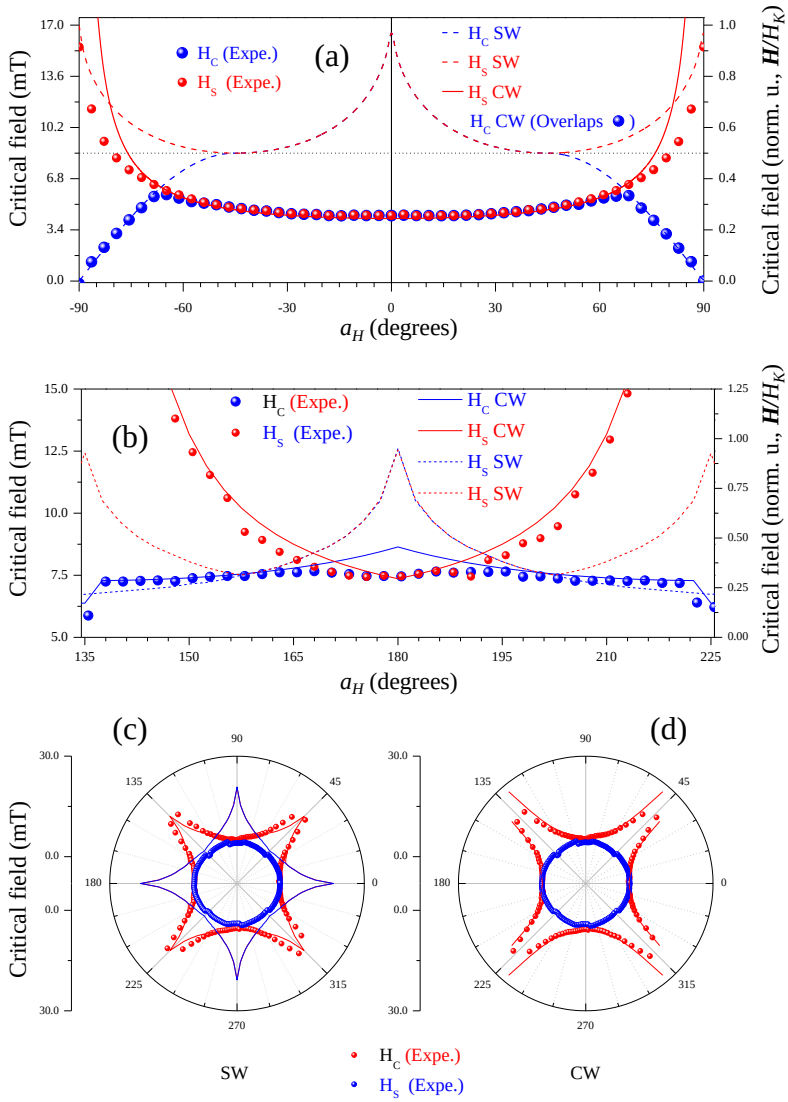


Figure 1.11: General comparison between SW model and pinning models, explained in the text. (a) SW v.s. pinning in uniaxial model system; (b) SW v.s. CW model in biaxial-uniaxial system; (c) Polar plot with SW (left) and CW (right) for the same system as in (b).

We assume that away from critical fields, the reversal process must occur according to rotative process in single domain states. So building a CW hysteresis loop would consist on taking SW loops and change the position of the irreversible transitions by the positions predicted by CW, leaving the reversible parts intact (however some

complexity on this resembling process would appear in the regions between two jumps in multiple step transitions, where more considerations should be done).

This idea will appear implicitly (but without explicitly going into the complexity of resembling loops) in the quantification of anisotropy constants that will be shown in chapter 5.2, where a combined method is established with remarkable results.

It is interesting to say that CW provides lower coercive fields than SW, because coherent switching of the magnetization has a higher energy cost than the cost of nucleating domains and expanding the DW. For this reason, in systems with SW like behavior the angular distance that the magnetization covers before switching, after surpassing the anisotropy axes, is higher than in systems with multi-domain reversal behavior. In fact, CW predicts no surpassing of the axes at all, while real multi-domain systems present some surpassing of the anisotropy axes, which is related to the starting point of the nucleation process, the depinning distribution of energies and the balance between nucleation and DW motion, among other effects.

### 1.6.4 Strengths and weaknesses of each model

A global revision of both models allows to establish a comparison between SW and CW.

SW works very well for single-particle systems in all the magnetic parameters and their angular dependence. For extended systems, it still accounts quite well for $M_{SAT}$ and $M_R$, since they are (in general) measured far from irreversible transitions. However, as the transition fields are very sensitive to the reversal mechanism, the SW model fails to compute them correctly around easy axis regions. Around hard axis, where the reversal process is mostly rotative, it works rather well. The symmetries given by SW for transition fields should be correct, but that is not true for certain intermixed anisotropy systems, such as uniaxial-biaxial competing anisotropy systems (see later chapter 5.2). CW model works really fine in those cases, both for computing transition fields and their angular evolution. In turn CW does not compute $M_{SAT}$ and $M_R$, as already stated.

It can be seen that in general, calculations of transition fields in pinning models around hard axes are less accurate and tends to diverge, while SW tends to converge. On the contrary, once we move away from hard axes, pinning models become better.

In figure 1.11 a joined SW and pinning models are presented, with a real experimental data for some of the systems studied in this thesis. Figure 1.11(a) corresponds to a comparation between SW and pinning model for uniaxial system. Notice that SW fails to account transition fields in a large angular region around easy axis, where pinning models are very accurate. Upon approaching hard axis, SW gets closer to experimental values, while pinning models tends to diverge. In figure 1.11(b), CW pinning model and SW models are compared in a biaxial system with a very small collinear parallel uniaxial contribution, with ratio of $K_1/K_2$ around 0.02 (this is an advance of what will be seen in later chapters). In this case, SW model is not capable of detecting the presence of uniaxial contribution, while CW is very sensitive to it. The difference between the two models is dramatic. In 1.11(c) and (d), polar plots for this same case allows to have a global overview of this issue. Notice that SW, at the scale of the figure, presents its maximum discrepancy at easy axes. At hard axes, both seems to work well, although SW rapidly separates from experimental as you

move away from hard axes, while in this case, CW still works well here.

## 1.7 MOKE magnetometry

Here we introduce the vectorial Magneto-optical Kerr Effect magnetometry (MOKE) developed in our group in recent years, as a preparation for the description of the new instrument developed during this thesis, called TRISTAN, (described in chapter 2) created to face the study of thermal and dynamical effects.

MOKE magnetometry is one of the most widely used techniques for the characterization of magnetic nanostructures [77, 78, 79], because of its high sensitivity (down to nanometer thickness), its limited penetration depth (avoiding substrate effects) and the immunity to external fields, this last aspect is because no charged particles are used, since it is a photon-in/photon-out probing method. In addition, it can be implemented in relatively simple experimental set-ups. The main technique that has been used in this thesis is vectorial MOKE (v-MOKE), where simultaneous acquisition of two magnetization components (usually in-plane) can be realized.

### 1.7.1 Kerr effect and its application as experimental technique

Polarization and intensity of light propagating in a magnetic media present dependence on the magnetization state of that media. It was Faraday in 1845 who observed polarization rotation for light traversing magnetized materials, and later in 1877 J. Kerr observed rotation of polarization upon reflection of light in magnetized surfaces [77]. Today the term Kerr effect is used to refer both polarization and intensity changes upon reflection in magnetic materials. The effect can be described in two contexts, the macroscopic dielectric theory or the microscopic quantum theory. In the macroscopic approach, the effect can be explain through the dependence that the dielectric constants have with the magnetization state of the media in which light propagates, a dependence that makes the antisymmetric part of the dielectric tensor anisotropic. To account for the effect Maxwell proposed that a linearly polarized light could be described as a superposition of two circularly polarized components, and that both circular modes had different velocities of propagation due to the difference in the dielectric constants of left- and right-circularly polarized light (circular birefringence). The combination of both components after traveling through a material media leads to polarization rotation in the resultant wave. Detailed mathematical demonstration (including reflectivity changes phenomena) in the frame of macroscopic dielectric theory is given in appendix F. The first account for the application of the Kerr effect to the investigation in magnetism came in 1985 with experiments by Moog and Bader on Fe epitaxially grown on Au(100) [80].

### 1.7.2 Vectorial MOKE

Polarization rotation and reflectivity changes are directly linked to the parallel and perpendicular components of the magnetization with respect to the optical plane (see appendix F). In general this means that the two in-plane components of the reflecting surface can be accessed through this changes. The possibility of *simultaneously* and

*quantitatively* measuring both when the sample is subjected to an external field sweep gives access to vectorial Kerr magnetometry. This technique has been developed in our group to accomplish full angular vectorial studies [81] at room temperature, permitting us to perform automated angular-dependent magnetic measurements of different magnetic nanostructures at room temperature without the need to change Kerr geometry in the process [82, 83, 84, 85, 86, 87, 88]. We have coined for this technique the term v-MOKE to emphasize on the vectorial capability and simultaneity of the acquisition of both components.

To understand better the advantages of v-MOKE technique, note that in standard MOKE techniques only Kerr rotation is exploited by using different Kerr geometries to obtain the different components of magnetization with respect to the applied external field. This normally requires tedious physical changing of optical components, magnet and/or sample orientation with respect to the optical plane to complete a single vectorial measurement [89, 90, 91, 92].

In practice, simultaneous acquisition of polarization rotation and reflectivity changes is possible by using a combination of a Wollaston prism and a twin phtodiode (TP), so that reflected light is split into its two polarization components, parallel and perpendicular to the optical plane respectively, and each one is redirected to one of the photodiodes. The summation of signals in the TP leads to reflectivity changes and its difference leads to polarization rotation.

### 1.7.3 Practical realization of v-MOKE technique

After the mathematical development (see Appendix F) we end up with the following expressions for the intensity variation and polarization rotation upon reflection of linear polarized light on a magnetize surface (only expressions for p-polarized are presented here):

$$\frac{I_{\Delta}}{I_{\Sigma}^{\mathrm{DC}}} \propto m_x, \tag{1.3}$$

$$\frac{I_{\Sigma}^{\mathrm{AC}}}{I_{\Sigma}^{\mathrm{DC}}} \propto m_y \tag{1.4}$$

i.e., Kerr rotation and reflectivity changes are proportional to the two in-plane components of the magnetization $m_x$ and $m_y$, respectively.

Practical realization of v-MOKE, consist on the detection of both polarization rotation and reflectivity changes in a simultaneous measurement. This is carried out by using a TP. The polarized beam reflected on a sample which is undergoing changes in its magnetization state driven by an external field, will consist on a polarized beam where the polarization and the intensity are varying around a certain direction and intensity values respectively, and having a certain ellipticity. In figure 1.12 the two first effects are depicted. Notice that the incident polarization is set to 0° in the figure 1.12(a), i.e., we have chosen p-polarization, but the reflected beam characteristics ($\vec{E}$ and $\epsilon$) have been depicted at 45°. This fact together with the suppression of the ellipticity in the drawings will be clear later. Polarization rotation is really small, tenths of a degree at most, so that in this figure, its angular range has been

exaggerated for clarity. Figure 1.12(a) shows the region (soft red) where the amplitude of the electric field is varying. In order to simultaneously measure reflected intensity and rotation variations, the reflected beam is decomposed into its p and s polarization components by using a Wollaston prism, that sends each component to its corresponding photodiode in a TP detector. In order to get similar intensities in both photodiodes, so that both work in the same intensity regime, it is preferable to have the polarization rotation happening around 45°. This is achieved by using a half wave plate before the Wollaston prism, so that we can rotate the polarization average angle to force it to vary around 45°. The suppression of the ellipticity referred above now comes for free, since using a half wave plate suppresses its contribution (see details in appendix F). In 1.12(b), the squared electric field components are depicted (photodiodes are sensible to intensity, i.e. square electric field), so that the region of variation is now constrained to the soft red sector. The blue arrow arc of the sector represents the polarization rotation $\epsilon$ while red radial arrow represents the sector width, where the squared of electric field, i.e., intensity, is varying. Decomposition into p and s polarizations gives the two squared electric field components, i.e., the two intensities sent to the corresponding photodiodes by the Wollaston prism. The addition of these variations, represented by the blue horizontal arrow and the red vertical one, directly give intensity variations, while its subtraction accounts for polarization variations (additional argument is required that the amplitude of the rotation is small enough as to approximated the blue arc that constitutes the sector to nearly straight line, otherwise, some trigonometric operation would have been required).

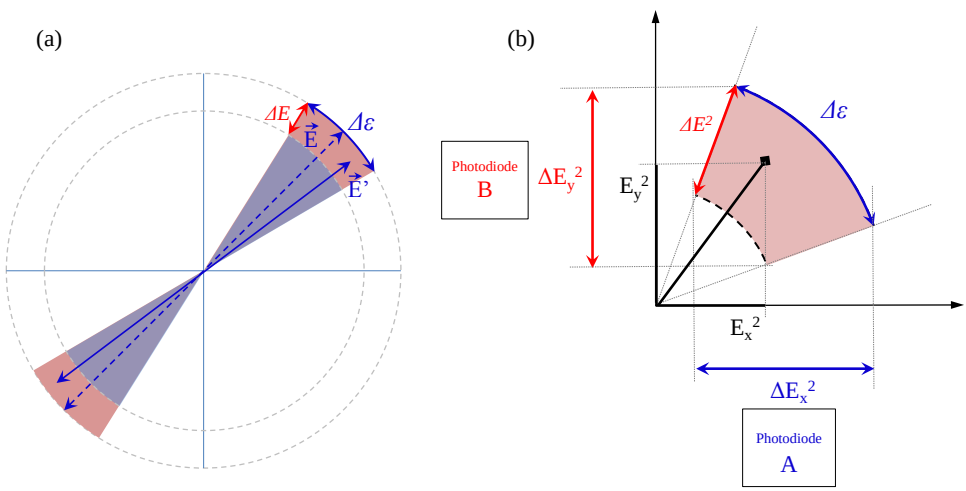


Figure 1.12: Representation of the two main effects, reflectivity changes and polarization rotations. In (a), as seen by the electric field vector, and in (b), as seen through the intensities, i.e., as the square of electric field components. Details are explained in the text. The practical set-up can be seen in figure 1.13.

In figure 1.13, the practical implementation of the technique is depicted, with all the basic components used and a representation of the instrument. Effect of polarization rotation and reflectivity changes are depicted in the reflected beam. The magnetization components have been depicted as well as their relation with the photodiodes intensities. The TP detector, where photodiodes have been named A and B, has three outputs, the total intensity, after A+B, the intensity changes as the AC component of A+B, and the rotation variations as A-B. The total intensity is used to normalize.

More information on the signal processing and errors are detailed in the appendix F, and some additional details are included in chapter 2.

It is customary in all the v-MOKE instruments to keep external field fixed and rotate the sample to perform full angular range v-MOKE (i.e. Kerr geometry is fixed). The angle of the sample with respect to external field will be referred to as $\alpha_H$, as seen in figure 1.14, where diagram of sample layout is depicted. Note that this convention adopted for the angles are in accordance with convention used in the SW simulation software and CW calculations (see figure E.2 in appendix E).

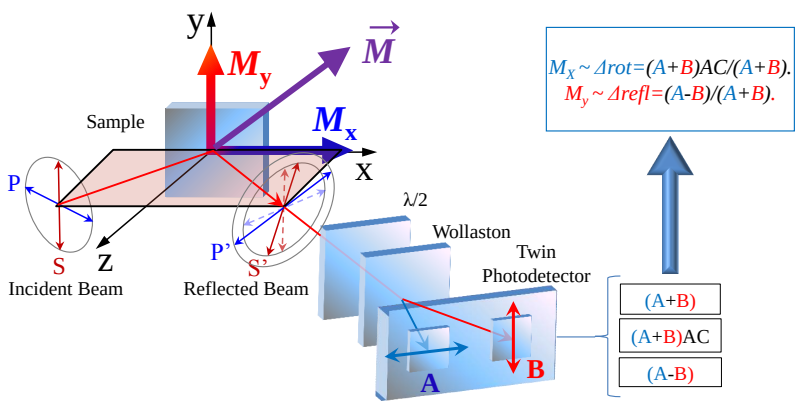


Figure 1.13: Practical realization of the signal detection depicted in figure 1.12. Incident p or s-polarize beam (blue or red double arrows inscribed in a circle left side of Z axis) is reflected on the sample, that has in-plane magnetization $\vec{M} = \vec{M_X} + \vec{M_Y}$. Upon reflection, the reflected beam undergoes changes in intensity, polarization and ellipticity (the last one is not depicted), represented by corresponding new blue or red arrows (circle at the right side of Z axis, original beam now in dashed double arrows). The reflected beam traverses the $\lambda/2$ retarder, suppressing ellipticity and allowing to align the polarization angle in a more efficient way to detect its variations (i.e., to 45°). Then the beam is split into two horizontal and vertical components that are redirected to photodiodes A and B of the TP. The AC-sum and the difference of the signals at the TP are proportional to reflectivity changes and rotation respectively, and hence, through equations 1.3, to $M_{\parallel}$ and $M_{\perp}$ [81, 93].

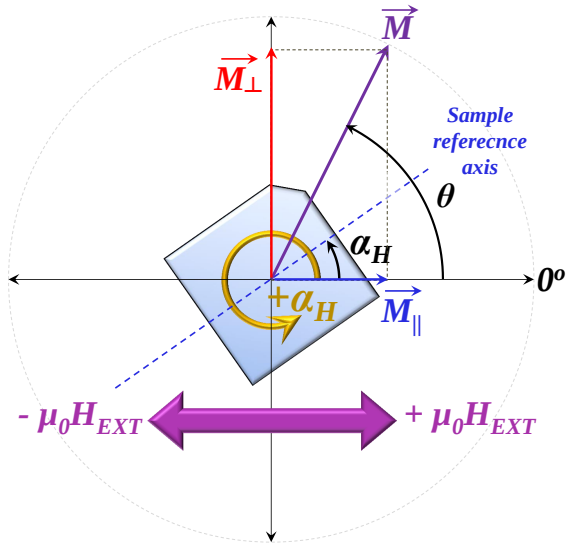


Figure 1.14: Sample and external magnetic field relative angles, and the angle of magnetization, as it is customary used in our v-MOKE set-ups, both the RT set-ups and Tristan.

# 2 TRISTAN set-up

**In this chapter we describe the instrument that has been built at the beginning of the thesis for thermal and field effect studies. It is a v-MOKE (Vectorial Magneto-Optic Kerr Effect) device that covers three very important aspects of magnetometry: vectorial capability, full angular range, and variable temperature.**

**The possibility of carrying out variable temperature-full angular range vectorial-MOKE magnetometry is critical to explore the magnetic anisotropy. This is because magnetic anisotropy is strongly dependent on temperature, and then, when an effective anisotropy is composed of anisotropies coming from different origins, the temperature evolution will separate them, allowing disentangling each contribution. In chapter 5 section 5.2 we shall demonstrate this aspect in a model system consisting of Fe on MgO(001) grown at oblique angle, illustrating the capabilities of the new set-up.**

**As this instrument has three enhancements with respect to classical MOKE magnetometry, the vectorial, angular and variable temperature capabilities, it is quite difficult to find an acronym to give it a name. Until a reasonable one is found for it, we shall use a familiar name given to it, TRISTAN.**

## 2.1 Introduction

In chapter section 1.7 we have made and introduction to the vectorial MOKE technique, v-MOKE. This technique has been exploited in our group since some years ago, a complete report on that can be found in [81]. When control over temperature is required, a cryostat must be used. The sample under study must be set in a sample holder inside the cryostat, and any intervention on it during the measurement will be dramatically time- and resource-consuming. In classical MOKE set-ups acquisition of parallel and perpendicular components with single photodiode must be done by changing Kerr geometry. A measurement in longitudinal geometry gives the parallel component and then, both the magnet and the sample must be rotated by 90° so that we get the perpendicular component, through what we call a transverse Kerr geometry. Keeping the sample surface well perpendicular to the laser is critical to make the reflexion hit the photodiode. If the sample is inside a cryostat, these adjustments will require opening it, every time we change the geometry.

Not only that, when studying magnetic symmetries, where angular dependent measurements are required, the process would have to be repeated for each angle in the whole angular range, and for each selected temperature. In classical MOKE set-

ups this is simply unrealizable. The instrument described here, takes advantage of the v-MOKE technique developed in our group, described in introductory chapter 1 section 1.7, adapted to the cryogenic environment required to cope with thermal studies.

We have developed a variable-temperature full angular range vectorial-Kerr magnetometer, named TRISTAN where both in-plane magnetization components with respect to the applied magnetic field direction, i.e., parallel $M_{\parallel}$ and perpendicular $M_{\perp}$ to the external magnetic field $\mu_0 H$, can be obtained simultaneously, allowing to do full angular range rotation of the sample holder, under controlled temperature, from liquid Helium up to 500 K, without the need to rotate the magnet nor opening the cryostat, allowing for a considerably reduction of alignment problems and reducing time in the process.

The sample holder of the cryostat has been motorized, and in addition it has been provided with a tilt-adjustable device to keep the sample's normal correctly aligned with the rotation axis during all the time. The reflection plane then remains fixed at all angles, preventing the reflected light to precess over the detectors and, eventually, to move outside of them. The tilt is adjusted before closing the cryostat, and no re-adjustments are required even when changing temperatures over the whole range from 4 K to 450 K. The measurement process can then be carried out in a continuous fully automated way, controlled by software. For instance, anisotropy studies, i.e., angular dependent measurements (in-situ 360 degrees sample rotation), as well as operation in a broad temperature range (5-500 K) can be carried out without breaking vacuum, optical realignment, or stopping the measurement process. Automation of the process allows to program experiments with different temperature ramps, measurement intervals, field cooling options, as well as with different applied field sweep rates and angular ranges.

Many technical drawbacks have been overcome to put this system in order. For instance, the specific requirements that the cryostat should have to suit our needs were such that there was only one brand that met the specifications, after modifying a standard model with our own specifications. The requisite of using a cryostat is combined with the necessity of putting the magnet poles as close to the sample as possible, determining the specific characteristics of the optical access among others.

We divide this chapter in the following sections: first one is devoted to description of the instrument, from the hardware stand point. The second is devoted to all the electronics used to control the set-up. The third is dedicated to the software that has been developed during this thesis to control the system in an unmanned way. The fourth is a special section dedicated to describe how does the measurement process takes place normally, from the setting up of the sample to the programming of the measurement cycle. Another section is dedicated to the post-analysis of the measurements, including a subsection with some details of the error sources and examples. This last part is new on the literature of our group.

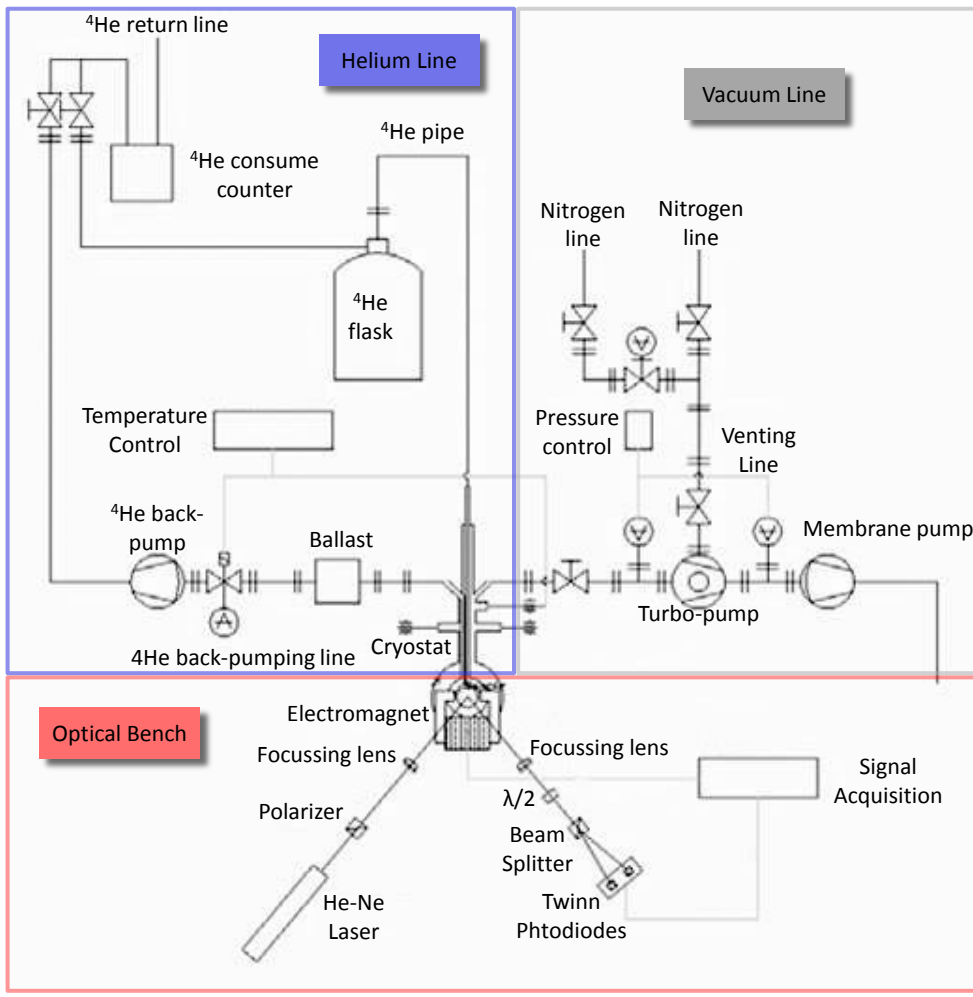


Figure 2.1: TRISTAN device layout. Red frame encloses the optical bench, blue frame encloses the cryostat and He line (delivery and recovery), and grey frame encloses the vacuum line of the cryostat. Instruments have been depicted only schematically, with connections in grey line. Computer connections are omitted.

## 2.2 TRISTAN description

### 2.2.1 Set-up overview

In this section we give a global overview of the set-up, with some insight on what makes the device relevant for the technique, in such a way that those who are already familiar with this kind of devices can jump the detailed sections that follow, without a loss of the understanding of critical aspects. The next sections enter more in deep into

the details. A general diagram and picture of the instrument TRISTAN are shown in figures 2.1 and 2.3, respectively, while figures 2.2 and 2.5 show a detailed diagram of the cryostat and optical elements, and a close-up picture of them, respectively.

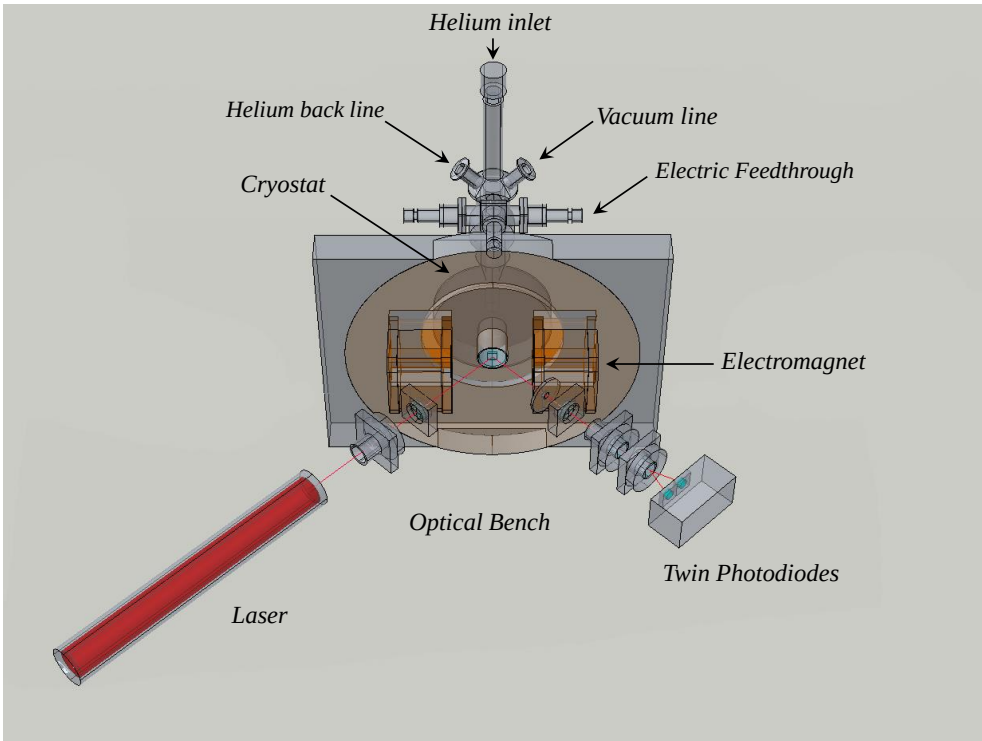


Figure 2.2: Schematic layout of TRISTAN main parts: The cryostat's main body appears behind the (bulky) electromagnet, with its Helium, Vacuum lines and electrical feedthroughs emerging from behind. The cryostat nose with sample holder is represented by the small blue square in the nose window, which traverses the electromagnet. The electromagnet appears in the middle of the picture as a big square structure with a movable disk supporting the coils (orange). The optical parts (see figure 3 for details) can be seen following the red line that represents the laser beam.

The device consists of a vectorial MOKE set-up based on our twin photodiodes system. [81] (red frame in figure 2.1), externally mounted in front of a back-flow $^4$He cryostat with optical access and He line (blue frame in figure 2.1). The vacuum line for the cryostat can be seen in the grey frame in figure 2.1.

In the red frame, the optical elements of the vectorial MOKE set-up can be seen. They are the same that has been already explained in chapter 1.7 and we detail them again in the next paragraph. The blue frame comprises the cryostat, and the He delivery/recovery line, with the He flask and relief line, the back-pump and valves, and the recovery line. The gray frame comprises the vacuum line, whit a turbo-pump and a membrane pump, and the corresponding valves and gauges. In the picture of

figure 2.3, all the elements can be easily identified, with the exception of the cryostat itself, because is almost covered with the electromagnet and its mounting bridge. In this image, the mounting of the electromagnet can be seen as a massive transversal joist that keeps the magnet fixed to the table frame, above the optical bench without contacting it. The optical bench is supported by pneumatic dampers, that can be seen in the picture of figure 2.3. The optical elements and the cryostat itself are fixed to the bench, so that the electromagnet does not introduce vibrations to the set, as it is fixed out of the bench. In figure 2.11 a diagram of the bridge construction can be viewed. The optical bench floats beneath it with the pneumatic dampers.

The cryostat optical window is located at the end of a cylindrical nose that extends some centimeters away from the main cryostat body. Around this nose, the external electromagnet is located, with the core's gap as close to it as possible. In figure 2.2 a detailed 3D sketch of the cryostat, magnet and optical bench is seen. The magnet is the gray square frame with a rotary disk inside in orange-gray color, where the magnet's coils are depicted (without the cores) as a couple of orange pieces. Transparency of this 3D sketch of the magnet allows to see the cryostat behind it, as a concentric cylindrical body, with the nose getting in the magnet's hole. The different elements of the cryostat, such as He feedthroughs and pipe connection, vacuum feedthroughs and electrical sockets are seen appearing behind the magnet and above it. The optical window is depicted as a small blue disk where the laser, red color line, is reflecting. The optical elements appear in front of the figure (without the bench that supports it) as a sequence of elements beginning in the laser, seen to the left, ending on the twin photodiode, seen on the right. Following the laser line from the laser we find the polarizer first, then a focusing lens, then the reflection on the sample, an iris right at the outcome, followed by another focusing lens, the $\lambda/2$ plate, the beam splitter and the twin photodiode. Al these elements can be easily recognized in picture of figure 2.5.

The sample is located inside the cryostat just behind this window, supported by the sample holder which is in thermal contact with a cold finger located in the main body of the cryostat. The sample can be set at a certain controlled temperature by the combined action of the helium flow through the so called "cold finger" (controlled with an electromechanical valve located in the $^4$He back-flow pump) and the current on a heating filament in thermal contact with it. The sample holder can be rotated by 360°. In order to prevent precession of the reflected beam during rotation, it has an eucentric mechanism designed on purpose to ensure perpendicularity of the surface sample plane with both rotation axis and reflection plane, as aforementioned. The miniaturization of these parts is very important in order not to increase the magnet's gap required to enclose the cryostat nose, avoiding a dramatic reduction of the external field applied.

Electromagnet driving, temperature control, axis rotation and signal acquisition are based on specific electronics connected via GP-IB to a computer, with software developed on purpose to automate measurement process.

### 2.2.2 Cryostat

The cryostat is a *Cryovac* KONTI Cryostat Micro, a Helium back-flow type cryostat with single casing (vacuum shield with radiation shield). This cryostat is in its origins

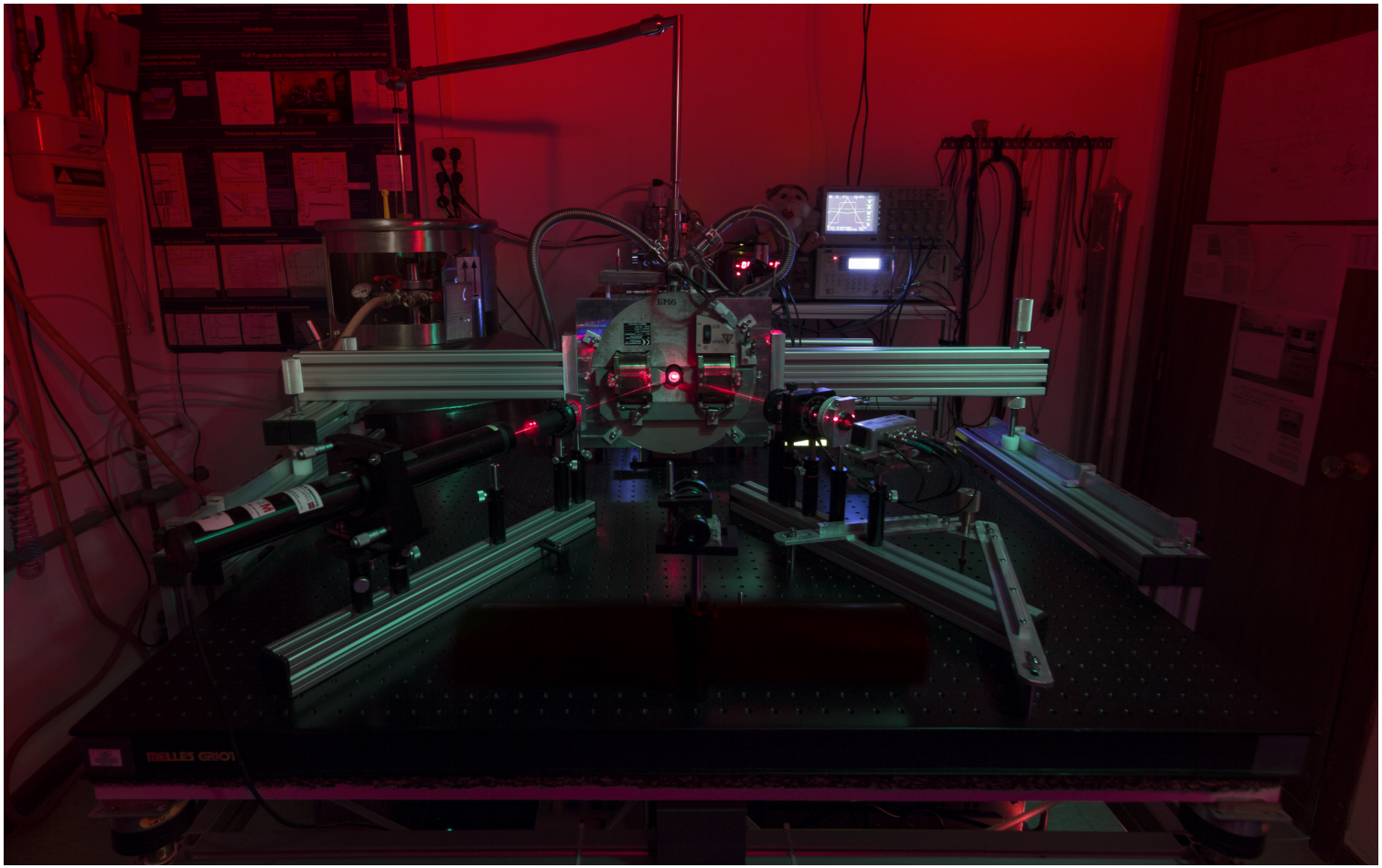

Figure 2.3: TRISTAN laboratory. In the center of this picture the cryostat window illuminated by laser beam can be distinguished surrounded by the electromagnet and its mounting bridge. The cryostat is barely seen behind, with the vacuum and helium hoses, as well as transfer pipe. The optical elements are mounted on the two aluminum rails visible in the optical bench.

designed for microscopy so that would not permit the rotation of the sample holder, neither positioning of the electromagnet around it. For that reason, we asked for some modifications to be done at the factory according to our specifications.

First, the sample holder was provided with a shaft and feedthrough so it can be rotated. As a consequence a set of braids had to be suited to allow for this movement and ensure heat transfer with the cold finger. Second, a prolongation of the sample holder was done so that it emerges from the main body as a cylindrical nose. Radiation shields and sample holder have been prolonged accordingly, and the optical window is then located at the end of the nose. The optical access is 25 mm diameter, and the nose external diameter is 30 mm. To excite the sample, an external electromagnet with 31 mm gap can be used, having in mind that the maximum distance allowed between the gap center of the magnet and the farthest part of it is no greater than 40mm, the nose's length. Our actual option for electromagnet is a specially designed electromagnet from *evico magnetic GmbH* (this brand is typed in lowercase), that will be described later. In figure 2.4 the original KONTI cryostat is shown in the upper picture, and the actually modified in the lower one, after fixing on the XYZ stage to the optical bench. Details about the rotary feedthrough are presented in a later section.

Vacuum better than $10^{-7}$ mbar inside the cryostat is obtained by using a small turbo-molecular pump with membrane backing pump.

The cryogenic liquid is pumped using a back-flow rotary vane pump that has an electromagnetic valve at its entrance to control the flow. The flow ranges from 0 to 1200 l/h, in a voltage linear range between 2.5V and 5.5V. The electrovalve is commanded by voltage signal, since the valve has its own power supply. Normally it is commanded by signal between 0 and 10V subject to PID control by the electronics, described later. So it has some dead regions that in practice are not very important. Liquid He hoses going from the cryostat to the back pump traverses a concrete ballast to absorb vibrations from the pump.

The Helium comes from the flask through a pipe provided with a needle valve. The pipe gets into the cryostat from the top, and goes into the cold finger, that a ring shaped and is located around the rotation shaft and sample holder. Four braids connect the cold finger to the sample pre-holder. In figure 2.6 the cold finger and braids connecting the sample pre-holder can be seen. The sample holder set up is actually modified and is described later. As an advance, the sample holder shown in this picture is the new eucentric head designed in this thesis, and not the original one from *Cryovac*. The braids are four flexible oxygen-free Cu braids, gold plated, putting the sample pre-holder in contact with a platform that is in close contact with the cold finger ring. The platform is seen in this picture, but the cold finger is not seen, as is behind it. It acts efficiently as heat exchanger allowing the required sample rotation and temperature control. The cold finger is provided (not easy to see in the picture) with 6 screws with heater filament rolled over them, to act as a heat source for temperature control.

After running through the cold finger, the Helium goes out through a lateral feedthrough on the left, and passes by the ballast all the way to the back-pump. The back-pump exit is connected to the Helium recovery line that goes to the Institution's Helium Liquefier at SEGAINVEX. No Helium loses occur since piping this system happens always with the Helium flask nearly closed, the pipe entering through a

Viton collar that avoids losses in the process. All the Helium is recovered with a very small retail lost.

The Helium consumption during operation is no more than 3 or 4 litres per day.

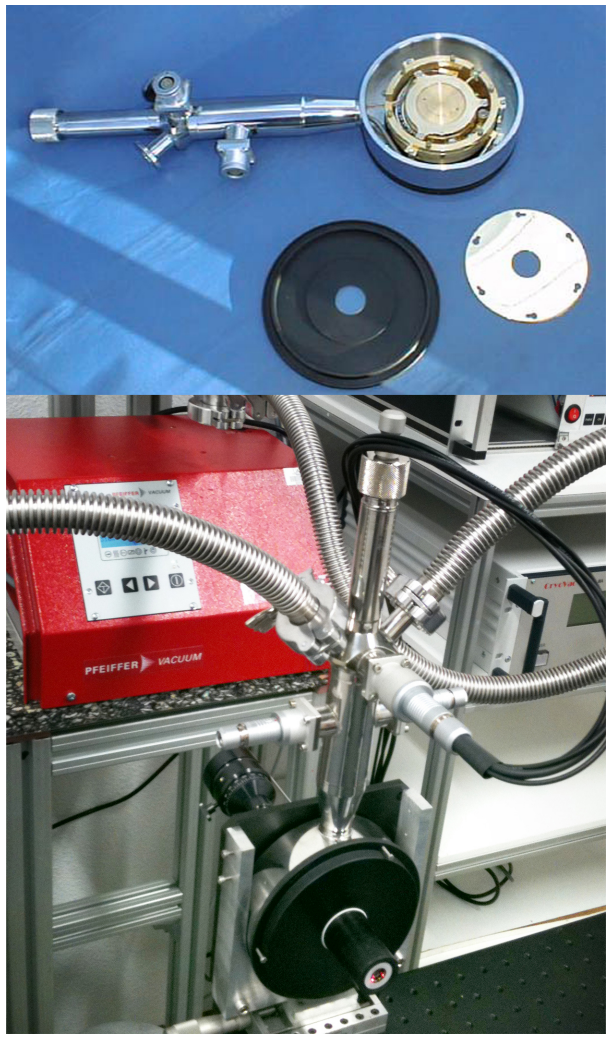


Figure 2.4: Top: original Konti Cryostat Micro, from *Cryovac GmbH & Co. KG* This commercial standard model does not have rotary sample holder, and the sample holder is deep behind the optical window, that in turn is flush with the wall, so that it is impossible to surround the sample with an electromagnet. Bottom: the cryostat after modifications done at *Cryovac*, In this picture the cryostat is already mounted on the optical bench though an XYZ stage and a support that has been done in our workshops.

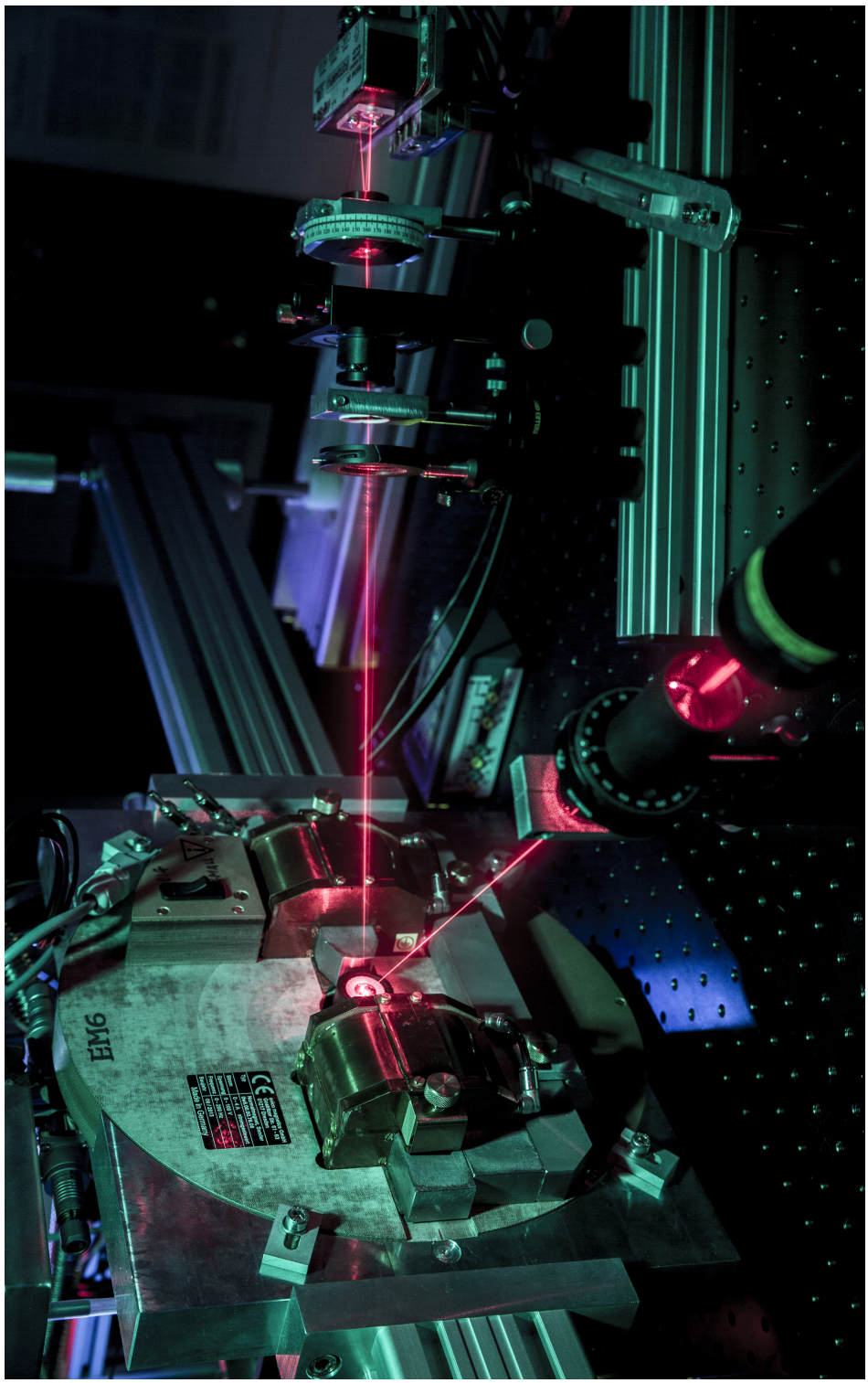


Figure 2.5: Close-up view of the electromagnet, the cryostat nose in the middle, and the laser path with optical elements.

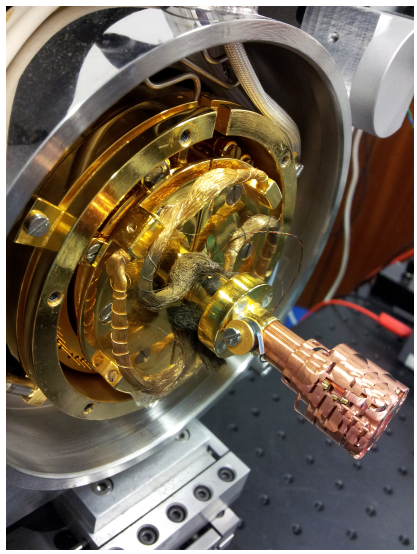

Figure 2.6: Sample pre-holder and eucentric head, showing the cold finger and braids. Actual pre-holder and braids are the originals. They have been servicing later, and the pre-holder has now a new design. Sample holder is not the original in this picture. Instead the new eucentric head is shown in the figure, before gold plating.

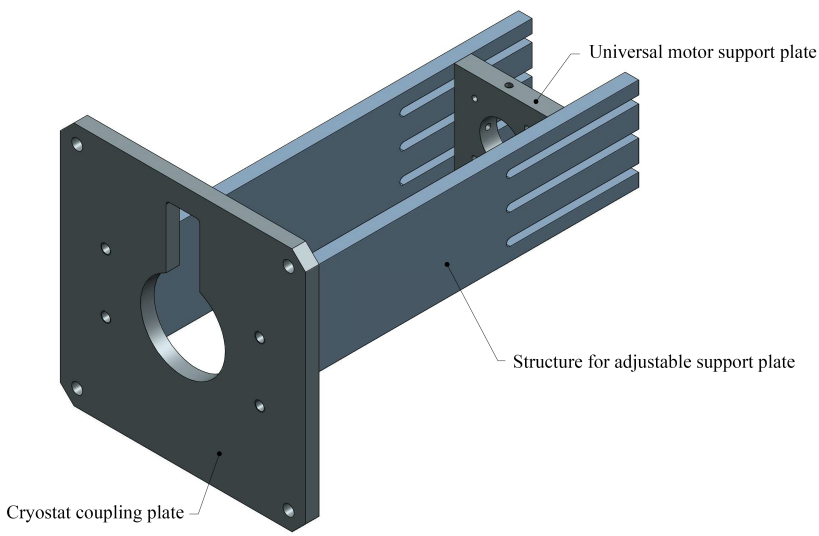


Figure 2.7: 3D diagram of the motor assembly, parts are labeled.

### 2.2.3 Rotary assembly

The cryostat is provided with two *Lakeshore* DT-670 silicon diodes, one very close to the cold finger, called S1, and other one in the sample pre-holder, very close to the sample holder, called S2. This S2 can be seen in figure 2.6, as a small cylinder screwed at the end of the pre-holder (gold plated), right at the base of the sample eucentric holder (in cooper). Feedthroughs for their electrical connections together with the contacts for the heater are provided in the cryostat. Fast an efficient stabilization of the temperature in the sample is obtained by the combined action of the heater filament located in the heat exchanger (cold finger) and the cryogenic flow, controlled by a specialized PID electronic device.

The cryostat is fixed with a base placed in the middle of one side of the optical bench and with the nose axis pointing to the centre of the bench. The base includes adjustable micrometric XYZ translation stages.

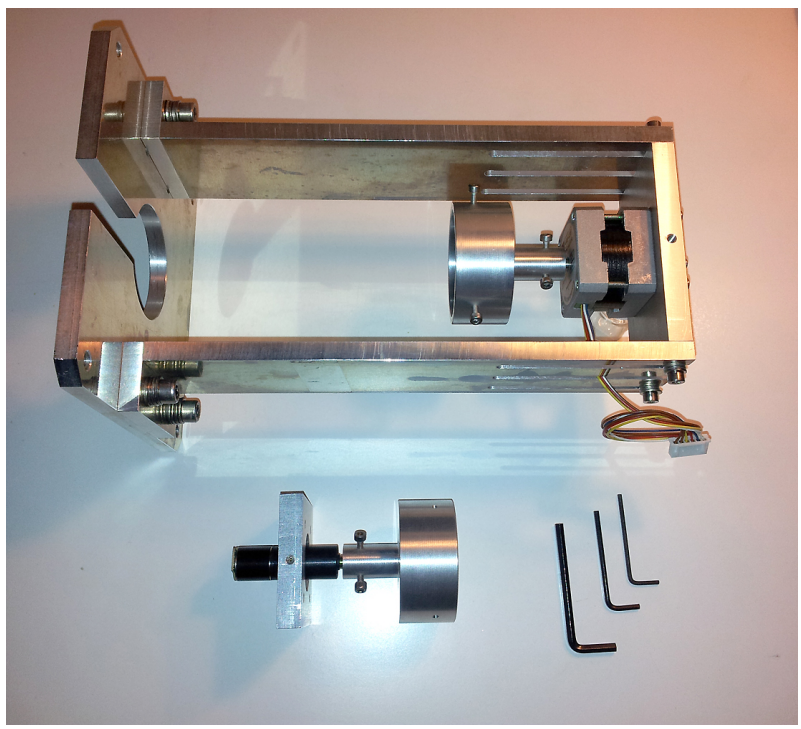

Figure 2.8: The assembly spread on the table. The interchangeable plate is provided with standard market stepper motor. This same plate can be directly used, with the help of an adapting collar, with an *Arsape* motor, shown bellow.

The sample pre-holder is attached to a rotary axis that can be actuated to the desired angle externally. The sample pre-holder is thermally isolated from the cold finger in order to avoid thermal losses. The shaft feedthrough was set up in the *Cryovac* factory, but its motorization has been developed in our lab. A coupling has

been designed to support different motors, and has been fabricated at our workshops. In figure 2.7 the diagram of the support, design on purpose to fit at the rear part of the cryostat, is shown. This support is said to be universal, because the motor holder consists of a sliding plate with adapter for each different motors in the market. Actual plate is prepared for the standard stepper motors of size 42mm, and for *Arsape* motors. Because the plate can slide in the assembly forward and backward through a set of three sliding slots (two are for sliding of the plate and locking it on its final position, and one in between is to actuate the locker screws for the setting up of different adaptation collards), this plate is said to be interchangeable and universal. Each motor axis is then coupled directly to the shaft knob by using specific crown piece with radial lockers. Mounting or unmounting a motor to set a different one in is a very easy operation. In picture shown in figure 2.8, the set-up can be seen still dismantled. In figure 2.9, an *Arsape* motor with the adapting crown is ready in a interchangeable try, and in 2.9 the assembly is already mounted on the cryostat.

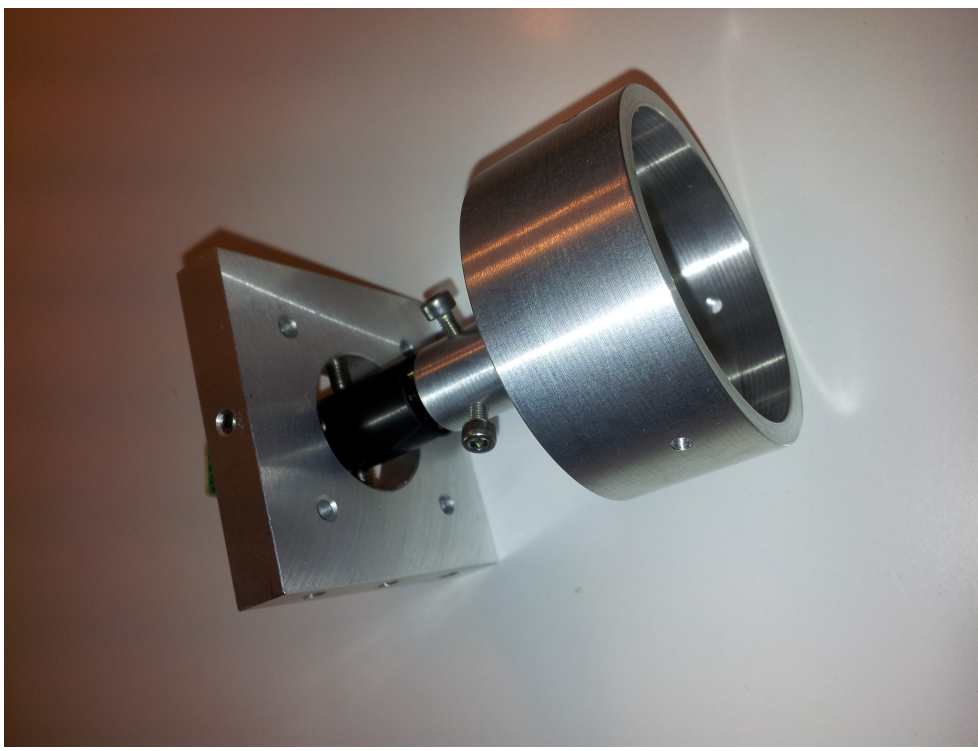

Figure 2.9: A detail of the adaptation crown that connects the motor shaft to the rotary knob. This piece is standard from the side of the knob, and the drill to connect the motor axis is mechanized for each model of motor. In this picture, an *Arsape* motor (small black cylinder traversing the plate on the left) is temporarily connected in the interchangeable plate with the locker screws.

As the braids inside the radiation shield box are really hard to move, a conventional

stepper motor did not have enough torque to move the load, so we decided to use an *Arsape* motor with built-in gear box. The motor has 102:1 reduction ratio with corresponding angle resolution of 0.09 degrees (4096 steps per turn). An electronic based on Arduino UNO has been developed in our group on purpose to drive this motor. Both the microprogram for Arduino and the additional software at the link level for the control application have also been developed. To prevent rotation of the axis beyond limits, so that braids do not get broken, end-of-track system has been set up in the device using optical sensor and crossing flag.

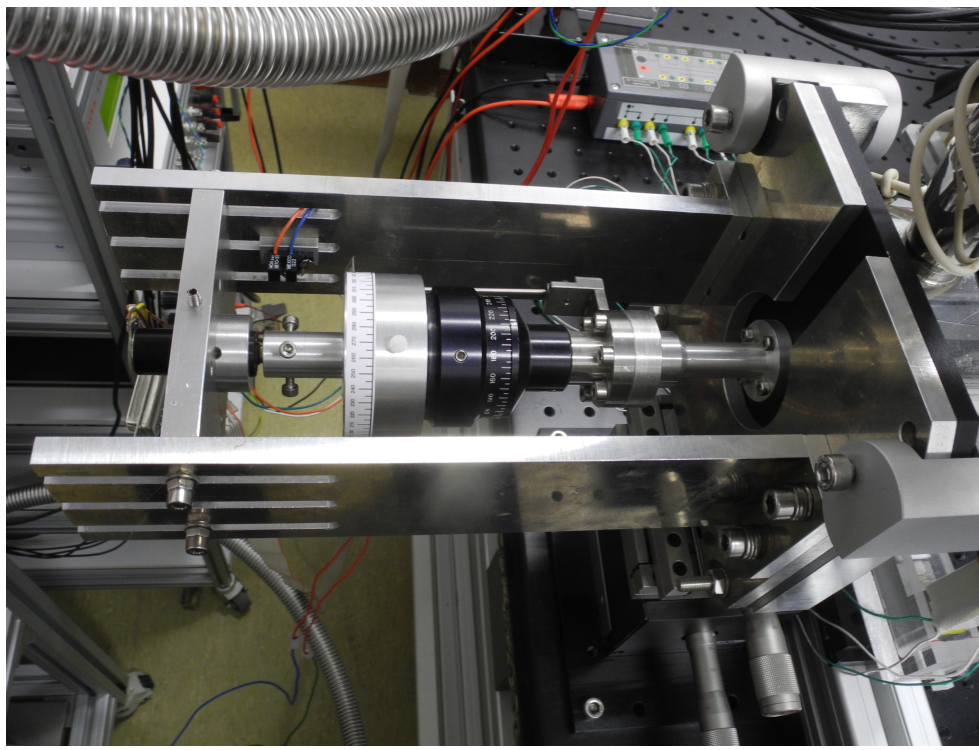

Figure 2.10: The assembly as is operating today in the cryostat. The *Arsape* motor with gear box is set in.

### 2.2.4 Eucentric head for sample holder

Some additional modifications have been carried out in our laboratory to improve the capabilities of the cryostat. We have designed and built an eucentric stage to replace the original sample holder. It is a rather small eucentric head only 15mm diameter with a set of screws and springs to allow tilting, mounted in such a way that reflection plane upon sample rotation can be correctly set without breaking thermal contact. A third temperature sensor is located in the sample holder just at the position of the sample clamp, to ensure correct thermalization. This sample holder can be seen in picture 2.6.

### 2.2.5 Vectorial-MOKE optical set-up

Vectorial MOKE magnetometry has been already explained in detail in chapter 1.7. Here we focus on how the technique is set up in TRISTAN. The v-MOKE set-up we use in TRISTAN is the standard one, with twin photodiodes (TP). All its components are pre-mounted in aluminum rails to ease moving for alignment laser path. In previous diagrams and pictures, both branches appear as a V shape put upside down, the left branch is called the incoming branch, and the right one is the detection branch. The incoming branch is normally fixed, with the beam correctly set in the bench's plane, pointing to the optical window of the cryostat. Instead of changing this branch of the optical part, what we do is to use the X movement of the XYZ stage to which the cryostat is fixed. Normally it takes very little to get the laser to hit the sample inside the cryostat. The alignment procedure is done with the cryostat open, so that the eucentric sample holder can be adjusted to make the sample's surface normal vector be as close to the rotation axis as possible. This prevents the laser reflection to precess during rotation of the sample. After this is fixed, the cryostat can be closed and evacuation can be started. The eucentric head is working fine, and after evacuation it keeps in the same state as when the sample surface was adjusted. This eucentric head is explained in a later section. Full angular range vectorial studies with variable temperature can then be carried out without any additional adjustments, other than decide if we prefer to do vectorial Kerr in longitudinal configuration (i.e., parallel component comes from the difference of intensities in the diodes, and perpendicular from the AC summation of intensities) or in transversal (i.e., the other way round). The sensitivity and appearance of quadratic terms are different in both cases, so that a full angular measurement in one configuration sometimes is duplicated to have the same measurement in the other one, just to compare (remember that scaling factor between components, however, needs to be done only once). The only action to do in that case of duplication or selecting a different measurement configuration is a rotation of the external magnet by 90°. In order to compare both angular measurements, the angle of the parallel component measured in one configuration corresponds to that of the other with 90° shift, because the angular scan normally goes from 0° to 360° in both cases. Something that must be taken into account in case that there is a need to compare both measurements. In practical, we use to work always in longitudinal configuration, for reasons already explained.

The presence of the optical window adds a (not very big) problem in the v-MOKE set-up: that of multiple reflections coming out of the window, as well as the risk of having some magnetic response from the window material itself, by Faraday effect. For the first problem, if the window surface is parallel to the sample surface, multiple reflections on it will run parallel towards the optical elements in the detection branch, making it difficult to block them with an iris. This problem is easily solved by setting the cryostat window slightly unparalleled to the sample surface, forcing the reflection on the window to run divergent with respect to the beam reflected on the sample. In figure 2.5, the beam reflected in the window, with a weaker intensity, can be clearly seen going out with a slight divergence. It is then blocked by the iris, so it disappears behind it.

In this same picture, v-MOKE elements are visible, by following the laser path. First it is the laser, almost hidden in the bottom center of the picture. The laser

emerges from it and enters into the polarization prism that is mounted in a circular ruler. After it, the focusing lens is mounted in a non-anodized aluminum plate, that presents a red halo in the picture, and immediately after it, the laser goes directly to the cryostat window, in the middle of the EM6 electromagnet (see this later). The window looks like a black-white ring, with another black-out area in the center where the laser spots the sample surface and makes it shine strongly on the photograph. The reflecting beam goes then directly to the detection branch, traversing first the iris, second (in not black-anodized aluminum) the focusing lens, then the $\lambda/2$, then the beam splitter (with a circular ruler that is useless here) and finally, the beam appears split into two, with different intensities in this case, that goes to each one of the twin photodiode detector. Interestingly but not very transcendental is the visibility of the laser's path in this picture: this path is not artificially depicted in the photo, it is rather the real laser manifested by using a very simple trick with liquid nitrogen and a bit of photography knowledge.

The electromagnet covers the visibility of the cryostat in this picture. We have already explained that the electromagnet is a piece apart from the optical bench: it is decoupled from it as will be explained later.

### 2.2.6 Optical bench support

The optical bench is provided with passive pneumatic dumpers to minimize building vibrations (in the range of 0.1 to 10 Hz), or people walking around careless. This dampers are located between the table frame (made of massive 90 mm x 90 mm aluminum profile) and the optical bench (optical table pre-drilled every 25mmx25mm). To minimize vibrations induced in the optical elements by the electromagnet, especially when using high currents, the electromagnet itself has been decoupled from the optical bench, by using a bridge that allows fixing it directly to the frame, so that the optical bench is not coupled to it. In figure 2.5, the bridge scheme is depicted, it has been designed during this thesis and built at our workshops, both SEGAINVEX and the department's workshop.

### 2.2.7 Electromagnet and its support

We have been working with many different magnets during this thesis. For each electromagnet, a translation (callibration) table that converts current into magnetic field must be obtained by using a hall sensor. Whenever we work in the linear regime of that calibration curve, translation from current to field consists just in a proportional factor. Specially designed magnet built for us by *evico magnetic GmbH* can be seen in the pictures. It is a standard model from the company, with different size, magnet gap, and cores holders. In order to put the magnet as close as possible to the cryostat so that the window is placed in the middle of the cores, we had to design the rear part of the magnet support with precision. This magnet is capable of giving up to 300 mT. Above 200 mT coils heat up and a chiller is required. The chiller hoses, (not connected in the picture), are conducted through the right arm of the magnet support. Vibrations from the chiller do not affect the optical bench, neither vibrations from the magnet itself.

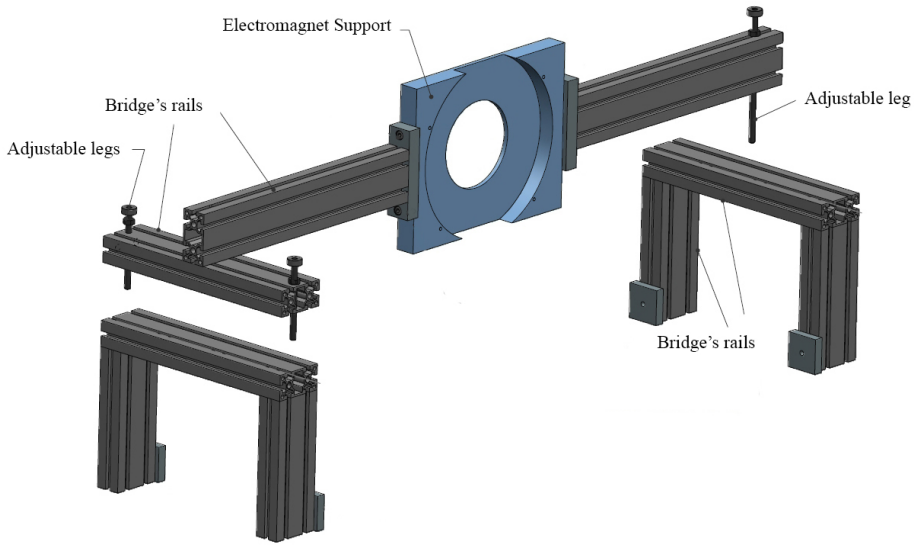


Figure 2.11: Magnet bridge has been built over the specifications required to support the *evico* electromagnet. A massive aluminum piece has been designed (1) and mechanized in our workshops at SEGAINVEX to encase the electromagnet in such a way that this one can be rotated so that a longitudinal configuration or transversal one can be selected for the measurements. A bridge made of aluminum rails (2-5, seen separated) supports rigidly this massive encasing and is fixed to the bench's frame, decoupled from the optical bench.

A close-up of the magnet can be seen in pictures 2.12 and 2.5, called EM6.

The location of the cryostat window inside the electromagnets central hole has margin enough as to allow for some movement of the bench without hitting the electromagnet structure. This is very important not for the measurement process, where we do not expect to have such movements, but in case a damper blasted, making the bench drop down. For that case, four PVC stoppers limit the vertical drop down, so that the cryostat nose never hits the electromagnet structure, jet they have a gap enough as to move the cryostat a little inside. The electromagnet support has the possibility of vertical and lateral movement, so that after moving the cryostat for aligning the spot of the laser, the magnet can be relocated to be correctly coaxial to the cryostat's nose.

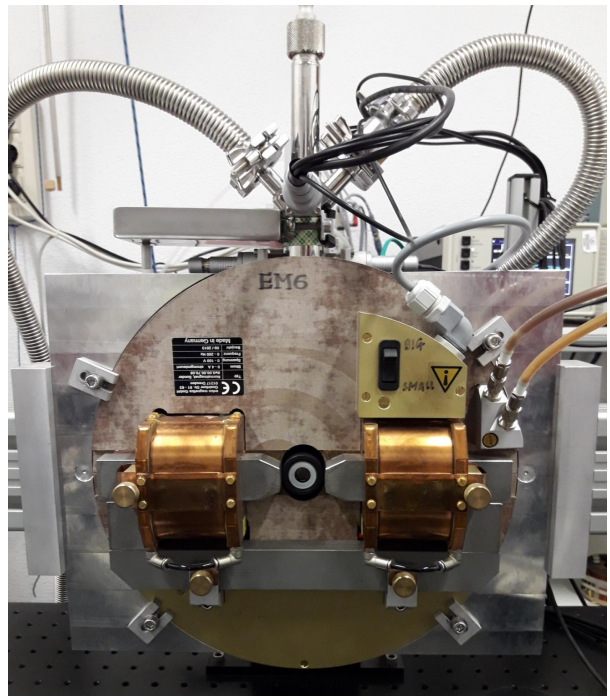


Figure 2.12: On-purpose electromagnet built for us by *evico Magnet GMBH*, under our specifications. Central feedthrough allows to set the nose of the cryostat between magnet cores. Massive aluminum support can be also seen. Rapid clamps are set to allow for magnet rotation, so that vectorial magnetometry can be carried out in longitudinal configuration ($M_{\parallel}$ proportional to Kerr rotation, and $M_{\perp}$ proportional to reflectivity changes) or in transversal ($M_{\parallel}$ proportional to reflectivity changes, and $M_{\perp}$ proportional to Kerr rotation). This allows as to interplay with S an d P incoming polarization, and different geometries, so as to get the higher sensitivity, as explained in the section 1.7 of the introduction.

A sketch of the electromagnet support can be seen in figure 2.11. This support is composed of massive 90 mm x 45 mm aluminum rails, with a bulky aluminum piece mechanized to hold the magnet. This last piece is solidly attached to two profile arms by two coupling aluminum prisms, with heavy duty screws. The left arm has a transversal short secondary arm, so that two adjustable legs are located on its extremes. The right arm has only one such adjustable legs directly located in the extreme of that arm. Figure 2.5 shows this clearly. The three legs rest on three cylindrical nylon stoppers that can slide forward and backward on two lateral rails that are solidly fixed to the bench's frame. This is important because the set is very heavy and we have to move it apart when the cryostat has to be opened. Vertical movement can be done with the adjustable legs, and a little lateral movement can be done as well. Two railings prevent the legs from going behind the support, and fixed to that railings, two cursors prevent us from forcing the magnet to collide with

the cryostat when positioning back after been opened, or against the optical elements when it must be set apart from the cryostat.

The set in all has demonstrated to be very effective and easy to set and move.

### 2.2.8 Other internals

As the original braids for thermal contact with the cold finger where welded with Sn-Ag alloy, Cu braids become brittle in the process, and they broke rapidly. This was also promoted by the very little space left for the braids inside the thermal radiation shield. We had to change the braid's assembly by a new design developed during the thesis. The new assembly comprises a new D-shape braids base, and a new pre-holder, that do not need welding. The pre-holder can be seen in figure 2.13.

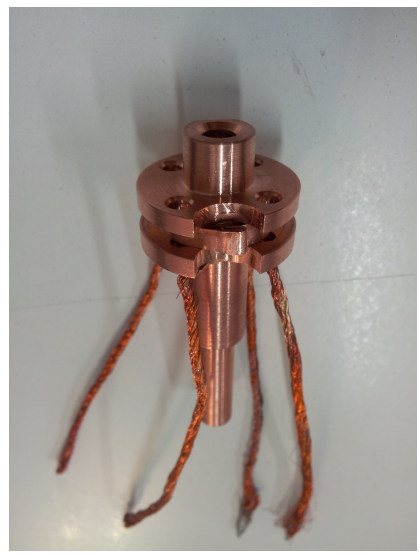

Figure 2.13: New pre-holder designed during this thesis, to replace original one from *Cryovac*. This sample pre-holder does not need soldering of the braids, reducing the risk of getting broken after many rotation cycles due to copper brittling after heating for welding.

The set-up is based on under-pressure support contact system. The pre-holder has two plates very close to the sample holder end. The two disks have holes that allow the braid to pass through, and leave a slot in between where the braids, once in, can be rolled around in sections of a quarter circumference. Then they are surrounded by a cooper plate that is closed so that it exerts pressure on the enclosed braids. The way to close this plate is by rolling its extremes in "French sewing" way, something very similar to a herring's can opening system. The D-shape plates that connects the braids to the cold finger were re-designed from the original ones. This way we prevent brittling Cu, but at the cost of losing some K in the lowest temperature that can be reached, that now is 10 K. This is still good enough for the studies we have carried

out.

## 2.3 Control electronics

Different electronics commanded by computer software are used to control the set-up and the measurement process. At the beginning we had the option to do a compact system with a powerful DAQ board, but finally we found it not flexible enough when manual operations are required. So we kept the original plans of having separated specific electronics, and communicate them with computer software developed on purpose for the system.

Control electronics comprises all the instruments to control vacuum, temperature, electromagnet driving signal, current amplifier, rotary axis, laser and signal acquisition, as well as some devices set for security in the operation, such as heat checks at the electromagnet and dead locks in communications.

### 2.3.1 Vacuum

Vacuum is controlled by *Pfeiffer* Cold Cathode and Pirani Gauges, and their corresponding dual channel electronics. The Cold Cathode gauge is set right at the entrance of the Turbo Molecular pump, while the Pirani is set between the turbo exhaust and the membrane pump. In normal system operation the Pirani gage reads 2.4 mbar, and the final vacuum obtained inside the cryostat at room temperature is around 4x$10^{-7}$ mbar. This final vacuum gets to 2x$10^{-8}$ mbar when cooling down below 100 K, and rises up to order $10^{-6}$ mbar when heating. To get a final order $10^{-7}$ mbar vacuum after servicing the cryostat or opening it for changing the sample takes around one day. However the time that takes to get order $10^{-4}$ mbar is around 10 minutes, so that at this point one can start to measure at moderate temperatures. Getting into order $10^{-6}$ mbar takes around a couple of hours, so that at this point, low temperature measurements can be started up because the cryopump effect will do the rest of the work. The electronics used to control the system are stand-alone, and do not have any remote control from the computer. Until today we have not had the need to do so. Vacuum on this very small system is not a big deal.

### 2.3.2 Temperature control

The temperature control was realized by using a *CryoVac* TIC-304-MA with PID control during this thesis, but it become obsolete after a fail in the main board, so it has been substituted by a more modern and sophisticated TIC-500 device. The explanations that follow are the same, no matter which of both electronics we refer to. Two Si-diode sensors of the type DT-670-C-Co and DT-670-A-Cu/HT from *Lakeshore* are located inside the cryostat. Both are DT-670 type, however they differ on the encapsulation (this is described by the C-Co and A-Cu/HY codes). The electronics controls the electromechanical valve located at the He back-flow pump entrance, capable to regulate the flow between 0 and 1200 l/h, and the voltage in the heater inside the cryostat (max. 30 W), to stabilize the temperature by its combined cooling and heating action under PID control. In figure 2.14 the TIC-304-MA display can be seen.

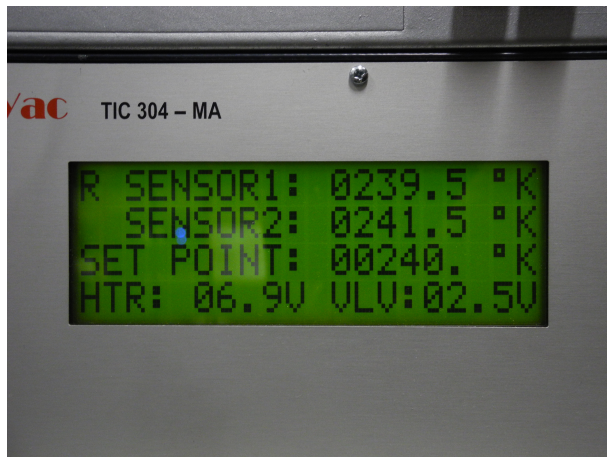


Figure 2.14: *CryoVac* TIC-304MA temperature electronics, showing the two DT-670 channels, actual set point and the values of heater (HTR) and He valve (VLV) controlled by PID.

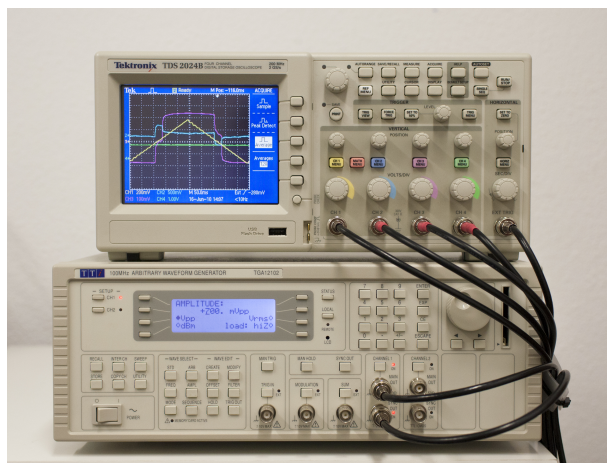


Figure 2.15: The excitation-response electronics are seen here together. The function generator (below) drives a current amplifier (not seen in the figure). The upper instrument is a four-channels oscilloscope, triggered by the function generator. A monitor signal from the current source enters into channel one. This is the current in units of volts, that translates directly into the applied field by using a calibration curve. The other 3 channels read the outputs from the twin photodiodes: AC-sum, DC-diff and DC-sum.

The instrument is connected to the computer via GP-IB, and the software allows to control the set point, PID settings and limits.

### 2.3.3 Electromagnet control

The electromagnets used during this thesis are controlled by a function generator *TTI* TGA12102 that drives a current amplifier. Two different current amplifiers have been used depending on the electromagnetic requirements. A current source developed at SEGAINVEX capable of giving up to 4 A of current has been used in low field electromagnets, while a *KEPCO* BOP 100 with up to 10 A for the more powerful electromagnets. In figure 2.15 the *TTI* TGA12102 function generator is seen bellow the oscilloscope. This is a two channels function generator, so that magnetoresistance measurements can also be carried out simultaneously with the v-MOKE.

### 2.3.4 Motor control

Rotation of the sample axis is carried out by a stepper motor controlled with L297/298 chipset driver, developed in our group. An Arduino UNO board acts as Driver and Computer interface. As the motor support is designed to be compatible with different standard motor models, the control software can be configured as required. Actually we are using an *Arsape* Motor with gearhead of 102:1 reduction ratio with corresponding angle resolution of 0.09 degrees (4096 steps per turn). To prevent rotation of the axis beyond cryostat construction limits, end-of-track system has been set up in the device.

### 2.3.5 Oscilloscope for signal acquisition

Signals from the twin photodiode are registered in a four channel oscilloscope (*Tektronix* TDS 2024B, or DPO 3000 series are used). Its trigger source is set to external, connected to the trigger output signal at the function generator. The actual current passing through the magnet is monitored by measuring voltage at the monitor output provided on the current amplifiers. This voltage comes in through channel 1, and a calibration curve is used to transform it into magnetic field during the post-analysis (explained later). The three outputs of the TP detector ($I_{\Sigma}^{\mathrm{AC}}$, $I_{\Delta}$ and $I_{\Sigma}^{\mathrm{DC}}$) are connected to the other three input channels. In figures 2.15 and 2.16 connections and screenshot of oscilloscope can be seen. The oscilloscope is set to average option so that some noise is reduced directly during signal acquisition. After the desired time of averaging has passed, the four channels stream data set is sent to the computer. Oscilloscope can be operated manually during alignment processes or for setting the $\lambda/2$ to the optimum position for the measurement. In a section later, the process is detailed.

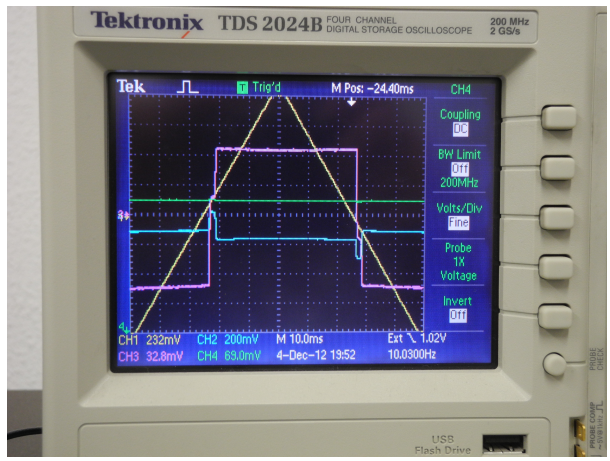


Figure 2.16: Oscilloscope showing the four channels. Yellow corresponds to the current (some ripple in the figure is due self induction at the electromagnet happening when frequency or current is higher than the maximum allowed for the magnet). Blue channel represents a perpendicular magnetization component, pink is the parallel and green is teh absolute intensity. Blue and pink correspond to a double transition loop, seen as a function of timebase. It becomes a loop after combining with current by the software or post-analysis.

### 2.3.6 Measurement automation software

The aforementioned control electronics are connected via IEEE 488.2 to a computer that runs specialized software developed in this thesis, called THERMOKE. The main basic aspects controlled by the software are temperature, sample axis angle, external magnetic Field, and signals from the twin photodiode. The software allows configuring the parameters to perform specific measurement procedures, including temperature ramps and angular ranges for each temperature. Field cooling and transiting field options, different noise reduction methods, external field options, and temperature PID control parameters can be set so that the set-up can work in an unattended way, storing data for post-analysis. The oscilloscope channels are read together with the time base. The software combines in real time the signals with the current to give final hysteresis loops, and stores them in text files that can be read by the post-analysis software. The translation of the magnet current, given as voltage by channel 1 of the oscilloscope, into magnetic field, is done in post-analysis process with the help of a calibration table previously prepared after characterizing the electromagnet with a hall sensor.

In figures 2.17 and 2.18 the aspect of the software can be seen. In figure 2.19 a functional diagram of the software is seen, where the measurement loops appears in different colours: blue for the temperature loop, and red for the angle loop. Temperature loops are typically ramps, while angle loops are a complete turn of the axis every 2.5 or 5 degrees.

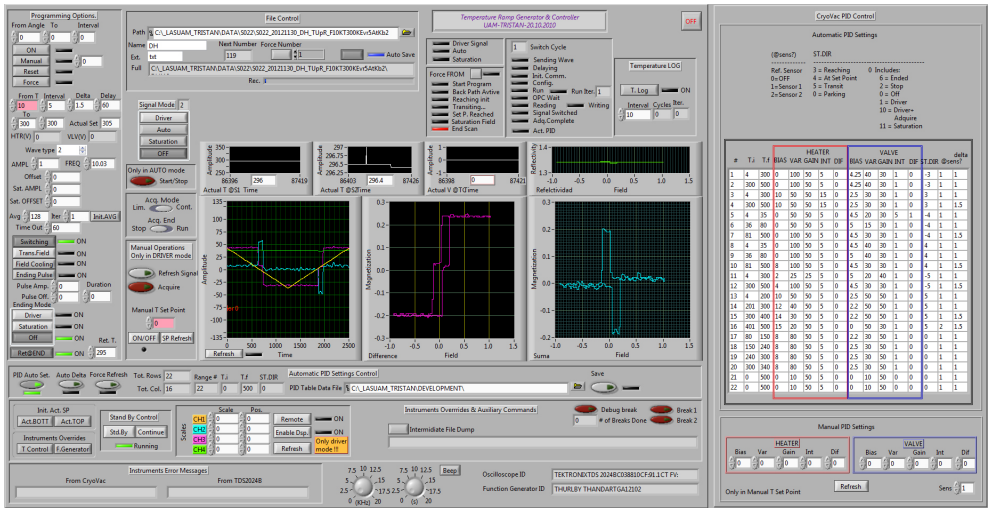

Figure 2.17: Thermoke software screenshot, temperature ramp control. Only for illustration (not explained).

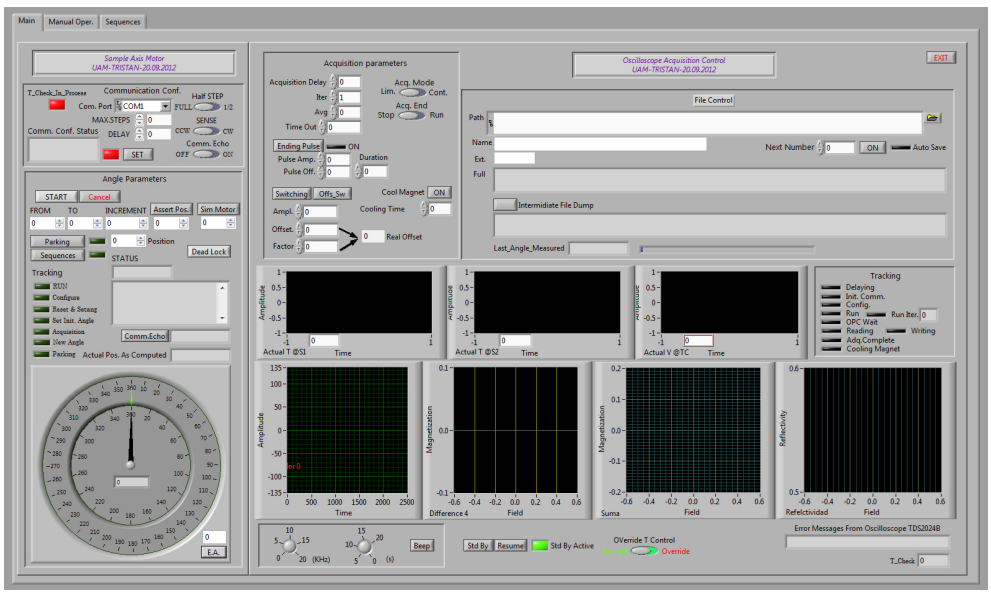

Figure 2.18: Thermoke software screenshot, angle ramp control. Only for illustration (not explained).

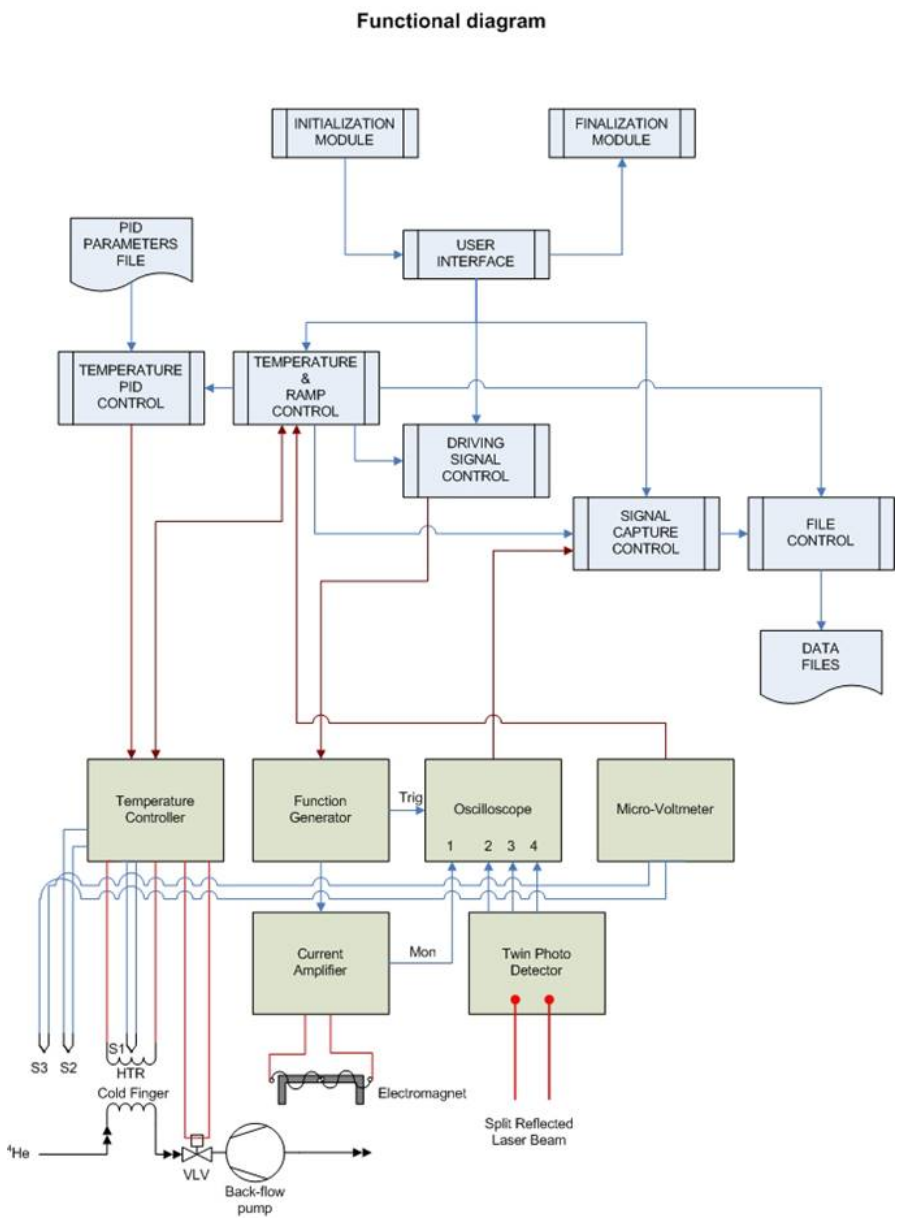


Figure 2.19: Functional block diagram of Thermoke software, with software modules and electronics, and the logical links connecting them. Soft blue boxes correspond to software modules, while pastel green correspond to electronics. Temperature sensors are signaled with S1, S2 and S3. Heater and Cold Finger can be seen bottom left, and the heater control and helium valve control are indicated with red connections to the corresponding electronics. The motor control software is not depicted here. Electromagnet control and photodiodes are depicted at the bottom as well.

## 2.4 Measurement process

After mounting a new sample and before starting pumping the cryostat, the eucentric head is adjusted manually in order to have a fixed reflection plane at all rotation angles. The good mechanical stability of the sample holder keeps fixed the reflection plane under vacuum conditions at any temperature. This allows comparison of the absolute values of the magnetization acquired at different angles and temperatures. In addition, a fixed reflection plane allows for the compensation of diamagnetic or paramagnetic contributions, by subtracting the same linear function to the whole angular study when necessary.

In order to improve the signal-to-noise ratio, the $\lambda/2$ retarder must be tuned to obtain comparable signals in both photodiodes. This is carried out by rotating the $\lambda/2$ plate until DC-diff signal is vertically centered around zero voltage on the oscilloscope display. At this point, polarization rotation is oscillating around 45° axis, and the Wollaston prism produce splitting of similar signals. Magnetic fields should also be carefully set so that they remain big enough to saturate sample during the whole temperature range of the measurement.

Then the parameters for the experiment are set in THERMOKE software: applied field, frequency, number of hysteresis loops per temperature and angle set-point, as well as temperature ramp, angular range, field cooling/warming parameters, transient fields an so. Then the ramp can get started, and the software captures vectorial-resolved hysteresis loops automatically at each temperature and angle set point. Hereafter we refer the in-plane angle of the sample with respect to the (fixed) external field as $\alpha_H$. For each angle $\alpha_H$, hysteresis loops with the given field parameters are recorded. A temperature ramp at fixed angle, from 4 K to 500 K and back to RT with set-points every 5 K can take around 10 hours. A full angular study every 5 degrees at a certain (fixed) temperature can take around 2 hours. A combined temperature and angular study can take longer depending on how many temperature set-points we use.

Measurements are typically performed with a 4 Hz triangular-shaped magnetic field ramp. At a fixed $T$, for each angular condition the signals are averaged during 2 min (i.e., over 500 loops). The set-up provides a sensitivity better than 1 $\mu$rad and $10^{-6}$ V for Kerr rotation angles and reflectivity changes, respectively. The accuracy of both in-plane magnetization components normalized to the saturation magnetization value are better than $10^{-3}$.

## 2.5 Post analysis

Post analysis of the data acquired is carried out by using a set of Origin macros. These macros are in charge of combining positive and negative hysteresis loop cycles to remove quadratic terms, as explained before, and extract the magnetic parameters as a function of the angle, such as transition fields, remanence, saturation and exchange bias field. Special macros are created to plot hysteresis loops over the angular range all at once, necessary to get a global idea of where the characteristic axes are located.

Improvement on these macros have been carried out during this thesis, and more specifically, a hysteresis loops navigator has been created to facilitate exploring the results. In figure 2.20, the hysteresis navigator is depicted. With this navigator,

detailed exploration of the vectorial hysteresis loops can be carried out, in order to investigate magnetic parameters and refine or remove artifacts if necessary.

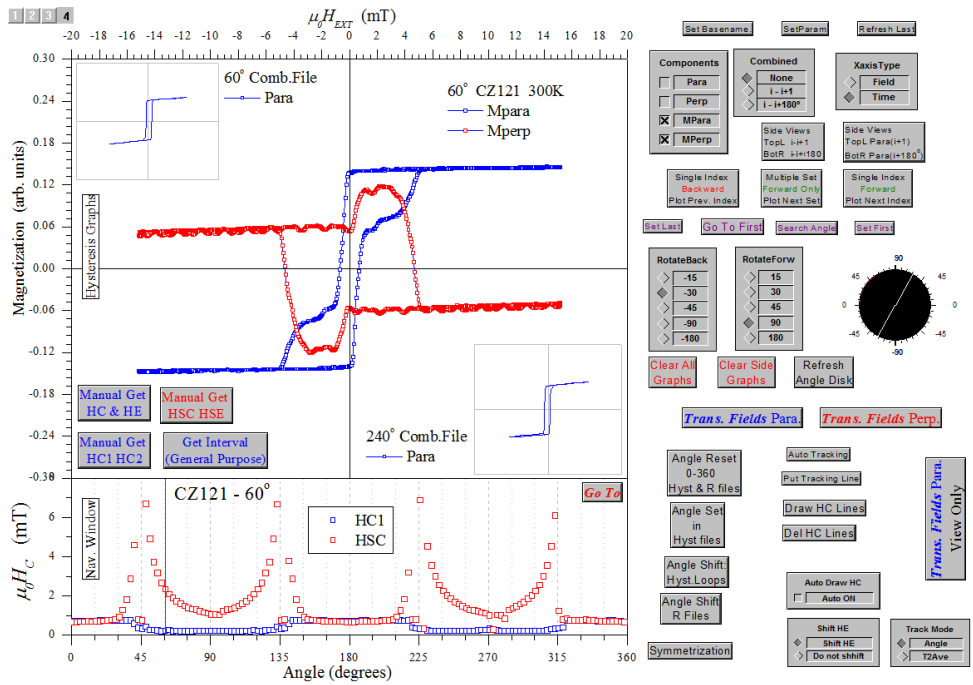


Figure 2.20: Hysteresis loops navigation panel. It provides four plots: the upper plot with its two inserts at its corners corresponds to the hysteresis loop viewer, while the bottom plot corresponds to the angle navigator. By clicking any point on this angle navigator panel, the corresponding hysteresis loop is automatically placed on the loop viewer. Checking he loops that have been used in the quadratic term removal procedure is easy through the insets. Different controls have been set for navigation, as well as automatic processes for transition field acquisition trough derivatives.

## 2.6 Error sources and noise reduction

The main error sources come from electromagnetic noise, mechanical vibrations and laser stability. They turn to be critical for small Kerr signal. Other sources of error are asymmetries in the current supplied by the amplifiers, remanence at the electromagnets, and capacitive coupling in signal transmission to the oscilloscope. We comment here very briefly how important this error sources are, and how can we get rid of them.

Random noise is avoidable by using the oscilloscope averaging built-in features and/or multiple acquisitions with further averaging process via THERMOKE software. Choosing the number of averages and iterations is a matter of time saving: as the averages and iterations increase, also do the time that takes to make a complete

measurement at a certain set-point. Averaging cancels random spikes as they are not located at fixed positions. Harmonic components coming from the mains or from ambient can be reduced by using as exciting frequency an inexact multiple of the mains frequency, leading to the same cancellation in the time averaging process. Ambient light is avoided by using velvet or felt shadow mask to enclose the TP.

Noise from natural building vibrations affecting the optical components (1 Hz to 10 Hz) are filtered by supporting the optical bench with dumpers. Vibrations coming from the turbo-molecular pump (1500 Hz) are reduced by using ballast in the vacuum hose, and the vibrations from the $^4$He back-flow pump (100 Hz) are reduced in the same way. Heavy ballast is used in this case.

Finally, another source of error, and quite difficult to avoid comes from the asymmetries in the electronic devices that generates the current at the electromagnets, and from the remanence of some type of electromagnet cores. These error sources can only be managed by carefully characterization of the electronics and the magnets.

More details on errors source in v-MOKE technique have been detailed in appendix F.

## 2.7 Conclusions

A complete instrumental development has been done, to cover the gap of thermal investigations with v-MOKE magnetometer, setting an unprecedented instrument which is unique worldwide up today.

The characteristics of the set-up are summarized here:

1. Vectorial capacity: simultaneous acquisition of both parallel and perpendicular components of the magnetization.
2. Full angular range exploring capacity.
3. Variable temperature measurements between 5 K and 500 K.
4. Fully automated.
5. Improvements on the post analysis of data.

# 3 Dynamical effects in model uniaxial systems

**The reversal of magnetization in extended systems is encompassed in the framework of multi-domain nucleation and domain wall motion. While in general domain wall motion is the dominant process, when field sweep rate is increased single-particle like behavior is recovered, compatible with a domination of nucleation process. Here we show this emergence of single-particle like magnetic behavior for extended thin films at dynamic regime.**

## 3.1 Introduction

The Stoner-Wohlfarth (SW) model is the simplest model that describes adequately the magnetization reversal of nanoscale systems that are small enough to contain single magnetic domains [9, 67]. However for larger sizes where multi-domain effects are present, e.g., in thin films, this simple macrospin approximation fails and the experimental critical curve, referred as SW astroid, is far from its predictions. This SW astroid corresponds to the critical curve given by the polar representation of the switching field as a function of the applied field angle, and is the identity card of a SW-like behavior. The SW astroid exhibits identical switching field at the easy-axis (e.a.) and hard-axis (h.a.) magnetization directions (solid line of figure 3.2,right)[2]

Here we show that this discrepancy vanishes at dynamic regime. We present a detailed angular-dependent study of magnetization reversal dynamics of a thin film with well-defined uniaxial magnetic anisotropy. The angular-dependent properties display a gradual transition from *domain wall pinning and motion*-like behaviour to a *nucleative single-particle* one, as $\mathrm{d}H/\mathrm{d}t$ increases. Remarkably, in the high dynamic regime, where nucleation of reversed domains is the dominant mechanism of the magnetization reversal (nucleative regime), the magnetic properties including the astroid become closer to the ones predicted by SW model. The results also show why the SW model can successfully describe other extended systems that present nucleative regime, even in quasi-static conditions. A model system with well define uniaxial anisotropy consisting on a Co layer (thickness in the order of a couple of tens) is studied here in the dynamical regions where field rate of change is above the mean time that domain walls need to travel from a certain pinning configuration to the next one. This is the regime where propagative phenomena gives way to nucleative.

[2]It is interesting to note that other models for rotation, as the curling model, predicts smaller values at e.a. direction [94], depending on the aspect ratio of the one-dimensional magnetic nanostructure.

## 3.2 Co/Si(111) thin film

A schematic representation of the sample structure is shown in figure 3.1. Co thin films were fabricated by DC magnetron sputtering at room temperature (RT) on thermally oxidized Si substrates covered with a 2 nm thick Ta buffer layer to avoid oxidation from the substrate. The samples were grown in a 0.2 T in-plane external magnetic field to induce a well-defined uniaxial magnetic anisotropy ($K_U$) in the ferromagnetic (FM) layer, with the anisotropy direction parallel to the field direction. The samples were finally capped with a 2 nm thick Ta layer to prevent oxidation. Three samples with different thicknesses were prepared, $t_{Co}$ = 5, 10, and 20 nm, all of them presenting the aforementioned uniaxial magnetic anisotropy. Similar quasi-static and dynamic behaviors have been found for the three samples. The quasi-static case is described in chapter 4. The data presented in this chapter correspond to a 20 nm thick Co thin film.

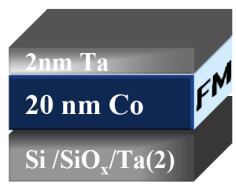


Figure 3.1: Scheme of the Co/Si(111) thin film sample structure.

## 3.3 Time-resolved v-MOKE setup

Angular dependent, time-resolved, vectorial Kerr magnetometry measurements have been performed with our standard RT vectorial v-MOKE set-up and with TRISTAN (see citations [81, 93]), over 9 decades of applied magnetic field sweep rates ($dH/dt$), allowing the acquisition of the two in-plane magnetization components, i.e., parallel ($M_{||}$) and transverse ($M_{\perp}$) to the external applied field. For this dynamical studies, detectors (the Twin Photodiodes, see for instance section 1.7) and electromagnets have been adapted to suit the requirements of dynamical measurements over a wide range of $dH/dt$, from $10^{-4}$ to $10^{+4}$ T/s. Special electronics capable of driving enough current at high frequencies where also used. In particular, the magnetic field response of the electromagnet is linear with the driving current up to 80 mT for frequencies ranging from 1 mHz to 150 kHz, and the rise-time of the detectors has been set to 20 ns. A cross-check that ensures that both electromagnet and detection systems are properly chosen comes from the experimental observation of non-hysteretic loops at the hard-axis direction in the whole dynamical range investigated (see bottom left hysteresis loops in figure 3.3, corresponding to 90°, i.e., the hard axis).

## 3.4 Angular evolution of transition fields at dynamic regimes

The effect of a propagative multi-domain reversal process turning into nucleative as field sweep rate is increased can be easily visualized in figure 3.2 by observing that the dynamical behavior of coercive field ($\mu_0 H_C$) and switching field ($\mu_0 H_S$) approaches to the SW prediction as the applied field sweep rate ($dH/dt$) increases. In this figure, detailed dynamical study on the angular dependence of the magnetic properties for the model system described in section 3.2 are detailed. The magnetization reversal dynamics of the two in-plane magnetization components, i.e., parallel ($M_{||}$) and transverse ($M_{\perp}$) to the external applied field, have been investigated over 9 decades of $dH/dt$ and in the whole angular range.

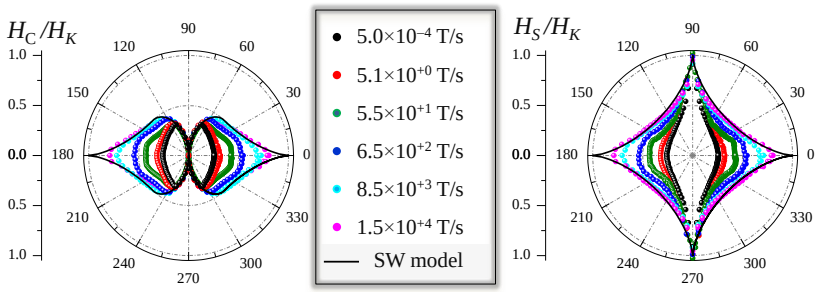


Figure 3.2: Angular dependence of the dynamic coercivity $\mu_0 H_C$ (left polar plot) and switching field $\mu_0 H_S$ (right polar plot) for a thin film with well-defined uniaxial anisotropy. Symbols are the experimental data normalized to the anisotropy field $\mu_0 H_K$ derived from vectorial-resolved kerr hysteresis loops acquired at the indicated applied field sweep rate ($dH/dt$) values. Solid lines are the expected values from the Stoner-Wohlfarth (SW) model that assumes uniform rotation and switching of the entire system. Notice that the experimental data are approaching to the SW prediction as $dH/dt$ increases.

Thermal activated dynamical effects are found during irreversible processes and depend strongly on the orientation of the anisotropy axis with respect to the external field (referred as the angle $\alpha_H$). The effects are more relevant near the e.a. direction ($\alpha_H = 0°$) and vanishes near the h.a. direction ($\alpha_H = 90°$). In contrast, the reversible transitions are not affected by dynamical effects. The data have been interpreted in the framework of magnetic domain pinning and rotation models for quasi-static and dynamic conditions, respectively.

The reversal processes can be determined directly by a simple inspection of the in-plane vectorial magnetization loops [81, 93], highlighting the importance of vectorial-resolved magnetometry. Full angular-dependent studies were carried out at selected $dH/dt$ values. A detailed analysis in quasi-static condition is given in chapter 4.

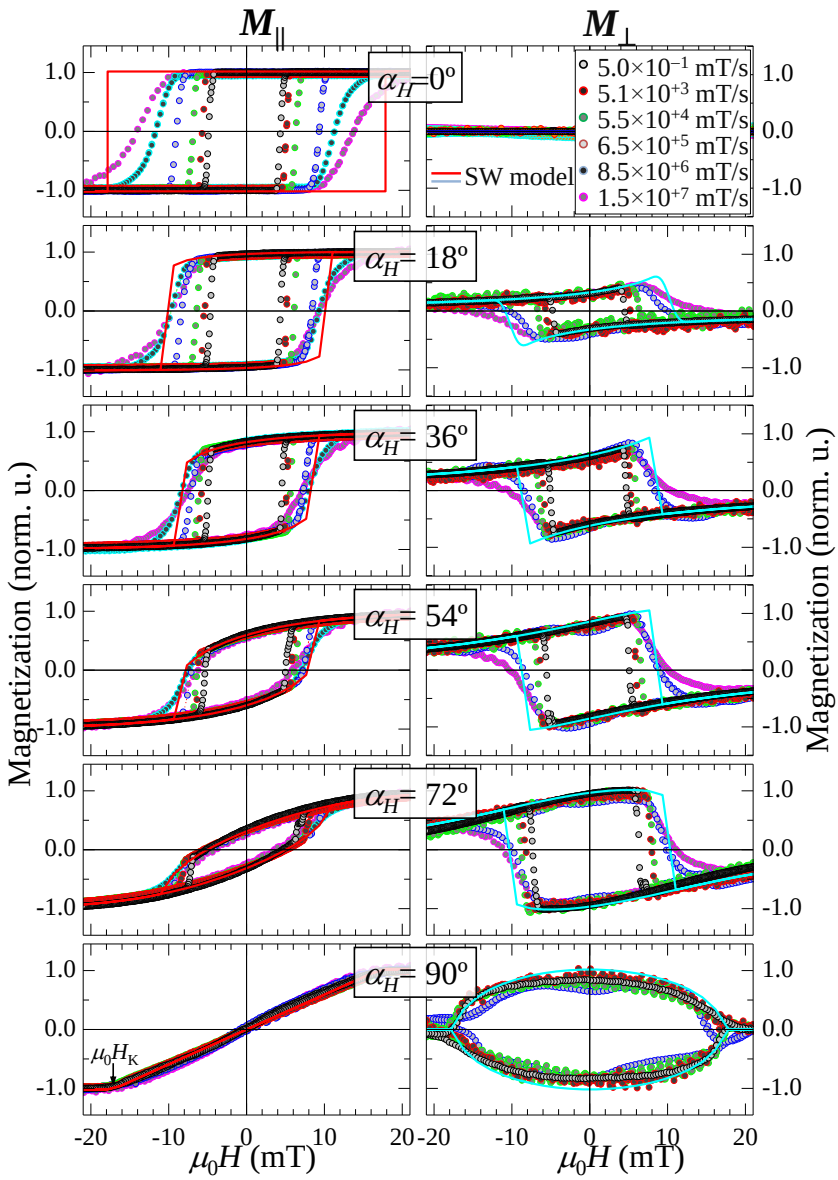


Figure 3.3: Angular-dependent dynamical hysteresis loops for a FM thin film with well-defined uniaxial magnetic anisotropy. The applied magnetic field angle $\alpha_{\mathrm{H}}$ and sweep rate $\mathrm{d}H/\mathrm{d}t$ are indicated. For each $\alpha_{\mathrm{H}}$, both parallel $M_{||}(H)$ (left plots) and transversal $M_{\perp}(H)$ (right plots) magnetization Kerr hysteresis loops were acquired simultaneously at room temperature for several $\mathrm{d}H/\mathrm{d}t$ values. The solid lines correspond to the predicted ones from SW model using the experimental anisotropy field $\mu_0 H_{\mathrm{K}}$ indicated in the bottom graph.

## 3.5 Inspection of the vectorial hysteresis loops

Figure 3.3 shows representative parallel ($M_{||}$) and transversal ($M_{\perp}$) magnetization loops at selected $\alpha_{\mathrm{H}}$ acquired at different $\mathrm{d}H/\mathrm{d}t$. For a given $dH/dt$, in general, irreversible (sharp) transitions and/or fully reversible (smoother) transitions are observed in both $M_{||}(H)$ and $M_{\perp}(H)$ loops, which correspond to nucleation of magnetic domains followed by domain wall propagation and to rotation processes, respectively. The relative weight of these two reversal mechanisms depends on $\alpha_{\mathrm{H}}$ and $dH/dt$ and reveals the uniaxial magnetic anisotropy of the film.

For a given $\alpha_{\mathrm{H}}$, the shapes that both $M_{||}(H)$ and $M_{\perp}(H)$ loops have before the irreversible transition are similar for the whole dynamic range of $\mathrm{d}H/\mathrm{d}t$ investigated, as can be seen on the left and right graphs of figure 3.3, respectively: dynamical effects result in a lengthening of the reversible processes, but without changing their shape, which indicates that reversible processes are non-thermally activated. Dynamical effects are only observed in the irreversible transitions: increment of the reversal fields and broadening of the transitions as the applied field sweep rate is increased. As for the first aspect, the reversal field enhancement indicates that the irreversible processes are thermally activated. For the second aspect, the broadening of the irreversible transitions suggests that the reversal is governed by two different mechanisms depending on the dynamic regime: at lower $\mathrm{d}H/\mathrm{d}t$ the reversal is mainly governed by domain wall propagation processes (characterized by more abrupt jumps), while at higher sweep rates, domain nucleation processes dominate (softening the irreversible jumps), as discussed in more detail below.

Over the last decades, several studies have addressed the magnetization reversal dynamics in several magnetic thin film-based nanostructures at different timescales. In general, precessional reversal of magnetization takes place at subnanosecond time scales (ultra-fast dynamic regime) [95], while nucleative and propagative processes can take variable amounts of time [11], from submicrosecond (high dynamic regime) to large fractions of a second (quasi-static or low dynamic regime) [96]. For instance, hysteresis loop measurements as a function of the applied magnetic field sweep rate ($\mathrm{d}H/\mathrm{d}t$) support the picture of nucleation-dominated reversal in the high dynamic regime and wall propagation-dominated reversal in the low dynamic regime [97, 69]. This scenario has been found in dynamical studies of single ferromagnetic (FM) layers with both in-plane [98, 99] and out-of-plane [100] anisotropy as well as in more complex structures, such as in-plane [101, 102] and out-of-plane [103] exchange-biased FM/antiferromagnetic systems and trilayer FM1/non magnetic/FM2 magnetic structures [104]. The crossover between propagative and nucleative regimes depends on the strength of the anisotropy of the system: higher anisotropy favors earlier nucleative regimes. It is worth mentioning that all these studies were performed only at the e.a. direction, and with sensitivity only to the magnetization component parallel to the external field.

In our study, in addition, we can determine the angular dependence of the dynamical effects. For instance, by comparing the loops of figure 3.3 acquired at the minimum and maximum $\mathrm{d}H/\mathrm{d}t$ values for the different angles, we find out that the rise of the dynamic effects are more pronounced at the e.a. direction (top graph), i.e., $\alpha_{\mathrm{H}} = 0°$, diminishing progressively as the applied field angle increases (middle graphs), and vanishing at the h.a. direction (bottom graph), i.e., $\alpha_{\mathrm{H}} = 90°$. Notice that as $\mathrm{d}H/\mathrm{d}t$

increases, the experimental loops approaches the ones predicted with the SW model (solid lines in figure 3.3). In turn, the remanent magnetization (or remanence) $M_{\mathrm{R}}$, i.e., magnetization at zero field, of both magnetization components is independent of the applied field sweep rate in the whole angular range. Figure 3.4 show similar angular dependence at two different $\mathrm{d}H/\mathrm{d}t$ values that differ in six orders of magnitude, i.e., for quasi-static and high dynamic conditions. The corresponding polar plots depicted in figure 3.4(b) show the characteristic (two-fold) symmetry of a well-defined uniaxial magnetic anisotropy system: $M_{\mathrm{R},\parallel}(\alpha_{\mathrm{H}})$ and $|M_{\perp,\mathrm{R}}(\alpha_{\mathrm{H}})|$ display *"two-lobes"* shape rotated 90° with respect to each other. This unambiguously indicates that the orientation of the magnetization vector at remanence does not present dynamical effects. In fact, this is preserved until the irreversible transition takes place. These features are in accordance with the relevance of the (non-thermal activated) reversible and (thermal activated) irreversible transitions. Therefore, the magnetic symmetry is preserved and larger dynamic effects are found where irreversible processes are more relevant during reversal.

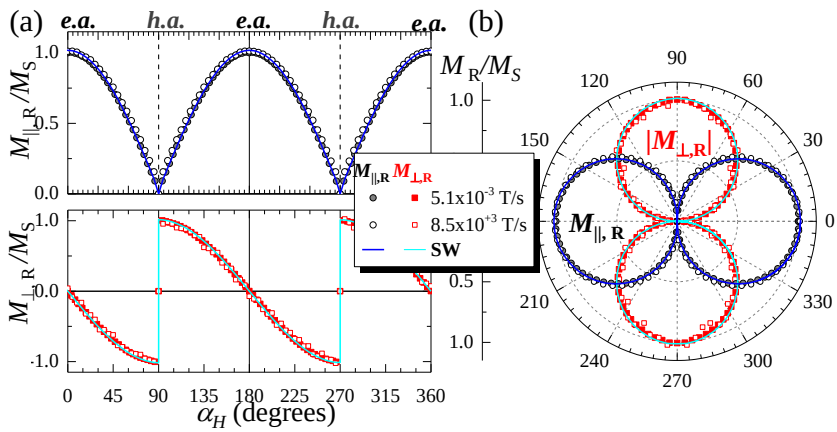


Figure 3.4: (a) Angular dependence of the normalized remanent magnetization components of a well-defined uniaxial magnetic anisotropy system at indicated $\mathrm{d}H/\mathrm{d}t$ values. For clarity, $M_{||,\mathrm{R}}$ and $M_{\perp,\mathrm{R}}$ are depicted in separated plots, top and bottom respectively. (b) Corresponding polar plot representation. Symbols represent the experimental data extracted from the in-plane resolved hysteresis loops acquired in quasi-static (circles) and at high dynamic (squares) conditions, as the ones shown in figure 4.1. The solid lines correspond to theoretical evolution derived from the SW model.

## 3.6 Detailed analysis of the transition reversal fields

Thermal *vs.* non-thermal activation effects on magnetization reversal dynamics manifest directly through the analysis of the dynamic transition reversal fields of both magnetization components, referred as coercive field $\mu_0 H_{\mathrm{C}}$ and switching field $\mu_0 H_{\mathrm{S}}$, and defined as the fields at which $M_{||}(\mu_0 H_{\mathrm{C}}) = 0$ and $M_{\perp}(\mu_0 H_{\mathrm{S}}) = 0$, respectively.

Figure 3.5 shows the corresponding dynamic evolution of coercive and switching fields at representative $\alpha_H$. The global behavior is summarized as an increase in $\mu_0 H_S$ as $dH/dt$ increases, but clearly two dynamical behaviors at low and high sweep rates can be distinguished, where $\mu_0 H_S$ varies very slowly at low sweep rate, and increases more rapidly at high rates. The crossover between the two regimes, marked with vertical arrows in figure 3.5, takes place at higher $dH/dt$ for larger angles (yellow arrow shifts to the right as angle is increased). In contrast, $\mu_0 H_C$ shows three dynamical evolutions for different angular ranges. In general, all can be associated to the relevant mechanism during reversal, where (thermally activated) irreversible and (non-thermally activated) reversible processes govern the dynamics around the e.a. and h.a. directions, respectively. For intermediate angles, the dynamic fields result from the competition between them.

Around the e.a. direction, for $\alpha_H < 45°$, both reversal fields are taken just when the reversible transition have finished and similar dynamic coercive and switching field values are found, which depend on both $dH/dt$ and $\alpha_H$ (see top graph of figure 3.5). In general, the reversal fields increase slowly and logarithmically in $dH/dt$ for low sweep rates (low dynamic regime). For high sweep rates the increase of the reversal field with field sweep rate becomes much faster (high dynamic regime). This behavior has been explained in the literature in terms of a transition between two different thermally activated reversal regimes [100, 101, 102]. At low sweep rates the magnetization reverses mainly by domain wall propagation while at higher sweep rates, where the propagation process becomes relatively slow compared to the variation of the applied magnetic field, successive nucleations of reversed domains dominate the reversal. Since the activation energy for domain nucleation is larger than that for domain wall motion, the reversal field varies more strongly with $dH/dt$ in this reversal regime. In addition, in both regimes the dynamic reversal field increases and the rising slope decreases as $\alpha_H$, increases. As a result, the crossover between these two thermally activated regimes is found at higher $dH/dt$ as we move away the e.a. direction.

For $\alpha_H > 45°$, while the dynamic switching field shows the trend already described, the dynamic coercivity presents a peculiar evolution in which three behaviors for different $dH/dt$ ranges can be distinguished, defining a low, crossover and high dynamical regime regions, respectively (see central graph of figure 3.5). Two of these regions (low and high dynamic regimes) present an approximately linear relationship between $\mu_0 H_C$ and $log(dH/dt)$ but with different slope, which is higher at high dynamic regime. A third region characterized by a dip in $\mu_0 H_C$ is found at the crossover from low dynamic regime to high dynamic regime. Similar behavior was found in epitaxial Fe/GaAs(001) films, where the dip was shifted to lower $dH/dt$ as the temperature was reduced [105]. It has been suggested that forced depinning from nucleation sites at these sweep rates is responsible for the dip in coercive field, and that there are two distinct timescales associated with the reversal process which correspond to domain nucleation and wall motion, respectively. In our case, this behavior can be simply understood taking into account that for $\alpha_H > 45°$ the dynamic coercive field can be derived from a still reversible process, happening before the irreversible transition related to the switching field takes place. Therefore, for this angular range, nucleation dynamics cannot be derived from the dynamic coercivity, but from the dynamic switching field. In fact, the latter presents two clear dynamical behaviors following the trend discussed above, i.e., propagative to nucleative regimes. In addi-

tion, the crossover between the two regimes still shifts to higher $\mathrm{d}H/\mathrm{d}t$ values when $\alpha_{\mathrm{H}}$ increases.

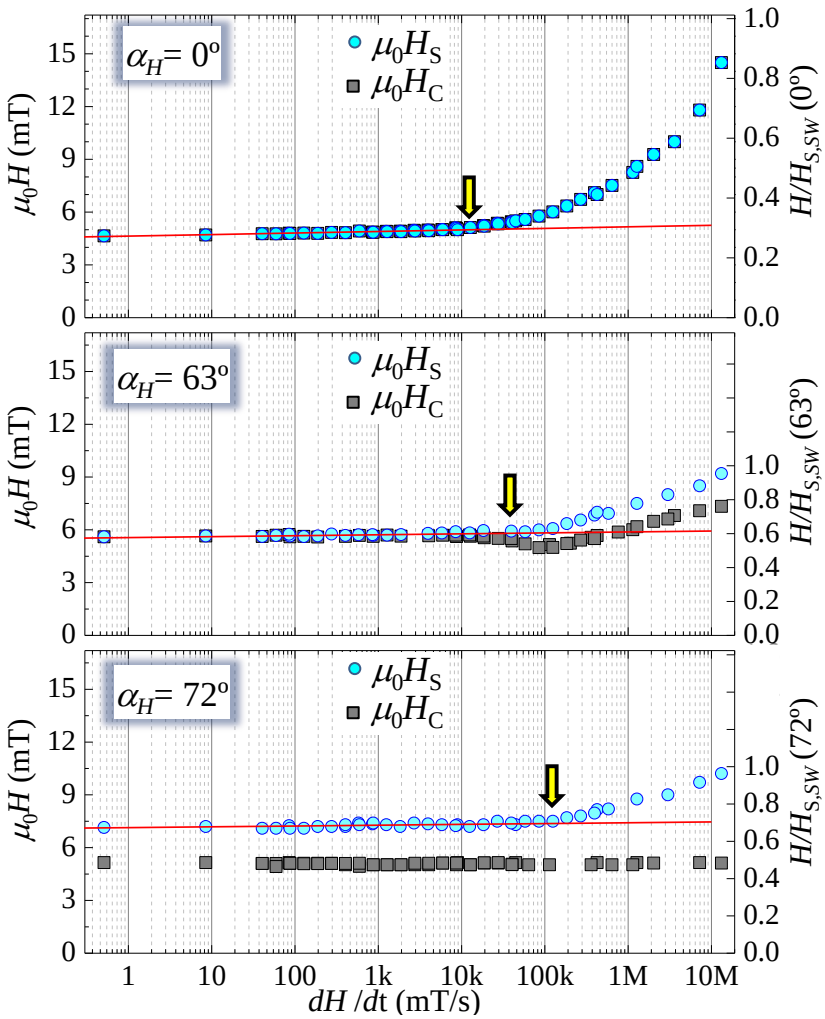


Figure 3.5: Evolution of the coercive field $\mu_0 H_{\mathrm{C}}$ (square symbols) and switching field $\mu_0 H_{\mathrm{S}}$ (circles) as a function of the applied field sweep rate $\mathrm{d}H/\mathrm{d}t$ for selected applied field angles $\alpha_{\mathrm{H}}$. The right-Y axes have been normalized by the corresponding switching fields predicted by the SW model ($H_{\mathrm{S,\,SW}}(\alpha_{\mathrm{H}})$). The symbols are the experimental data taken from the in-plane resolved magnetization curves such as those shown in figure 4.1. The lines are the expected behavior predicted by a phenomenological model based on domain wall dynamics (see text). A semi-logarithmic scale has been used to identify the range of sweep rates where domain wall propagation dominates the reversal [101, 102]. Vertical arrows remark the crossover between the propagative to nucleative regime.

Around the h.a. direction, different dynamic $\mu_0 H_C$ and $\mu_0 H_S$ values are found, as expected from the definition of both reversal fields, which depend on $\alpha_H$. In this angular range the coercivities are taken long before the reversible processes have finished, resulting in a non-dependency of $\mu_0 H_C$ with $dH/dt$, and in a decrease as $\alpha_H$ increases, vanishing when approaching the h.a. direction. In turn, $\mu_0 H_S$ increases as $\alpha_H$ and $dH/dt$ increase. At low dynamic regime the switching field increases, with a maximum at the h.a., and its dynamic slope decreases approaching the h.a. direction. This indicates that the magnetization reversal dynamics close to the h.a. is governed mainly by non-thermally activated rotation processes.

The low dynamic regime of the irreversible transition can be simulated by using a phenomenological model based on thermally activated relaxation "single relaxation time approximation" of propagating magnetic domains walls [97, 69]. The model assumes that the energy barrier for magnetization reversal varies linearly with the applied magnetic field (i.e., domain wall propagation with weak pinning centers) and predicts a logarithmic dependence of the reversal field on the applied sweep rate (equation (7) of [100]). We want to point out that this analysis has been performed in $\mu_0 H_S(dH/dt)$ because the switching field is sensitive just to irreversible processes for the whole angular range. Notice that, although this is also valid for the dynamic coercivity for $\alpha_H < 45°$, it is not correct for larger angles where mixed reversible and irreversible processes are present. The solid lines of figure 3.5 derived from this model reproduce the experimental dynamic evolution for the low dynamic regime. Moreover, the $dH/dt$ validity range of the simulation indicates that the transition from the domain wall propagation regime at lower $dH/dt$ to the domain nucleation regime at higher $dH/dt$ shifts to higher sweep rates as $\alpha_H$ increases (see arrows in figure 3.5). This indicates that the higher irreversible field values found as we move away from the e.a. make nucleation processes more relevant and delay the transition between the dynamic regimes.

The tendency in the high dynamic regime, i.e., where nucleation becomes more relevant during the irreversible transition, can be figured out by simply inspecting the angular dependence evolution of the coercive and switching fields as $dH/dt$ increases. Figure 3.6 compares the data extracted from the experimental loops (symbols) with the predicted ones by the domain wall pinned (dashed line) model and the Stoner-Wohlfarth (SW) (solid line) models. It is worth noting that the experimental data show a clear transition from a pinned-like behavior at low $dH/dt$ (propagative regime) to a SW-like behavior at high $dH/dt$ (nucleative regime).

The SW model assumes a single particle behavior, i.e., coherent reversal by switching (irreversible process) and/or rotation (reversible) of the whole magnetization, without taking into account any other irreversible magnetization reversal process like nucleation and propagation of magnetic domains. The latter is, in fact, energetically much more favorable in extended systems, in which defects of any kind—structural or morphological—play the main role to activate irreversible magnetic domain nucleation processes at magnetic fields that are significantly lower than expected by the SW model. In fact, low coordination sites such as sample edges, grain boundaries, and topographic roughness, are unavoidable in real samples. These defects can act as pinning centers[3] for the created magnetic domain walls and the reversal subsequently

[3]They also act as nucleation centers, but we do not enter into this aspect here.

continues via domain wall propagation. In this case, a simple model of pinned 180° magnetic domain walls (pinning model) [106] predicts a $1/|\cos\alpha_{\mathrm{H}}|$ law for the angular dependence of the reversal field, i.e., only the projection of the field along the magnetization is effective. As a consequence coercive field is no longer maximum at the e.a. direction, in clear contrast with the SW model that predicts a maximum value of the coercive field, which is similar to the anisotropy field.

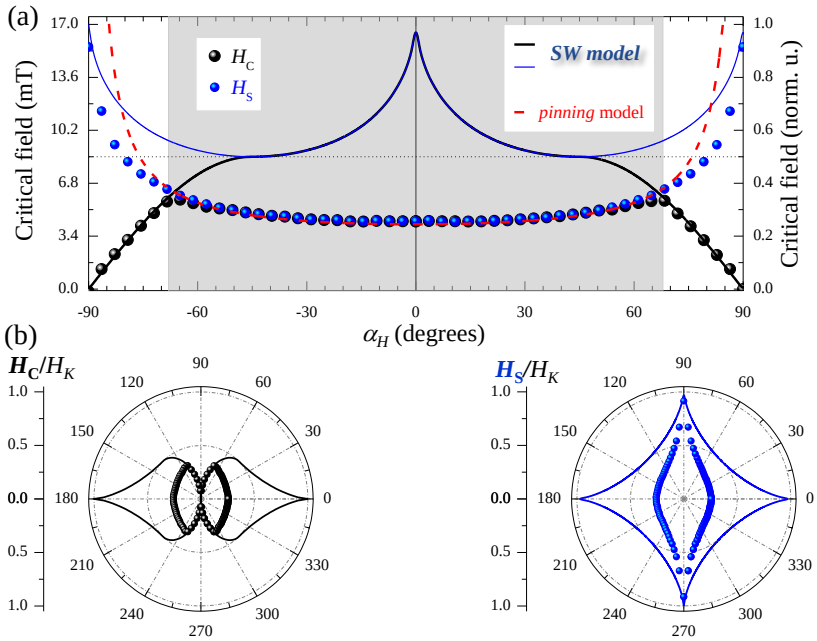


Figure 3.6: Angle-dependent coercive field $\mu_0 H_{\mathrm{C}}$ (a) and switching field $\mu_0 H_{\mathrm{S}}$ (b) for selected applied magnetic field sweep rates $\mathrm{d}H/\mathrm{d}t$. The symbols are obtained from the experimental vectorial-resolved dynamic hysteresis curves (see for instance cycles in figure 4.1), as described in the text. The polar plot representation of this data is shown in figure 3.2. The direct comparison between experiment and the predictions derived from the pinning model (red line) and the SW model (black lines) indicates a gradual transition between pinning-like behavior and SW-like one as $\mathrm{d}H/\mathrm{d}t$ increases.

## 3.7 Comparison with the low dynamic regime

From our dynamic study, at low $\mathrm{d}H/\mathrm{d}t$ the angular evolution of the irreversible transition shows a pinned-like behavior in a broad angular range around the e.a. direction, In particular, both $H_{\mathrm{C}}(\alpha_{\mathrm{H}})$ and $H_{\mathrm{C}}(\alpha_{\mathrm{H}})$ follow the predicted behavior by the pinning model for an angle range $\pm 60°$ (see red solid line in figure 3.6(b)). Similar findings have been reported in both perpendicular [107] and in-plane [88] anisotropy systems, from angular-dependence quasi-static measurements. The experimental data increase as $\mathrm{d}H/\mathrm{d}t$ increases, but always limited by the expected values from the SW model

(see black solid lines in figure 3.6). Remarkably, the similarity between the experimental data at the highest dynamic regime investigated and those predicted by the SW model are very high. Dynamic measurements performed just at the e.a. direction in perpendicular anisotropy systems also showed this tendency, i.e., the coercive field at the e.a. direction becomes closer to the anisotropy field at the fastest dynamical regime. [108] In addition, we show that the whole angular range of transition fields, including both coercive and switching fields, approaches the SW-like behavior as $\mathrm{d}H/\mathrm{d}t$ increases (figure 3.6). The transition from the pinned to the SW model with increasing $\mathrm{d}H/\mathrm{d}t$ can be observed clearly in the polar representation shown in figure 3.2. Thus, our dynamic study shows that pinned-like and SW-like behaviors can be found at low $\mathrm{d}H/\mathrm{d}t$ and high $\mathrm{d}H/\mathrm{d}t$, respectively. Moreover, the data show that this is directly connected with propagative and nucleative regimes, respectively.

## 3.8 Why SW-like behavior at nucleative regime

A "hand-waving" clarifying note on why at nucleative regime the behavior is very close to SW model is presented here. As it has been said, at high dynamic regimes the density of nucleated domains increases, an indication that domain wall motion time scales become larger compared with the time that takes the external field to provide energy enough to activate more and more nucleation centers. At high field rates there is no time for DW to propagate before the nearby region is activated. In the limit where the density of nucleated domains is such that they cover the whole system before any domain wall have had the time to expand, the landscape is as if a single domain, with the size of the whole system, had nucleated at once. This is then like a macrospin behavior, and hence the behavior must be described by SW model.

## 3.9 Conclusions

In summary, we have carried out vectorial-resolved angular-dependent studies of the magnetization reversal dynamics, in the whole angular range, for dynamical regimes extended over 9 decades of $\mathrm{d}H/\mathrm{d}t$. Our studies provide a general view on the magnetization reversal processes in magnetic nanostructures. While thermal activation processes take place during the irreversible transitions, which correspond to nucleation and propagation of magnetic domains, reversible transition via rotation processes are not thermally activated. Propagative and nucleative processes governs the reversal at low $\mathrm{d}H/\mathrm{d}t$ and high $\mathrm{d}H/\mathrm{d}t$, respectively. The transition between both regimes depends on $\alpha_{\mathrm{H}}$, increasing as $\alpha_{\mathrm{H}}$ increases. In addition, dynamical effects are also shown on the angular dependence of the transition fields, where a transition from pinned-like to SW-like behaviors has been found. In particular, the reversal fields behave accordingly to the pinning model for the propagative regime whereas become closer to the SW model for the nucleative regime.

The results also explain why the SW model can describe successfully the angular-dependence properties of more complex extended systems, i.e., exchange biased ferromagnetic/antiferromagnetic bilayers [86, 87, 109, 110] and ripple patterned films [111], where nucleative processes are much more relevant even in quasi-static conditions.

# 4 Dynamical effects at quasi-static regime

**In this chapter we describe angular-resolved magnetic study in model thin films with well-defined uniaxial magnetic anisotropy, at quasi-static regime. Data are discussed in the framework of both domain wall pinning and macrospin Stoner-Wohlfarth reversal models. This chapter links to the previous one, as a case in which dynamical effects may happen even at room temperature for extended systems, under certain conditions.**

## 4.1 Introduction

The same model system studied in chapter 3, with well defined uniaxial anisotropy consisting on a Co layer (thickness in the order of a couple of tens) is studied here in the dynamical regions where field rate of change is below the mean time that domain walls need to travel from a certain pinning configuration to the next one. It has been observed that even at low field rates of change, nucleative processes may happen, and we discuss it here. Sample description has been already addressed in chapter 3, section 3.2. Here we present a detailed analysis of the quasi-static properties of the thicker FM layer whereas the dynamical. Quasi-static conditions in this context represents a field sweep rate in the order of a few mT/s. The frontier between what is called quasi-static and dynamic regimes was already accurately established in the previous chapter.

## 4.2 Hysteresis and magnetization reversal

Representative in-plane resolved hysteresis loops acquired in quasi-static conditions at different $\alpha_H$ angles are shown in figure 4.1. The angles have been selected to show the rich variety of hysteresis and magnetization reversal processes that a single film with well-defined uniaxial magnetic anisotropy presents. Two different representations, standard $M - H$ (top graphs) and polar $M_\perp - M_\parallel$ (bottom graphs) curves, have been used in order to identify relevant magnetic properties. In the middle, the sample orientation has been depicted for each case with the corresponding relative directions. Remarkably, a simple inspection of the in-plane resolved hysteresis loops provides direct information about the magnetization easy-axis (e.a.) and hard-axis (h.a.) directions, critical fields, domain wall angles and magnetization reversal processes.

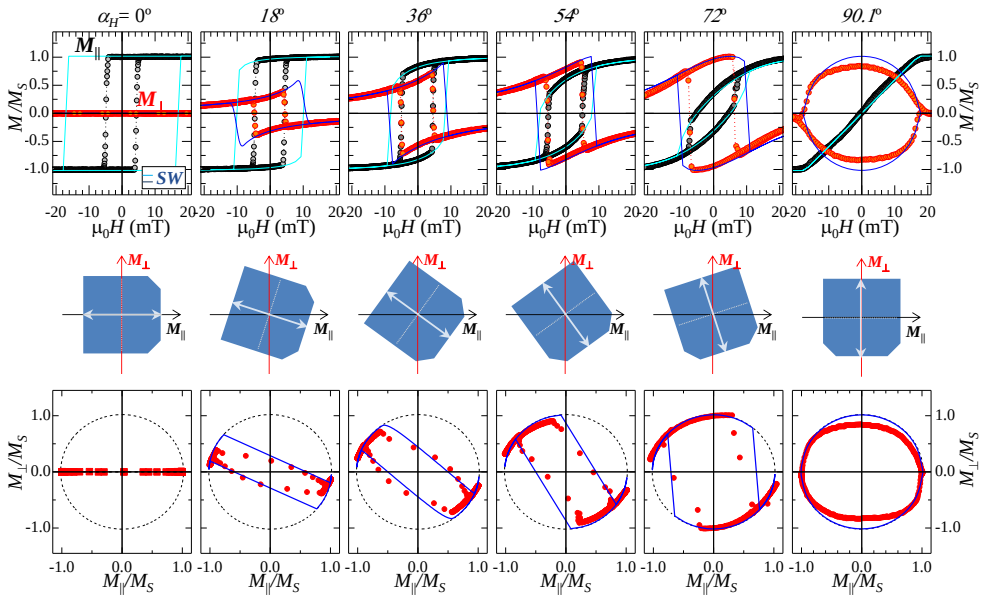


Figure 4.1: Angular-dependent quasi-static hysteresis loops of a FM thin film with well-defined uniaxial magnetic anisotropy. The applied magnetic field angle $\alpha_{\rm H}$ is indicated. (Top): standard $M-H$ representation. Symbols represent the parallel $M_{||}$ and transversal $M_\perp$ magnetization Kerr hysteresis loops acquired simultaneously. The descending (forward) and ascending (backward) field branches are depicted with filled and empty symbols, respectively. The solid lines correspond to the loops expected from SW model calculation. (Middle): experimental configuration scheme. Solid arrow ended and dashed straight lines indicate the position of the e.a. and h.a. directions, respectively. (Bottom): corresponding polar plot $M_\perp - M_{||}$ representation. Filled and open symbols have been used for the forward and the backward branch, respectively. The circle of radius unity depicted with a dashed line indicates the pure rotation of the magnetization vector. The solid lines correspond to the behavior expected from SW model.

At a first glance, vectorial (in-plane) resolved hysteresis loops display different magnetization reversal pathways in both magnetization components, which strongly depend on $\alpha_H$, highlighting the importance of the simultaneous determination of both components provided by our setup. The different pathways are more evident for the $M_\perp(H)$ loop. In general, irreversible (sharp) transitions and/or fully reversible (smoother) transitions are observed in both $M_{||}(H)$ and $M_\perp(H)$ loops, corresponding to nucleation of magnetic domains followed by domain wall propagation and rotation processes respectively. The relative weight of these two reversal mechanisms depends on $\alpha_{\rm H}$. The directional dependence originates from the symmetry breaking introduced by the magnetic anisotropy of the film.

At $\alpha_{\rm H} = 0°$ the parallel component presents a perfect squared shape hysteresis loop (top left graph of figure 4.1). $M_{||}$ does not change from the saturation ($M_{\rm S}$)

to the remanence ($M_{\parallel,\mathrm{R}}$), i.e., $M_{\parallel,\mathrm{R}}/M_\mathrm{S} \approx 1$, and there is only a sharp irreversible jump at the coercive field $\mu_0 H_\mathrm{C}$, in which the magnetization reverses. In turn the perpendicular component is negligible in the whole field swept, i.e., $M_\perp(H) \approx 0$. Both are expected behaviors of a magnetization easy-axis (e.a.) direction, in which the magnetization reversal takes place via nucleation and subsequent propagation of magnetic domains oriented parallel to the field direction.

For $\alpha_\mathrm{H} \neq 0°$, clear $M_\perp(H)$ loops with both reversible and irreversible transitions are found, in correspondence to the $M_{||}(H)$ loops, as shown in the central graphs of figure 4.1 (from 18° to 72°). In addition, larger $M_\perp$ signals are found as $\alpha_\mathrm{H}$ increases, which indicates that the rotation processes (reversible transitions) becomes more relevant and that the magnetic domains nucleated during the irreversible transition are not oriented parallel to the field direction but to the e.a. direction, in accordance with the expected reversal features of well-defined uniaxial magnetic anisotropy systems. According to this, at $\alpha_\mathrm{H} = 90°$ the $M_{||}(H)$ loop shows an almost linear and reversible behavior of the magnetization, $M_{||,\mathrm{R}}/M_\mathrm{S} \approx 0$, and $\mu_0 H_\mathrm{C} \approx 0$ mT (see right-most graph of figure 4.1), typical of an uniaxial magnetic anisotropy hard-axis (h.a.) direction. Notice that this selected angle is not exactly $\alpha_\mathrm{H} = 90°$. If that were the case, a negligible signal would be found in the corresponding $M_\perp(H)$ loop because of a perfect alignment of the external field with the h.a. direction in conjunction with the acquisition procedure. To be more exact, a vanishing perpendicular component is the consequence of averaging during many successive iterations, where for each one of them, the magnetization would rotate alternatively along the positive and negative values of $M_\perp$. A little misalignment (notice that is just 0.1° in right-most graph of figure 4.1) ends up with a rather circular $M_\perp(H)$ loop since the misalignment promotes a selection of one of the sense of the rotation, alternated for each of the two semi-cycles of the loop.

The quantitative information obtained from our v-MOKE setup allows the visualization of the in-plane trajectory of the magnetization vector during reversal (see bottom graphs of figure 4.1). In this polar plot representation, the data lying on the circle of radius unity, depicted with a dashed line, represent rotation processes. Every time the data is off this circle, magnetic domains are present. The specific mechanisms of the magnetization reversal are easily to detect with this plots. In all the cases, except for e.a., as the field is decreased from the maximum field, the magnetization vector rotates reversibly along the circle of radius unity. The rotation continues beyond zero field with the opposite field sense until an irreversible process is initiated, as indicated by the departure of the magnetization vector from that circle. Notice that both departure and return points are closed to e.a. direction, which accounts for irreversible process due to nucleation of magnetic domains oriented along the e.a. directions and subsequent domain wall propagation. The return point is found c.a. 180° away from departure point, depending on $\alpha_H$. Note that the magnetization vector is far from being saturated along the field direction even for the largest field used, except for $\alpha_H = 0°$.

Therefore, the magnetization reversal proceeds by reversible magnetization processes, starting at saturation magnetization, all the way up to the closest e.a. direction, and from there it continues with a subsequent irreversible transition, which is related to nucleation of antiparallel magnetic domains and subsequent propagation of 180° domain walls. In addition, the magnetization in the magnetic domains is not

oriented necessarily parallel to the field direction but rather to the e.a. direction. In order to have quantitative analysis, relevant magnetic properties associated with the reversible and irreversible processes are discussed in the following.

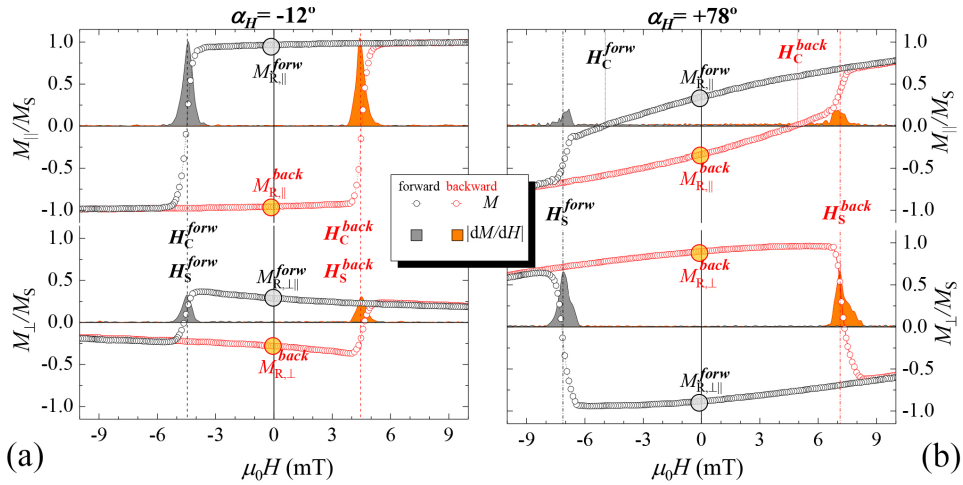


Figure 4.2: Vectorial-resolved hysteresis loops acquired at two representative $\alpha_H$ angles to illustrate the procedure to extract the magnetic parameters. The symbols are the experimental $M_{\parallel}(H)$ and $M_{\perp}(H)$ loops and the solid lines with filled colored areas are their corresponding derivative curves. The descending (forward) and ascending (backward) field branches are depicted with different colors. The remanences $M_{\mathrm{R},\parallel}$ and $M_{\mathrm{R},\perp}$ are indicated. The vertical dotted and dashed lines indicate the coercivity $H_{\mathrm{C}}$ and the switching field $H_{\mathrm{S}}$, respectively.

Relevant magnetic parameters, such as remanences and critical fields can be readily obtained as a function of $\alpha_H$ from the hysteresis loops, as indicates in figure 4.2. In both cases, the parameters are obtained after averaging the corresponding values of the forward and backward field branches at zero field and during reversal transitions for the remanences and the critical fields, respectively. In this sense, the two in-plane remanence values reads: $M_{\mathrm{R},\parallel} = \frac{1}{2}(M_{\mathrm{R},\parallel}^{\mathrm{forw}} - M_{\mathrm{R},\parallel}^{\mathrm{forw}})$, $M_{\mathrm{R},\perp} = \frac{1}{2}(M_{\mathrm{R},\perp}^{\mathrm{forw}} - M_{\mathrm{R},\perp}^{\mathrm{forw}})$. Notice that $M_{\mathrm{R},\parallel}$ is always positive, whereas $M_{\mathrm{R},\perp}$ can be either positive (e.g., figure 4.2(a)) or negative (e.g., figure 4.2(b)), so there must be an angle where it vanishes. That angle is used to identify the characteristic magnetization easy-axis and hard-axis directions with great accuracy. In turn, the critical fields reads: $H_{\mathrm{C}} = \frac{1}{2}(H_{\mathrm{C}}^{\mathrm{back}} - H_{\mathrm{C}}^{\mathrm{forw}})$; $H_{\mathrm{S}} = \frac{1}{2}(H_{\mathrm{S}}^{\mathrm{back}} - H_{\mathrm{S}}^{\mathrm{forw}})$. The coercive field $H_{\mathrm{C}}$ refers to the magnetic field required to reduce the magnetization to zero, i.e., $M_{\parallel}(H_{\mathrm{C}}) = 0$, whereas the switching field $H_{\mathrm{S}}$ is the magnetic field where the irreversible transition takes place. In analogy, $H_{\mathrm{S}}$ can be derived from the magnetization curve of the transverse component, i.e., $M_{\perp}(H_{\mathrm{S}}) = 0$, or more accurately from its derivative curve (shadow area in figure 4.2) looking for the field where its maximum is located (indicated with vertical dashed lines in figure 4.2). Notice that there is an angular range around the e.a. where both coercive and switching field coincide (e.g., figure 4.2(a)),

and in particular for $\alpha_H < \pm 70°$). Within (out of) this angular range, coercivity and switching field have the same (different) meaning, as discussed below.

## 4.3 Remanence and magnetic symmetry

The simplest information that can be extracted from the angular evolution, is the anisotropy directions, determined by the magnetic symmetry of the system. This can be done easily by plotting the normalized remanence values of the two in-plane magnetization components as a function of $\alpha_H$ (see figure 4.3). Both magnetization components display a pronounced oscillation with periodicity of 180°. The parallel component follows a $|\cos 2\alpha_H|$ law dependence, the perpendicular component changes the sign when a characteristic e.a. or h.a. direction is crossed, and both components are complementary, i.e., $M_S^2 = (M_{R,\parallel}^2 + M_{R,\perp}^2)$. The polar plots of $M_{R,\parallel}$ and $M_{\perp,R}$ display characteristic *"two-lobes"* shapes rotated 90° (see figure 4.3(b)). This originates from the two-fold magnetic symmetry induced by the field applied during growth. All these features confirm a well-defined uniaxial magnetic anisotropy behavior of the film, where the anisotropy axis was field-induced as already explained.

## 4.4 Irreversible transitions and relevant fields

The more relevant transition fields are the coercivity ($\mu_0 H_C$) and the switching field ($\mu_0 H_S$), which are related to the field required to compensate the magnetization along the field direction and to the effective anisotropy of the system, respectively. Coercivity describes the stability of the remanent state and gives rise to the classification of magnets into hard magnetic materials (permanent magnets), semihard materials (storage media) and soft magnetic materials (core applications). The switching field determines the field needed to control the stable magnetization direction in any magnetic system, crucial in both permanent magnet and spintronic applications. Both can easily be determined from the $M - H$ curves by looking for the applied field values at which $M_{R,\parallel}$ and $M_{R,\perp}$ crosses zero, respectively. Notice that the coercive field does not always indicate the field value at which the irreversible transition takes place, while the switching field does. The sharp irreversible transitions are associated with the nucleation field and results in an abrupt change in the $M - H$ loop, i.e., in a large peak in the corresponding numerical derivative curves (see figure 4.2).

Notice that the irreversible hysteresis jumps found in both components, and their corresponding derivative curves, are not necessarily of the same height. Close to the e.a. direction the $M_\parallel(H)$ loops present significantly larger irreversible jumps, and higher maximum values of the corresponding derivative curves, in comparison with the ones found in the $M_\perp(H)$ loops, whereas approaching the h.a. direction the difference exchanges, as the right graphs of figure 4.2 shows. In this case, the angular evolution of switching field is more precise to determine from the $M_\perp(H)$ loops.

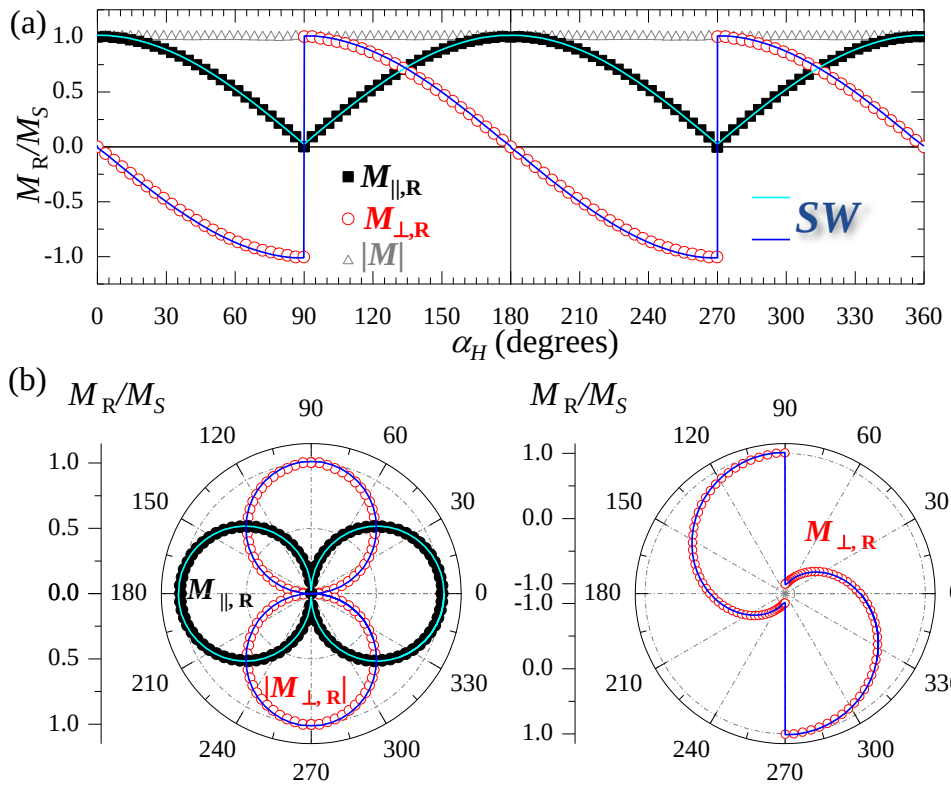


Figure 4.3: (a) Angular dependence of the normalized remanent magnetization components of a well-defined uniaxial magnetic anisotropy system in quasi-static conditions. (b) Corresponding polar plot representations. The values of $M_{R,\parallel}$ (filled square symbols) and $M_{R,\perp}$ (open circle symbols) have been extracted from the in-plane resolved hysteresis loops, as the ones shown in figure 4.1. Solid lines are derived from the SW model.

Figure 4.4 displays the angular dependence of the relevant fields extracted from $M-H$ loops. In general, the two-fold symmetry of the magnetic properties is also found in the experimental data of the angular dependence of both $\mu_0 H_C$ and $\mu_0 H_S$, as revealed by the 180° periodicity presented in both cases (figure 4.4(a)). The coercive field presents a roughly constant value around the e.a. direction, i.e., $\mu_0 H_C(0°) = 4.5$ mT, increasing slightly until $\alpha_H \approx \pm 75°$. The switching field presents an identical angular evolution in this angular range. Above this angle, $\mu_0 H_C$ starts to decrease, vanishing at the h.a. direction, i.e., $\mu_0 H_S(90°) = 0$ mT. In contrast, $\mu_0 H_S$ presents a larger rising evolution as the angle approaches to the h.a. direction. The switching field at the h.a. direction is the effective anisotropy field, i.e., $\mu_0 H_S(90°) = \mu_0 H_K = 17$ mT. Notice that there is a factor of nearly four between the coercive field at the e.a. and the anisotropy field.

In order to understand the angular evolution of the relevant fields, we have compared the experimental results in quasi-static conditions with the expected ones from two, in principle, opposite models, which assumes rotation and single domain switching (SW model [67]) and rotation and nucleation of magnetic domains and subsequent propagation of domain walls pinned at defects (pinning-model [106]). There are two angular ranges where each model reproduces the experimental data. The SW model assumes a single particle behavior, i.e., reversal by switching (irreversible process) and/or rotation (reversible) of the whole magnetization, without taking into account any other irreversible magnetization reversal process like nucleation and propagation of magnetic domains. The latter is, in fact, energetically much more favorable in extended systems, in which defects of any kind—structural or morphological—play the main role to activate irreversible magnetic domain nucleation processes at magnetic fields that are significantly lower than expected by the SW model. In particular, even in epitaxial thin films, low coordination sites such as sample edges and topographic roughness are unavoidable. These defects will act as pinning centers for the created magnetic domain walls, and the reversal subsequently continues via domain wall propagation, as the field pressure allows the wall to unpin (overcoming its local energy barrier), just to reach other (higher energy barrier) pinning centers, and so on until all the reversal is completed. In this case, a simple model of pinned 180° magnetic domain walls (pinning model) predicts a $1/|\cos\alpha_{\mathrm{H}}|$ law for the angular dependence of the reversal field, which has been already observed in both perpendicular [107] and in-plane [88] anisotropy systems.

In a wide angular region around the e.a. direction, i.e., $|\alpha_{\mathrm{H}}| < 70°$, both fields are similar and follow a $1/|\cos\alpha_{\mathrm{H}}|$ law (discontinuous line in figure 4.4(b)), accordingly to the domain pinning model prediction. Thus, nucleation and subsequent propagation of pinned magnetic domains is the relevant process during the irreversible transitions. Close to the h.a. direction, i.e., $|\alpha_{\mathrm{H}}| > 70°$, the pinning model cannot reproduce the experimental data, and the predicted evolution tends to deviate more and more from experimental values. On the other hand, SW model, which does not reproduce well the experimental results below 70° becomes closer and closer as h.a. is reached, reproducing quite satisfactory the results at the exact h.a. For instance, the coercive field (switching field) decreases (increases) to zero (up to the anisotropy field) as approaching the h.a. direction, as predicted by the SW model (solid lines in figure 4.4). This indicates that close to the h.a. direction the magnetization reversal is mainly governed by rotation processes. Note that the SW model only reproduces their angular evolution around the h.a. directions, where reversible processes are the relevant mechanism during reversal (clear area in figure 4.4). It fails around the e.a. directions, where irreversible (nucleation and propagation of magnetic domains) processes dominate, as described above.

## 4.5 Conclusions

In summary, the quasi-static magnetic properties of a well-defined uniaxial magnetic anisotropy system have been disentangled by means of a detailed angular dependence vectorial-resolved magnetization reversal study. In general, both reversible and irreversible transitions take place during reversal, and their relevance depends strongly

on $\alpha_H$. The reversible transitions correspond to magnetization rotation processes whereas the irreversible ones are related to nucleation of magnetic domains aligned with respect to the anisotropy axis and a subsequent domain wall propagation. The data are discussed in the framework of both domain wall pinning and macrospin SW reversal models for different angular ranges. In particular, the pinning and SW models reproduce the experimental data close to the e.a. and h.a., respectively.

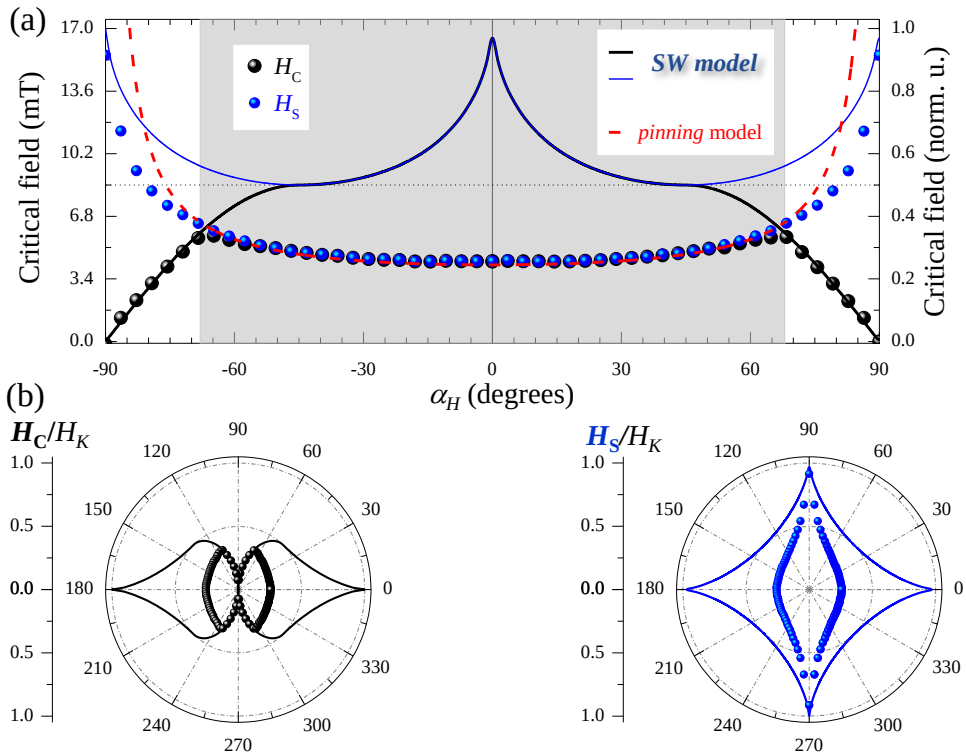


Figure 4.4: (a) Angular dependence of the critical fields for a well-defined uniaxial magnetic anisotropy film in quasi-static conditions. $H_C$ (solid symbols) and $H_S$ (open symbols) are the experimental coercivity and switching field values, respectively (see figure 4.1). Solid and dashed lines are the expected behaviors from the SW model and the pinning model, respectively (see text). (b) Corresponding polar plot representations. Notice that the experimental data are reproduced with the two models in different angular regions where the irreversible (pinning) and reversible (SW) processes are more relevant during magnetization reversal, and the irreversibilities are associated with a more propagative and nucleative regime, respectively.

# 5 Temperature-driven spin reorientation in model systems

The following sections are devoted to three aspects enclosed in the same subject of thermal effects:

1. Spin reorientations at the Verwey transition in $Fe_3O_4$ magnetite thin film grown by PLD on StO is discussed in section 5.1, where the relative orientations of the magnetic anisotropy axes have been found to be rotated with respect to what is stated in the literature for other magnetite systems.
2. In section 5.2, symmetry breaking effects are explored in model system Fe/MgO(001) where the Fe was grown at oblique deposition angle to induce a superimposed (dipolar) magnetic anisotropy to the ordinary four-fold symmetry of Fe. Here we explore the competition of magnetic anisotropy, leading to magnetic symmetry breaking effects driven by temperature, as the effective magnetic anisotropy resulting for the uniaxial-biaxial competition evolves in a different fashion with T.
3. Finally in section 5.3 exchange anisotropy is explored in model FM/AFM system, where a surprising positive field-induced exchange bias effect have been found, not yet reported in the literature.

## 5.1 Spin reorientation in epitaxial $Fe_3O_4$ thin films

**Magnetite is a deeply studied system that undergoes a structural change at the so called Verwey transition. Here we report on temperature driven spin reorientation phenomena of stoichiometric magnetite films grown on SrTiO3:Nb by infrared pulsed-laser deposition. The room temperature easy axes are aligned along $\langle 100 \rangle$ of the cubic magnetite unit cell, in contrast with the room temperature anisotropy axes aligned in $\langle 110 \rangle$ directions for bulky magnetite at the surface. Remarkably, these RT in-plane magnetic anisotropy directions reorients by 45° below the Verwey transition temperature ($T_V$), but remains four-fold. In this section we show the measurements carried out with our Variable Temperature/Full Angular Range v-MOKE TRISTAN device on this system. The results corroborates room temperature anisotropy directions previously reported by CSIC collaborators using other techniques, and (correspondingly) the low temperature rotated axes by 45 degrees with respect to those RT directions.**

### 5.1.1 Introduction

Magnetite ($Fe_3O_4$) is an inverse spinel (cubic) crystal that changes its structure at a temperature around 125 K, the so called Verwey transition, $T_V$ [112, 113], where it transforms from semi-metal to an insulator. Different phenomena can be observed when traversing the transition, such as conductivity reduction [114], anomalies in the heat capacity [112, 115], magnetic relaxation processes [116], magnetocaloric effect [117], magnetoresistance [117], spontaneous magnetization [118], magnetocrystalline anisotropy [119, 120, 121] and magnetostriction [122, 123]. The Verwey transition is influenced by variations in stoichiometry [124, 125, 126] and pressure [127] and can be spread over a certain temperature interval, a phenomenon that can be explained by the way the different sublattices of the magnetite interact with each other. A dramatic broadening of the transition is observed in a temperature range of 100 K around the transition, and it could also be due to impurity of the magnetite [128].

The cubic magnetite crystal structure above the Verwey transition transforms into monoclinic polycrystalline upon traversing $T_V$, with different local monoclinic orientations. This is associated to a ferroelastic transition [129]. It has also been observed that at a temperature some Kelvin above $T_V$, the structural transition presents an isotropic point, i.e., a region where magnetic anisotropy seems to vanish, assume to be due to the intermixing of the two structural phases, the cubic phase above $T_V$, and the monoclinic one below it. It has been discuss a strong reduction of magnetization at that temperature region [130]. Many studies have reported about the existence of a very rich anti-phase boundaries (APB's) landscape that alters the magnetic behavior, among others (see for instance [131].

The Verwey transition was first considered to consist in a complex structural distortion driven by a charge ordering of the $Fe^{2+}$ and $Fe^{3+}$ cations, as proposed by Verwey (1939) [113]. The Verwey hypothesis has been reconsidered as experimental techniques have thrown new data, and there are actually various models and hypothesis trying to account for the different phenomena observed in the transition [128, 132], all of them are based in some charge redistribution at the transition, driving the structural change from cubic at room temperature to monoclinic below Verwey transition. The monoclinic structure would be inscribed inside eight of the rhombohedrally distorted room temperature cubic cells [128, 133], covering four such cells in volume. It has been also proposed the lack of an inversion center at low temperature as responsible for the the monoclinic structure [134, 135].

Concerning the magnetic properties, it has been shown that spontaneous magnetization presents some features near the Verwey transition [136, 118]. As the transition affects the conductivity of the material [114], the reflectivity also presents features at the transition, more specifically a drastic decay. Remarkably, magnetite suffers a spin reorientation transition, affecting the anisotropy axes directions upon traversing $T_V$. Magnetic symmetry in magnetite is four-fold at room temperature, and rotates $45^o$ below $T_V$. Many works on the subject of magnetite anisotropy axes reported a room temperature alignment along $\langle 110 \rangle$ of the inverse spinel cubic cell, rotating to $\langle 100 \rangle$ below $T_V$. However systems consisting on magnetite films grown by PLD (Pulsed-Laser Deposition) on substrates such as $MgO$, $Si(111)$ and $SrTiO_3$ have been explored at room temperature (and also at low temperature, with limited re-

sults by the date) using FMR, SQUID and MOKE by one of the CSIC groups with whom we have collaboration. In particular, people from Instituto Rocasolano have reported anisotropy axes aligned along ⟨100⟩ in magnetite thin films grown by PLD on $SrTiO_3$:Nb [137].

In the framework of our collaboration, an extended broad range temperature study has been carried out during this thesis, in parallel with investigations from CSIC with other techniques. We concentrated in v-MOKE temperature study of the magnetic anisotropy reorientation across the Verwey transition. We have taken advantage of the Variable Temperature Full Angular Range v-MOKE set-up, TRISTAN (described in chapter 2 as well as in reference [138]), to map the magnetic parameters and transition features by looking at both the temperature evolution at fixed directions and the angular evolution at fixed temperatures. Remarkably we obtain coherent results with aforementioned reported works [137], compatible with ⟨100⟩ alignment above $T_V$ and ⟨110⟩ below. We also observed particular phenomena happening around $T_V$, in the so called isotropic region, where remanence and coercive fields present a dip as if either magnetic anisotropy or total magnetization dropped down.

An attempt to clarify the regrouping of the monoclinic low temperature structure, the so called "twining" of the monoclinic cells, was made, to infer if the low temperature anisotropy arises from [100] and [010] directions of the monoclinic cell or from [001] with no definitive conclusions (not described in this thesis).

There have been more advances on the subject by the collaboration up to today, in particular, very recent reported results using spin-polarized low energy electron microscopy (SPLEEM) [139], where interesting cites can also be found in the bibliography section(see for instance [140, 141, 142] and topical review [143]).

### 5.1.2 Sample structure

Magnetite ($Fe_3O_4$) films used in this experiment have been grown by pulsed laser deposition (PLD). High quality stoichiometric magnetite thin films of about 50 nm have been grown by ablation from a self-prepared sintered hematite target using a nanosecond infrared (IR) laser at 1064 nm and a substrate temperature of 750 K. Single crystal substrates of $SrTiO_3$:Nb, $MgAl_2O_4$ and MgO have been used in the preparation of $Fe_3O_4$ epitaxial films. By comparison, polycrystalline $Fe_3O_4$ films were grown on $Al_2O_3$ and Si substrates. The films were characterized using XRD, AFM, Raman and Mössbauer spectroscopies, vectorial magneto-optical Kerr effect microscopy (v-MOKE) and SQUID magnetometry. All films consisted of stoichiometric magnetite and presented a Verwey transition at TV=115-118 K. Room temperature (RT) coercivity values (3545 mT) agree well with values reported in the literature for magnetite films in this thickness range. The well-defined four-fold symmetry in the magnetic easy axis measured with Kerr technique at room temperature is indicative of biaxial magnetic anisotropy, highlighting the high quality of the films grown by IR-PLD. Specifically in this experiment, a sample of $Fe_3O_4$ on $SrTiO_3$:Nb with around 0.1% of Nb doping has been used.

Characterization of this sample and details on growth procedures can be seen in reference [137]. Here we summarize the crystallographic aspects with the help of figure 5.1. The room temperature bulk magnetite has inverse spinel structure, with some deformation of the cubic unit cell, while below $T_V$ temperature the structure

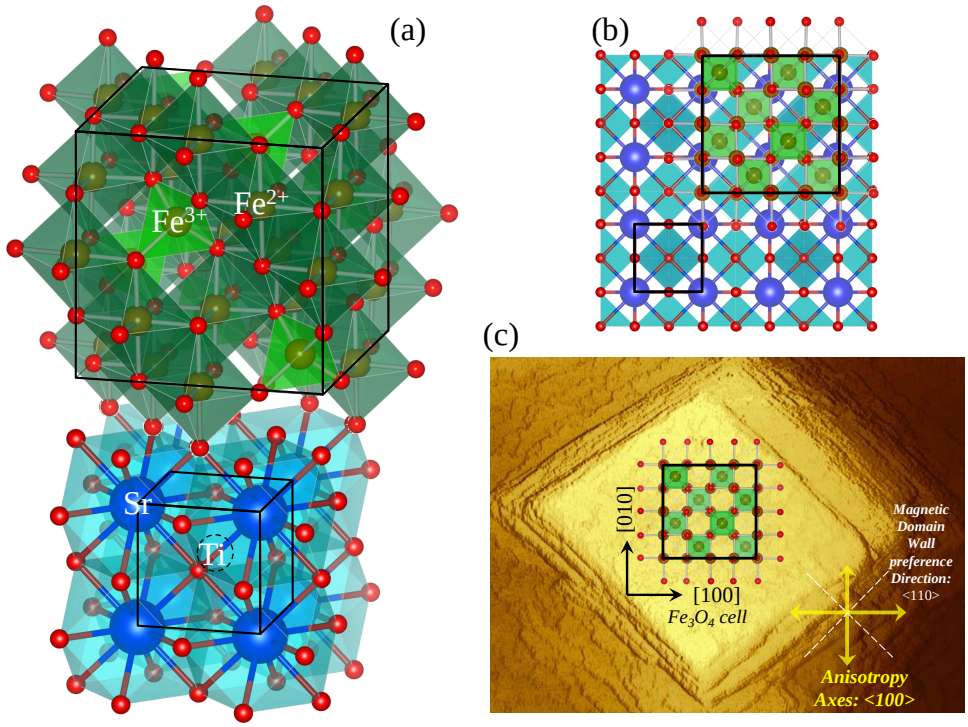


Figure 5.1: Magnetite has an inverse spinel crystal structure, while $SrTiO_3$:Nb is a perovskite with some Ti sites occupied (substitutional) by Nb. (a) Vesta [144] schemes of the crystal structures, showing the unit cells. Top cell corresponds to $Fe_3O_4$ inverse spinel, where $Fe^{3+}$ and $Fe^{2+}$ are located in the center inside oxygen tetrahedrons (light green) and octahedrons (dark green) respectively. At the bottom, the unit cell of $SrTiO_3$ (Nb is omitted) is depicted, where Strontium atoms are located in the center of oxygen cuboctahedron, and they form the vertex of the unit cell, inside of which the Ti are located (dashed circle). In this scheme, cube-on-cube connection between magnetite and $SrTiO_3$:Nb happens through the oxygens. Unit cells have been remarked in black. (b) top view of both crystal structures ($SrTiO_3$:Nb has been extended over various unit cells). Unit cells are depicted as black squares. (c) Topography details of mesas whose edges run along $\langle 110 \rangle$ directions. Top view of the room temperature magnetite unit cell is set for clarity. RT anisotropy directions are depicted with yellow arrows in the bottom right part of the picture, together with the directions that magnetic domain walls follow during the reversal. Topography corresponds to AFM image already published by our group in reference [137].

transforms into a monoclinic, double in height and four times in volume. Lattice parameter of the RT cubic unit cell is around 8.4 $\mathring{A}$, while the low temperature monoclinic structure would be prisms with around 12 $\mathring{A}$ x 12 $\mathring{A}$ of base, and 17 $\mathring{A}$ in height. For the thin films of magnetite on $SrTiO_3$, the $Fe_3O_4$ deposits following a cube-on-cube rule as seen in figure 5.1. The cube-on-cube setting of magnetite onto $SrTiO_3$ structure is shown in (a), where questions concerning APB's have been omitted (APB's will not be taken into account in this work). The magnetite crystal sits on the $SrTiO_3$ (001) face with its unit cell aligned in parallel with that of the $SrTiO_3$. So that in the following, whenever we talk about [100] direction of magnetite at RT, we are referring to the [100] direction of the substrate as well. For simplicity, all directions are taken with respect to the substrate, for the following reason: the monoclinic unit cell of of magnetite below $T_V$ is a prism whose in-plane sides are rotated by $45^o$ with respect to the cubic cell sides of magnetite above $T_V$. So the RT $\langle 100 \rangle$ directions for the cubic unit cell, corresponds to the $\langle 110 \rangle$ ones of the LT monoclinic unit cell, see for instance figure 5.2. In consequence it is very easy to mix up with the true directions. On the other hand the $SrTiO_3$ $\langle 100 \rangle$ directions remains the same no matter if we are below or above the Verwey transition. Notice that $SrTiO_3$ $\langle 100 \rangle$ coincides with the RT magnetite's $\langle 100 \rangle$ direction, and with the LT magnetite's $\langle 110 \rangle$ one. In (b) of figure 5.1, top view of RT magnetite on $SrTiO_3$ is depicted to show the aforementioned cube-on-cube alignment, and in (c) an AFM topography image showing the so called "mesas" is depicted together with the RT magnetite top view of the unit cell and the relevant crystallographic directions.

### 5.1.3 Room temperature magnetic characterization

The magnetization bulk easy-axis directions of magnetite at RT are the cubic diagonals $\langle 111 \rangle$, so that in a (100) thin film surface the in-plane magnetization is expected to be the projection of bulk $\langle 111 \rangle$ on that surface, i.e. the in-plane diagonals $\langle 110 \rangle$. Although in most cases $\langle 110 \rangle$ in-plane magnetization has been reported for magnetite thin films, it has been shown that $Fe_3O_4$ thin films grown on $SrTiO_3$ by infrared PLD present in-plane magnetization in the $\langle 100 \rangle$ direction of the $Fe_3O_4$ surface unit cell [137]. In figure 5.1, picture (c), the magnetic anisotropy axes are in yellow bottom-right, parallel to $\langle 100 \rangle$ directions, and the diagonal yellow dashed lines represent the domain walls preference directions, aligned with $\langle 110 \rangle$ directions. This domain walls directions are in agreement with the fact that domain walls tends to propagated by successively pinning at defects, irregularities or morphological/topological structures. In this cases, the edges of the mesas, and the terrace steps are in the $\langle 110 \rangle$ orientations.

In figure 5.2, the RT cell cube is depicted with the directions of the anisotropy for PLD magnetite films on $SrTiO_3$:Nb. Very recent studies on magnetite grown by PLD on MgO and Si(111) in the same framework also have demonstrated to present the same anisotropy directions at room temperature [145].

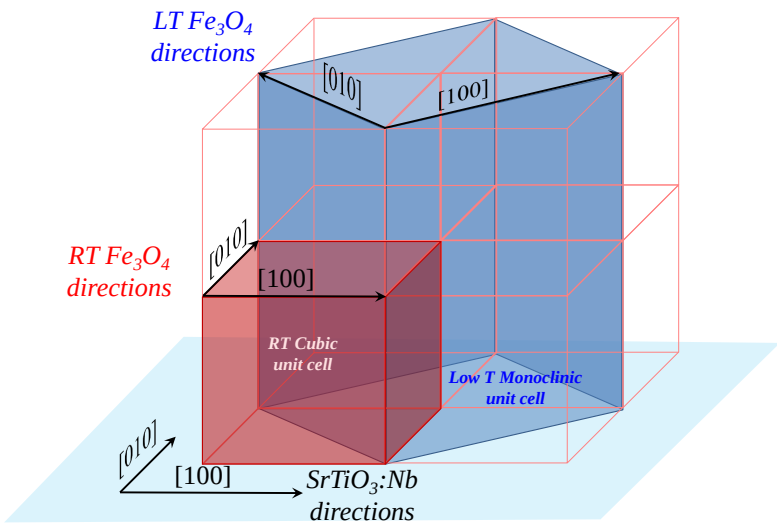


Figure 5.2: RT cubic unit cell of magnetite (red) is depicted at one side of the monoclinic low temperature structure, after traversing the Verwey transition temperature. There is some tilt in the monoclinic cell of about 3° (not represented for simplicity). Relevant crystallographic directions have been depicted. Despite the position that the monoclinic cubic cell has in this figure, no assumption is made here about whether this is the true relative position (i.e. vertically oriented) or there are other possible structures (in-plane monoclinic twins).

### 5.1.4 Temperature dependence angular evolutions

Two kinds of in-plane hysteresis loops measurements were carried out using TRISTAN v-MOKE device [138]: temperature upward and downward ramps with the external field fixed at directions [100] and [110], and full angular range measurements every 5° at different fixed temperatures. We worked in the temperature range between 80 K and 300 K, covering the transition region.

In 5.3 hysteresis loops at [100] and [110] direction, at different temperatures, are plotted. The black loops are measured at the [100] room temperature direction and the red ones at the [110]. Below the Verwey transition the highest coercivity is found at [110] direction, while above it, the highest is located at [100] direction, and remains here all the way up to room temperature (not shown in the figure). Note that close to the Verwey transition temperature, both coercivities are almost equal. As the isotropic regime is between 150 K and the Verwey transition temperature (117 K), these data confirms that no spin reorientation is happening through the isotropic region as we lower temperature, but rather the reorientation occurs closer to $T_V$.

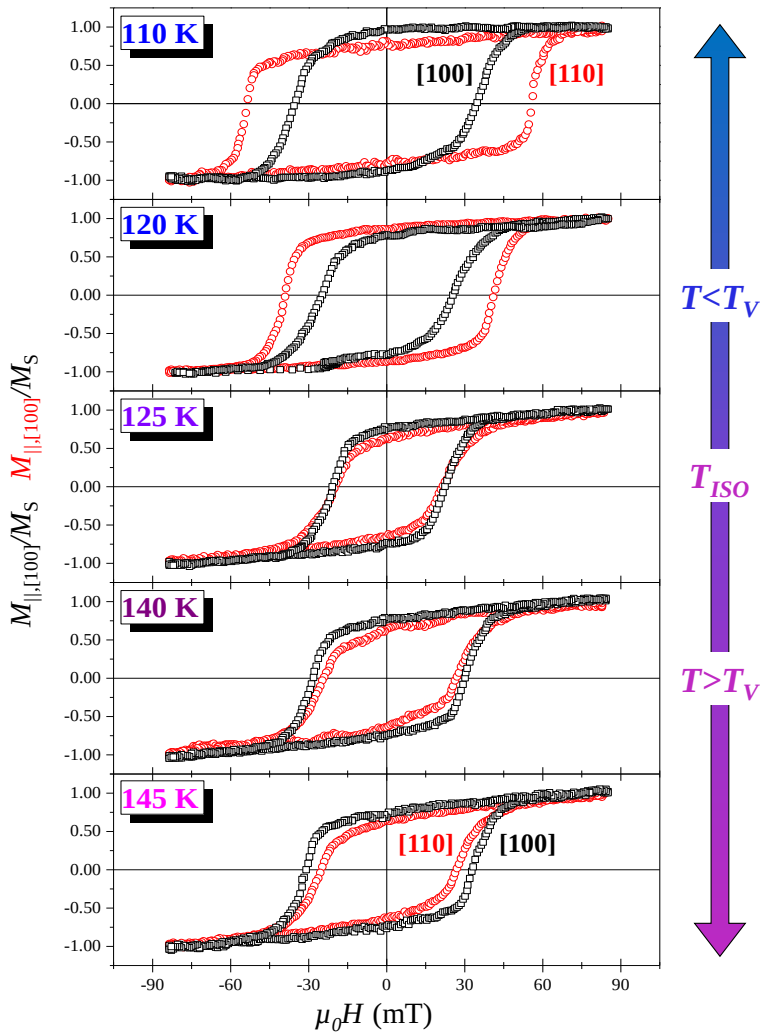


Figure 5.3: Temperature evolution around Verwey transition of (normalized) magnetization parallel component at relevant directions ([100] in black and [110] in red). Upon traversing Verwey transition temperature (117 K as tabulated for bulk), a general change in the trend of the curves happens, and the curves are complementary: higher $H_C$ below $T_V$ for [110] with respect to [100], reversing to lower $H_C$ at [110] with respect to [100] above $T_V$. This change in the trend denotes a reorientation of the magnetic anisotropy axis, as can be seen in 5.4.

300 K and 110 K angular plots are exhibited in figure 5.4. Reference directions [100] and [110] are marked in the figures. Graphs (a) and (c) show linear plots of coercive field for both temperatures, where the 45° shift between them can be seen, whereas graphs (b) and (d) show the corresponding full angular polar plots for both

temperatures. At room temperature, maximums of coercivity are found at 0°, 90°, 180° and 270° of the [100] directions, while the lowest coercivity is found at 45° from those angles. This is indicative of four-fold symmetry with axes along [100] direction. On the other hand, at 110 K the maximums are 45° rotated, indicative of a magnetic anisotropy reorientation to align on the ⟨110⟩ directions. The easy axes directions of the magnetite thus obtained confirm the already reported results [137], where anisotropy axes where measured using different techniques. In contrast, v-MOKE is more precise at confirming low temperature axes directions than other techniques previously used by our group. Our full angular range measurements explore all the directions from 0° to 360° allowing as to accurately determine the aforementioned axes directions.

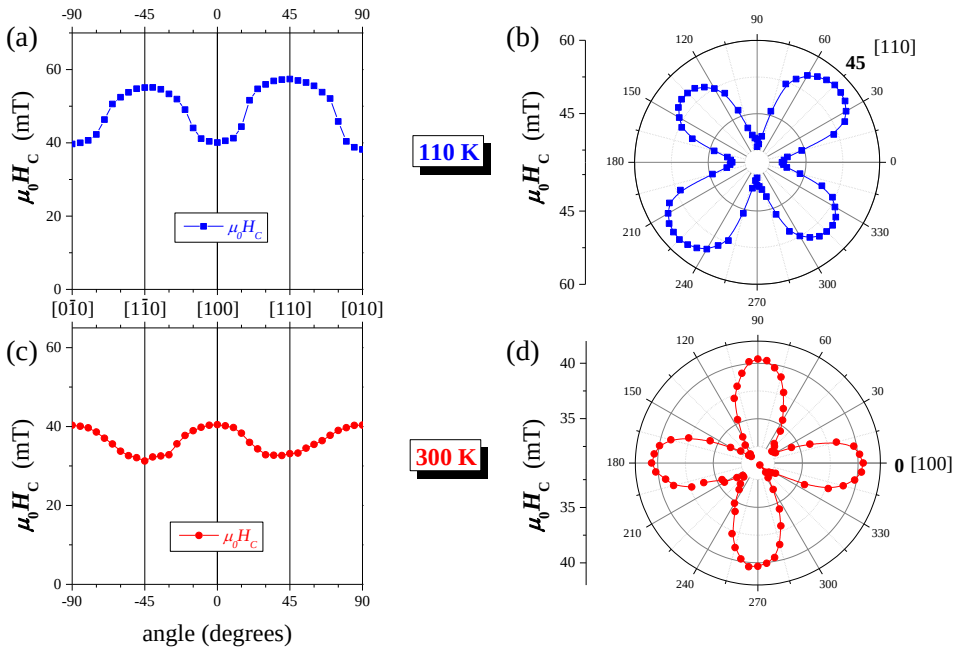


Figure 5.4: Linear graphs (a and c) and polar graphs (b and d) for low temperature (a and b) and room temperature (c and d). Characteristic axes at 110 K are aligned with [110] direction while at 300 K they are aligned with [100] directions. Low temperature axes are rotated by 45° with respect to those at room temperature.

In figure 5.5 the Temperature ramps at both [110] and [100] directions can be seen. The complementary behavior below and above $T_V$ is clearly seen, as well as the crossover at around 125 K, where the coercive field that was maximum at the [100] direction and minimum at [110] above that temperature, interchange their roles, being minimum for [100] and maximum for [110] once below $T_V$. In addition, the

evolution of $H_C$ with temperature deviates from the expected behavior for thermal activated processes. As temperature goes down to the isotropic regime, its value decreases instead of increasing.

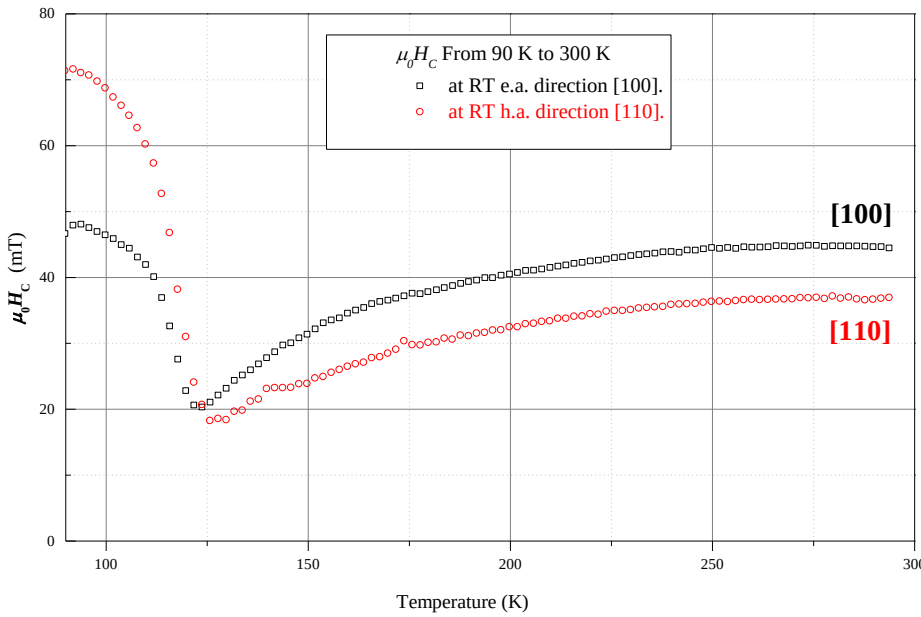


Figure 5.5: Temperature ramps from 80 K to 300 K taken at the [110] (red curve) and [100] (black curve) directions. Above the Verwey transition [100] direction exhibits higher coercive fields, than [110], and vice-versa below the Verwey transition. This is a manifestation of the symmetry axis reorientation, that can be easily seen in 5.4. The crossover of both branches happens at around the temperature of the Verwey transition. However the minimum position of the observed dips in the curves occurs at different temperature for each direction, [110] and [100].

Thermally activated behavior should be patent from the very beginning of the downward temperature ramp, manifesting through an increasing evolution of coercive fields. The observed behavior is the opposite one down to $T_N$, indicative that there must be a mechanism that drastically alters this natural thermal activated behavior, forcing coercivity to drop instead of increase. This mechanism must be linked to the structural change at $T_N$ and/or possibly to a reduction of magnetization (as proposed in [130]) and today there are still open questions. After traversing the Verwey temperature, the magnetic anisotropy axes turn out to be reoriented by 45° and the temperature evolution, down to the lowest temperature explored, is now increasing as the temperature decreases. The evolution with temperature in this region is

closer to the expected behavior for thermal activated reversal processes, thought $H_C$ tends to saturate too rapidly as the temperature goes down. Thermally activated effects are then mixed up with other structural aspects in magnetite. Besides, the position of the dips in $H_C(T)$ in each direction do not coincide in temperature. The dip at the Verwey transition temperature is happening first in the [110] direction at around 125 K, while in the [100] direction occurs more close to the tabulated Verwey temperature, 117 K. This is an indication of a complex transition where each of the two anisotropy axes might be evolving independently.

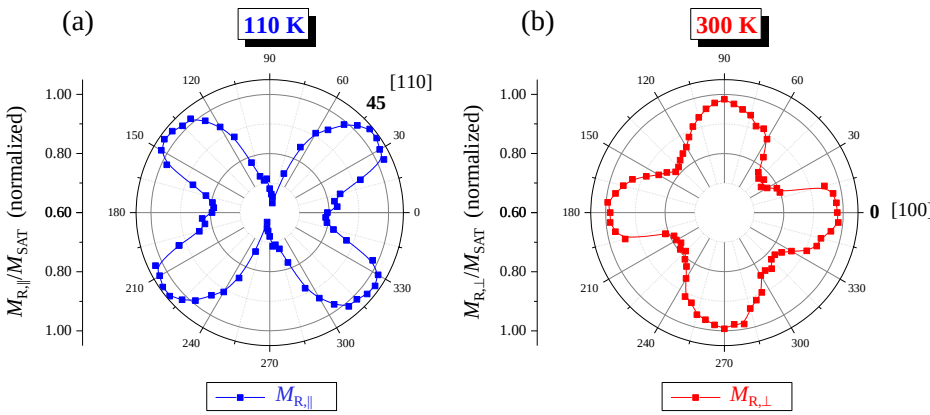


Figure 5.6: Remanence follows the same angular evolution as coercive field, and their maximums coincide in angle with respect to the corresponding coercive field angular evolution. However, some asymmetries can be observed in the remanence, that remains an open question.

In figure 5.6, remanence evolution with angle is shown for room temperature and 100 K. Remanence presents the four-fold behavior of $H_C$, following the same symmetry: it is maximum at $\langle 100 \rangle$ directions for RT, and at $\langle 110 \rangle$ for low T. Petals are not fully axis-symmetric, an indication that the system is not perfectly biaxial as far as remanence is concerned, although $H_C$ are perfectly four-fold. This question is still under discussion. However, measurement of remanence is more sensible to experimental errors such as noise in the instruments and other effects, in contrast with the case of $H_C$.

### 5.1.5 Conclusions

Magnetite on $SrTiO_3$:Nb has been explored at temperatures from 80 K up to room temperature by using vectorial v-MOKE magnetometry. Both temperature ramps at characteristic axes and angular evolutions at significant temperatures has been carried out. They confirm the $\langle 100 \rangle$ alignment of anisotropy axes at room temperature, and the reorientation of 45° after traversing the Verwey transition. Remarkably, the anisotropy axes do not reorient in the isotropic region as temperature is decreased, but rather they reorient after passing that region although this question cannot be fully

asserted with the present v-MOKE data, and needs more experiments. Besides, the coercive fields evolutions present dips in the isotropic regions, reaching its minimum very close to the crossover of the anisotropy directions, near the Verwey transition. The behavior is not easy to understand by thermal activation mechanism and another mechanism clearly takes part on the evolution, associated with the structural changes that magnetite suffers as it evolves from the cubic to monoclinic structure.

## 5.2 Symmetry breaking effects in biaxial-uniaxial competing anisotropy systems

**In this chapter we explore Fe/MgO(001) model system with competing biaxial and collinear growth-induced uniaxial magnetic anisotropies. Different temperature evolution of each anisotropy contribution is the key to disentangle them via Temperature Dependant/Full Angular Range Vectorial MOKE measurements, using our new instrument TRISTAN. Temperature-driven symmetry breaking effects have been found, together with other thermal/non thermal effects on the relevant magnetic properties.**

### 5.2.1 Introduction

Effective magnetic anisotropy in magnetic systems can be the result of various (independent/competing) anisotropy contributions arising from different physical aspects. This is more common in low dimensionality systems than in the bulk, as surface effects become important. The different origin of each anisotropy contribution may lead to different temperature evolution on each one, as is the case for biaxial Fe/MgO(001) with induced uniaxial anisotropy, where the biaxial anisotropy has its origins in the natural magnetocrystalline anisotropy of the iron, and the superimposed uniaxial anisotropy arises from dipolar effects at the surface, induced by oblique angle deposition. This oblique angular deposition leads to "self-shadowing" effects causing surface structure which, in turns, establishes preferential directions due to dipolar interaction. While magnetocrystalline anisotropy is expected to increase upon lowering temperature, as for thermal activated processes, dipolar effects is expected to present constant behavior.

Single temperature measurement is not enough to fully understand magnetic anisotropies of this (and other similar) system, since both anisotropy contributions are mixed up. If we want to distinguish between each independent contribution, temperature dependent measurements are required: evolution in temperature will in general exhibit symmetry breaking effects, indicative of the presence of various competing magnetic anisotropies with different temperature dependence. From this symmetry braking effects, and the temperature evolution in general, we can deduce the real underlying magnetic anisotropy contributions.

For the Fe/MgO(001) model system explored here, the uniaxial contribution has been tuned to be parallel with one of the natural four-fold magnetic anisotropy axes of the Fe, and the experimental method applied is a general procedure for the investigation of thermal effects that will be applied throughout this thesis.

We take advantage of the capabilities of TRISTAN for the investigation, demonstrating the necessity of temperature dependent measurements, as well as the versatility and efficiency of our new set-up.

In the following sections we proceed first by explaining in brief Fe/MgO(001) collinear biaxial-uniaxial model system. Then we go through the experimental investigations using TRISTAN. Sample preparation is explained. Then, detailed discussions of thermal effects on magnetic symmetries are given. We show relevant experimental

data in order to illustrate the capabilities of the set-up, and the relevance of temperature dependent measurements. In particular, exploiting

- vectorial capability: to determine characteristic axes and reversal processes;
- temperature capability: to identify magnetic transitions with temperature;
- combined angular with temperature capabilities: to show how magnetic symmetry evolves with $T$.

We confirm qualitatively the presence of the two competing magnetic anisotropies. For the qualitative description, a combination of Stoner-Wohlfarth (SW) and Cowburn (CW) theoretical models is used to quantify each magnetic anisotropy contributions.

### 5.2.2 Fe/MgO(001) model system

#### 5.2.2.1 Generalities

The study of magnetic properties in iron surfaces begun after some problems on samples preparation were successfully solved. Fe surface structure dates back to the sixties of precedent century, and had to face the problem of obtaining clean and oxide-free surfaces. First studies on (001), (011) and (111) polished faces of bulk Fe using Low Energy Electron Diffraction (LEED) technique were reported by Pignocco and Pellissier, as well as by Molier and Portele [146, 147, 148]. A step forward was given by using epitaxial growth. First Fe (001) and (011) faces epitaxially grown are reported in private communications by Molier and Meischner [149]. Fe(001) grown on MgO(001) is reported by Kanaji, Asano and Nagata [150], followed by other works [151] (see also refs. 4 to 8 in article by Kanaji, Asano and Nagata). Going into the subject of magnetism, Liu, Park and Bader were the first to study magnetic properties of such structures [152, 153]. Magnetic anisotropies of metallic thin films have been widely studied ever since, a reference review can be seen in [154] among others.

The magnetic anisotropy directions of bulk bcc Fe are aligned with the cube edges: easy axes follow <100> family of directions, while hard axes follow the cube diagonals [155]. In figure 5.7, a diagram with the directions along the Fe cube is depicted, together with the magnetization as a function of the external field for each direction.

Thin films of bcc Fe cubic system preserve its bulk structure when grown on MgO(100) with at most some 4% of distortion due to lattice mismatch. The epitaxial relations are Fe(001)‖MgO(001) and Fe[100]‖MgO[110] [150]. The unit cell of bcc Fe is 45° rotated with respect to MgO unit cell. If we consider the Mg positions as forming a prism with a Mg in the center, the iron bcc cube lies in the same orientation as that prism. In figure 5.8 a diagram of the structure is depicted, with the lattice parameters. In (a) we see a perspective view of both Fe and MgO crystals, as they are aligned when bcc Fe is epitaxially grown on MgO(001) surface. As can be seen, Fe(001) face orients parallel to MgO(001) with Fe aligned with Mg atoms. In (b) surface cells of Fe and MgO are depicted superimposed to each other, so that relative orientations can be clearly seen. In (c) the epitaxial relation Fe(001)‖MgO(001) and Fe[100]‖MgO[110] can be seen. It is important in what follows to note that [100] direction is different depending on whether we refer to Fe or to the substrate MgO unit cell. If [100] refers to the substrate, the corresponding direction in the Fe unit

cell is [110]. Whenever a direction is mentioned in the text or figures, this aspect will be clear on the text or on inset diagrams in figures. As distance between in-plane (001) Mg atoms is 2.98$\mathring{A}$ and bcc Fe has lattice parameter of 2.87$\mathring{A}$, there is a little mismatch between Fe cell and the Mg cell it lies on.

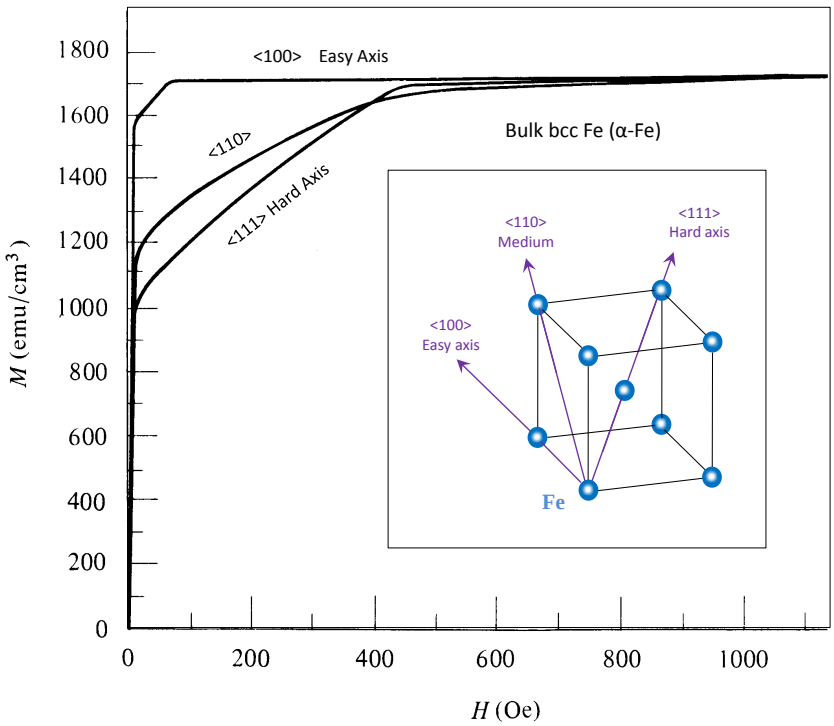


Figure 5.7: Crystallographic magnetic anisotropy directions of bulk $\alpha$-Fe phase (bcc). Magnetization is given as a function of the external field, for the basic three crystallographic directions of the bcc cube (depicted in the inset). Easy axes are aligned with <100>cube family of directions. figure source: S. Blugel, 1999 [156], after K. Honda S. Kaya, Sci. Reports Tohoku Univ. 1926 [155].

Recent DFT studies for Fe/MgO(001) with a few Fe monolayers have established a direct relation between this mismatch and the magnetic moments [154, 157]. For the case under study in this thesis, this local aspect at the interface will be of no relevance, since we are going to deal with order of 20 nm of Fe layer. It has been shown that during epitaxial growth of Fe on MgO, below 500$\mathring{A}$ the Fe forms islands (fuzzy LEED patterns, see [150]), and the surface coalescence happens at around 500$\mathring{A}$. This means that an Fe film of 20 nm thickness is below the coalescense region, and a considerable island-like roughness is expected.

### 5.2.2.2 Magnetic Anisotropy of Fe/MgO(001)

In the thin film, the bcc Fe bulk magnetocrystalline anisotropy directions are forced to lie down onto the surface plane, with the exception of thin films with very few Fe layers [154], where the anisotropy goes out of plane. For instance, if the thin film surface corresponds to (001) bcc Fe face, the [001] anisotropy direction (edge perpendicular to film face) will be absent. This is a general behavior in many systems when going from bulk to thin film.

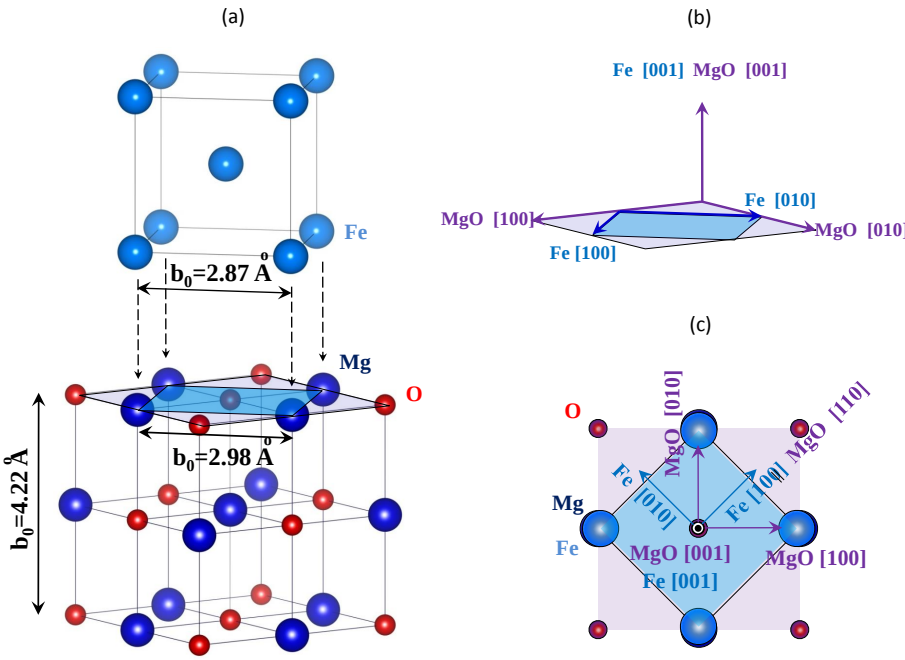


Figure 5.8: Summary of structural information of Fe/MgO(001). (a) Perspective view, showing the lattice distances for each Fe and MgO monocrystals, as well as the relative position of the Fe crystals with respect to MgO structure. The MgO monocrystal rock salt has the NaCl (fcc) structure, while $\alpha$-Fe has bcc structure. (b) relative orientations of the surface cells with the basic directions involved, light blue color refers to Fe, and violet to MgO. (c) Top view showing those directions, remarking the epitaxial relation fe[100]||MgO[110].

The cancellation of out of plane anisotropy depends on many factors, some of them are intrinsic, such as changes in orbital configuration affecting to the bondings of interfae/surface atoms, and other factors are related to shape and morphology, including film thickness, number of layers of different chemical species present, shape, surface reconstruction and vicinal structure, among others. In the bcc Fe film grown on

MgO(001), in-plane magnetic anisotropy is a consequence of the interaction between the magnetization and the stray field that it creates (outside and around the sample), so that a considerable reduction of energy occurs when the magnetization vector remains parallel to the surface plane. This magnetostatic phenomenon is specially relevant in low dimensionality systems, where the ratio between relevant dimensions and the shape of the sample plays a very important [154, 27] [158]. As the only anisotropy directions corresponds to (in-plane) [100] and [010] directions of the grown bcc Fe, the system has a four-fold magnetic symmetry, with easy axes along those in-plane directions, and hard axes at 45° of them, i.e. on [110] and [-110] directions.

#### 5.2.2.3 Induced Unidirectional Anisotropy

There are many ways to induce uniaxial magnetic anisotropies in thin films. For instance, using stepped surfaces or growing films at oblique incidence angle or under external magnetic field, can induce in-plane uniaxial anisotropies. In addition to the four-fold (biaxial) magnetic anisotropy of Fe(001)/MgO(001), Park, Fullerton and Bader induced an in-plane two-fold (uniaxial) magnetic anisotropy by growing the Fe at oblique angle with respect to [001] MgO direction (cut face perpendicular axis). This oblique deposition promotes an uniaxial magnetic anisotropy with the anisotropy axis oriented perpendicular to the deposition direction [159]. By tuning azimuthal angle of the MgO(001) with respect to the deposition direction, the uniaxial axis can be set to be either parallel to one of the biaxial axes, or to be at any other angle such as 45°. The Fe film thus created presents its natural biaxial anisotropy together with an uniaxial one, giving rise to an effective magnetic anisotropy that will be a combination of both. The relation between the corresponding anisotropy constants will determine the symmetry of this effective anisotropy. In general, the competition between four-fold and two-fold anisotropy contributions depends on intrinsic parameters, such as angle of deposition [159, 160], substrate step density [161, 162, 163], and ferromagnetic thicknesses [161, 163] and/or extrinsic ones, such as temperature. It is known that Fe grown on MgO(001) does not coalesce until at least 10 nm thickness. Although in the studies presented here we have explored Fe(001)/MgO(001) with 10 nm Fe, we present the case of 20 nm, since at lower thickness we could be dealing with out of plane anisotropies of the iron.

As for the practical utilities of this induced unidirectional anisotropy in Fe, we find it useful in recording media. Although Fe is a high remanence material, it has the drawback of a low coercive field, i.e., it is a soft material. This makes it useless for applications where the system should be resistant against external fields, since they could accidentally reverse the magnetization, altering the information stored. Magnetic storage devices require remanence high enough as to make bits of information easy to read and distinguish (two magnetization states are used to represent 0 and 1 bits), and at the same time they require high coercive field to retain the bit information securely in the long-term. The presence of uniaxial anisotropy in Fe enhances the coercive field, converting the magnetically soft Fe into a hard material while preserving its high remanence. As the uniaxial anisotropy can be induced under controlled conditions, it is possible to tune the relation between $H_C$ and $M_R$ in order to get the best compromise between both parameters.

### 5.2.3 Experimental

Vectorial-resolved measurements have been performed with TRISTAN set-up on the model system Fe/MgO(001) with 20nm of Fe grown at oblique angle, as a function of the temperature $T$ and the in-plane angular rotation $\alpha_H$ of the sample with respect to (fixed in direction) external field. Incoming $p$-polarized light has been used in the v-MOKE set-up of TRISTAN, i.e., fixed MOKE geometry. The direction $\alpha_H = 0°$ refers to the external field aligned with the in-plane [100] crystal direction of the Fe(001). The hysteresis loop of the in-plane magnetization components, parallel $M_{\parallel}$ and perpendicular $M_{\perp}$ to the field direction, are determined simultaneously for a given $\alpha_H$ and $T$. Full 360° was probed every 2.5°, with 0.5° angular resolution, at different temperatures ranging from 15 K to 400 K.

In the following, a brief description of sample preparation is given first, and then representative vectorial-resolved loops acquired at different angles $\alpha_H$ and temperatures $T$ are shown, followed by discussion of the results.

#### 5.2.3.1 Sample preparation

The sample used consists of 20 nm thickness Fe film grown at oblique incidence on a MgO(100) single crystal substrate in ultra-high-vacuum conditions.The substrate was first cleaned by repeated cycles of sputtering with 0.5 kV $Ar^+$ ions and annealing up to 800 K. The Fe film grows epitaxially on MgO(100) according to aforementioned Fe(001)‖MgO(001), Fe[100]‖MgO[110] epitaxial relation [150]. Fe deposition was performed at 400 K with a home-made electron-beam evaporator at a rate of about 0.4 nm/min. The angle of deposition was 30° with respect to the surface normal with azimuth along the Fe[100] direction, in order to induce unidirectional anisotropy in the Fe as already mentioned. The film was then capped at room temperature with a 3 nm thick Cu film, to prevent oxidation.

In figure 5.9 (a) the deposition of iron on MgO is depicted. The azimuthal angle is such that Fe(100) direction is aligned with MgO(110) direction. The angle of deposition with respect to the surface normal MgO cut face is 30°, tilted in the MgO(-1-10) direction (not shown) in the figure. In part (b), the natural four-fold in-plane magnetic anisotropy axes of the iron are shown, which are aligned along (100) and (010) directions of the iron (top). In the bottom part of (b) the two-fold induced magnetic anisotropy arising from the oblique incidence deposition of the Fe is shown, which is aligned to the (100) direction, and then is collinear to one of the four-fold anisotropy axes.

The sample was provided with reference mark to set the [100] Fe direction. MgO [100] direction is the natural sample edge. In figure 5.10, (a) the sample is seen as mounted, at 0° of TRISTAN's rotatable sample holder. During the sections to come, all the angles will be referenced to the red line in the image, so this will be our real 0° reference, corresponding to Fe[100] direction. Sample rotates anticlockwise, while external magnetic field remains fixed in the direction indicated by the green arrow. This means in practice that the angles expressed in the graphs corresponds to clockwise positions of the external magnetic field with respect to Fe[100] direction. In (c) of this figure, a schematic diagram is depicted to show this angle references.

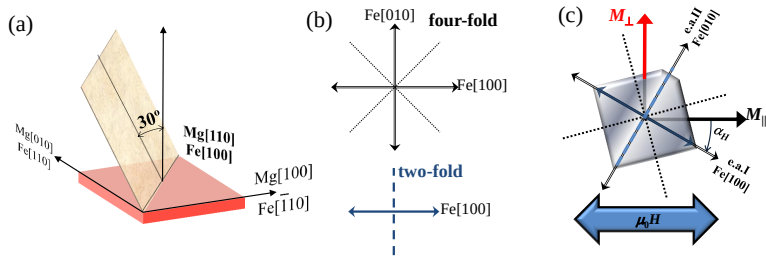


Figure 5.9: Schematic representation of the Fe film growth geometry (a) employed to promote a collinear anisotropy configuration (b). The easy axes of the growth-induced uniaxial anisotropy coincides with one of the easy axis of the biaxial one, referred as e.a.I. The other easy axis of the biaxial anisotropy coincides with the hard axis direction of the uniaxial one, referred as e.a.II. (b) Scheme of the v-MOKE geometry. $\alpha_H = 0°$ was referred when the Fe[100] direction was aligned parallel to the field direction.

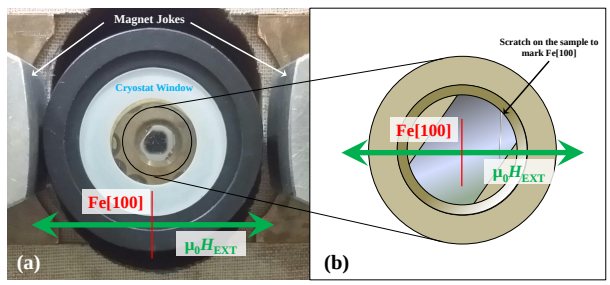


Figure 5.10: (a) Picture of the 20nm Fe/MgO(001) sample as it is mounted on the sample holder, at 0° of the rotating axis. A red line is superimposed to mark the 0° reference that will be used in figures, corresponding to Fe[100] direction. External filed direction (fixed) corresponds to the horizontal double green arrow, and is fixed as the sample rotates anticlockwise. The magnet jokes can be seen at both sides of this picture. A schematic diagram is depictied in (b), expressing the same ideas.

#### 5.2.3.2 Angular study at room temperature

At room temperature, when looking at remanence evolution with angle, the system presents biaxial magnetic anisotropy, as can be seen in figure 5.11. Examination of transition fields will show that this is not an exact picture of the real symmetry and the explanation will be given, remarking the importance of looking to different magnetic parameters. In general, the hysteresis loops of both magnetization components show sharp irreversible transitions and smoother fully reversible transitions, as can be seen in figures 5.12,5.13 and 5.14. Depending on $\alpha_H$ and $T$, either one or more than one irreversible transitions are found. The simple inspection of the vectorial-resolved

hysteresis loops provides direct information about the characteristic anisotropy axis, i.e., easy axis and hard axis directions, critical fields, domain wall angles and magnetization reversal processes, as will be seen in the following sections.

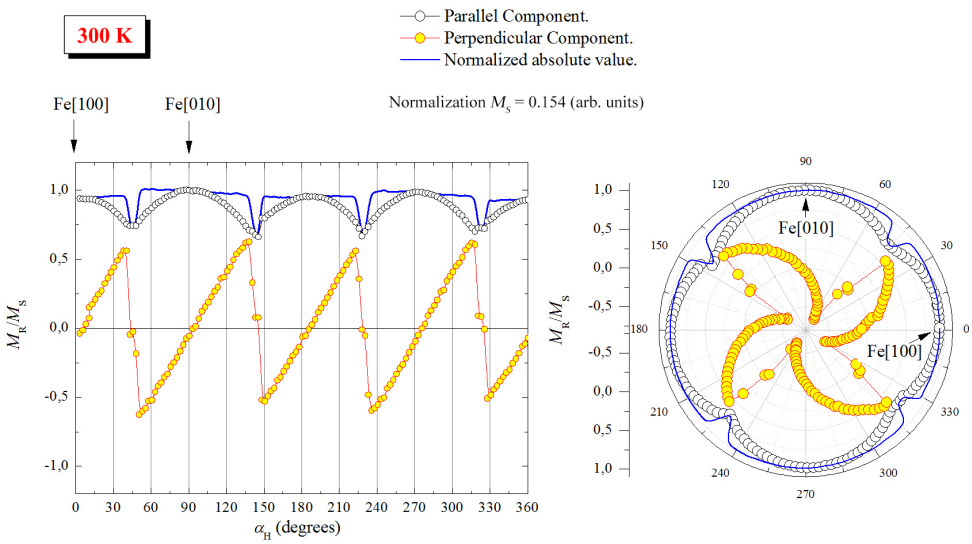


Figure 5.11: Angular evolution of parallel and perpendicular remanence components at 300 K. (a) linear plot, (b) polar plot. Apparent four-fold symmetry is patent.

#### 5.2.3.3 Characteristic axes

In experimental studies using standard magnetometry techniques, with only $M_{\parallel}$ sensitivity, the magnetic anisotropy axes of a given system are usually deduced by looking for the maximum squareness of the hysteresis loop acquired at different angles. Two measures of squareness are in common use: the remanence of magnetization $M_R$ and the coercive field $H_C$. However, this method is not reliable since in many systems both $H_C$ and/or $M_R$ behave with a cosine like function, i.e., less than 4% variation in a $\pm 10^{\circ}$ range, around the anisotropy axes.

In contrast, vectorial-resolved hysteresis curves provide an accurate method to determine the anisotropy axes of a given system, as has been pointed out in precedent studies [82, 83, 84, 85, 86, 87, 88]. In order to illustrate the method, figure 5.12 shows representative $M_{\parallel}(H)$ and $M_{\perp}(H)$ loops around the characteristic easy axis and hard axis directions of a well-defined biaxial magnetic anisotropy system. The four-fold magnetic symmetry originates from the cubic crystal symmetry of a Fe(100) film. The simple inspection of the vectorial-resolved hysteresis loops acquired at different angles allows to precisely locate the characteristic directions, by looking for the change of sign of the $M_{\perp}(H)$ loops when a characteristic direction is crossed, as revealed in the evolution of the corresponding graphs. This is due to the sensitivity of $M_{\perp}$ to the anisotropy direction. Comprehensive diagrams of this change of sign of $M_{\perp}$ upon

traversing characteristic axes can be found in appendix B, sections B.3 and B.4.1..

The hysteresis around the easy and hard directions show one and two irreversible transitions, respectively. Larger perpendicular signals are found around a hard axis direction. Moreover, the $M_\perp(H)$ loop vanishes progressively when approaching an easy axis direction from negative angles, changing its sign for positive ones, whereas it suddenly changes around a hard axis direction. This dissimilar zero-crossing evolution can be therefore exploited in order to distinguish between easy or hard magnetization directions and to evaluate different anisotropy contributions.

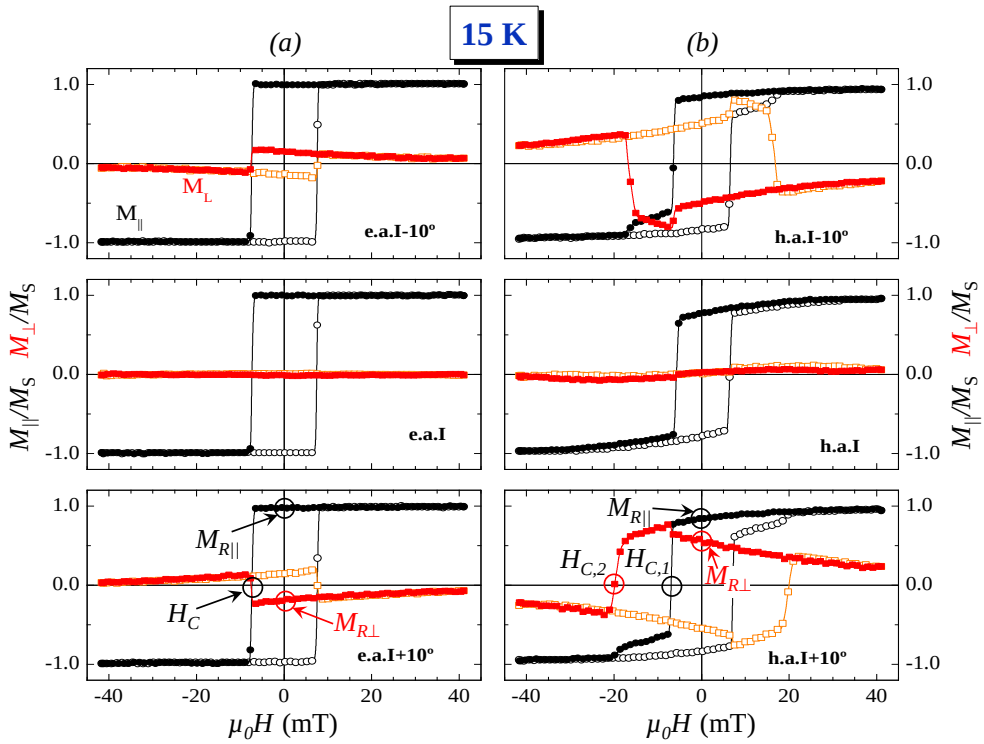


Figure 5.12: Selected in-plane resolved magnetization hysteresis curves around an easy axis (a) and a hard axis (b) direction of a Fe(100) film with competing uniaxial and biaxial anisotropies. The measurements have been performed at 15 K. $M_\parallel(H,\alpha_H)$ and $M_\perp(H,\alpha_H)$ loops are represented by circles and squares, respectively. The descending (forward) and ascending (backward) field branches are depicted with filled and empty symbols, respectively. Notice that $M_\perp(H)$ loops acquired at opposite angles around a characteristic axis direction present similar shape but different sign.

#### 5.2.3.4 Reversal processes

The specific pathways of the magnetization reversal are easily deduced by looking at the trajectory followed by the magnetization vector during the reversal, i.e., by looking

at the so called polar plots $M_\perp$ *vs.* $M_\parallel$, where quantitative information is possible thanks to the v-MOKE technique. Figure 5.13 shows representative $M_\perp$-$M_\parallel$ loops in order to illustrate magnetization reversal via one and two irreversible processes. In this polar-plot representation, the data lying on the circle of radius unity represent rotation processes. Every time the data is off this circle, i.e., at sharp transitions, magnetic domains are present and a fast domain wall (DW) propagation reverses the magnetization. Notice that the departure and return points off the unity circle are always closed to anisotropy directions. This indicates that nucleated magnetic domains are not oriented necessarily parallel to the field direction but rather to the easy axis directions. The angle between departure and return points is related with the angle of the domain wall ($\Omega_{\mathrm{DW}}$). For the present cases, c.a. 180° for the single transition when $\alpha_H = -10°$ and c.a. 90° for the two consecutive transitions when $\alpha_H = +35°$. Thereafter, rotation of magnetization continues until the maximum field is reached. Note that the magnetization vector is far from being saturated along the field direction even for the largest field used.

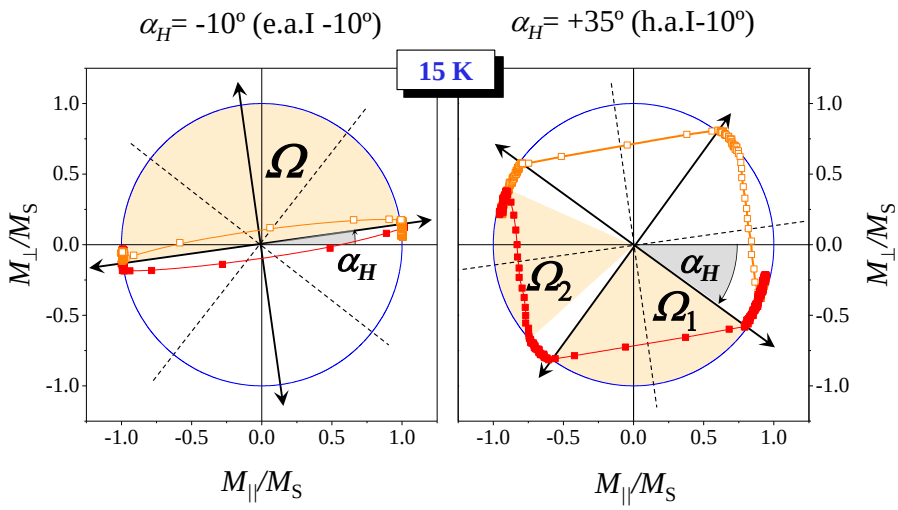


Figure 5.13: Vectorial analysis of in-plane resolved hysteresis loops with one (left) and two (right) irreversible transitions (example taken from 15 K hysteresis loops). Polar-plot $M_\perp$-$M_\parallel$ representation derived from figure 5.12(a,top) and figure 5.12(b,top), respectively. The descending (forward) and ascending (backward) field branches are depicted with filled and empty symbols,respectively. The circle of radius unity depicted with a solid line indicates the pure rotation of the magnetization vector. The domain wall angles $\Omega_1$ and $\Omega_2$ are indicated.

From this vectorial analysis, and in general for the present study, depending on $\alpha_H$ and $T$, either one or two irreversible transitions are found, which are related to nucleation of antiparallel or orthogonal magnetic domains and further propagation of 180° or 90° DWs, respectively. Moreover, the magnetic domains are not oriented necessarily parallel to the field direction but rather to the anisotropy directions.

Representative temperature-dependent in-plane vectorial resolved hysteresis loops acquired at two different angles are shown in figure 5.14. The angles have been selected in order to show two very different temperature evolutions in the same magnetic system. For $\alpha_H = 0°$, i.e., at e.a.I, the shape of the hysteresis loop does not vary with T, whereas its coercivity $H_C$ decreases as temperature increases. This behavior is the expected for thermally activated processes. For all temperatures, one irreversible transition with a negligible perpendicular component indicates that the reversal takes place via nucleation of antiparallel domains aligned with the anisotropy axis and fast propagation of 180° DWs, as explained previously. Therefore, thermally-assisted reversal would explain the temperature evolution without introducing any symmetry breaking effect.

#### 5.2.3.5 Magnetic transition: temperature evolution of reversal process

A very different scenario is found at $\alpha_H = +25°$ (see figure 5.14.b), where the magnetization reversal path changes at a critical temperature. In particular, both parallel and perpendicular components show that the reversal takes place via two consecutive (one) irreversible transitions below (above) 60 $K$. In the two temperature ranges the reversal fields are thermally activated, decreasing as the temperature increases. Taking into account the discussion above, the magnetization reverses via nucleation and further 90° (180°) DW propagation below (above) the critical temperature. Therefore, the well-defined low temperature biaxial magnetic anisotropy is dominated by another anisotropy contribution at high temperature. In fact, this is the fingerprint of the growth induced additional two-fold uniaxial magnetic anisotropy with its easy axis direction aligned with one of the easy axis directions of the biaxial one (the one that we have called e.a.I). As we can see, studying this temperature-dependent symmetry-breaking effects requires both temperature and angle dependent measurements.

#### 5.2.3.6 Angle and temperature dependent measurements of Remanence

The angular evolution of relevant magnetic parameters such as the magnetization remanence and reversal fields, should manifest the magnetic symmetries of a magnetic system. Looking at only one of them is sometimes not enough to correctly determine the true effective magnetic anisotropies. When the chosen magnetic parameter is related with the irreversible processes, as is the number of transitions, its angular dependence reveals the symmetry breaking coming from the two-fold growth-induced uniaxial anisotropy.

Figure 5.15 shows the angular dependence of the magnetization remanence of both in-plane magnetization components at two temperatures, 15 K and 300 K, well below and well above the observed symmetry-breaking magnetic transition, respectively. In both cases, the angular dependence of $M_{R,\parallel}$ and $M_{R,\perp}$ display a pronounced oscillation with periodicity of 90°. The parallel component follows a $|cos2\alpha_H|$ law dependence, the perpendicular component changes its sign when a characteristic easy or hard axis direction is crossed, and both components are complementary, i.e., $M_S = \sqrt{(M_{R,\parallel}^2 + M_{R,\perp}^2)}$ (not shown).

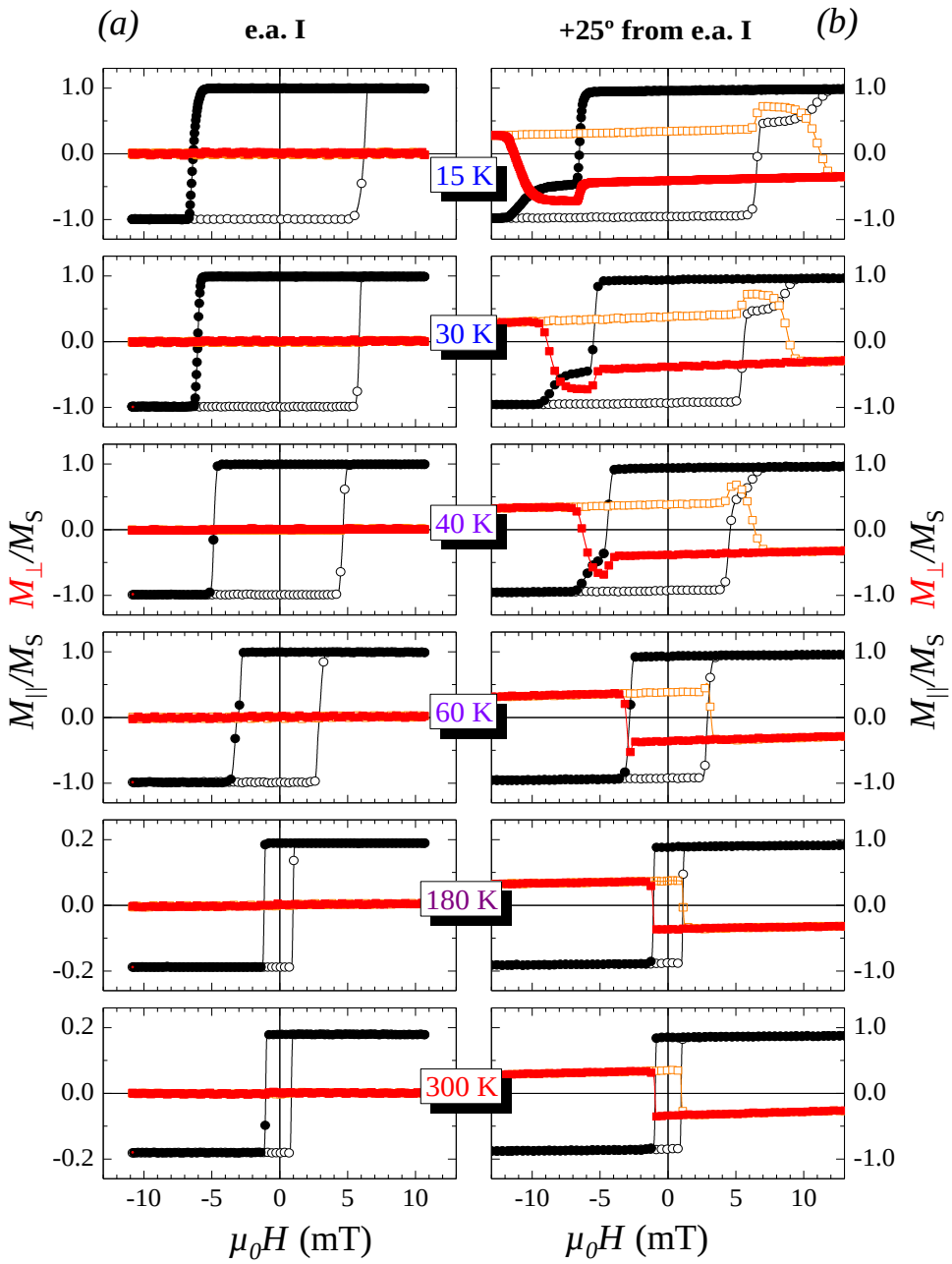


Figure 5.14: Representative temperature dependent in-plane resolved hysteresis loops at two selected angles, e.a.I. (left graphs) and +25° off e.a.I (right graphs). $M_{\parallel}(H,T)$ and $M_{\perp}(H,T)$ loops are represented by circles and squares, respectively. The descending (forward) and ascending (backward) field branches are depicted with filled and empty symbols, respectively. Notice the change of reversal pathway from above 60 K at $\alpha_H = +25°$ .

Therefore, no relevant differences are found in these angular evolutions. With this limited analysis we would end up with the wrong conclusion that the effective magnetic symmetry of the system would be pure four-fold. The observed symmetry breaking above 60 K (see figure 5.14) will remain hidden. The reason for that is the absence of irreversible processes before zero magnetic field, where the remanence is measured.

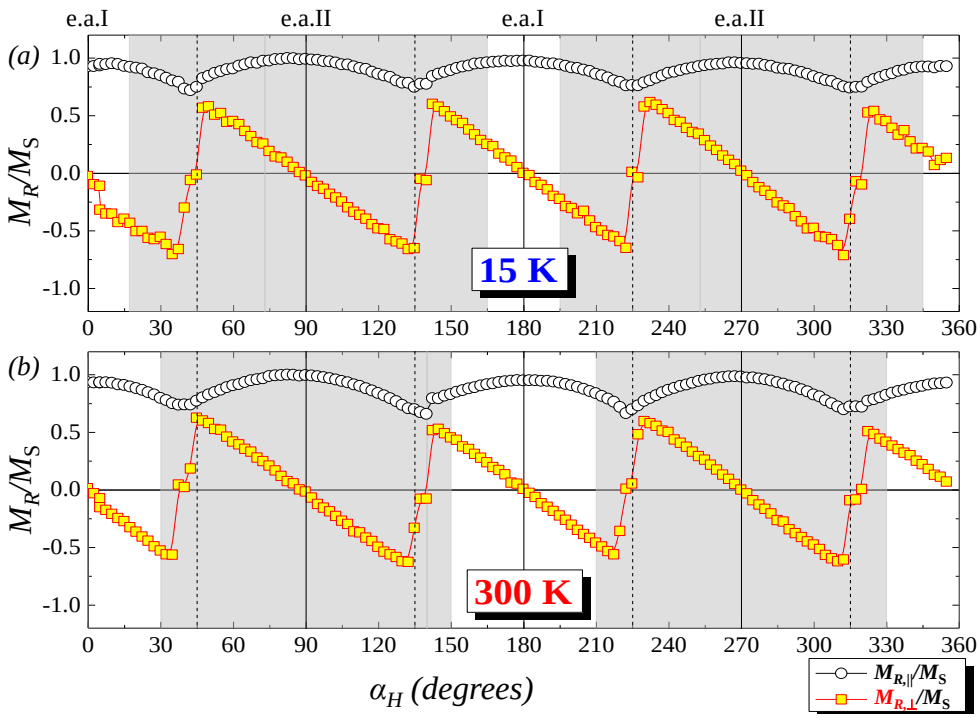


Figure 5.15: Angular dependence of the normalized remanence magnetization components of a Fe(100) film with competing collinear biaxial and growth-induced uniaxial contributions obtained at 20 K (a) and 300 K (b). The values of $M_{\mathrm{R},\parallel}$ (open circle symbols) and $M_{\mathrm{R},\perp}$ (filled square symbols) have been extracted from the in-plane resolved hysteresis loops, as the ones shown in figure 5.12 and figure 5.14. The angular range where two irreversible transitions take place during the reversal are highlighted by shadowed areas. Notice that the effect of the growth-induced uniaxial contribution is not observable in the remanence evolutions.

However, when the chosen magnetic parameter is related with the irreversible processes, the symmetry breaking coming from the two-fold growth-induced uniaxial anisotropy is revealed. This can be figured out in the slightly asymmetric reversal around h.a.I that can be observed in figure 5.12(b) at 15 K (i.e., slightly different loops at h.a.I $+10^\circ$ and h.a.I $-10^\circ$) or from the angular-dependence of the number of irreversible transitions. Respect to the later, the angular regions where the reversal

takes place by two irreversible transitions display 180° (two-fold) periodicity, as can be seen in the shaded regions of figure 5.15. The angular range is higher for the lower temperature although the relevance of the two-fold anisotropy contribution on the effective magnetic symmetry is much lower, as will be shown below (see figure 5.29).

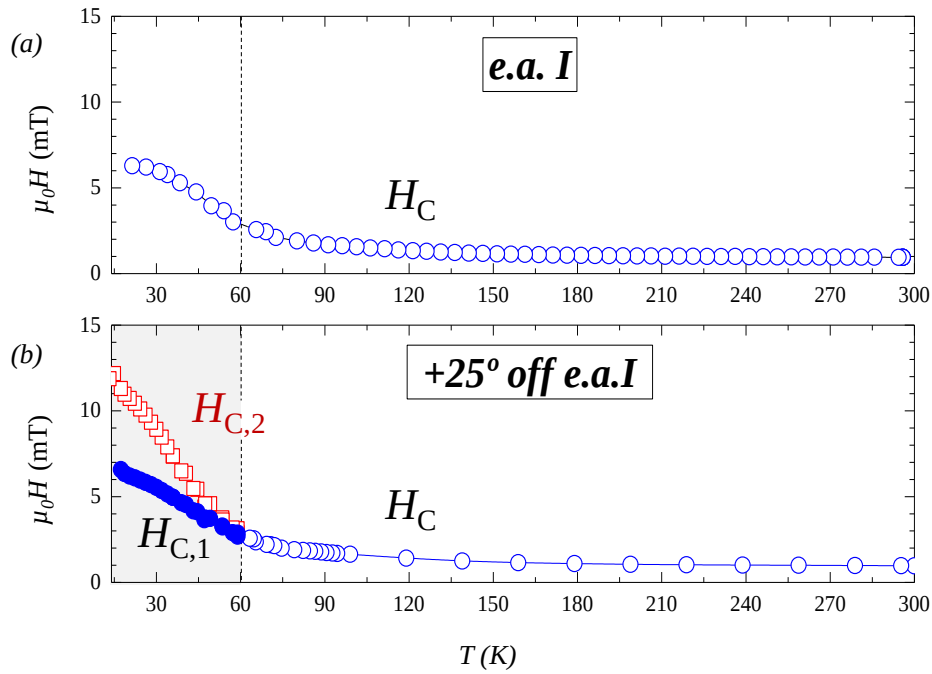


Figure 5.16: Comparison of the temperature dependence of the critical fields at e.a.I (a) and +25° off e.a.I (b) of a Fe(100) film with competing collinear biaxial and growth-induced uniaxial contributions. The critical fields have been extracted from the in-plane resolved hysteresis loops, as the ones shown in figure 5.14. $H_C$ (open circles) are the critical field values of 180°-DW driven irreversible transitions. $H_{C,1}$ (filled circles) and $H_{C,2}$ (open squares) correspond to the first and second irreversible 90°-DW driven transitions, respectively.

To gain further insight on how the symmetry-breaking transition takes place as well as to figure out the temperature dependence of the different anisotropy contributions, a quantitative analysis of both temperature and angular dependence must be done, as will be shown in later sections. As an example the figure 5.16 compares the temperature evolution of the critical fields extracted from measurements performed at $\alpha_H = 0°$, i.e., e.a.I, and +25°. Three critical fields $H_C$, $H_{C,1}$ and $H_{C,2}$ are defined as follows. For the hysteresis loops with just one irreversible (180°-DW driven) transition per half cycle only one critical field $H_C$ exists. This is the case at e.a.I for all temperatures and at +25° for temperatures above 60 K. For the loops with two con-

secutive irreversible (90°-DW driven) transitions, as those displayed in column (b) of figure 5.14 for T below 60 K, the critical field $H_{C,1}$ corresponds to the first transition and $H_{C,2}$ to the second transition.

Figure 5.16 shows that, in general, the critical fields increases as temperature decreases, as expected for thermal activated processes. However, different slopes can be observed for the different critical fields as temperature decreases, which indicates different activation energies. Above 60 K, a similar trend is found for the critical field at both angles, whereas it rises faster below this critical temperature. This indicates that the symmetry-breaking transition also affects the critical field at e.a.I. Below 60 K, the critical field at +25° splits into two branches smoothly as temperature decreases. Again, it is very important to notice that an analysis in temperature carried out only at a single angle, lets say the easy axis as in graph (a) of figure 5.16, would have not revealed the symmetry breaking that, on the other hand, is clearly visible at +25° from it, graph (b) of figure 5.16. With this we want to remark the importance of having combined full angular range and variable temperature vectorial magnetometry in this kind of studies where magnetic symmetry breaking effects are investigated.

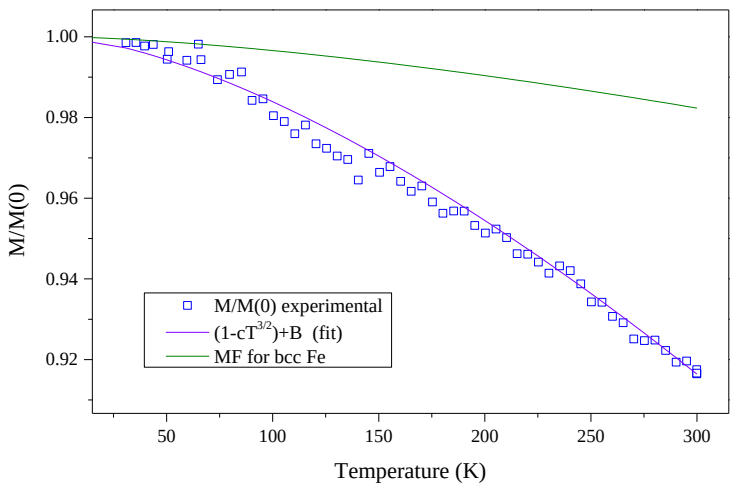


Figure 5.17: Magnetization evolution with Temperature is shown in this figure, red open square symbols, together with $1 - cT^{3/2}$ fitting curve (purple continuous line) after Spin Wave Theory, and theoretical Mean Filed Theory for bcc Fe.

### 5.2.4 Temperature dependence of magnetization

The evolution with temperature of the magnetization is presented here, as a previous step for further quantitative analysis. As v-MOKE does not account for absolute

values of M, all we can get with this technique is its relative evolution. As far as angular measurements are concerned, the common practice is to normalize hysteresis loops to the saturation magnetization obtained at the easy axis. Angular evolutions of the saturation and remanence are presented then in relative values with respect to unity, for the symmetry analysis. In order to explore temperature evolution of magnetization, temperature ramps can be carried out at characteristic axis, and M can be normalized to extrapolated zero-temperature value, i.e. the expected M(0), which is really closed to the lowest T value for M(T). In the following, for magnetization M(T) the symbol $M_S(T)$ is also used, since M(T) is measured at saturating field values.

Figure 5.17 shows the experimental evolution of M, compared with Mean Field Theory (MFT) for Fe. As can be seen, the experimental evolution of M with T is faster than MFT. This is in accordance with Spin Waves Theory (SWT), supposed to be dominant at low temperatures [60].

From SWT a $T^{3/2}$ behavior is expected for $\Delta$M/M(0). The purple curve shown in figure 5.17 is the fitting curve. As we have plotted M/M(0), the true law exhibited in the purple line is of the form $1 - cT^{3/2}$, up to some vertical shift used to account for a non fully saturated system. We see good agreement of experimental results with SWT theory.

### 5.2.5 Anisotropy landscape analyzed with critical fields

For the quantitative analysis of the magnetic anisotropies, angular and temperature evolutions of critical fields must be analyzed with the help of theoretical models. We have already introduced in the introductory chapter 1 section 1.6 the two basic models we are going to use: the Stoner-Wohlfarth (SW) model based on single domain systems with macro-spin" coherent rotation, and Cowburn model based on domains distributions and domain wall propagation under depinning energies. In both cases when the magnetic field is expressed in Tesla we obtain the anisotropy constants divided by the saturation magnetization, $M_S$, so that anisotropy constants are given in Tesla as well. As MOKE technique does not measure absolute value of $M_S$ we get rid of this problem by using always K over $M_S$.

In order to analyze the magnetic anisotropy constants of the Fe/MgO(001) we developed a combined SW/CW method as follows. As stated in the literature, the uniaxial magnetic anisotropy induced by oblique angle deposition of the Fe on this system is very small compared with the biaxial one. For this reason, trying to detect symmetry effects due to this small uniaxial component by comparing experimental angular evolution with SW model will reveal useless, even at the hard axes regions, where SW is expected to work well. In other words, very small $K_1/K_2$ ratios cannot be distinguished in between in the framework of SW model. In turn this is an advantage for the calculation of $K_2$: we can neglect $K_1$ in SW and proceed with pure biaxial SW model simulations to fit the reversible (rotative) part of the reversal, since the shape of the hysteresis loop in those regions is very little influenced by $K_1$. We then expect to fix $K_2$ as if the rotative part corresponded to pure biaxial system. Note that the cut-off in the experimental initial point of the first abrupt transition will appear at lower fields, yet the rotative part must match anyway in the segment left over up to the saturation. In addition, only a single unitary $K_2$ SW simulation is required (see

appendix C, section C.3), the fitting procedure will consist on a single scale factor on SW loops to match the curvature of that segment. On the other hand, we use CW model to get $K_1$, since we expect to be in its validity regime $K_1 << K_2$, and should work quite well. It is important to note that CW model does not require to know $K_2$ in advance because $K_2$ does not explicitly appear in the model: $K_2$ is implicitly encoded in the experimental transition fields values at e.a.I and e.a.II, which are the phenomenological parameters used in this model.

#### 5.2.5.1 Calculation of $K_2$

Following previous discussion, a first comparison of experimental angular evolutions with SW model, using some (unrealistic) a-priori $K_1/K_2$ test ratios, allows to detect symmetry breaking effects in the temperature evolution of the effective magnetic anisotropy, but with (first) bad $K_1/K_2$ ratios and (second) poor prediction of the transition field angular evolution. In figure 5.18 polar plots are depicted for 300 K, 70 K, 45 K and 15 K, together with the SW simulations to compare with. Experimental plots correspond to square symbols, and continuous lines to simulations. This is a non accurate method, as anticipated. First, the system does not behave as a single domain particle where coherent rotation model could be applied, so that transition field values are overestimated. Second, it is expected that $K_1/K_2$ ratio for this system is lower than 0.1. (see for instance the similar case of Fe/Ag(001), often used as a model ultrathin, in reference [16]). At those lower ratios, SW model presents very little differences with respect to the pure biaxial. Moreover, around easy axes the qualitative shape of the SW predictions are different than experimental. Nevertheless, in figure 5.18 the evolution in temperature can be seen. At 300K, transition fields are not 4-fold. $H_{C,1}$ (blue open and filled squares) presents dramatic kinks at the hard axes (<110>directions), and it has higher values at e.a. I ([100] and $[\bar{1}00]$) than at e.a.II. $H_{C,2}$ has higher values at e.a. II, splitting from $H_{C,1}$ values in a curve with a pronounced peak inwards, while around e.a. I, $H_{C,2}$ remains stacked to $H_{C,1}$ with lower values than at e.a. II. In other words, while around e.a.I single transitions are present, at e.a.II double transitions are found. All these features are representative of biaxial system with an extra uniaxial anisotropy contribution along [100]. The corresponding SW simulation, with the restrictions already mentioned, presents similar futures, with the limitation of the overestimation of transition fields, and the non flat behavior of $H_{C,1}$ around easy axes. If we now jump to low temperature, at 15 K, the 4-fold symmetry is clearly visible. SW for pure biaxial predicts quite well the qualitative shape of $H_{C,2}$, failing to predict $H_{C,1}$, but at least predicts the 4-fold symmetry. In conclusion, the fitting of SW is quite poor, with bad predictions on transition fields and anisotropy rations, but it still can account for symmetry breaking effects.

In figure 5.19 selected polar plots at 300 K and 15 K for transition field evolutions have been enhanced, where regions of double transitions have been remarked with shaded circular-sectors. Pastel green are used for the double transition regions derived from SW model, while pastel red are for experimental data. Although the onsets of the double transitions occur at different angles when comparing SW model with experimental data, the symmetry of the regions are the same at both temperatures. Although experimental data exhibits an almost four-fold symmetry, the double transitions never extinguishes at the [010] directions (e.a. II). This is indicative of

the statement that even extremely low uniaxial contribution are still influencing the reversal process [16]. SW does not detect this effect: note that SW fitting is two-fold at hight T, and four-fold at low T (pastel green shaded regions) indicative of its insensitivity to small values of $K_1$ anisotropy constant. Single transition regions have been remarked with filled blue symbols for $H_{C,1}$ in experimental data. In spite of this, the pastel red shades clearly points out the symmetry breaking effects with temperature. In fact, there is a "flee effect" from [100] direction for the angle of onset of double transitions as temperature is increased, indicative of the increasing relative strength of $K_1$ with respect to $K_2$.

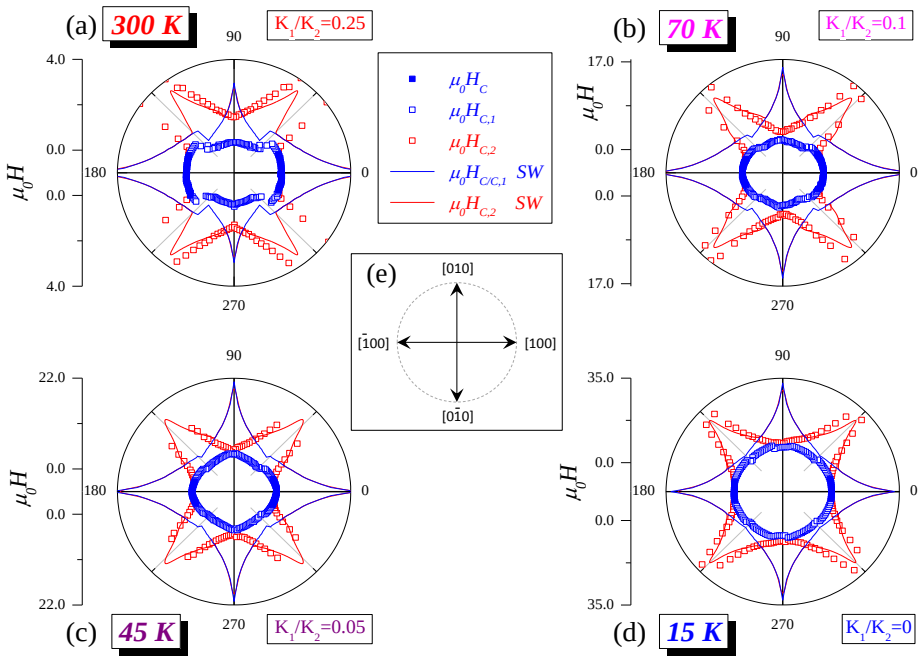


Figure 5.18: Angular evolution of transition fields $H_{C,1}$ and $H_{C,2}$ for (a) 300 K, (b) 70 K, (c) 45 K and (d) 15 K. Anisotropy ratios $K_1/K_2$ indicated in each graph are non significant, but just a-priori values taken to manifest how the symmetries evolve as the ratio $K_1/K_2$ decreases with T, from a qualitatively point of view. True ratios will be obtained later in this chapter. SW curves have been re-scaled according to experimental $H_{C,1}$ at 45°, so as to better show the similarity of the evolutions. In the center of the figure there is a diagram with the corresponding crystallographic directions. Transition fields evolve from elongated shape on [100] direction at 300K to almost fully symmetric shape at 15 K, indicative of the presence of uniaxial anisotropy collinear with [100] biaxial axis, whose relevance becomes smaller as temperature goes down. This is in accordance with the SW curves, that exhibit the same behavior when evolving from higher $K_1/K_2$ ratios at 300 K to vanishing ratio at 15 K.

Detailed quantification of anisotropy constants evolutions will reveal that it is a consequence of thermal effects affecting (decreasing strength as T increases) to $K_2$ (shown later). It is important to mention that SW simulations for experimental curves shown here have been carried out with unrealistic $K_1/K_2$ ratios, that needs to be explained: this ratios have been chosen so that the second transition field between h.a. and e.a.II could be as closed as possible to experimental data. Other possibilities could be used as well, fixing other regions (not explained here), with more dramatic failures.

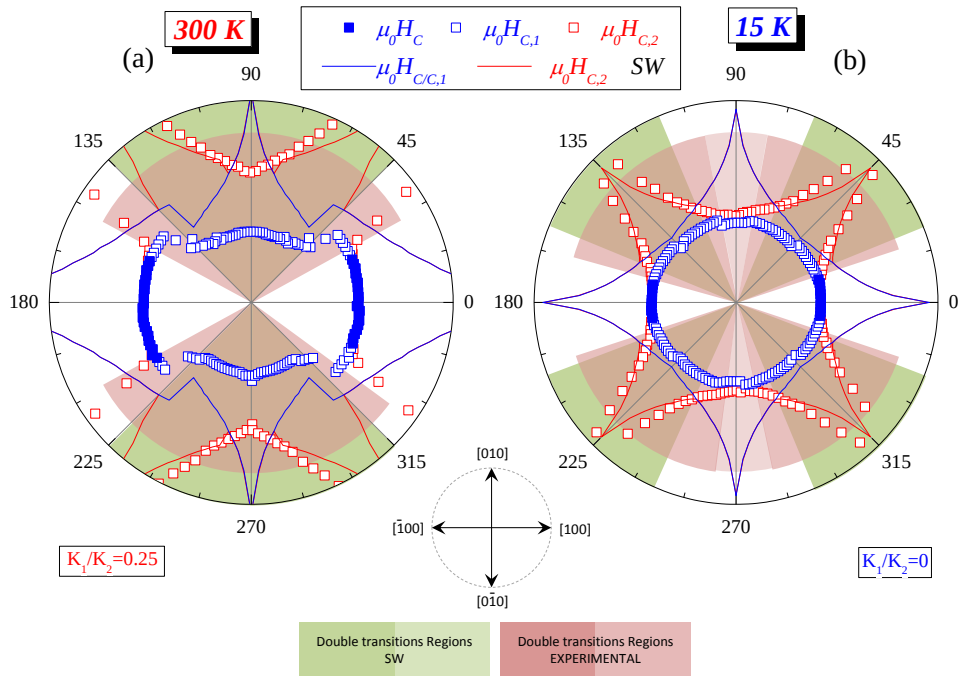


Figure 5.19: Angular evolutions (polar plots) of transition fields $H_{C,1}$ (open and filled blue symbols) and $H_{C,2}$ (open red symbols) are plot here as enhancement from figure 5.18. Corresponding SW curves are depicted with blue and red lines. Shaded circular sector regions remark double transition angular ranges for experimental data (dark and soft pastel red) and SW simulations (pastel green). Agreement between SW and experimental data for this system is hard to establish (explained in the text).

In spite of the non agreement with the transition fields, where SW is not accurate for the kind of systems we are dealing with, we use its predictions for the rotative part of the hysteresis loops in order to fix $K_2$ values, since the curvature of that part of the loops, where evolution corresponds to reversible processes, must be well predicted. We assume for this purpose $K_1 \ll K_2$, so $K_1$ is negligible compared to $K_2$ as to influence on the rotative part of the reversal, and then pure biaxial SW model

can be used. The validity of this assumption relays on multiple tests carried out with Stoner-Wohlfarth simulation software at different ratios, where for $K_1$ values lower that 0.05 effects in the curvature are not detected by the model.

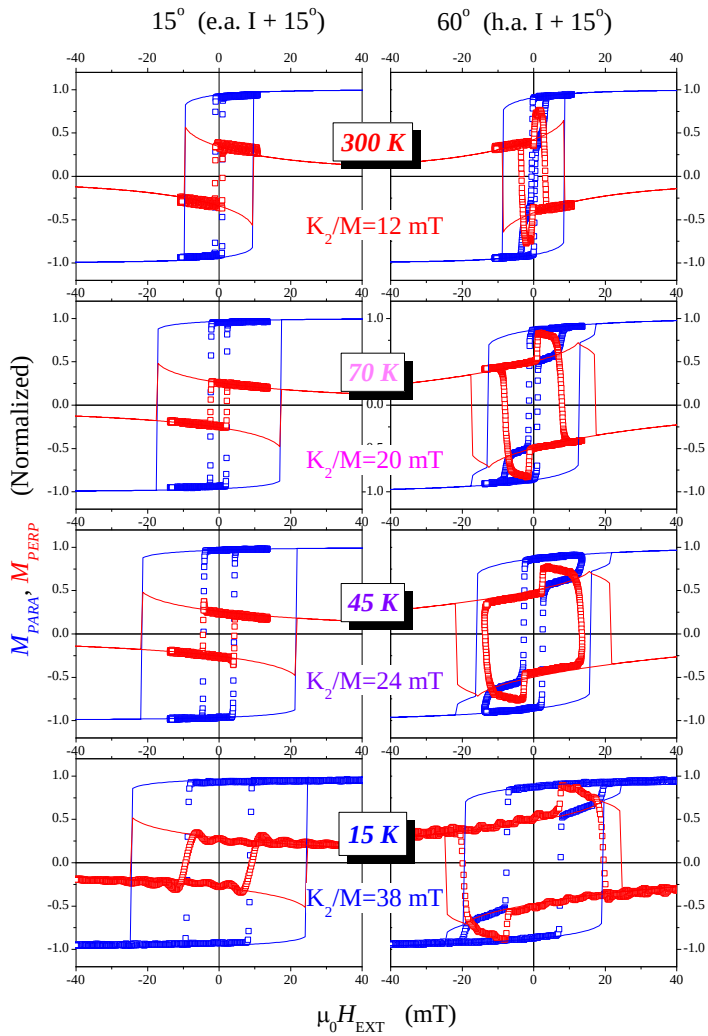


Figure 5.20: Representative hysteresis loops with SW curvature fitting, and the corresponding $K_2$ value, are shown for representative temperatures, around e.a. I and h.a. Note the overestimation of transition fields in SW fitting loops, but the good accordance in the reversible parts of them.

Under these assumptions, we make use of SW model with only biaxial anisotropy to fit curvature of the hysteresis loops at the four temperatures explored over the full angular range for each one. We use as starting point the regions around hard axes,

where reversal process is mainly reversible, and with a first tentative value for $K_2$ we compare the rest of the experimental loops with corresponding SW loops for each angle, and check consistency of the curvature fit. In figure 5.20 representative hysteresis loops around e.a.I and h.a. are depicted for each temperature. Corresponding values of $K_2$ obtained after the fitting of the curvature are presented in table 5.1. Figure 5.21 presents the $K_2$ temperature evolution, with a tentative fitting curve based on a $T^{-1/3}$ law.

Table 5.1: $K_2$ after SW fit.

| Temperature (K) | $K_2/M(mT)$ | Error |
|---|---|---|
| 300 | 12 | ± 0.96 |
| 70 | 20 | ± 1.60 |
| 45 | 24 | ± 1.92 |
| 15 | 38 | ± 3.04 |

Avg. error = 8%

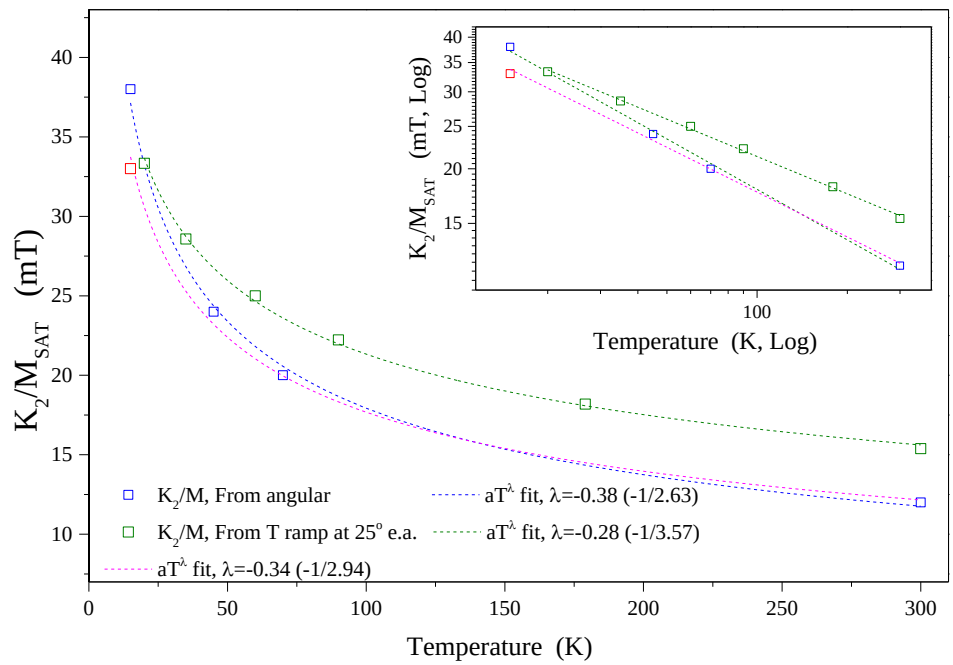


Figure 5.21: Calculated $K_2$ after SW fit as a function of T is plotted together with the $T^{-1/3}$ law that better fits the T evolution. The inset represent the same in logarithmic scale to make emphasis of how close it is to this behavior.

Fitting SW hysteresis loops to match experimental curvature of the rotative parts of the cycles to obtain $K_2$ is very compromised thing, since small slope variations leads to large differences in $K_2$. However when doing this from the angular evolutions, we can compare up to 146 hysteresis loops (one every 2.5°) at each temperature where angular measurements have been done. In addition we have hard axes as reference to check if we are doing things correctly, since SW model is supposed to predict switching fields quite well. The drawback of using angular evolutions is that (in this case) we only took four significant temperatures where angular evolutions were measured. Fitting temperature evolution curves with only four points is not so ideal. In order to add a bit more information, temperature ramps where used (at fixed angles) to obtain additional values of $K_2$. Using temperature evolutions at fixed angles has the drawback that neighbor loops just some degrees apart from the reference angle of the ramp cannot be compared. As a consequence, this measurements are more exposed to errors. With the aforementioned advises, in figure 5.21 we show experimental values of $K_2$ with the closest fitting curves. For the fitting curves, we have made a linear fit from the logarithmic representation (inset in the figure), converting then the slope into the $T^{\alpha}$ law. As can be seen, $\alpha$ values are very close to -1/3, i.e., curves are close to $aT^{-1/3}$ behavior. In the figure, two family of values are plot. In blue, we have $K_2$ obtained after angular evolutions at four different temperatures, while in dark green $K_2$ obtained from temperature evolutions at fixed angle of 25° out of the easy axis. It was not possible to take loops at the (desired) exact hard axis, were the rotative contribution to the reversal is maximum, due to limitations in the maximum field that we could apply in our set-up (that would have led to minor loops and bad $K_2$ values). It can be seen that there is a vertical shift. Here we claim to the aforementioned difficulty to compare neighbor loops to get the better $K_2$ value.

The $T^{-1/3}$ experimental behavior cannot be assimilated to any of the established relations for the anisotropy constants of cubic systems, as stated by Akulov or Callen-Callen (through the power law equation A.5), and neither to Spin Wave theory results (equation A.9), that is the applicable one after having obtained for $M(T)$ over $M(0)$ a behavior with a 3/2 power law (see equations and additional material in appendix A, section A.2). Notice that the $T^{-1/3}$ behavior is the best fit for $K_2(T)$/M(T), while all the aforementioned relations are expressed for $K_2(T)$ over $K_2(0)$. It is easy to show that even after eliminating the denominator in $K_2(T)$/M(T) multiplying it by the experimental $M(T)$, and then dividing it by (yet unknown but constant) $K_2(0)$, the general shape of the curve will still be a decreasing concave function, while the theoretical relations as a function of T give decreasing convex functions. The power law $T^{-1/3}$ for $K_2$ follows a similar trend as coercive field with temperature, as can be seen in figure 5.16 in the region down to 40 K. Below this region, coercive field seems to change the convexity, something that is not observed in $K_2$. We thus observe a deviation from Akulov/Callen-Callen theory in this system. Note that the aforementioned theories were established for bulk cubic systems, while we are dealing here with in-plane projection of such cubic anisotropy due to the presence of the surface. Works reporting this kind of deviations with additional important citations can be seen in reference [61], but there are still many open questions.

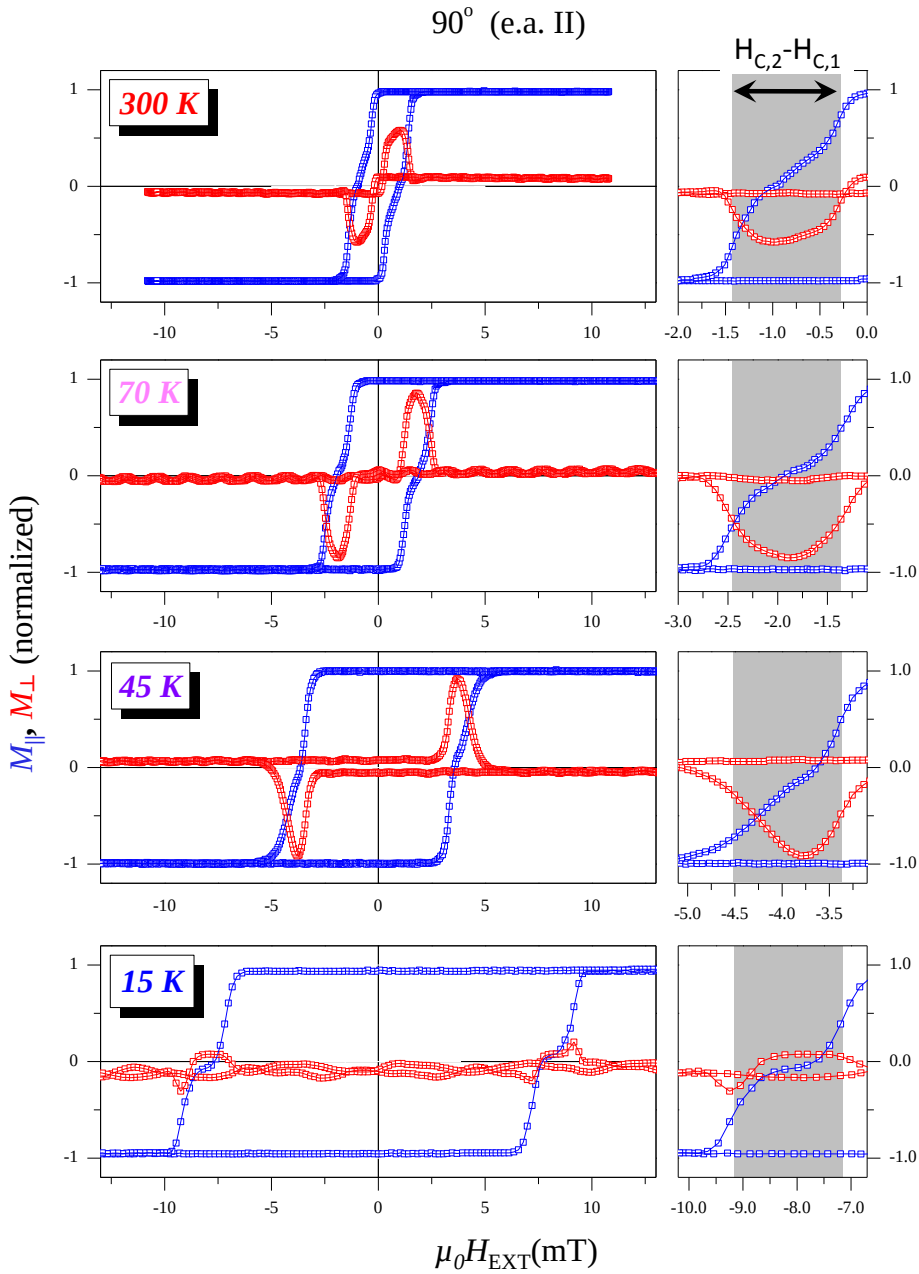


Figure 5.22: Temperature evolution at e.a. II, (left column plots), and corresponding detail of the transitions (right column plots). The regions between $H_{C,1}$ and $H_{C,2}$ are marked with a gray shadow. Notice that the size of this region is almost constant in all the temperature range (with just a slight increasing deviation at low temperature), an indication that $K_1$ is almost constant over temperature.

#### 5.2.5.2 Calculation of $K_1$

Following the program established at the beginning of section 5.2.5 we proceed now to obtain $K_1$ using Cowburn model. Cowburn model initially gives a tentative value of $K_1$ calculated directly by using phenomenological formula

$$K_1 = \frac{1}{2} M (H_{C,2}^{[010]} - H_{C,1}^{[010]}) \tag{5.1}$$

where $H_{C,1}$ and $H_{C,2}$ are taken from experimental values at direction [010], i.e., at e.a. II (see formulation details in appendix E, section E.2). Then a subsequent fitting procedure based on the angular evolutions of transition fields calculated by the model is done, by varying phenomenological parameters (tentative $K_1$ value and domain wall energies).

With equation 5.1, direct calculation of $K_1$ temperature evolution can be given at a first stage. Figure 5.22 shows temperature evolution of hysteresis loops for selected temperatures, at direction [010] (e.a. II), from which transition fields $H_{C,1}$ and $H_{C,2}$ are extracted for this first direct $K_1$ calculation. Left column shows complete hysteresis loops, while column to the right enhance the transition region. The regions between $H_{C,1}$ and $H_{C,2}$ have been shaded in grey in this right column. The width of this regions (proportional to $K_1$ through equation 5.1) is almost constant for all the temperature range (with just a slightly increment at low temperature), an indication that $K_1$ is almost constant over temperature. The hysteresis loops taken in this figure correspond to the temperatures for which we have measured in full angular range. In figure 5.23 the evolution of calculated $K_1/M$ is depicted together with $H_{C,1}$ and $H_{C,2}$ taken after temperature ramps (with many more experimental points). Although $K_1/M$ has some structure at low temperatures, it remains almost constant when compared to $K_2$, as expected for surface dipolar effects. Double transitions are quite difficult to see when measuring exactly at e.a. II at low temperatures, where $K_1$ is extremely small compared with $K_2$. Errors in the corresponding calculated $K_1$ are more likely to be expected. We have moved slightly apart from [010] direction, just 5° away, to carry out another temperature ramp measurement. In figure 5.24 the transition fields and corresponding calculated $K_1$ are plotted. Linear fits are plot in both figures. Comparison of both $K_1$ calculations are displayed in figure 5.25. When compared with $K_2$, it is very reasonable to estimate $K_1$ to be quite constant with T, with a value around 0.7 mT. The results of blind $K_1$ calculations after these temperature ramps are summarized in table 5.3 for specific reference values of T (300 K, 70 K, 45 K and 15 K). This values will be compared later.

This direct blind calculation of $K_1/M$ after temperature evolution of $H_{C,1}$ and $H_{C,2}$ at [010] direction gives initial estimation value around 0.7 mT. Together, CW also gives initial estimation of depinning energies, $\epsilon_{90^o}$ and $\epsilon_{180^o}$, after equations 5.2 and 5.3, and the corresponding angular evolution of transition fields. Further fitting is done varying the three phenomenological parameters in order to get a good agreement of CW transition field angular curves with experimental curves. i.e., changing $K_1/M$, and the domain wall energy values, $\epsilon_{90^o}$ and $\epsilon_{180^o}$, to make CW transition field angular evolutions as close as possible to the experimental data.

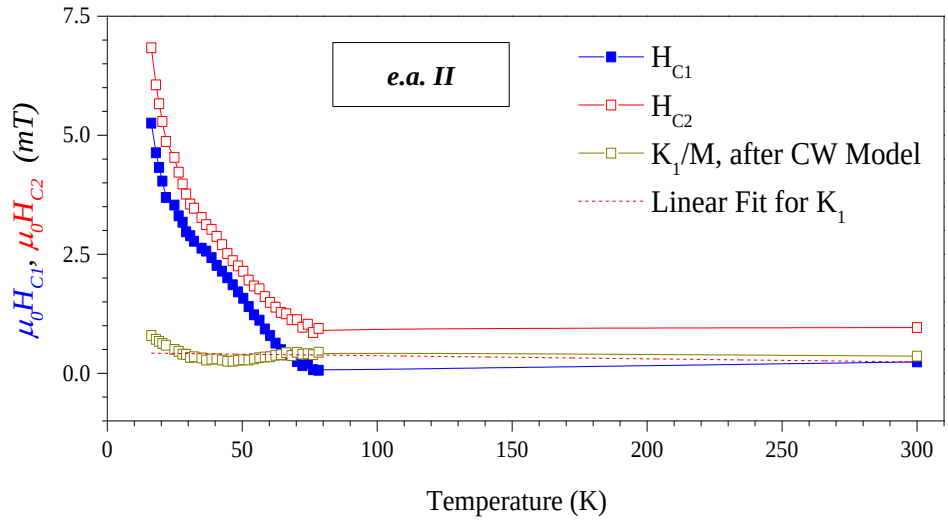


Figure 5.23: Plot of $K_1/M$ as a function of T, after CW formula, with the transition fields at e.a. II ([010] direction) from which it is derived. A linear fit appears in red dashed line. $K_1/M$ is around 0.7 mT.

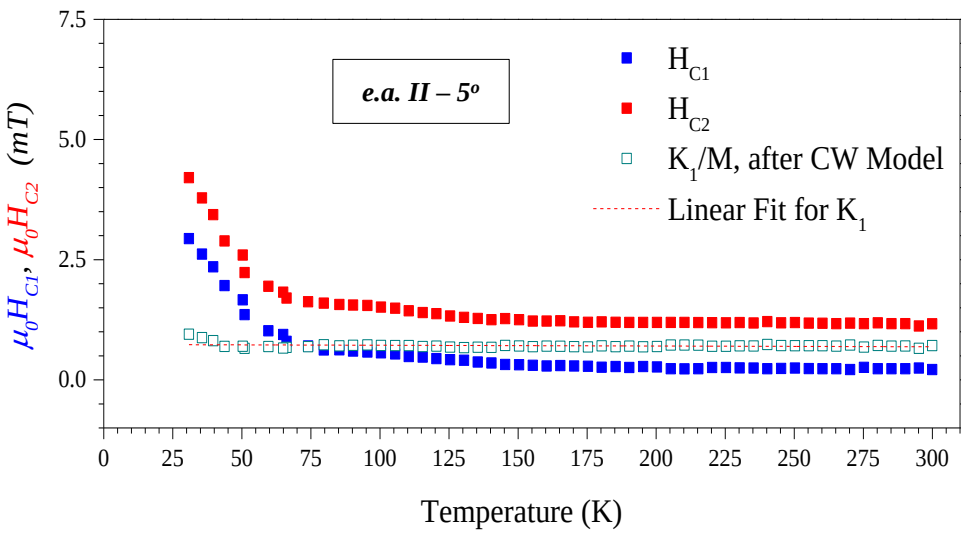


Figure 5.24: Plot of $K_1/M$ as a function of T, after CW formula, with the transition fields at 5° from e.a. II (i.e. from [010] direction) from which it is derived. A linear fit appears in red dashed line.

$$\epsilon_{180^\circ} = 2MH_C^{[100]} \tag{5.2}$$

$$\epsilon_{90^\circ} = \frac{1}{2}M(H_{C,1}^{[010]} + H_{C,2}^{[010]}) \tag{5.3}$$

In figure 5.26, the evolution of transition fields are depicted with symbols for the four temperatures, 300 K, 70 K, 45 K and 15 K, together with the corresponding CW curves after the fit. For this fitting process we have taken into account a global $H_C$ shift following dynamical effects as reported by Carpene et al [164].

Table 5.2 summarizes the results of the fit. The shifting $H_C$ values are also include in the table, as well as the domain wall energy barriers. As can be seen, there is some oscillation in the values, around 0.7 mT. A comparison of values obtained after fitting procedure of the angular evolutions and values obtained by blind calculation after temperature ramps can be seen in table 5.3. Notice that blind calculations are already very close to final fitting values. With all this information, it is very reasonable to set $K_1/M$ as almost constant. Notice however that we are showing $K_1/M$ all time. This means that values are divided by a magnetization that is not constant with temperature. Nevertheless, for temperatures below room temperature, the variation of M is quite small, no more than an 8 %, as can be seen in figure 5.17, and we can still claim a "close to constant" behavior of $K_1$, specially when compared wiht $K_2$.

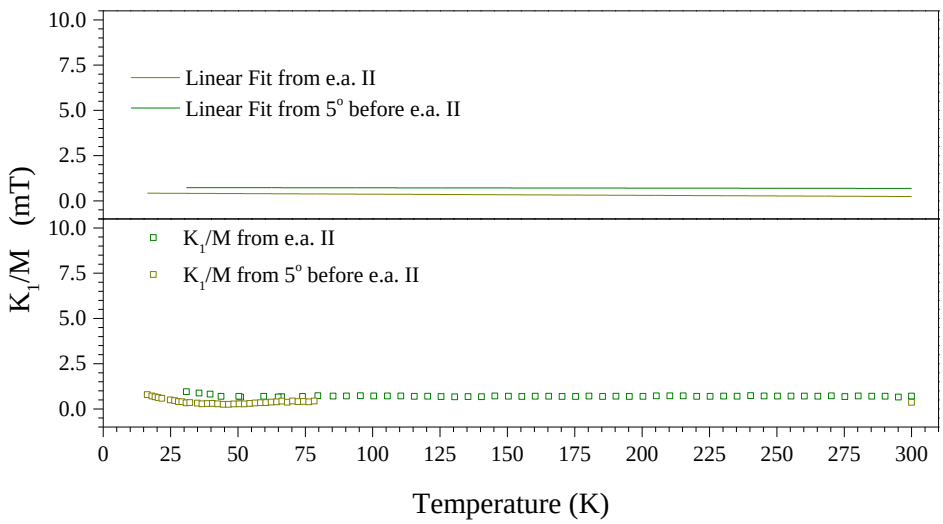


Figure 5.25: Comparison of the calculated $K_1/M$ after CW formula as a function of T for temperature ramps at e.a.II and at 5° from e.a. II. Both calculations runs very similar with T, with very little difference in the regime above 70 K, and some features below it. IT can be said that $K_1/M$ is somewhere around 0.7 mT, with a bit higher value at low temperatures, due to particular (unexplained) features.

In figure 5.27 and 5.28 polar plots are shown, comparing experimental results (blue

and red symbols for $H_{C,1}$ and $H_{C,2}$ respectively) with CW fit curves (corresponding lines of the same color scheme). The accuracy of the CW model to predict the transition fields is very good at all temperatures. Enhanced polar plots for room temperature and low temperature behavior are shown in figure 5.29 with significant shaded regions set to emphasize the very good agreements of the CW model fit curves and experiment. Shaded regions for the experimental and theoretical double transitions zones overlap. Here theoretical model predicts that influence of $K_1$ is still present at low T, since around [010] direction double transitions are still present (blue shade regions), in agreement with what is observed experimentally. In spite of this, the system is very close to four-fold biaxial at low temperature, demonstrating the temperature dependent symmetry breaking effect.

Table 5.2: $K_1/M$ (mT) after CW fitting of full angular measurements.

| T (K) | $K_1/M$ | error | $\epsilon_{180^o}$ | $\epsilon_{90^o}$ | $H_{C,shift}$ |
|---|---|---|---|---|---|
| 300 | 0.55 | ± 0.04 | 2.1 | 0.9 | 0 |
| 70 | 0.80 | ± 0.05 | 3.8 | 1.7 | 1.2 |
| 45 | 0.60 | ± 0.04 | 6 | 3 | 1.4 |
| 15 | 0.80 | ± 0.06 | 16 | 5 | 4 |

Avg. $K_1$=0.7 Avg. error=6% $\epsilon$=E/M (mT)

Table 5.3: $K_1/M$ (mT) comparison: angular fit and blind calc. from T Ramps.

| T (K) | $K_1/M$ ($\alpha$-fit) | $K_1/M$ (at e.a.II) | $K_1/M$ (at e.a.II-5°) |
|---|---|---|---|
| 300 | 0.55 | 0.32 | 0.71 |
| 70 | 0.80 | 0.42 | 0.70 |
| 45 | 0.60 | 0.38 | 0.70 |
| 15 | 0.80 | 0.78 | 1.11 |

Considering as the best values for $K_1/M$ those coming from the CW angular fit (table 5.2) and for $K_2/M$ the values listed in table 5.1, we compute the $K_1/K_2$ ratio, which is summarized in table 5.4. These values are also indicated in the polar plots of the angular evolutions of transition fields with the CW fit, shown in figures 5.27 and 5.28, as well as in the linear plots of the angular evolutions in figure 5.26.

Table 5.4: $K_1/K_2$.

| T (K) | $K_1/K_2$ | Error |
|---|---|---|
| 300 | 0.054 | ± 0.008 |
| 70 | 0.040 | ± 0.006 |
| 45 | 0.025 | ± 0.004 |
| 15 | 0.021 | ± 0.003 |

Average error = 14%

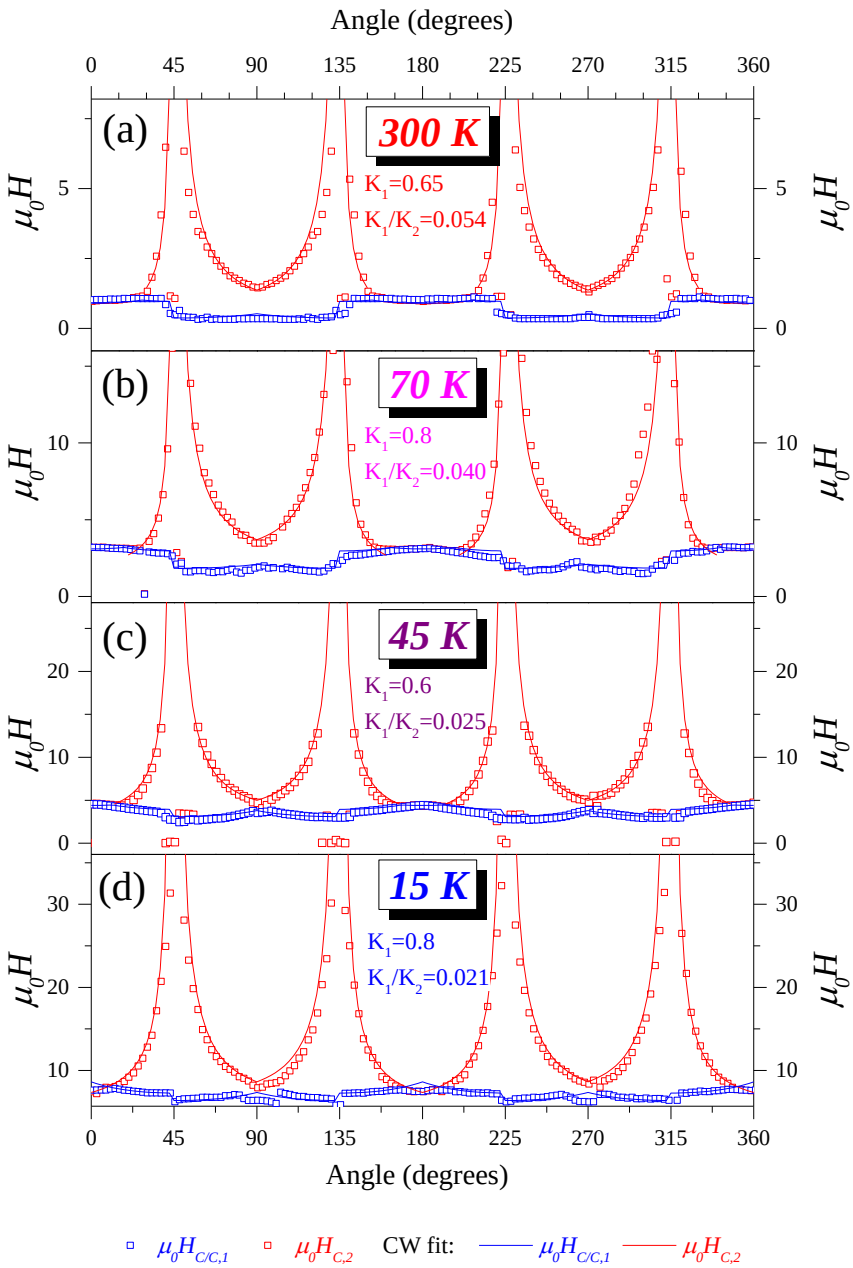


Figure 5.26: Angular evolution of transition fields as a function of temperature, with Cowburn theoretical curves. See explanation in main text.

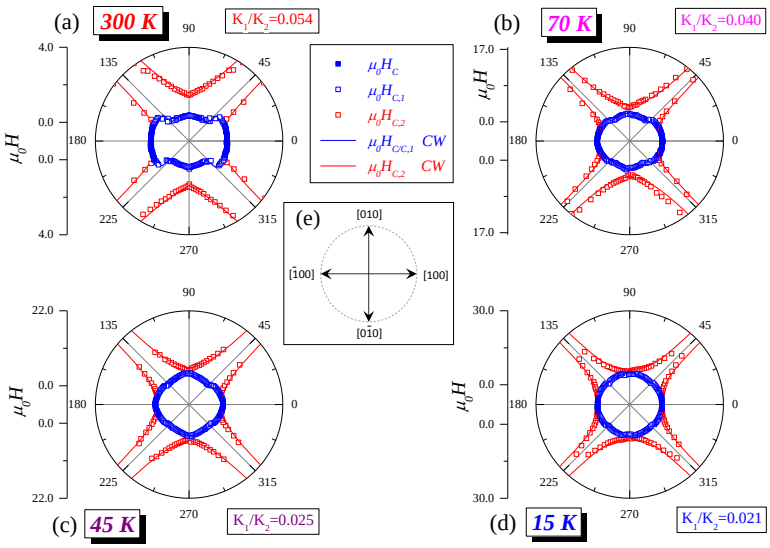


Figure 5.27: Corresponding polar plot of figure 5.26.

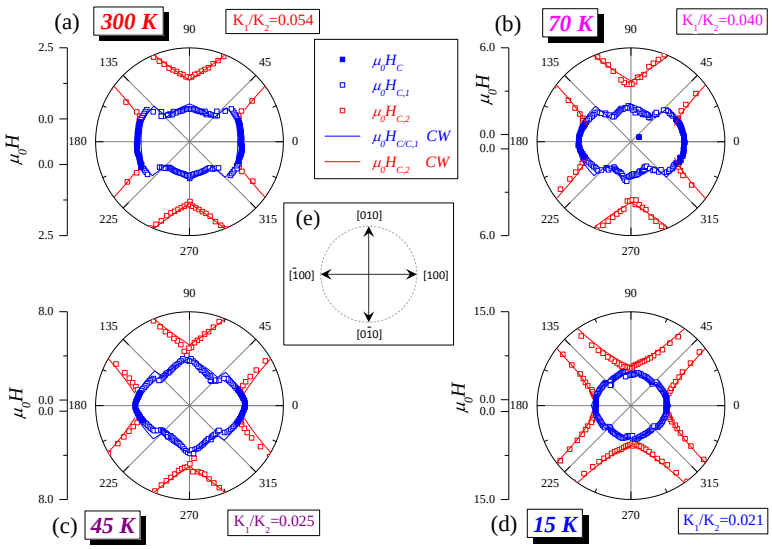


Figure 5.28: The same plot as in figure 5.27, with enhanced scale to better appreciate details.

In figure 5.30 the two anisotropies evolutions with T are exhibited together for comparison. While $K_2/M$ increases with decreasing temperature, as expected for thermal activated process, $K_1/M$ remains almost constant at the scales of $K_2/M$. This confirms the dipolar origins of the induced uniaxial magnetic anisotropy.

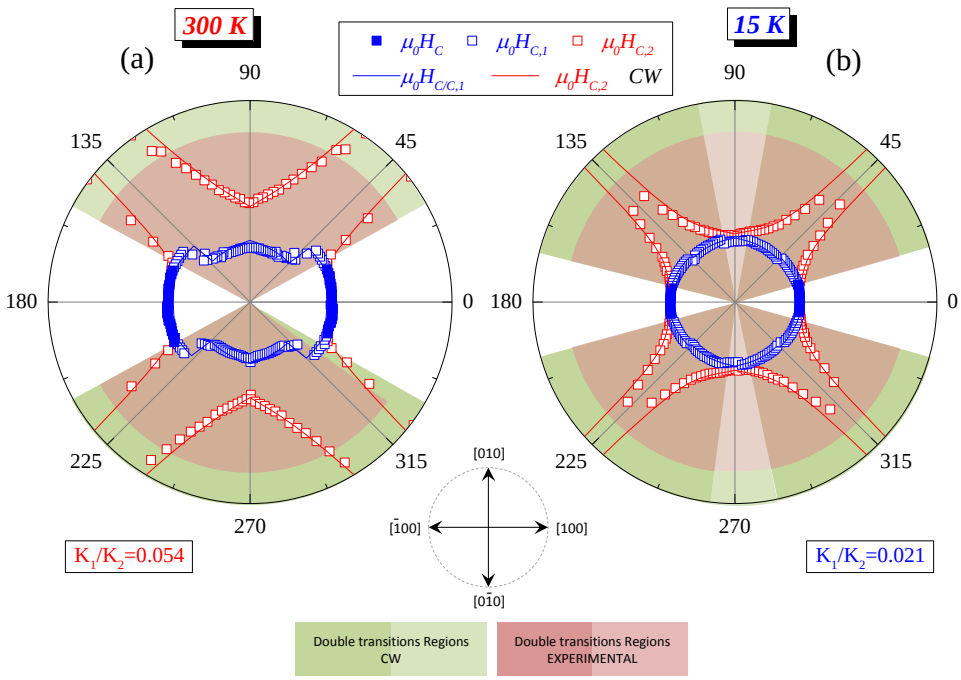


Figure 5.29: Angular evolutions (polar plots) of transition fields $H_{C,1}$ (open and filled blue symbols) and $H_{C,2}$ (open red symbols), depicted here as enhancement from figure 5.27. Corresponding CW curves are depicted with blue and red lines. Shaded circular sector regions remark double transition angular ranges for experimental data (dark and soft pastel red) and CW fitting (dark and soft pastel green). Note the good agreement between theoretical CW fitting and experimental data, as the corresponding shaded regions fully overlap. Details are given in the text.

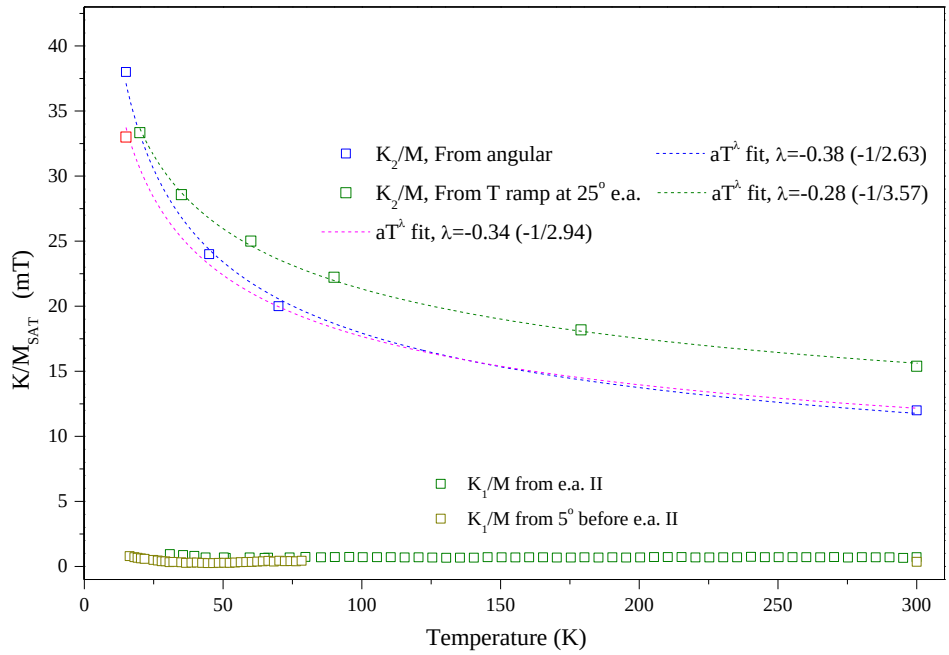


Figure 5.30: Global comparison between experimental values of $K_1/M$ and $K_2/M$. Observe the almost null temperature dependence of $K_1/M$ when compare with $K_2/M$, confirming the origins of the uniaxial magnetic anisotropy as a surface effect originated by dipolar interaction induced by the oblique deposition of Fe.

### 5.2.6 Conclusions

The conclusions of this section are:

1. We have shown the necessity of having vectorial resolved magnetometry with both full-angular range and variable temperature capacity in order to investigate magnetic anisotropies, and we have demonstrated that TRISTAN set-up is a versatile instrument for this purpose.

2. Anisotropy contributions to the effective magnetic anisotropy of Fe/MgO(001) biaxial system with induced uniaxial anisotropy have been disentangled. While thermal activation effects govern the biaxial magnetic anisotropy contribution, the uniaxial contribution is non-thermal activated, originated by dipolar surface effects.

3. We have obtained both the uniaxial and biaxial anisotropy constants for the temperature range between 15 K and 300 K in this Fe/MgO(001) model system,

revealing the origins of the thermal-activated magnetic symmetry breaking effects that operates on it. We demonstrate:

   (a) Uniaxial anisotropy, of dipolar origin, remains almost constant at all temperatures, as expected by theory.

   (b) Biaxial anisotropy follows a power rule that is different than expected by Akulov/Callen-Callen power law.

4. We have established a method for the calculation of anisotropy constants by a combination of two well established theoretical models. The method is summarized here:

   (a) We use the Stoner-Wohlfarth model for a pure biaxial system to find the $K_2$ value that better fits the reversible part of the experimental hysteresis loops, under the assumption that $K_1 \ll K_2$.

   (b) Transition fields angular evolution are fitted with Cowburn model, allowing to obtain $K_1$.

   (c) The ratio $K_1/K_2$ as a function of temperature is then computed.

5. We have tested various theoretical fittings for $K_2$.

## 5.3 Thermal and field induced effects in exchange coupled FM/AFM systems

**In this chapter we review the exchange bias effect (EB) in a model system based on FM/AFM thin film heterostructure. The system selected is $Co/MnF_2$, that was investigated in the framework of a collaboration with IOFFE Institute (St. Petersburg, Russia) and UNIMORE University (Modena, Italy). We cover the subject of exchange anisotropy, and explore temperature-driven and field-induced effects on the magnetic symmetries and spin reorientations. Surprisingly new phenomena have been found which has not been reported up to today.**

### 5.3.1 Introduction

Hybrid systems composed of ferromagnetic (FM) and antiferromagnetic (AFM) layers are very intensively studied in search of the fundamentals of its interfacial magnetic phenomena. In addition, the unidirectional coupling between the AFM and FM layers, referred to as exchange bias [62], is of very special interest, because of its application in advanced magnetic in-plane spintronic devices [165], and future advances are promoted by the perpendicular exchange-coupling effects recently observed in several FM/AFM systems [166] at room temperature. The underlaying physics of exchange bias was already correctly described almost half a century ago by the original work of Meiklejohn and Bean [62]. After cooling a FM/AFM system in an applied magnetic field, down to below the Néel temperature of the AFM layer, the uncompensated AFM spins at the AFM/FM interface align with the polarized FM ones at the FM side. Although the exchange interaction is strongly reduced, i.e., up to two orders of magnitude, AFM materials are used to pin (or stabilize) the magnetization direction of a FM reference layer. Among others, coercivity enhancement, [165] and asymmetric magnetization reversal, [82, 86], are associated phenomena usually observed in exchange-coupled FM/AFM systems. Recent advances in element-selective synchrotron-based experimental techniques have thrown light on the basic mechanisms that explain some unusual properties observed in these systems. For example, only a small fraction of uncompensated AFM spins contribute in real FM/AFM systems (which have unavoidable rough interfaces), unlike for a perfectly flat interface, which explains the rather small size of the exchange bias field $H_E$. In addition, it was already found that pinned (unpinned) uncompensated AFM spins at the interface are correlated with the exchange bias [167] (coercivity enhancement [168]). These features have been addressed in both in-plane and perpendicular [169] exchange coupled FM/AFM systems. However, a microscopic imaging of most of the aforementioned effects during magnetization reversal, i.e., in external magnetic fields, is still lacking.

### 5.3.2 The $Co/MnF_2$ (FM/AFM) system

The $Co/MnF_2$ system under study consists of a layered system epitaxially grown in UHV at the IOFFE Physico-Technical Institute of Russian Academy of Sciences, St.

Petersburg, in the context of the EU-ONDA Project [4]. The bilayer system is grown on Si(111) substrate to induce specific (111) orientation of the $MnF_2$ crystal, which is the antiferromagnetic layer. A $CaF_2$ buffer layer is used between Si(111) and $MnF_2$ to allow for a better relaxation of the lattice parameter mismatch. On top of the $MnF_2$, Co grows polycrystalline. Figure 5.31 shows schematically the structure of one of the samples used in this thesis: an epitaxial 80 nm thick $MnF_2$ (AFM) layer was grown at 100°C on a buffer layer 20 nm thick $CaF_2$ grown at 770°C on a Si(111) substrate. A polycrystalline 10 nm thick Co layer (FM) was then grown on top. Finally, a capping layer of $CaF_2$ (5 nm) has been used to avoid oxidation under ambient conditions. During the growth of the AFM layer, half of the sample was masked with a shutter, so that the hidden part lacks of AFM coupled layer, allowing to measure the FM layer alone, as a reference. A set of three samples (including the aforementioned one) with different thicknesses of the FM and AFM layers have been grown in a this way in order to probe the relevance of the interface effects. They are summarized in table 5.5.

Table 5.5: $Co/MnF_2$ samples

| Co (nm) | $MnF_2$ (nm) |
|---|---|
| 10 | 80 |
| 5 | 20 |
| 5 | 10 |

The morphological and structural characterization of the sample was carried out at IOFFE (see for instance [170]). The system presents epitaxially grown layers of $CaF_2$ and $MnF_2$ and polycrystalline Co, as can be seen in the RHEED studies carried out by Sokolov's Group [170]. Figure 5.32, AFM images of the sample are shown for both regions with and without $MnF_2$, the Co presents in both cases the same polycrystalline aspect, with slightly different average grain size.

The magnetic characterization was carried out with our TRISTAN set-up, focusing in the sample area corresponding to the coupled $Co/MnF_2$ system. For comparison, some control measurements were performed in the region without the $MnF_2$ layer.

In figure 5.33, coercive field angular evolutions at room temperature are shown for the 10nmFM/80nmAFM sample (first in table 5.5), in the regions with and without $MnF_2$. The presence of the $MnF_2$ at room temperature does not affect the magnetic symmetry (plots (b) and (d)), however, a significant reduction of the coercive field is appreciated due to its presence, where $H_C(Co/CaF_2) \approx 2.7 \times H_C(Co/MnF_2/CaF_2)$. In general, the presence of antiferromagnetic layers promotes enhancement of the coercive field, while we observed a contrary effect. The magnetic symmetries are easier to view through the polar plots, depicted in figure 5.34. For clarity, $M_{\parallel}$ and $M_{\perp}$ have been plotted separately, so that now (a), (c) and (e) plots in the figure correspond to $H_C$, $M_{\parallel}$ and $M_{\perp}$ for the region without $MnF_2$, while (b), (d) and (f) plots are the respective for the region with $MnF_2$.

[4] EU-ONDA Project stands for *Ordered hetero- and Nano-structures with epitaxial Dielectrics for magnetic and electronics Applications, ONDA project - FP7 - PEOPLE - 2009 - IRSES Scheme*, http://www.onda.unimo.it/

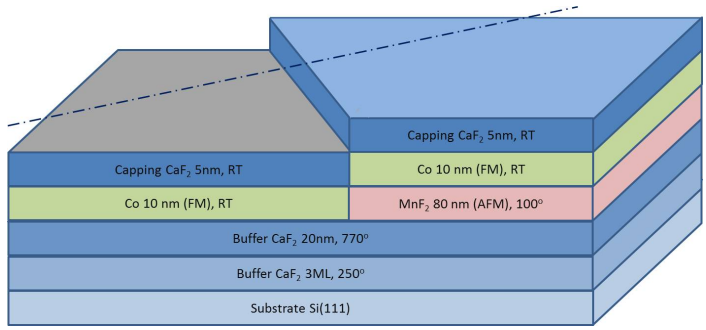


Figure 5.31: Scheme of the sample structure under investigation. The dashed blue line indicates the magnetization easy axis direction. The structure is a bilayer magnetic FM/AFM coupled system of $Co/MnF_2$, on a $Si(111)$ substrate with suitable $CaF_2$ buffer, and a final layer also of $CaF_2$ acting as capping. Each layer has been epitaxially grown at the temperatures indicated in the figure, except the Cobalt, that grows in polycrystalline structure. Part of the sample was covered with shadow mask or shutter, so that there is a region with $MnF_2$ layer (FM/AFM bilayer system), and a region without it (single FM system).

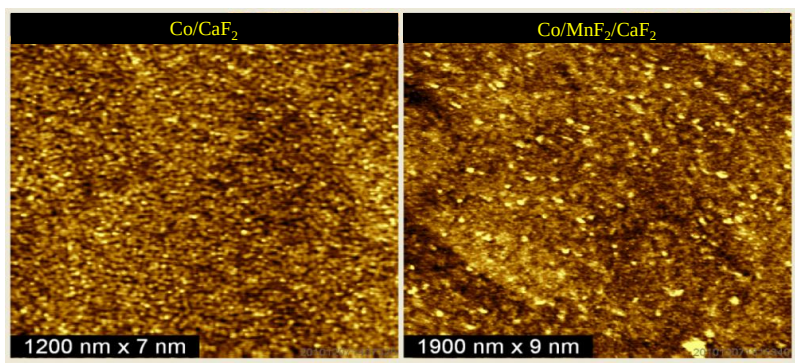


Figure 5.32: Topography AFM images. Left image corresponds to growth of Co without $MnF_2$, so that Co is grown directly on top of buffer layer of $CaF_2$, as indicated in legend. Right image corresponds to Co grown on top of $MnF_2$ layer. Notice that a slightly different scale has been used in both images. Taking this into account, it can be seen that grain size of polycrystalline Co is slightly different, yet the grain aspect remains the same. Image courtesy of N. Sokolov group at IOFFE Institute.

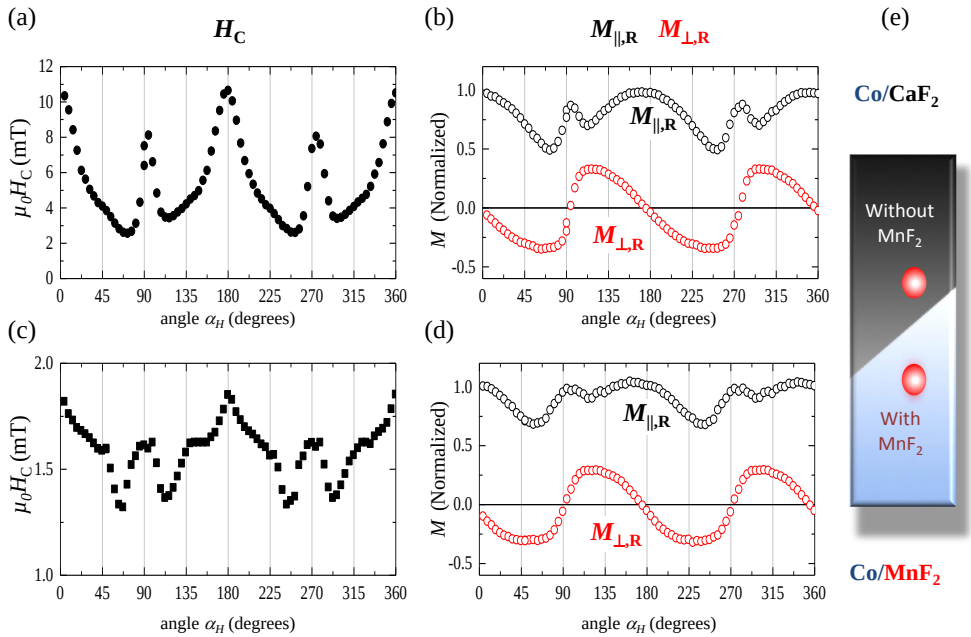


Figure 5.33: Test measurements of $H_C$, $M_\parallel$ and $M_\perp$ in the sample regions without $MnF_2$, (a) and (b) plots, and with it, (c) and (d) plots. In diagram (e) the sample is depicted with the two respective regions. Notice that both cases present similar magnetic symmetries, but there is a significant reduction in the coercive field when the $MnF_2$ is present.

### 5.3.3 Exchange-bias phenomena in $Co/MnF_2$

The first experiment on EB for the $Co/MnF_2$ system was performed for the sample with 10nm Co/80 nm $MnF_2$, with the external field applied along the e.a. direction by using a sinusoidal-shaped magnetic field at 4 Hz with a maximum field of +10 mT. In order to set the exchange bias direction a standard FC procedure was used, i.e., by cooling from 450K in a positive external field of +10mT. This value was chosen to be sure that the FM layer was saturated in all temperature range. After FC, the first hysteresis loop was acquired at 8 K. Hysteresis curves were acquired then every 5 K (temp. ramp of about 5 min/Kelvin) during warming up to 450 K, (figure 5.35(a)-(c)). Finally, the sample was cooled down to RT and hysteresis curves were acquired during cooling also every 5 K. (figure 5.35(d)). The hysteresis curves show a clearly distinguishable behavior in four different temperature ranges, as shown in figure 5.35. For clarity, since in principle the transversal component of magnetization is negligible at the e.a. direction, only the parallel component of magnetization is shown. In general, narrower hysteresis curves are found as temperature increases. The magnetization reversal occurs at lower field values as the temperature increases in both forward and backward field branches, but with a different temperature evolution. In

the lower temperature range (figure 5.35(a)), from 10 to 40 K, the hysteresis curves are shifted from zero magnetic field to negative values, indicative of a negative exchange bias, i.e., opposite to FC direction. In addition both branches behave similarly as T increases. Different behavior is found in the second T range (figure 5.35(b)). In particular, the backward branch seems to be frozen from 40 K to 70 K, i.e., the reversal takes place at the same field value whereas the forward branch follows the normal displacement to the right when T increases, i.e., reducing the coercive field of this branch. The negative shift of the hysteresis curve is hence decreasing as the temperature approaches to 70 K. This critical temperature coincides very well with the order transition temperature of the AFM, whose Néel temperature for bulky $MnF_2$ systems is tabulated as 67 K. Above the critical temperature ($T > 70K$). the reversal transition in both branches decreases continuously as T increases (figure 5.35(c) and (d)). Note that the hysteresis curves seem to be shifted to positive field values, i.e., positive exchange bias, as we can figure out by a simple inspection to the cleared central area of the hysteresis curves represented in both figure 5.35(c) (during warming) and figure 5.35(d) (during cooling).

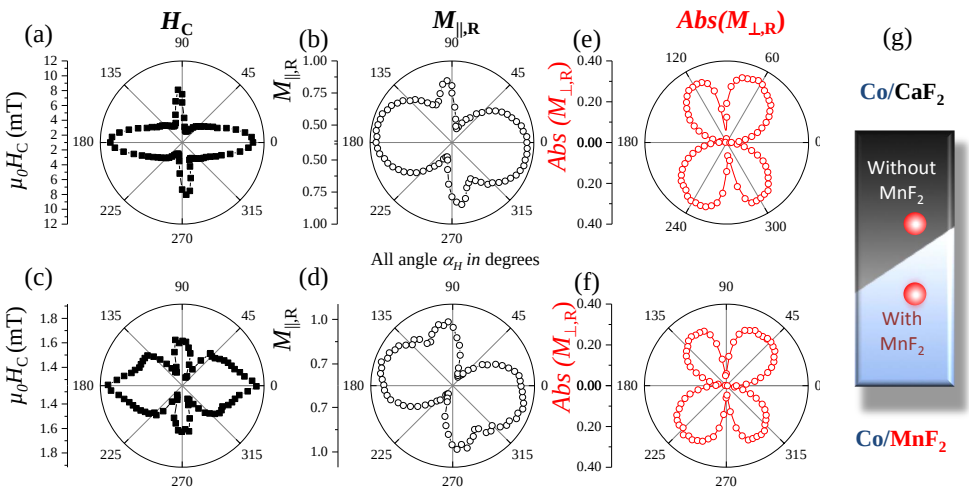


Figure 5.34: Polar plots of the test measurements of $H_C$, $M_\parallel$ and $M_\perp$ previously depicted in figure 5.33. (a), (c) and (e) plots correspond to $H_C$, $M_\parallel$ and $M_\perp$ for the region without $MnF_2$, while (b), (d) and (f) plots are the corresponding for the region with $MnF_2$. In (g) the sample is depicted with the two respective regions. Notice that magnetic symmetry is preserved, but with a reduction in coercive field for the region with $MnF_2$.

Quantitative magnetic information extracted from the hysteresis curves are depitcted in figure 5.36. 5.36(a) shows the temperature dependence of both coercivity $\mu_0 H_C$ and exchange bias field $\mu_0 H_E$. In general, $\mu_0 H_C$(T) decreases as temperature increases and a non monotonous temperature evolution is found in $\mu_0 H_E$(T). The plots show more clearly a change of behavior in $\mu_0 H_E$(T) at 70 K, passing from negative values (negative exchange bias) to positive ones (positive exchange bias). In

particular, both forward and backward coercive fields follow an exponential decay law with temperature, as shown in the 5.36(b). This behavior, called domain wall coercive field [171], is expected in magnetic systems where domain wall propagation is the relevant mechanism during reversal and thermally activated relaxation processes result in the mentioned exponential law. Experimentally, this behavior has been observed in well defined uniaxial systems with perpendicular anisotropy. In our system, different slopes are found for the two field branches, with larger slope for the forward field branch. In addition, while the forward branch continues its normal tendency in all temperature ranges, the backward branch seems to have a kink at the critical temperature, although its global tendency is the same. In 5.36c we concentrate more specifically in the exchange bias curve. Below 70 K the exchange bias field is negative, which is opposite to the field cooling direction (positive). This is the standard behavior of FM/AFM systems, i.e., called negative exchange bias, where the exchange bias direction is set opposite to the FC direction [62]. This effect originates from the interfacial-induced unidirectional anisotropy below the ordering Néel temperature of the AFM layer, as described below. On the contrary, above 70 K a non-negligible positive exchange bias is found. This exchange bias is along the FC direction and can be observed even up to 450 K. In addition, this positive exchange bias seems to have some decay with increasing temperature.

Similar findings, i.e., positive exchange bias, have been previously found in some FM/AFM systems after using special FC procedures (by using high magnetic fields during FC), but always below the bulk-Néel temperature of the AFM system [65, 172]. This was ascribed to the antiferromagnetic nature of the interfacial coupling between FM and AFM layers. We have considered the necessity to better verify both the positive exchange bias behavior over 70 K and the transition from negative to positive exchange bias across the critical temperature. For this purpose, we have repeated the same experiment several times, including under negative FC conditions. Results are well reproduced in all the measurements after using positive-FC, and when negative-FC is used, the magnetic properties behave in a symmetric fashion with respect to the former, as shown in figure 5.37 adding more confirmation of the behavior. Hysteresis loops for both positive-FC and negative-FC are compared for 50 K and 300 K in figure 5.37(a) and 5.37(b), respectively. The inversion in the direction of the displacement is fully coherent with the exchange bias behavior observed when inverting the sign of the field using during FC.

### 5.3.4 Field dependent phenomena in $Co/MnF_2$

Temperature and field cooling dependent measurements present a rich phenomenology in this exchange bias system due to proximity effects at the interface between FM and AFM layers. Both positive and negative exchange bias can be observed at different temperature ranges, as previously shown. Two additional exchange bias effects are discussed in the following. On the one hand, different magnetic symmetries such as uniaxial and trigonal symmetries (in transition field) with superimposed unidirectional (exchange bias), can be induced in the same system by tuning the field cooling direction. On the other hand, positive field induced exchange bias can be driven by asymmetric applied fields above $MnF_2$ Néel transition temperature.

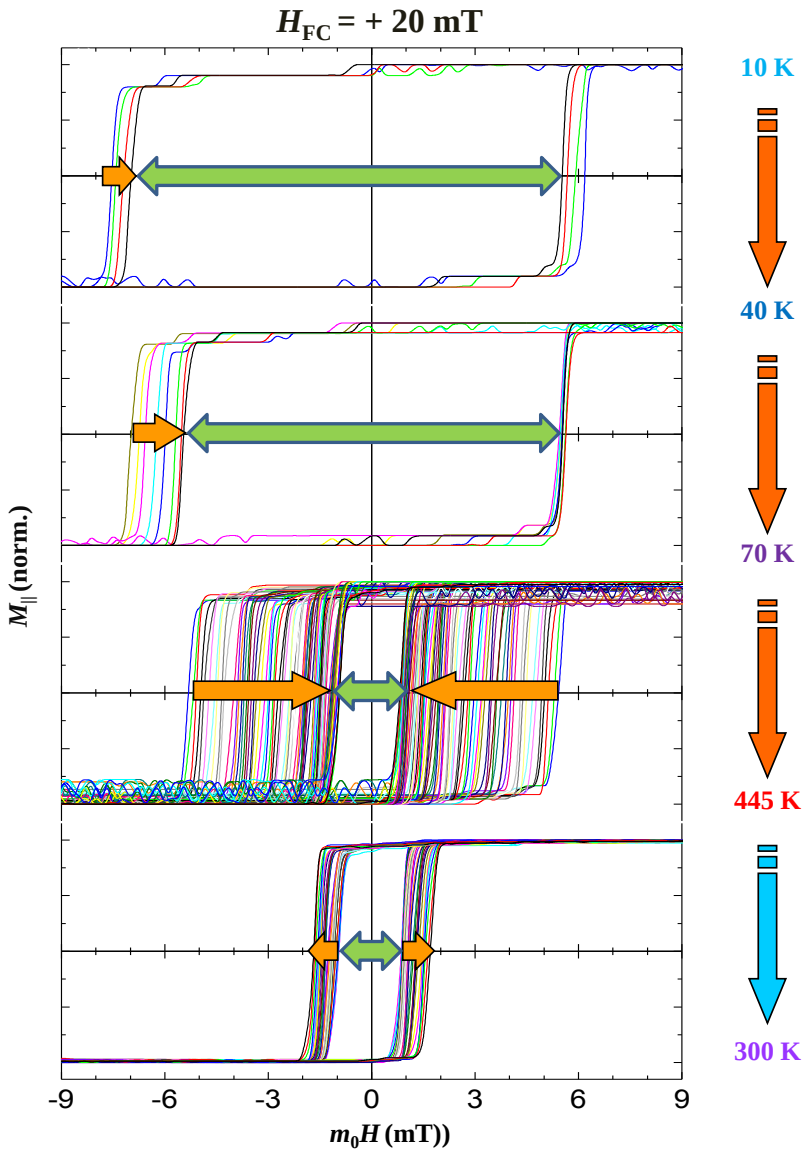


Figure 5.35: Temperature dependent hysteresis curves of a $Co/MnF_2$ (10 nm/80 nm) bilayer after the positive FC procedure described in the text. The hysteresis curves were acquired along the e.a. direction every 5 K. The temperature range and direction are also indicated. Four temperature ranges have been plotted, which correspond to the different ranges discussed in the text. Notice the negative shift of the hysteresis curves from zero field to negative field values in (a) and (b), whereas a clear positive shift is observed in (c) and (d).

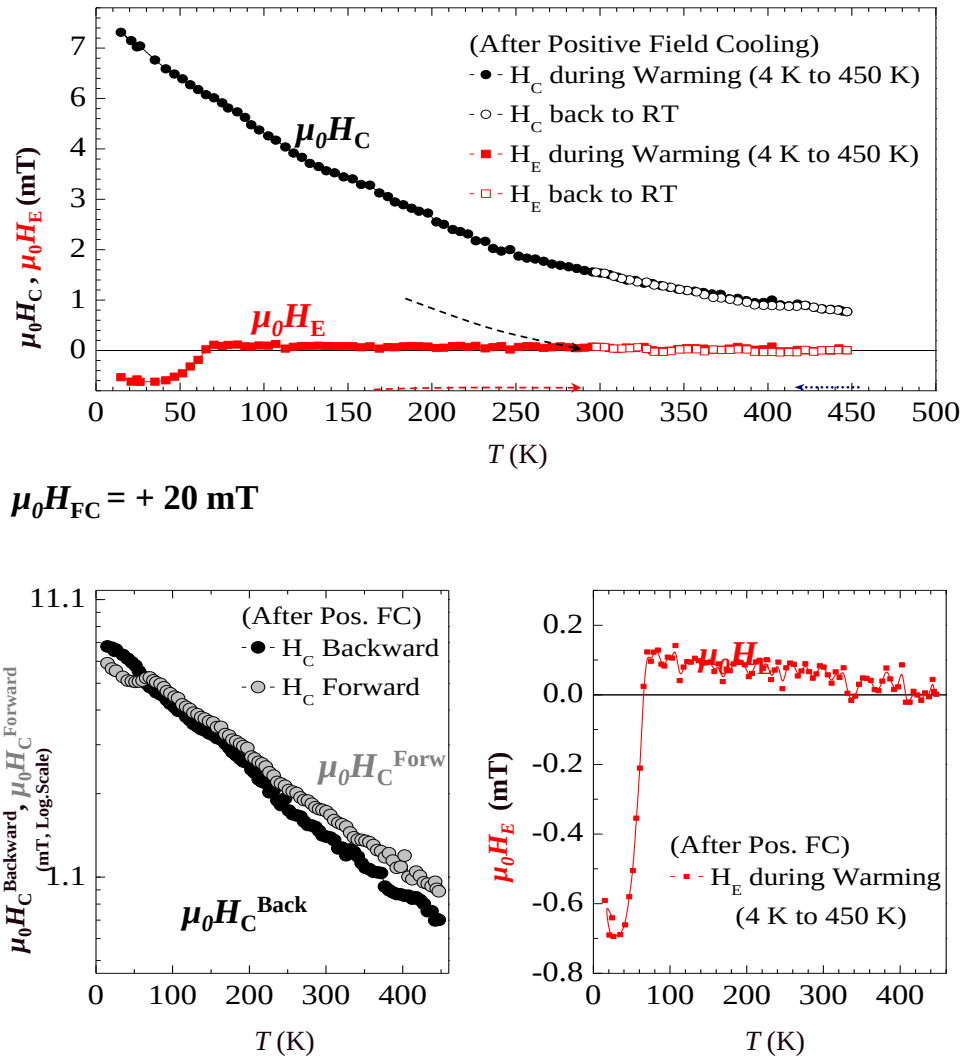


Figure 5.36: (a) Temperature dependence of the coercive field (black symbols) and the exchange bias field (red symbols) after the positive FC procedure described in the text. The values were extracted from the hysteresis curves as those shown in 5.35. Filled (empty) symbols correspond to warming (cooling) from 8 K (450 K) to 450 K (RT). (b) Temperature dependence of the forward and backward coercive fields during the warming from 8 K to 450 K. Both evolutions present an exponential decay with temperature, as their linear behaviors in this semilogarithmic scale representation demonstrate. (c) Detailed temperature dependence of the exchange bias field used to identify temperature range with both negative ($T < 70$) and positive ($T < 70$) exchange bias.

These are two cases where field-driven effects combined with temperature allow as to tune spin reorientations. Moreover, the asymmetric-field induced positive exchange bias above the Néel temperature is a surprise not yet reported.

#### 5.3.4.1 Field-induced positive exchange bias by asymmetric fields

In the previous section we have studied field-cooling effects at fixed angles, where a transition is observed at around the Néel temperature of $MnF_2$. Below this temperature, unidirectional anisotropy in the opposite direction to the cooling field appears, as a consequence of the frozen AFM moments at the interface, aligning antiparallel to the FM moments. However, at around the Néel temperature of $MnF_2$, the exchange bias field, $H_{EB}$ does not vanish, as it would be expected, but rather it change its sign to positive instead, i.e. the exchange bias field goes in the same direction as that of the cooling field, $H_{FC}$ (see figure 5.37).

Some other different tests have been done to ensure that the measurements are artifact free and reproducible (not shown).

This effect, although decaying with increasing T, does not vanishes at room temperature. Field dependent measurements were carried out at room temperature to probe this positive exchange bias. First, experiments varying the maximum external field applied, keeping the same field sweep rate (i.e. preserving the same dynamics) demonstrated a reduction of the coercive field as the maximum of the external field was increased. Second, as this was an indication that a positive exchange bias phenomena could be present, asymmetric field ramps where used to confirm the effect and the direction of the exchange bias shift.

In figure 5.38 we see the reduction of coercive field as the maximum of the external field is increased. Low values of external field appear in violet, and higher values in black, with a medium term in red. Top left plot of figure 5.38 shows the symmetric field sweeps applied, all of them sharing the same slope, i.e., the same dynamics or field change rate. In top right plot, the corresponding hysteresis loops can be seen, where higher coercive fields corresponds to violet loop, that is, the loop for which lower maximum field value was applied. Bottom plot in 5.38 shows the evolution of $\mu_0 H_C$ with increasing maximum field value, having linear behavior with negative slope.

Comparison of this $Co/MnF_2$ behavior with other model systems studied, such as Co/NiO [168] allows as to see the difference: while the former presents a negative slope, the last one presents positive.

Decreasing of the coercive field with increasing external field is an indication that exchange bias can be induced by applying asymmetric field sweep, in the following way: as loops starting at higher fields will have an associated transition field happening at a lower coercive field, and loops starting at lower fields will have an associated transition field happening at a higher coercive field, we could combine both cases by starting the forward branch at higher fields ending at lower fields, so that the corresponding backward branch starts at that lower field, and ends at the higher one. The forward branch will present lower coercive field as the backward, and the loop should

be shifted to the right. In other words, asymmetric field sweep shifted to positive values should generate right-shifted hysteresis loops, which is referred to as field-induced positive exchange bias.

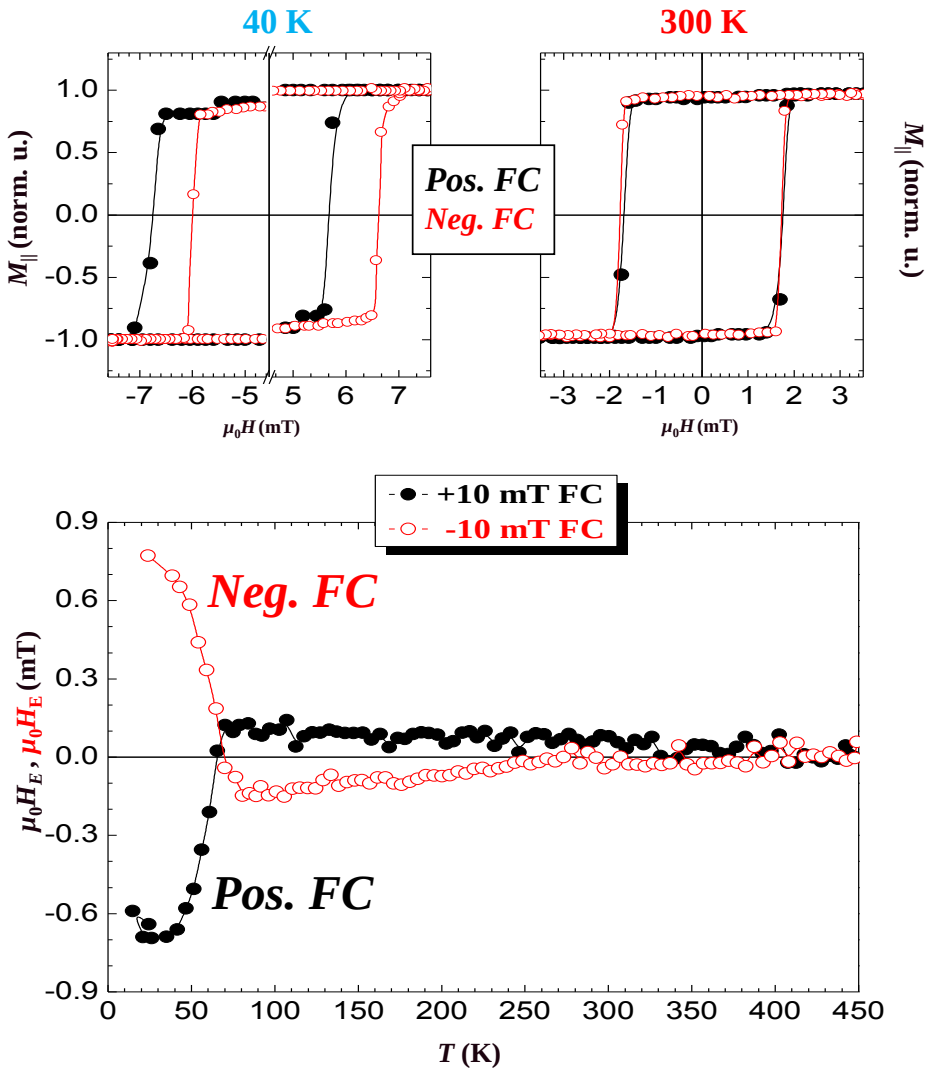


Figure 5.37: Selected hysteresis curves acquired below (a) and above (b) the critical temperature after positive (black filled symbols) and negative (red open symbols) FC procedures from 450 K to 8 K in the presence of an external magnetic field of +10 mT and -10 mT, respectively. (c) Comparison of the exchange bias field obtained after positive and negative FC procedures. Note the symmetric behavior between the opposite FC procedures.

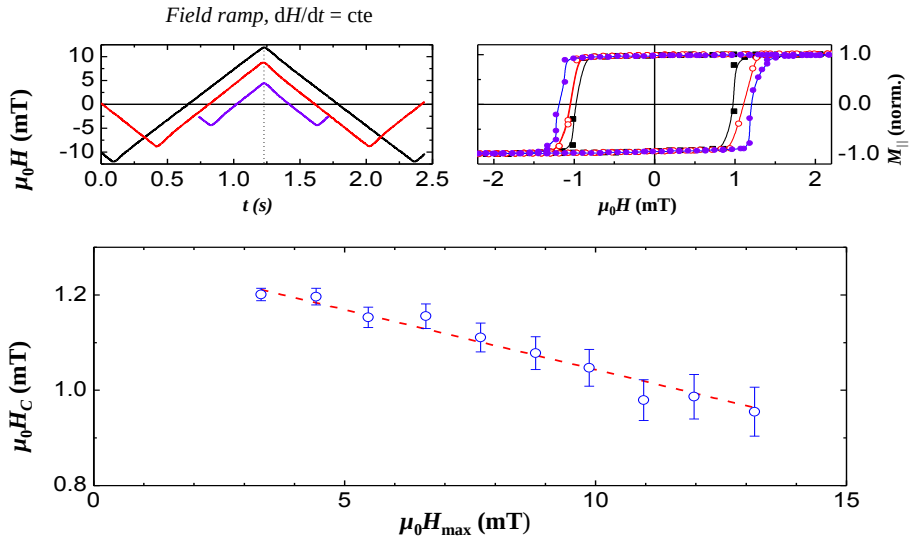


Figure 5.38: The coercive field $H_C$ decreases as $H_{MAX}$ increases. Note that this is the opposite trend with respect to other FM/AFM systems with standard negative exchange coupling [168].

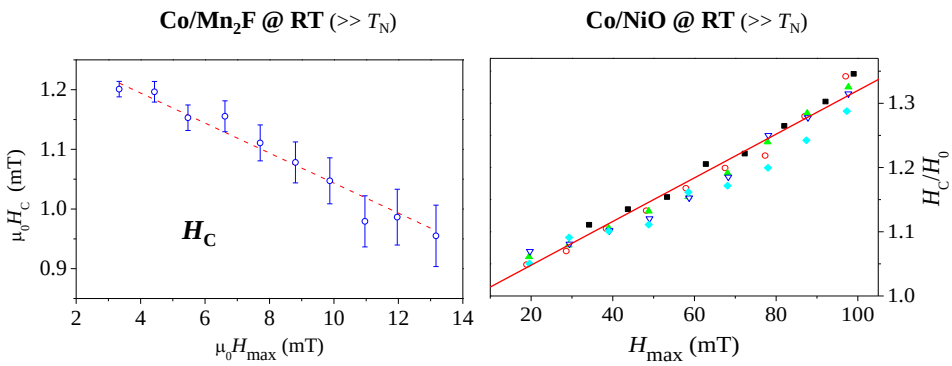


Figure 5.39: Coercive field evolution of $Co/MnF_2$ (left plot) and Co/NiO (right plot) with increasing maximum external field. The slopes are opposite.

Measurements with asymmetric external field where carried out at two temperatures. In figure 5.40 black color corresponds to loops acquired at 300 K and red corresponds to 400 K. On the left column, the hysteresis loops are depicted for negative-shifted asymmetric external field sweep (upper plot) zero shifted field sweep (middle plot) and positive-shifted asymmetric external field sweep (lowest plot). The corresponding field sweeps are plot in the column to the left. Notice that loops are shifted

in the same direction as the field sweep.

In figure 5.41, the Exchange Bias $H_E$ is now depicted, as a function of the maximum of the field, i.e., horizontal axis represent the maximum (positive or negative) field value, going from -11 mT upt to +11 mT. $H_E$ increases linearly as the maximum of the external field increases, indicative of a positive field induced exchange bias effect. Interestingly this effect is happening above the Néel temperature, without previous field cooling conditions. The asymmetric cycle must be acting as FC effect, as if the FC were happening between both extremes of the cycle. With the particularity that the direction of the induced EB is the same as the field shift.

It has been shown that at strong field coolings regimes, the EB below Néel temperature shows a similar positive EB effect, which is associated with antiparallel coupling at the interface [66]. The reason why we can reproduce a similar behavior at room temperature by using asymmetric field sweep relays on the external field capable of breaking the antiparallel coupling between some of the FM/AFM moments, at weak coupling regions of the interface, that becomes frozen upon reversing the field, promoting the positive exchange bias. To clearly disentangling this requires element sensitive techniques for the study of magnetic moment distributions during the reversal, and this will be shown later.

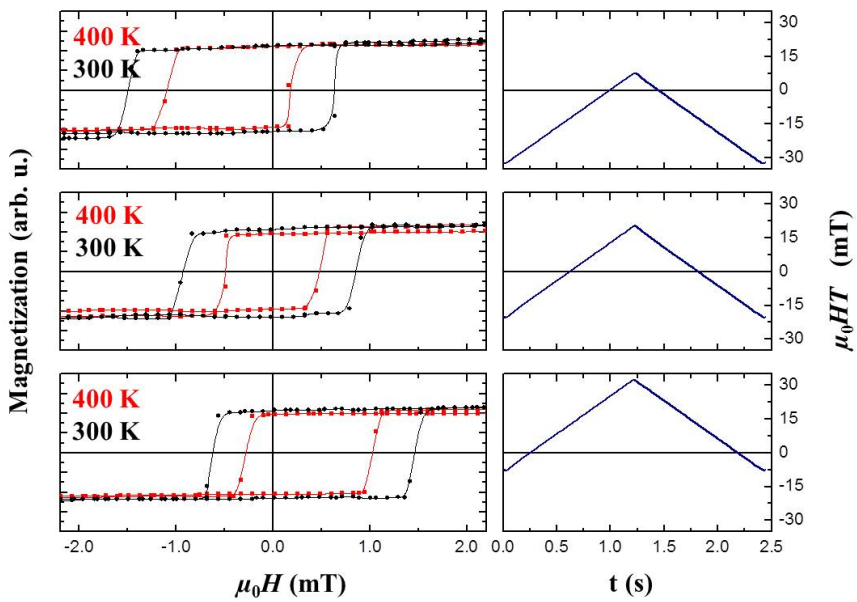


Figure 5.40: Asymmetric cycles show a shift of the hysteresis loop (i.e., $H_C$ not null). EB appears in the direction of the maximum field, indicative of positive EB. Coercive Field lower for higher maximum fields.

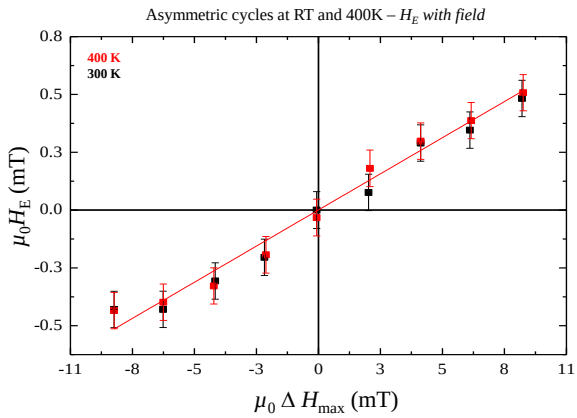


Figure 5.41: Asymmetric cycles show a positive linear behavior of $H_E$ as a function of the $\Delta H_{MAX}$. Note that this is the opposite behavior found in FM/AFM systems with standard negative exchange coupling [168].

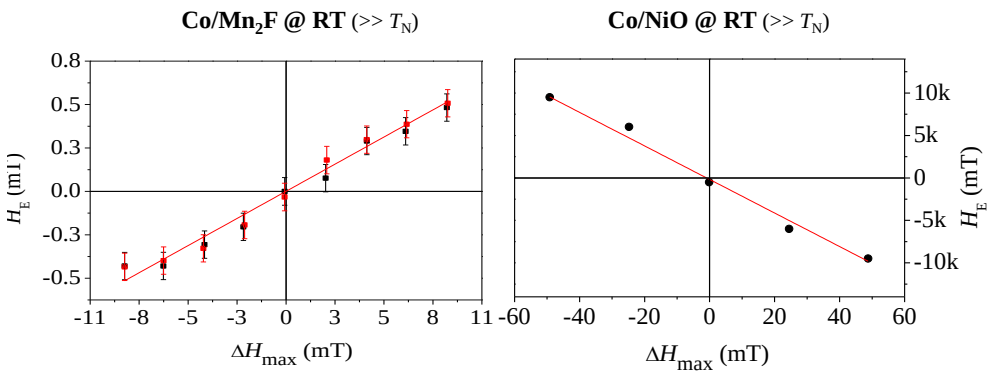


Figure 5.42: Exchange Bias field evolution of $Co/MnF_2$ (left plot) and Co/NiO (right plot) with increasing maximum external field. The slopes are opposite.

#### 5.3.4.2 Field cooling induced magnetic anisotropy

Field cooling at different directions are used here to study spin reorientation phenomena induced by proximity effects at the interface between the FM and AFM layers in the $Co/MnF_2$ bilayer heterostructure. The final magnetic symmetry in this system is directly linked to the underlying complex structure of $MnF_2$, [170].

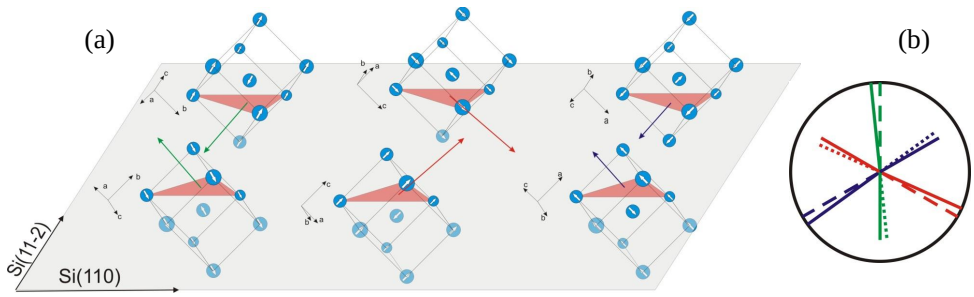


Figure 5.43: Crystal and spin configuration of antiferromagnetic epitaxially grown $MnF_2$ on Si(111). Two different sets of three crystal antiferromagnetic distributions are depicted in (a). The projected directions for the spins directions are depicted in the circle (b), after neutron studies [170].

In figure 5.43, the result of neutron studies shows the existence of a structure consisting of two trigonal domains, slightly rotated one with respect to the other, constituting twins.

On this trigonal antiferromagnetic crystal, the antiferromagnetic configurations that might be induced upon FC process down to below the $MnF_2$ Néel temperature will promote a variety of EB effects and magnetic symmetries. In the following sections, FC induced phenomena is explored for the different samples of table 5.5.

#### 5.3.4.3 $5nmCo/10nmMnF_2$

A first test at room temperature was made for this sample (with 5nm of Co and 10nm of $MnF_2$), where hysteresis loops where measured at 30 mT of field amplitude, and 4 Hz of field sweep frequency. Linear plot with error bars are depicted in figure 5.44. Experimental data are represented with filled symbols, while B-Spline based fit are shown in continuous lines. Coercive field presents an asymmetric 4-fold symmetry, where the maximums at 0° and 180° are higher than those at around 90° and 270°. This symmetry is assimilated to 2-fold, with anomalous coercive enhancement located at the hard axis, a behavior already reported [173, 174]). Notice that there is a slight shift with respect to the reference directions stated, of around +5° in all the axes, that must be observed by looking to the experimental points, and not to the B-Spline curve, which at this point can lead to mistakes. The exchange bias field $H_E$ has some structure, but the B-Spline fit lays well inside the error bars, and in purity nothing should be said about this $H_E$ structure, but only that is simply zero. In spite of this, when seen in polar plot, it looks like if some traces of 6-fold symmetry were present. Polar plots of both $H_C$ and $H_E$ can be seen in figure 5.45, with the same symbol/lines convention as in previous figure. Here a 6-fold distribution of lobes can be seen in $H_E$, where the significant directions would be 30°, 90°, 150°, 210°, 270° and 330° , with the aforementioned +5° shifts. Despite this 6-fold distribution of lobes at this angular positions, no change of sign in $H_E$ from the angles around those directions with respect to their opposite ones is appreciated, thus the condition necessary to claim for Exchange Bias is not fulfilled, with the exception of at 180° direction, where

the sign changes with respect to 0°, i.e. while at 0° there is an inward lobe (valley), at 180° we have an outward lobe (hill). This is the landmark of EB. In fact, the shaded region in $H_E$ polar plot of figure 5.45 corresponds to regions where there seems to be EB. Unfortunately, there are just a few points in those regions, and claiming for exchange bias cannot be done.

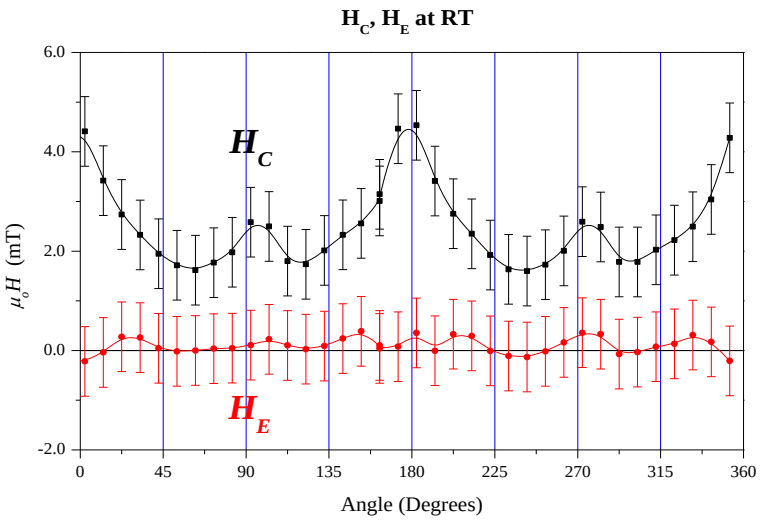


Figure 5.44: Linear plot of $H_C$ (in black) and $H_E$ (in red), for Co/$MnF_2$ 5nm/10nm at RT. Notice four non-equivalent local maximums in $H_C$, corresponding to 2-fold (uniaxial) symmetry with anomalous behavior at hard axes (as reported in [173, 174]). $H_E$ could be said to have no structure inside the error bars.

We carried out field cooling processes to examine field induced magnetic symmetries. Starting at 0°, we proceed to cool down the system under field cooling conditions at different reference angles. In figure 5.46, the reference directions for both positive and negative 90 mT Field Cooling are shown, at the easy axis direction (red line in figure), and 30° and 60° out of it (orange and green).

In figure 5.47, angular evolutions of $H_C$ (black plots) and $H_E$ (red plots), with symbols for experimental data and lines for B-Spline fit, taken at 20 K after 90 mT positive (upper plot) and negative FC (lower plot) are shown. While in this linear plot $H_C$ looks similar as at RT in both cases (compare with figure 5.44), $H_E$ presents now a clear EB behavior, where the EB for each angle is opposite in sign with respect to the corresponding opposite one. Changing the FC sign (equivalent to changing its direction), makes $H_E$ curve to convert into its point-symmetric image with respect to the center. In addition, three domes and three valleys are indicative of 3-fold symmetry in $H_E$. This is easier to see in the polar plots of figure 5.48, where the 3-fold symmetry appears as a 3-lobe regions separated by around 120°. Although the linear plot for $H_C$ looked 2-fold symmetry, its polar plot reveals a 6-fold symmetry, with non equivalent axes: the axis at 0° looks stronger than the other two axes, that

can be seen as 4 less pronounced lobes located at 60°, 120°, 240° and 300° from the 0° direction. In consequence, $H_C$ and $H_E$ are both consistent with trigonal underlaying structure with EB aligned in one of the trigonal directions.

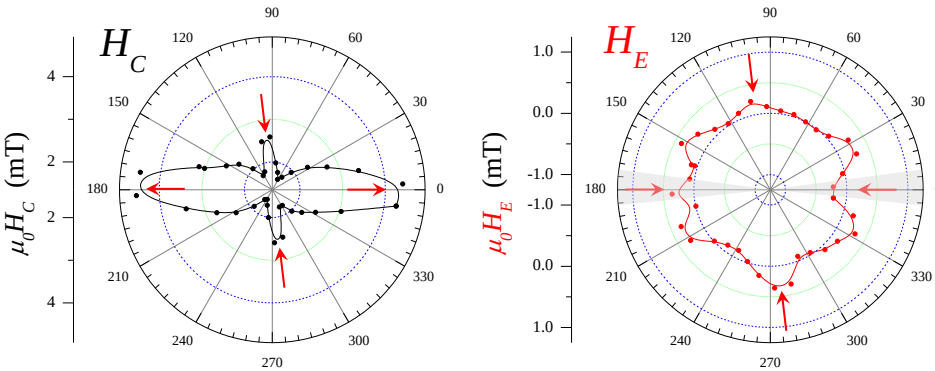


Figure 5.45: Polar plot of $H_C$ (left plot, in black) and $H_E$ (right plo, in red) corresponding to figure for 5.44. Experimental data are represented with filled symbols, while B-Spline fit is shown in continuous lines. Non equivalent and almost orthogonal easy axes can be seen in $H_C$, red arrows, while $H_E$ seems to exhibit 6-fold symmetry, which would be a direct manifestation of the underlying $MnF_2$ trigonal antiferromagnetic structure. However, a closer look into $H_E$ shows that the angle where the sign changes with respect to its opposite direction is 0°, 180°.

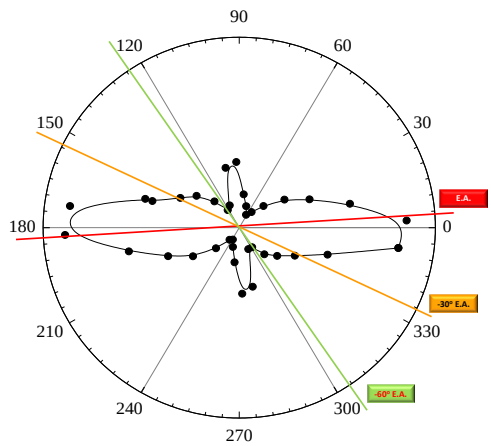


Figure 5.46: Reference directions taken from $H_C$ angular evolution for the subsequent positive and negative 90 mT Field Cooling investigations. The angles selected are the easy axis direction (red line in figure), and 30° and 60° out of it (orange and green).

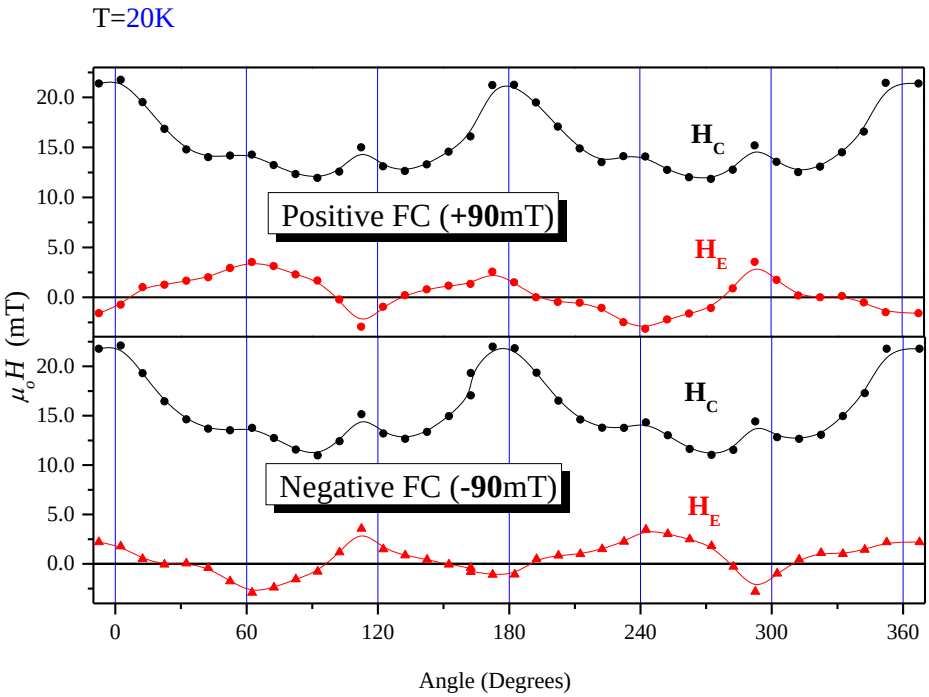


Figure 5.47: Linear plots of angular evolution of $H_C$ (black) and $H_E$ (red) at 20 K after field cooling of 90mT (upper plot) and -90 mT (lower plot) in the easy axes direction. Notice 2-fold symmetry of $H_C$ in both cases, and trigonal structure of the exchange bias field $H_E$. Remarkably the EB effect is opposite when cooling field sign is reversed (equivalent to doing 90mT FC at 180° from the initial direction).

Additional FC processes at representative directions of -30° and -60° off axis have been done, marked with orange and green lines in figure 5.46. In figure 5.49 we have incorporate linear and polar plots for $H_C$ and $H_E$ at the three positive FC directions explored, 0°, -30° and -60° (the first one has already shown in previous discussion). The same convention for plots is used, symbols for experimental data, lines for B-Spline fits, black color for $H_C$ and red for $H_E$. Upper plots corresponds to 0°. middle plots to -30° and lower plots to -60° positive FC. FC value of +90 mT has been used in the three cases. Red, dark yellow and green vertical thick arrows are set at the corresponding FC angles, while horizontal red arrow is set to emphasize the negative value of $H_E$ at those directions, in accordance with negative EB phenomenology. Additional vertical dashed arrows have been set in $H_C$ for the explanations.

The first observation arises when following the vertical dashed arrows in soft blue and violet. Soft blue arrows have been set to localize the lower lobes (or peaks) in the linear plots, and the violet ones to point at the higher lobes. When FC is applied at E.A. (upper plots), the lower and higher lobes in the linear plot are separated by around 60°, in a 6-fold symmetry with non equivalent axes. The soft blue arrows aims

at the weaker axes.

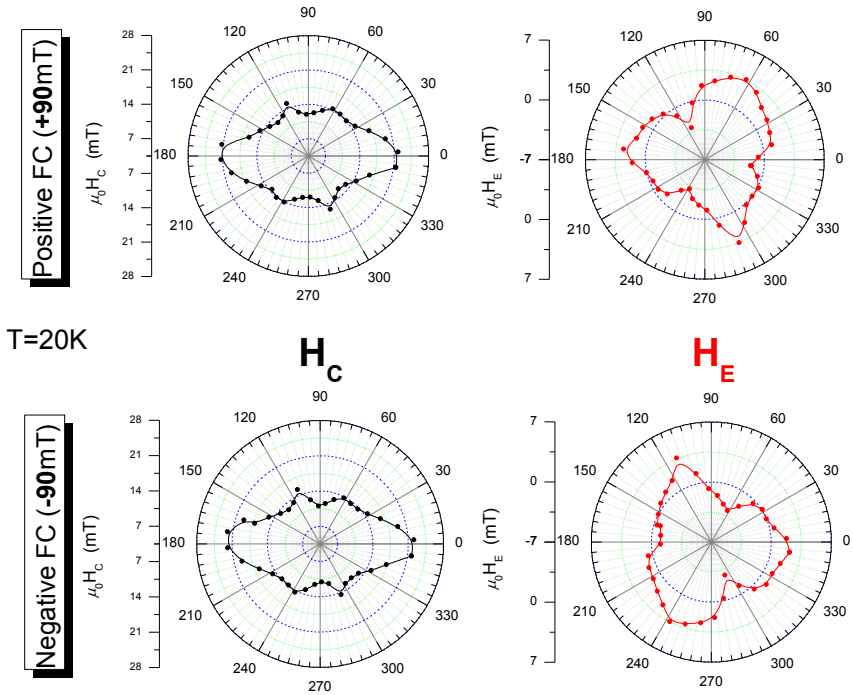


Figure 5.48: Corresponding polar plots for the same FC process as in figure 5.47. Upper and lower plots correspondsd to positive and negative 90 mT FC. Left plots represent $H_C$ while right plots are for $H_E$. Note that $H_C$ now seems to have some trigonal reminiscence, with small lobes at 60°, 120°, 240° and 300°, yet is globally 2-fold. Trigonal structure of $H_E$ is clearly seen here.

The corresponding polar plot of $H_C$ exhibits the aforementioned symmetry (already described with figures 5.47 and 5.48. When FC is applied at -30°, soft blue arrows show how the axis at 60° becomes even weaker, while the axis at 120° shifts to the left, that is, migrates backward towards angle 90°. In Polar plot for $H_C$, the effect is clearly seen, the looks to be loosing 6-fold symmetry. $H_E$ retains in both cases the 3-fold symmetry, with lobes at 60°, 180° and 300°, but is globally biasing towards direction 120°. This is signaled with two dashed green arrows in the polar plot of $H_E$, to emphasize the biasing direction of $H_E$, and with two dashed orange arrows in the same plot to emphasize how the corresponding 60° and 150° lobes are suffering an slight enhancement. When the FC is applied at -60° from E.A. (lower plot), the biasing of the $H_E$ is dramatic, the symmetry could be said to be 1-fold, with some internal structure. The main direction for EB is now somewhere around 110°. Linear plots exhibit 4-fold symmetry with non equivalent axes, weaker axis being the result of the shrinking of the corresponding two weaker axes appearing at FC 0° and

-30°. If we obviated the weakest axis for the case of FC at -60°, we could talk about an evolution of $H_C$ trigonal to uniaxial, and an evolution of 3-fold in $H_E$ to 1-fold. Putting the correct labels to the symmetries thus described is a bit compromised. The important message here is that we tune trigonal things into unidirectional by changing the FC angle.

#### 5.3.4.4 $5nmCo/20nmMnF_2$

Room temperature test angular measurement were carried out with 30 mT of field amplitude, and 4 Hz of field sweep frequency. Linear plot with error bars are depicted in figure 5.50. Coercive field presents 2-fold symmetry, and $H_E$ is almost null, yet it presents some structure which is now not so clearly inside the error bars. In the polar plot shown in figure 5.51, $H_C$ and $H_E$ can be seen in two different scales, aimed at showing the uniaxial symmetry and emergence of a trigonal structure respectively. Again $H_E$ trigonal structure cannot be surely asserted as it is very close to the resolution of the instrument.

A comparison of RT measurements for both samples with respective $MnF_2$ of thicknesses of 10nm and 20nm is shown in figure 5.52. Notice the same order of magnitude of $H_{C,MAX}$, but a higher value for $H_{C,MIN}$. The symmetry is preserved and the anomalous effects at hard axes seems to be disappearing.

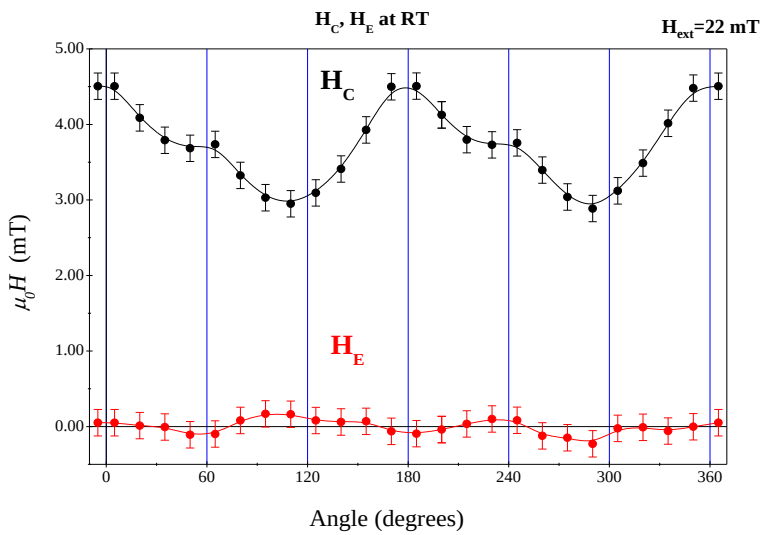


Figure 5.50: Linear plot of $H_C$ (in black) and $H_E$ (in red), for Co/$MnF_2$ 5nm/20nm at RT. Notice 2-fold (uniaxial) symmetry in $H_C$, and an almost null EB in $H_E$, however some structure is more noticeable.

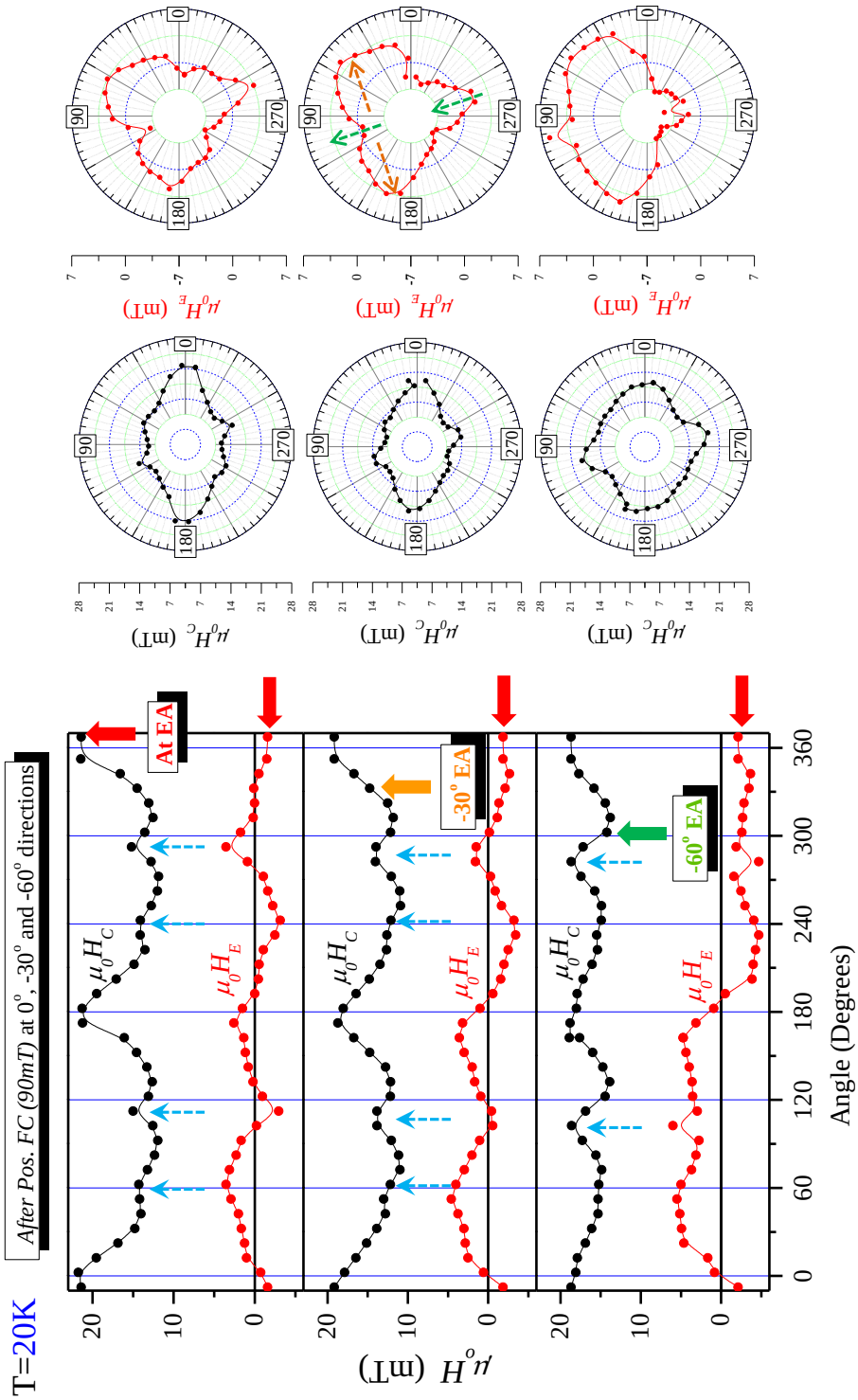


Figure 5.49: Explanation on main text.

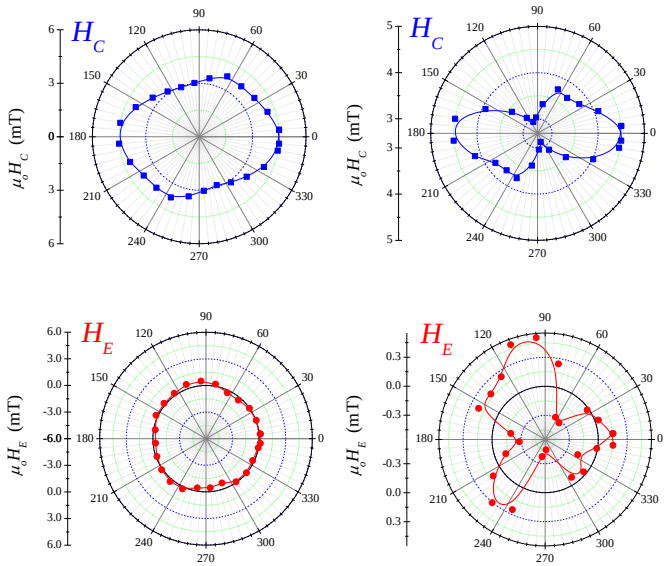


Figure 5.51: Polar plots of $H_C$ (in black) and $H_E$ (in red), for Co/$MnF_2$ 5nm/20nm at RT, with two different scalings, left and right, set in this way to notice the 2-fold (uniaxial) symmetry in $H_C$, and an almost null EB in $H_E$, but with a more clear trigonal structure.

When FC process is carried out with 30 mT in positive direction, the resulting symmetry in $H_C$ remains 2-fold, with no traces of any anomaly at the hard axes, and the axes positions are the same as at RT. But $H_E$ presents a standard negative exchange bias which is unidirectional. In figure 5.53, the linear plots of both $H_C$ and $H_E$ transition fields are depicted for temperatures of 10 K and 30 K. Comparing this $H_E$ symmetry with that of the sample with only 10 nm of $MnF_2$ at 20 K after field cooling at easy axis, figure 5.49, it can be seen that while for the sample with thinner $MnF_2$ layer the exchange bias structure is trigonal, for the thicker one it has become unidirectional. This is an indication of the dependence of interface effects on layer thickness.

In figure 5.54 the temperature evolution (on increasing temperature from below $T_N$, after the 30 mT of FC at easy axis direction) of the angular dependent transition fields is shown for temperatures 10 K, 30 K, 60 K, 80 K y RT, where the symmetry in $H_C$ seems to be going from 2-fold (1-fold $H_E$ symmetry) at 10 K and 30 K (black and red plots) to non-equivalent 4-fold symmetry, in the region right above $T_N$, i.e. 60 K and 80 K, ending up in a 2-fold at RT. This behavior is still today under study, since the non-equivalent axes of the 4-fold symmetry seen near $T_N$ does not seem to be a hard axes anomalous effect as mentioned at the begining. Evolution of $H_E$ is more drastic, with a flat evolution at all temperatures above $T_N$, and a 1-fold below.

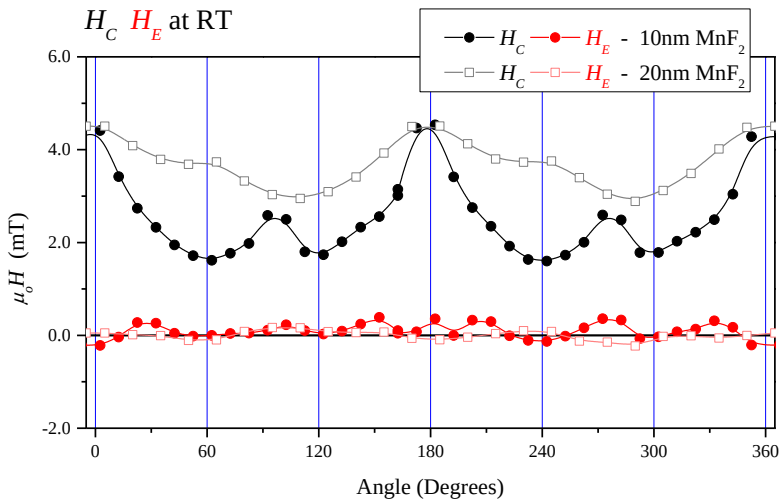


Figure 5.52: Comparison of samples $5nmCo/10nmMnF_2$ with $5nmCo/20nmMnF_2$, at RT. Although the symmetry in $H_C$ is the same in both samples, the sample with thicker $MnF_2$ layer presents a reduction or softening of the angular evolution, keeping the maximum coercive field value, but increasing the minimum value.

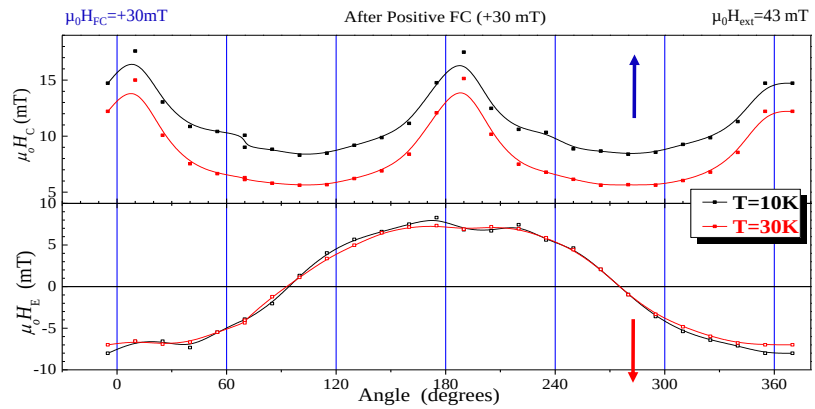


Figure 5.53: Angular evolution of $H_C$ and $H_E$ at 10 K and 30 K, for sample $5nmCo/20nmMnF_2$, where clear unidirectional symmetry can be seen: $H_E$ is 2-fold and $H_E$ presents is 1-fold symmetry. While coercive field increases with decreasing temperature (as expected for thermal activated reversal processes), the shift remains almost constant.

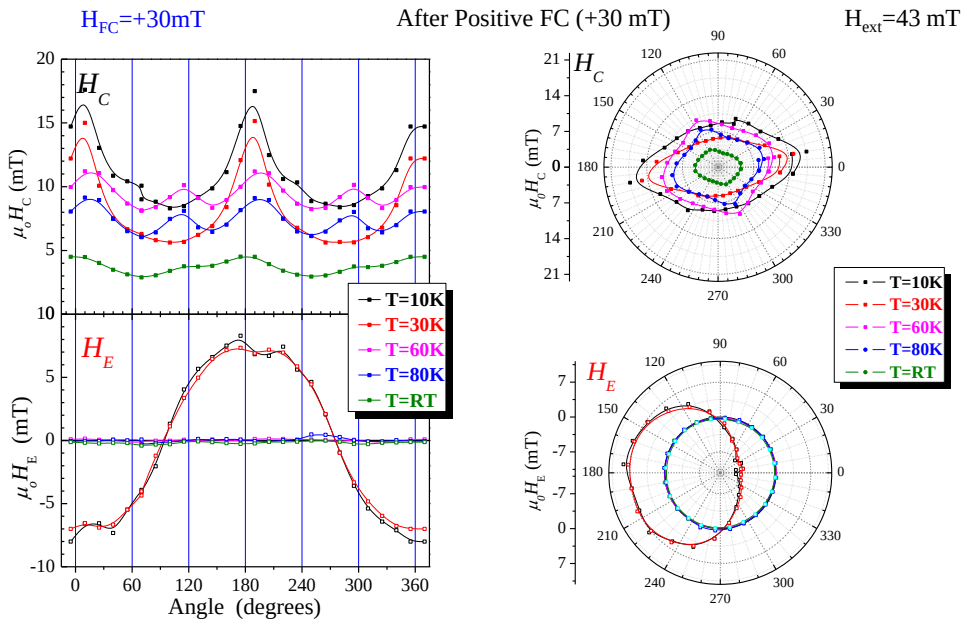


Figure 5.54: Temperature evolution of the angular dependent coercive field and exchange bias field (upper and lower plots respectively) in linear representation and polar plots (left and right plots respectively), for $5nmCo/20nmMnF_2$. Notice that basically $H_C$ preserves its symmetry at all temperatures, with special features at 60 K and 80 K at hard axes, and $H_E$ presents a dramatic evolution from 1-fold below $T_N$ to isotropic (flat curves) above it.

### 5.3.5 Investigation of interface coupling with element selective techniques

In order to determine the coupling at the $Co/MnF_2$ interface, XMCD technique were used at different synchrotron radiation laboratories, APE beamline at ELETTRA (Italy), BL7A at the Photon Factory (Japan) and BL25SU at SPring8 (Japan). In figure 5.55, the XMCD curves (difference between the absorption curves taken with left circularly polarized X-ray beam and right one) around Co and Mn L2,3 edges are shown (left and right plots respectively), for room temperature (RT label, red curves in the figure) and around 15K (LT label for low temperature, blue color in the figure). The different sign of the XMCD signal between Co and Mn is indicative of antiparallel alignment of the magnetic moments. The XMCD curves were taken at a saturation state, so that uncompensated Mn magnetic moments could be present at the interface, coupled to the Co interface moments. Otherwise an antiferromagnetic fully compensated configuration in $MnF_2$ would make magnetic moments invisible to the technique. Those uncompensated moments at the interface are responsible for the Mn XMCD signal, and the peak sign in Co are opposite to those of Mn, indicative of antiparallel alignment.

In figure 5.56, hysteresis loops obtained with XMCD for both Co and Mn at RT

(left plot) and at LT (right plot) respectively, are shown. Notice that the uncompensated rotatable Mn moments at LT follows, with the opposite sign, the same hysteresis loop as Co, indicative of dragging effect of the Co moments at the interface and the Mn rotatable ones. At RT the same dragging effect is seen, although no AFM magnetic order is present. Exchange coupling is strong enough to produce the dragging effect, so that rotatable moments at the interface manage to follow Co moments. However, the magnetization in Mn has the opposite with respect to Co magnetization. This is a confirmation of the antiparallel alignment of the magnetic moments of Co an Mn at the interface.

In order to confirm the RT field induced positive exchange bias, RT XRMR (X-ray Resonant Magnetic Scattering) technique were used at SOLEIL and ELETTRA synchrotrons [not published], trying to obtain the in-depth profile of Mn magnetic moments, with limited success. This technique is complex, and no definitive results have still been agreed. Nevertheless, confirmation of field dependent effects can be observed through the XRMR signal at remanence after 3 and 7 Tesla of saturating magnetic field.

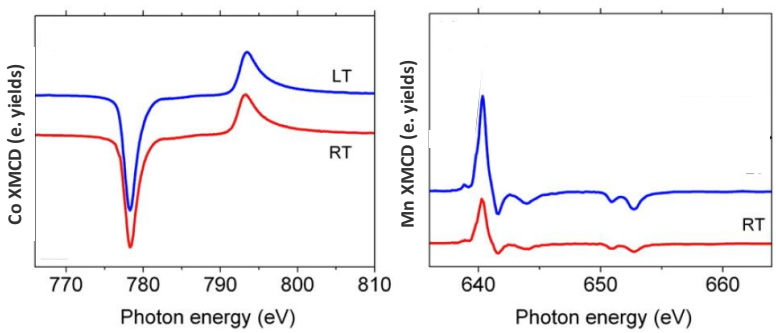


Figure 5.55: Antiparallel coupling at the interface can be seen through XMCD at L2,3 Co (left) and Mn (right) edges, for $5nmCo/20nmMnF_2$ sample. Both low temperature (LT) and room temperature (RT) can be seen in blue and red color in this figure for both Co (left) and Mn (right). Notice the change of sign between Co and Mn, indicative of the antiparallel alignment of the uncompensated Mn moments at the interface.

In figure 5.57, the results are shown. Blue XRMR signal corresponds to remanence after 3 T of positive saturating field, and red XRMR signal is the corresponding one but with 7 T. Both signals are clearly different. Higher red signal is indicative of higher Mn magnetic moments present at remanence, and those moments must be pinned by some mechanism in the field direction, otherwise the moments in the AFM which is at a temperature above $T_N$ would disorder, giving zero XRMR signal. As higher value of remanence corresponds to higher saturating field, this means that increasing external field will increase pinned population in the field direction, which is precisely the direction in which Co is aligned. The antiparallel coupling in between then will facilitate the reversing of the Co moments if the field begun to sweep to negative values, reducing the coercive field of the forward branch and then, producing the

positive shift of the loop, i.e., the positive exchange bias.

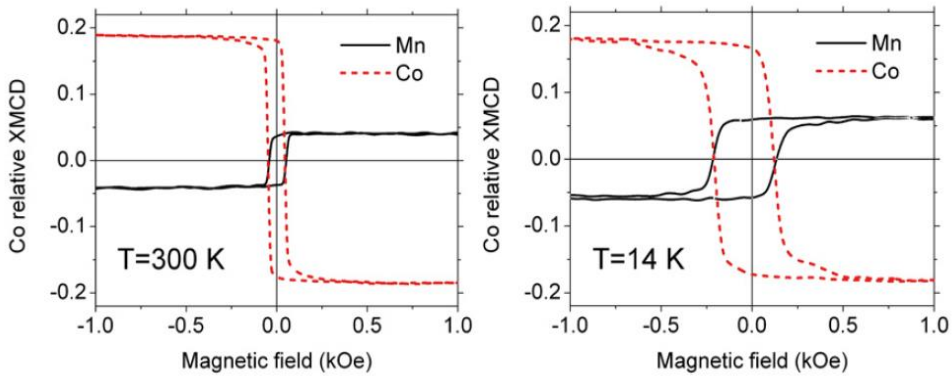


Figure 5.56: XMCD hysteresis loops for both Co (black line)and Mn (red dashed line) at RT (left plot) and at LT (right plot) respectively, are shown. Notice that the uncompensated rotatable Mn moments at LT (right plot) follows those of Co, but with reversed direction. The same happens at RT (left panel), even thought no AFM magnetic order is expected.

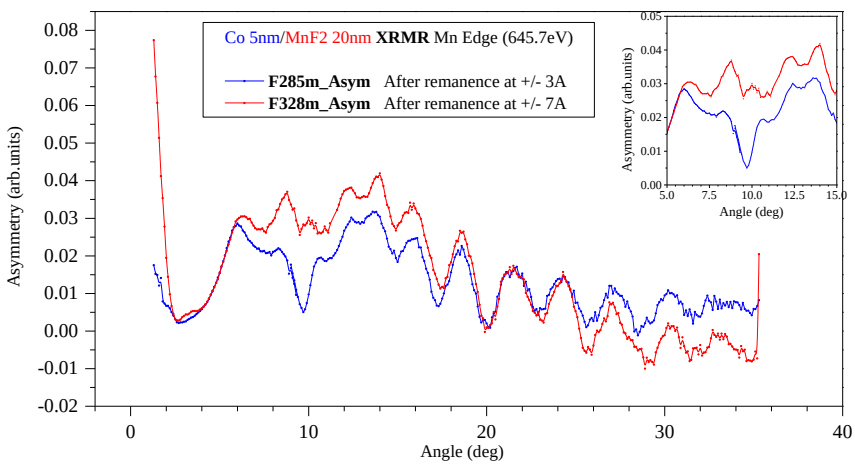


Figure 5.57: XRMR signal at Mn L2/L3 edges. at two remanence states, after 3 T saturating field (blue curve) and 7 T (red curve). The higher the saturating field, the higher the XRMR signal, indicative of increasing magnetic moments contributing to it. This is indicative of more pinned Mn moments at the interface, lined up with the field direction. This in turns reduces the reversing energy for the Co, as the interface coupling is antiparallel.

### 5.3.6 Conclusions

We have probed exchange anisotropy originated at the interface of $Co/MnF_2$ bilayer heterostructure. We have found that the coupling between the FM and AFM at the interface is antiparallel. Transition from negative to positive exchange bias behavior has been found as temperature increases from low temperatures and crosses a critical value of 70 K, close to the ordering bulk Néel temperature of the AFM layer. Remarkably, positive exchange coupling effects persist up to 450 K. In addition, positive exchange bias can be induced by field at temperatures above $T_N$, where no magnetic order in the AFM layer is expected. We have probed the system with element sensitive X-Ray techniques to address interface coupling and positive exchange bias, as well as in-depth profile of the antiferromagnetic Mn. Very rich magnetic anisotropy symmetries and spin reorientation effects induced by Field Cooling have also been studied, that are associated to the underlaying trigonal structure of the $MnF_2$. It has to be noticed that our experimental findings are new in the context of exchange coupling phenomena in FM/AFM systems. All the concepts are grouped in the following:

1. *Negative Exchange Bias* below $T_N$.
2. *Negative to positive EB transition* across critical T=70 k (which persists up to 450 K).
3. *Novel Field-Induced phenomena* (well above $T_N$):
   (a) *Narrowing* of the hysteresis loop with maximum field ($H_C$ decreases as maximum field increases)
   (b) *Positive exchange bias* above $T_N$ induced by asymmetric field sweep.
4. *Antiferromagnetic* Coupling at the FM/AFM interface in Co/MnF2 bilayers, for $T > T_N$.
5. *Field Cooling* induced spin reorientation due to the underlaying $MnF_2$ trigonal structure, at temperatures $T < T_N$.

# Appendices

# A Magnetic anisotropy supplement

## A.1 Anisotropy energy expressions

Here some of the general ideas are introduced by using a cubic system as an example, and additional insight will be given during the rest of the chapters whenever the need appears.

The magnetic anisotropy internal free energy of cubic systems can be written as [53, 56, 58, 175, 176, 177, 57]:

$$F(\alpha, e_{ij}) = F_A(\alpha) + F_M(\alpha, e_{ij}) \tag{A.1}$$

Where $F_A$ is the magnetocrystalline anisotropy term and $F_M$ is the magnetoelastic term. They are given as functions of $\alpha$, representing the direction of M with respect to the orthogonal reference frame sitting on the cubic axes, and $e_{ij}$ representing the strain components.

We center now our attention in the magnetocrystalline term. For symmetry reasons in cubic systems, $F_A$ can be written as an expansion on the direction cosines in this way [52, 53]:

$$F_A(\alpha) = K_1 s + K_2 p + K_3 s^2 + ... \tag{A.2}$$

where s=${\alpha_1}^2{\alpha_2}^2 + {\alpha_2}^2{\alpha_3}^2 + {\alpha_3}^2{\alpha_2}^2$ and p=${\alpha_1}^2{\alpha_2}^2{\alpha_3}^2$.

$K_1$, $K_2$, $K_3$ appearing in this equation are the first, second and so on anisotropy constants in the expansion of the free energy for cubic systems.

Depending on the systems, the relevance of each term can vary. For instance, it has been already demonstrated that for Iron below room temperature, the second anisotropy constant $K_2$ in the expansion of the free energy is not relevant [177].

When going to the surface, it is generally agreed that a ratio between surface anisotropy constant and bulk one is of the order of 10, or in other words,

$$F_M(\alpha, e_{ij}) = 10 F_A(\alpha) \tag{A.3}$$

## A.2 Temperature dependency

The first approach to temperature dependency of magnetic anisotropy constant in cubic crystals was given by Akulov and Callen-Callen [52, 54] in a classical framework. They considered the first term in expression A.2 for the internal free energy, i.e, a quartic form on the direction cosines,

$$F_A(\alpha) = K_1({\alpha_1}^2{\alpha_2}^2 + {\alpha_2}^2{\alpha_3}^2 + {\alpha_3}^2{\alpha_2}^2) \tag{A.4}$$

They obtained a $10^{th}$ power law for $K_1$ as a function of M(T), after statistical arguments on a distribution of small regions in the crystal having small temperature dependent deviations from the anisotropy directions:

$$\frac{K_1(T)}{K_1(0)} = \left(\frac{M(T)}{M(0)}\right)^{10} \tag{A.5}$$

Zener [55] improved the model incorporating the second order anisotropy constants, $K_2$, with a functional of the direction cosines of the form

$$F_A(\alpha) = K_1({\alpha_1}^2{\alpha_2}^2 + {\alpha_2}^2{\alpha_3}^2 + {\alpha_3}^2{\alpha_2}^2) + K_2({\alpha_1}^2{\alpha_2}^2{\alpha_3}^2) \tag{A.6}$$

His method was again statistical, and obtained a $21^{th}$ power law for the second anisotropy constant. Both results have been enclosed under Akulov-Zener macroscopic classical theory, but are also standard to refer them as Callen-Callen theory.

The standard quantum-mechanical approach was given by Van Vleck [56, 57, 58], where temperature dependency of the macroscopic anisotropy was given by quantum statistical deviations of neighbor spins from the maximum alignment. He expanded the indirect anisotropy between neighbor spins in a dipole-dipole interaction term and a quadrupole-quadrupole one, and evaluated them in the frame of the molecular field, assuming complete lack of correlations. He obtained a too slow temperature dependence for $K_1$. Keffer and Oguchi [59, 60] recoverd the $10^{th}$ power law by using correlations in the framework of Spin Wave theory (SWT).

In addition, SWT allowed to account for a better aproximation of the magnetization at low temperatures than that of Mean Field Theory.

If we use for temperature evolution of M the frequently observed law of

$$\frac{M(T)}{M(0)} = \left(1 - aT^2\right) \tag{A.7}$$

we obtain the empirical results from Brükhatov-Kirensky [178] for ferromagnetic metals:

$$\frac{K_1(T)}{K_1(0)} = \left(1 - aT^2\right)^{10} \sim exp\left(-aT^2\right) \tag{A.8}$$

while if we use M predicted by SWT as

$$\frac{M(T)}{M(0)} = \left(1 - bT^{\frac{3}{2}}\right) \tag{A.9}$$

we obtain

$$\frac{K_1(T)}{K_1(0)} = \left(1 - aT^{\frac{3}{2}}\right)^{10} \sim exp\left(-aT^{\frac{3}{2}}\right) \tag{A.10}$$

Thus far we are mainly speaking of the bulk anisotropy. Deviation of this when the surface is present is a more recent matter, since it was not until the technology

allowed the production of low dimensionality systems that surface/interface effects could be studied.

The availability of computers to face the complexity of the problem have open the route to solve many phenomena at the surface.

For instance Yanes et al [61] developed a Constrained Monte Carlo (CMC) method to study thickness and temperature dependencies in nanostructures. The method is based on computing the torque as a function of an statistical average of the thermodynamical effect due to local variations of classical spins, under a model Hamiltonian, keeping magnetization fixed a t a certain angle with respect to one of the anisotropy axis. The simulation method provides the Torque as a function of the angle with respect to one of the anisotropy directions. The torque is at the same time related to the anisotropy constants, establishing the link between them and the simulations. As on the one hand, model Hamiltonian is split into bulk and surface contributions, which are in turn related to thickness and surface dimensions, and on the other hand, statistics is carried through a Boltzmann weight function, both thickness and temperature studies can be done. With this model, they have been able to confirm the different power laws already established, and some spin reorientation phenomena such as thickness and temperature dependence on the in-plane versus out-of-plane surface anisotropy, among others.

The law

$$K_{SURF} = 10K_{BULK} \tag{A.11}$$

is not a guarantee that the corresponding temperature dependence still follows the same factor, that is, the question is open to whether equation A.11 still holds when we substitute $K_{SURF}$ by $K_{SURF}(\mathrm{T})$ and $K_{BULK}$ by $K_{BULK}(\mathrm{T})$, or we rather should deal with something like this:

$$K_{SURF}(T) = f(T)K_{BULK}(T) \tag{A.12}$$

## A.3 Binek's figure of merit an other details on exchange bias

A global scheme of EB phenomenology can be seen in figure by C. Binek [179], reproduced here in A.1. His review article on the subject is a very complete reference material for exchange bias.

In figure A.2(a), an ideal exchange bias FM/AFM system is depicted to the left, for which the shift in the coercive field, $H_E$ or *Exchange Bias Field*, can be computed as

$$H_E = \frac{\Delta\sigma}{M_{FM}t_{FM}} \tag{A.13}$$

where $\Delta\sigma$ is the density of the interface exchange energy (that can be expressed in terms of the exchange coupling constant, the spins and the surface area), $M_{FM}$ is the saturation magnetization of the ferromagnetic layer, and $t_{FM}$ is the ferromagnetic layer thickness.

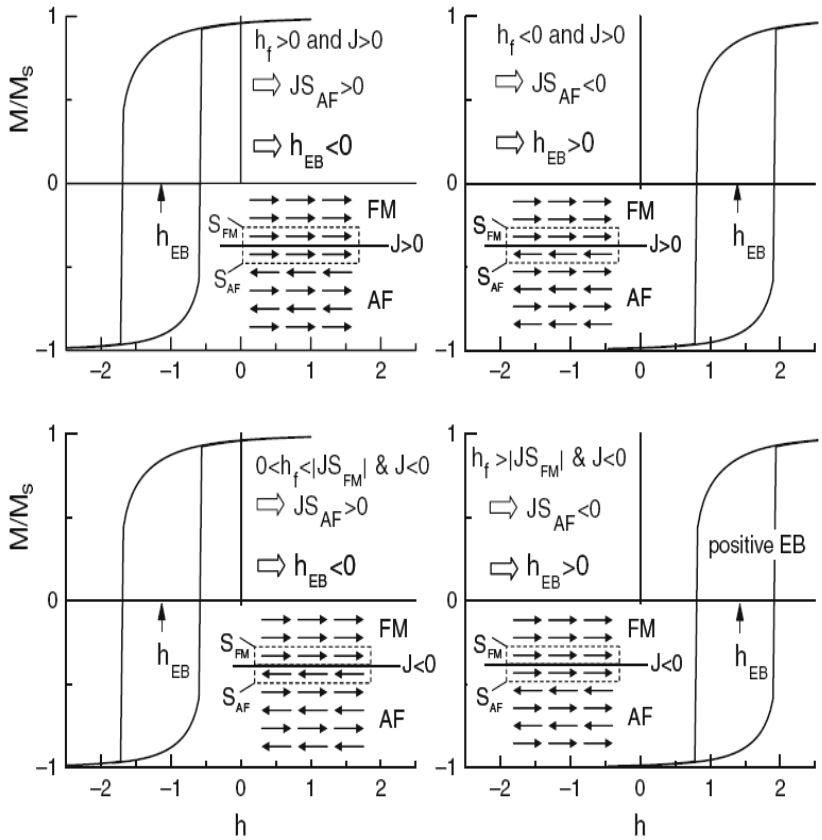


Figure A.1: Hysteresis loops of an ideal EB heterosystem with FM interface coupling $J > 0$ (upper left and right frames) and AF interface coupling $J < 0$ (lower left and right frames). For $J > 0$ (upper frames) negative (positive) EB fields $h_{EB}$ are indicated by arrows and achieved by field cooling in a freezing field $h_f > 0$ ( $h_f < 0$ ). For $J < 0$ (lower frames) field cooling in $0 < h_f < |JS_{FM}|$ creates a regular negative EB field while field cooling in $h_f > |JS_{FM}|$ gives rise to a positive EB field which is the fingerprint of the positive EB effect. The frozen AF spin structure and the FM spin structure during the field-cooling process are depicted by arrows. The ideal interface is indicated by a solid line, AF and FM interface spins are marked by boxes (dashed lines). [179]

In figure A.2(b) non-ideal EB system is depicted, where many effects such as magnetic frustration leads to asymmetries in the hysteresis loops, as illustrated in the introductory material in section 1.3, subsection 1.3.5. Calculations of the exchange bias field in this case becomes more complex.

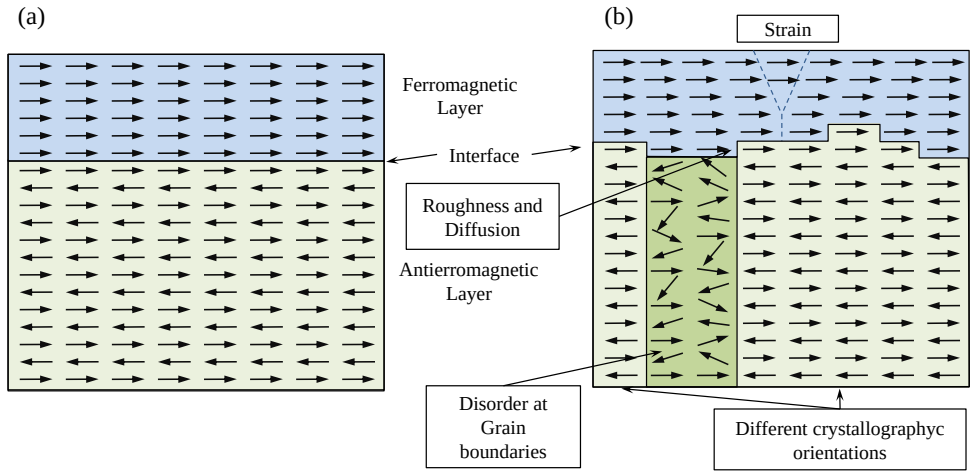


Figure A.2: Schematic view of the different effects that influence the exchange bias. (a) the ideal exchange bias FM/AFM heterosystem. (b) real exchange bias FM/AFM heterosystems with roughness and diffusion at the interface, different grain orientations in the AFM and boundary effects between grains. In epitaxially grown systems, grain effects are not expected to happen. However, interface features are unavoidable.

# B Hysteresis supplement

## B.1 Hysteresis and anisotropy

Hysteretic behavior is naturally linked to magnetic anisotropy. As anisotropy axes establish preferential directions for the magnetic moments to sit on, reversing the magnetization of a systems necessarily implies overcoming the extra energy provided by anisotropy. To illustrate how this translate into a hysteresis loop, let us think for a moment in a uniaxial system in which the external field is exactly applied in the anisotropy direction. Initially we apply the field in the positive direction. Then we reduce the field to zero and then to a negative differential value. If all the magnetic moments were free to follow the external field, and no anisotropy were present, at this point they would reverse to negative direction. As magnetic order imposes parallel alignment of the moments (due to exchange interaction), the magnetization would then be fully reversed at that point. A 180° switch of the magnetization vector has happened. When anisotropy is present, the energy that takes the moments to get out of the anisotropy direction will need to be overcome. The external field provides that energy, so that reversal of the magnetic moments happens after a certain additional negative field value is reached. That field is called (in this particular case) the anisotropy field, $H_K$. Once we overcome that field, the magnetization switches to the opposite direction. Now if we want to do the opposite external field sweep, the same phenomena happens but in the other direction. As a consequence, a plot of M as a function of the external field $H_{EXT}$ consists on an open loop, called hysteresis loop, that will have square shape. Notice that in this example, the only phenomena considered is uniform switching of the magnetization, where all the moments are either pointing to positive or negative direction.

In figure B.1 an oversimplified reversal of the magnetization in an ideal uniaxial anisotropy system (perfectly homogeneous at zero T) is illustrated for external field applied at the exact anisotropy direction. Significant points have been signaled, at the maximum field $H_{MAX}$ (positive or negative), zero field and at the coercive fields $H_C$, that have a letter as superscript to refer the pathway or branch where is located, F in the forward (field sweeps from positive $H_{MAX}$ to negative), and B in the backward (the other way around). Magnetic moments are positive aligned in the interval $H_C^F < H < H_{MAX}$, while they are negative aligned in the interval $-H_{MAX} < H < H_C^B$. This is because it takes an extra energy to overcome the anisotropy energy, so in the forward branch this extra energy leads to a reversal of the magnetization at the point $H_C^F$, which is negative. In the way back, the same happens, but now at a positive field value, $H_C^B$. In this particular case with $H_{EXT}$ at exactly parallel direction with respect to the anisotropy direction, $H_C$ is equivalent to $H_K$, the anisotropy field.

In the figure, perpendicular component has also been depicted in red (not explained in the figure caption), but it is null, the hysteresis loop consists only in parallel component in this case.

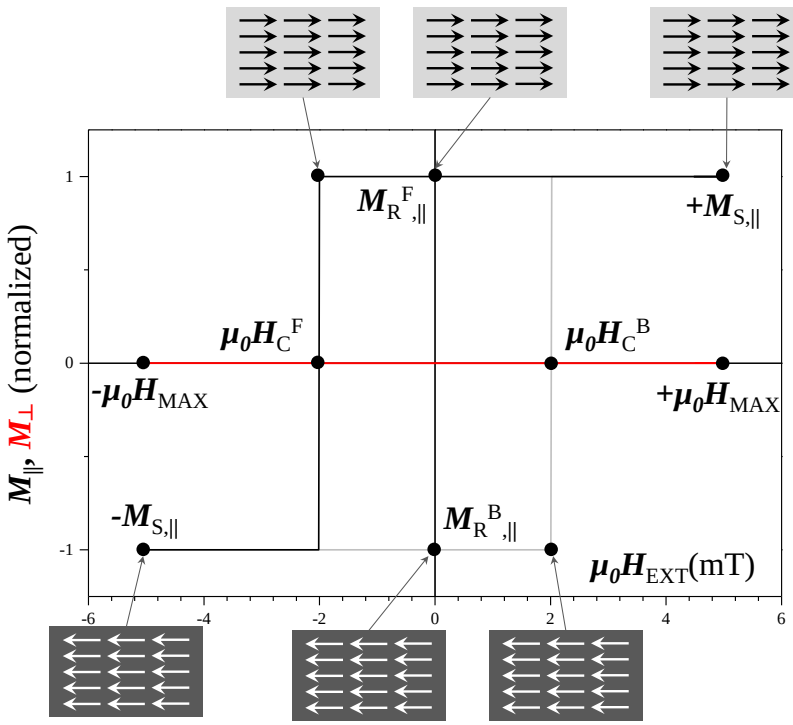


Figure B.1: In this figure, the reversal of the magnetization in uniaxial anisotropy system, where the external field is applied in the anisotropy direction, is illustrated to explain the origin of open hysteresis loops. Significant points have been located in the loop, at the maximum field $H_{MAX}$ (positive or negative), zero field and at the coercive fields $H_C$, that have a letter as superscript to refer the pathway or branch where is located, F in the forward, and B in the Backward. Notice that magnetic moments are positive aligned in the interval $H_C^F < H < H_{MAX}$, while they are negative aligned in the interval $-H_{MAX} < H < H_C^B$. Forward and backward branches have been depicted in black and gray respectively. $H_C$ in this particular exact parallel direction of $H_{EXT}$ to the anisotropy direction, is equivalent to $H_K$, the anisotropy field.

We note here that the coercive field, $H_C$, is in this case the point where the magnetization switches. We might feel cumbersome as we have previously stated that the true field at which magnetization switches is $H_S$, which is defined on the perpendicular component of the magnetization. The reason is that in this case, at the exact anisotropy axis, perpendicular component is zero and there is no possibility of defining $H_S$ through it. Instead, the switching of the magnetization exactly coincides with $H_C$, so one can say that in this case $H_C = H_S$. In the next section, where

angular dependencies are going to be examined, it will be shown that this same thing happens for certain angular ranges. This kind of "dancing" between $H_C$ and $H_S$ is not unusual in magnetism and the risk exist for mixing up concepts.

## B.2 Reversibility

It can be seen that if we reverse the field sweep direction from forward to backward at any point between $H_C^F$ and $H_{MAX}$ in figure B.1, the magnetization will follow the same pathway back to $M_S$. This means that in the region $H_C^F < H < H_{MAX}$, the reversal process is reversible. However, once we surpass $H_C^F$ in the forward direction, reversing the field sweep will make the magnetization to follow a different path, the backward branch depicted in gray in figure B.1. We then say that the system has suffered an irreversible transition, which in this case is an abrupt jump at $H_C^F$.

In general, reversible processes are associated to coherent rotation (or rotative process) of the magnetization. For instance, in figure 1.8 of section 1.4.1 in the introduction, in the shaded regions the magnetization is following the unit circle ($M$ is normalized in this graph), i.e. is rotating and this is a reversible process. The lines appearing in this polar plot that crosses from one shaded region to another one, on the other hand, correspond to irreversible processes where, once the jump has been produced, there is no way for the magnetization to go back through the same pathway upon reversing field sweep.

Reversible and irreversible process usually coexist in hysteresis loops, and their analysis allows to determine the magnetic anisotropy axes of magnetic systems, as will be shown later.

## B.3 Angular dependence in hysteresis and reversal processes

In the examples of figures 1.7 of section 1.4.1 in the introduction, and B.1 in this appendix, the loops presented have very different features, both in the parallel and perpendicular components. They have been taken at different angles with respect to anisotropy directions of a biaxial ideal system, the first at 30° and the second at 0° (scales are not important for this explanations).

A polar plot for the loops from figure 1.7 has been depicted in figure 1.8, while the polar plot of the loop seen in figure B.1 has been depicted in B.2(a). In figure B.2(b) a polar plot for a loop taken at an angle slightly off 0° has been depicted, to help in the discussion of what is going on.

While in 1.8 we see rotative processes and two jumps on each branch of the loop, corresponding to the steps in figure 1.7, in B.2(a) no rotative processes can be seen, and only two (overlapped) simple jumps are visible, happening exactly along the axis where the field is been applied (coincident with the anisotropy axis). In fact, B.2(a) presents the exact shape of a perfect squared parallel component and a perfect zero perpendicular one. In figure B.2(b) the same cycle taken slightly away from 0° is shown, the overlapping lines and points of the vectorial polar are slightly separated, and the two overlapping jumps are now visible.

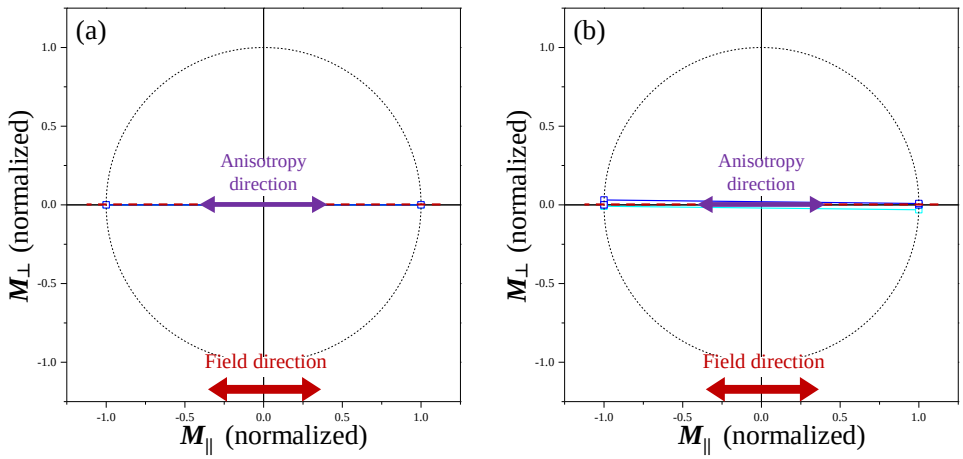


Figure B.2: Polar plot of the vectorial hysteresis loop shown in figure B.2. (a) the exact 0° field direction, and (b) slightly off 0° field direction.

Some general ideas will be used along this thesis. First, in general, rotative processes are more relevant when the external field is applied at angles away from the anisotropy directions, at the so called hard axis (h.a.). Second, at exact anisotropy directions, called easy axis (e.a.) in perfectly symmetric anisotropy systems, the perpendicular component vanishes. The subtlety behind "perfectly symmetric systems" resides in the fact that if the different axes are non equivalent, double transitions in one of the anisotropy direction may appear, that leads to a non vanishing perpendicular component during the reversal. Third, the perpendicular component changes its sign upon traversing any characteristic axis, be it easy or hard axis, a very important key to identify characteristic axis through angular evolutions of vectorial hysteresis loops (explained later).

At high external fields the more relevant effects acting on magnetic moments come from the Zeeman energy term and the magnetic anisotropy. The Zeeman term, the interaction between the external field and the magnetization, reduces energy when magnetization is aligned with the external field, so it pulls the magnetization towards the field direction. It vanishes at zero field. Anisotropy energy in turn, is lower when magnetic moments are siting on the anisotropy directions. Competition between both terms govern the process at fields away from transitions. As the external field is reduced (say from a maximum saturating field), Zeeman decreases and magnetic moments tends to rotate towards the closer anisotropy axis. The farther the field angle is from the anisotropy axis, the more rotation process we have, in order to go from the field direction to the axis. This situation occurs close to hard axes. The process can be reversed during this rotation just by reversing the field, and the rotation is then simply reversed back (reversibility). At high field values, magnetization tends to align with external field, but reaching fully alignment is only possible at exact anisotropy directions or when exactly in between two perfectly equivalent anisotropy axis. Otherwise,

anisotropy always pulls a little from magnetization, and fully alignment in the field direction is not reached. At zero field, the magnetic moments will sit on anisotropy axis, as the Zeeman term vanishes. From here, more rotation away from the axis will happen as field begins to increase in the opposite direction, until a magnetization switch occurs, either in a coherent (single domain) way, or by nucleation process with subsequent domain wall propagation (multi-domain). This happens when external field provides energy enough to activate reversed domains (single or multi-domain). Both give rise to irreversible processes, manifested in abrupt jumps, that cannot be followed back through the same pathway upon reversing the field sweep.

## B.4 Examples of hysteresis loops and reversibility

In order to better illustrate all this ideas and concepts, some examples are given in the following four subsections. The idea of detecting characteristic axes by looking at the change of sign in the perpendicular component is the first example. Then we go through two examples of model vectorial hysteresis loops in the frame of coherent rotation model (SW) (but the concepts are extensible to other models with little changes). They are intended to show how vectorial hysteresis loops are born as a consequence of the different paths that the reversal follows depending on the anisotropy configuration of the system. In the last subsection, model full angular evolution of hysteresis is shown in polar plots, so that the reversal paths as a function of angle are easy to identify. In addition, the angular evolution of some magnetic properties are shown.

In the three first examples, the pathways that magnetization follows are depicted with colored arrows for easy understanding. In the figures, a black horizontal line represents the external field direction, while soft violet lines represent anisotropy axes. Anisotropy axes are represented by double arrows. Blue arrow represents the magnetization parallel component and red arrow represents the perpendicular one. The final magnetization vector is represented in violet. Two dashed gray circles are depicted, the bigger one is used to enclose the anisotropy axes and the smaller one to enclose the magnetization vector. Whenever the magnetization vector follows the smaller circle, indicated by arrow-arcs, rotative process is happening. When the magnetization vector traverses from one point of the circle to another, an irreversible jump is happening. Below and to the right of the aforementioned scheme, M-H plots for the forward branch are depicted, with the pathways for the parallel and perpendicular components (bottom-left, and top-right on each figure). In diagonal (bottom-right) the final vectorial hysteresis loop is depicted for a complete "go and return" sweep of the magnetic field. Forward and backward branches are distinguished by dark and soft tones of the same color for each component.

### B.4.1 Perpendicular component change of sign around characteristic axes

A signature of the presence of a characteristic axis (easy or hard) is the change of sign that the perpendicular component undergoes upon traversing it. Here the term "traversing" a characteristic axis means to have the field at a certain angle with respect to that axis, and rotate the sample so that field passes to the other side of

that axis. As field is kept fixed in our experimental set-up, being the sample who is rotated, the real situation of traversing a characteristic axis means that the axis itself goes from negative angle with respect to field direction, to positive one. A figure is better than words in this case, as explanations could lead to a cumbersome long text. Thus in figure B.3 the situation is depicted for a uniaxial model system with field close to easy axis. While in (a) the easy axis (e.a) is at a positive angle with respect to field direction, in (c) is at negative one. Only the corresponding perpendicular component of the (hand made) associated hysteresis loop is depicted in both cases. The reversal process consists on a rotative part from positive saturation direction (blue arc arrow labeled "rotation"), followed by an abrupt switching of the magnetization (green straight arrow labeled "180°) at some point after surpassing anisotropy axis, that happens parallel to the anisotropy direction, and again a rotative part until negative saturation is reached (yellow arc labeled "rotation"). Note that perfectly fully alignment to the exact external field direction (by Zeeman energy, at saturating field values) is not possible due the presence of the anisotropy that always pulls towards the nearest anisotropy axis. For this reason, a non null (but small) perpendicular magnetization component is present at saturating field values, as can be seen in (b) and (d), where the hysteresis forward pathways corresponding to the reversal process illustrated respectively in (a) and (c) are depicted in red line. The backward pathway in (b) and (d) has been depicted in dashed soft red, for completeness of the loop (not illustrated in (a) and (c)). As can be seen, the perpendicular component, $M_\perp$ presents a change of sign from case (b) to (d). At the exact easy axis, perpendicular component must vanish, as has been also explained with different arguments in figure B.1. This is a general rule when an easy axis is traversed, and it can be easily shown that the same effect happens when the traversed axis is a hard axis, establishing the rule of thumb that a fingerprint of a characteristic axis is the change of sign of $M_\perp$ upon traversing it.

Just as anecdote, vanishing perpendicular component should be also (surprisingly) expected at an exact hard axis. A way to visualize this is by noticing that at that angle, there are two equivalent easy axis at the exact same angular distance, so that there must be an equilibrium point in anisotropy energy there, and parallel component should be square, with vanishing perpendicular one. However this equilibrium point is a local maximum, unstable by definition, and physically impossible to realize in practice, so that at hard axis the magnetization always rotates to one of the anisotropy axis, and we always encounter the larger rotative process here.

### B.4.2 Uniaxial system close to easy axis

In figure B.4, a uniaxial configuration is selected, with the external field at approximately 20° out of the axis. To represent the path that magnetization follows during the reversal, color scheme is used inside the gray disk. The blue and yellow arrow-arc represent the part of the reversal that takes place by rotation. The green straight arrow represents an abrupt jump of the magnetization vector (irreversible transition).

The branch of the cycle depicted in the disk, figure B.4(a), is a forward branch (from positive to negative field values). The first part of the branch corresponds to rotation of the magnetization around the positive direction of the easy axis. In the region where the external field is still above the transition field, Zeeman energy

and anisotropy energy compete to give the angle where the magnetization sits on. The two energy terms act as if magnetic moments were feeling a "pull" from their corresponding directions. As can be seen, rotation process goes beyond axis direction. This is because when the external field is reversed but is still not enough as to startup the irreversible process (towards the third quadrant, green arrow), the balance of the aforementioned energies still govern the magnetization angle after surpassing the anisotropy axis. After the irreversible transition, rotation happens again towards the field direction (yellow arc).

As already mentioned before, when the external field is not perfectly aligned with the easy axis, it is two difficult to fully align the magnetization vector in the field direction. For simplicity we have not taken this into account in our scheme, and the drawings present fully alignment at saturating fields, i.e., zero perpendicular saturation magnetization.

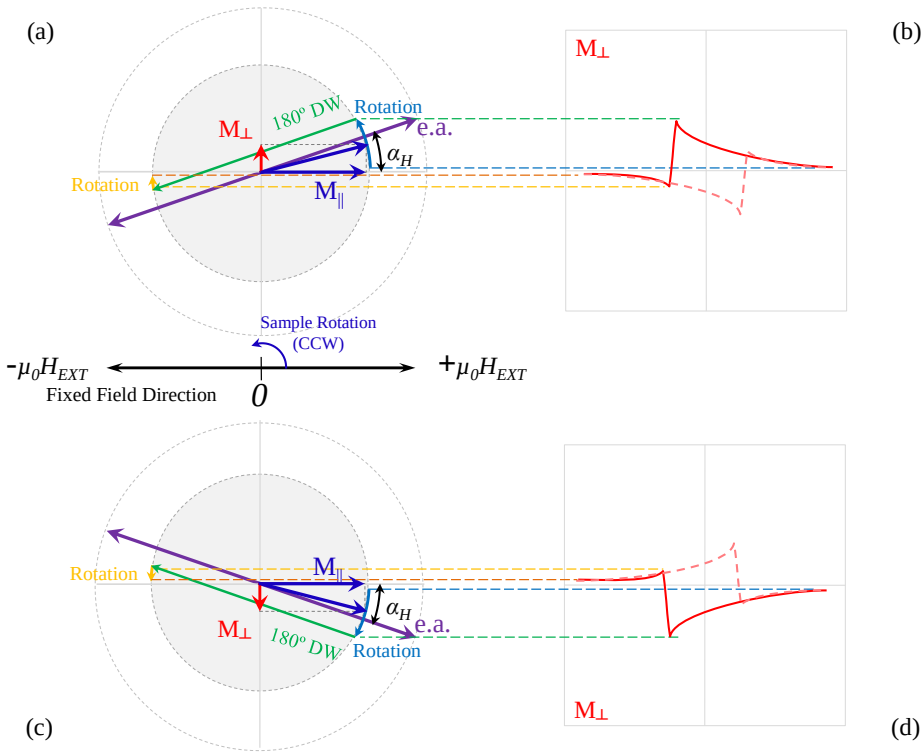


Figure B.3: A diagram of the reversal in uniaxial system at two symmetric angles around easy axes, to illustrate the general rule of thumb that a change of sign in $M_\perp$ component occurs upon traversing a characteristic axes. Details are explained in the text.

The corresponding forward branches of $M_\parallel$ and $M_\perp$ magnetization components are depicted in B.4(b) and B.4(c) respectively. The way back from negative saturation

to positive, follows a symmetric pathway as the forward branch, and the complete vectorial hysteresis loop is depicted in B.4(d), with the same color scheme of blue for $M_{\parallel}$ and red for $M_{\perp}$. The forward and backward branches have been distinguished with dark and soft color respectively in both cases.

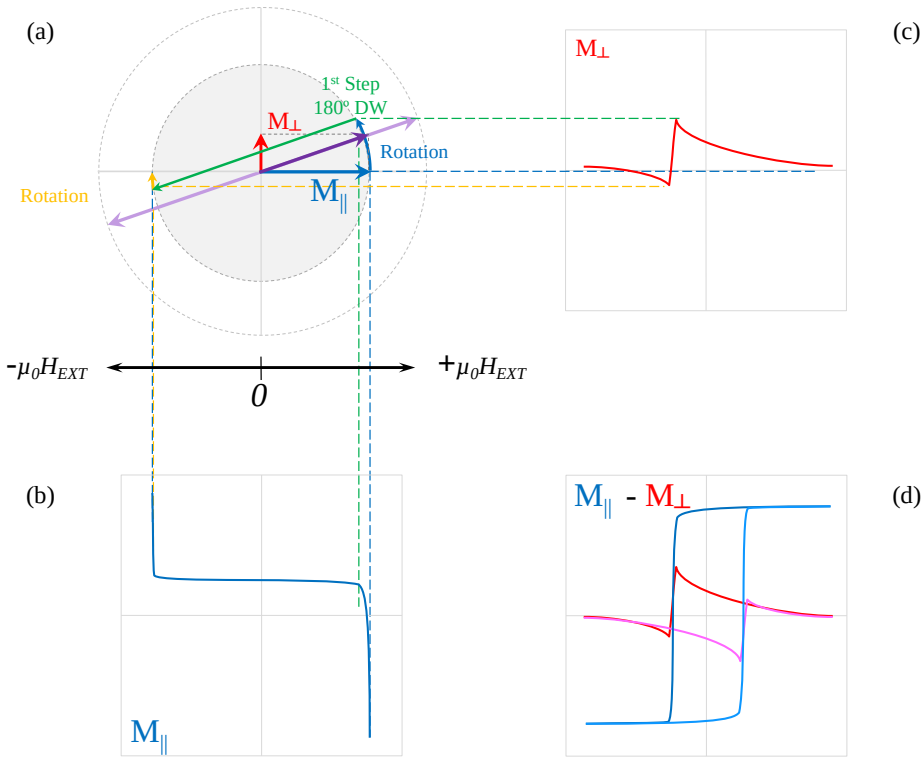


Figure B.4: A diagram of the reversal in uniaxial system with external field close to the anisotropy axis. In sketch (a), the magnetization vector follows the colored arc-arrows, rotating when reversible process takes place, and jumping in irreversible processes. Corresponding branches of the parallel and perpendicular magnetization components are depicted in (b) and (c) respectively. Composition of the forward and backward branches leads to the hysteresis loops of both components (blue and red respectively) in sketch (d). Deeper explanation in main text.

The reversal process in this example has taken place by rotation and subsequent (almost) 180° switching of the magnetization (note that departure and arrival points of the green arrow are not exactly separated by 180°). We have given the explanations from a macro-spin reversal process point of view. When multi-domain (nucleation and domain wall motion) is the reversal process involved, this macro-spin view is no longer fully correct, nucleation and domain wall motion processes make the abrupt jump happen earlier, with a reduction of coercive field. This means that the blue arrow-arc route beyond the easy axis is shorter, and after the jump, the yellow arrow-

arc is a bit longer. The switching is then closer to 180°. The domain walls involved corresponds to 180°. Nevertheless the global qualitative shape is still the same.

The complete polar plot with both branches can be seen in figure B.5(a), with the hysteresis loop in B.5(b).

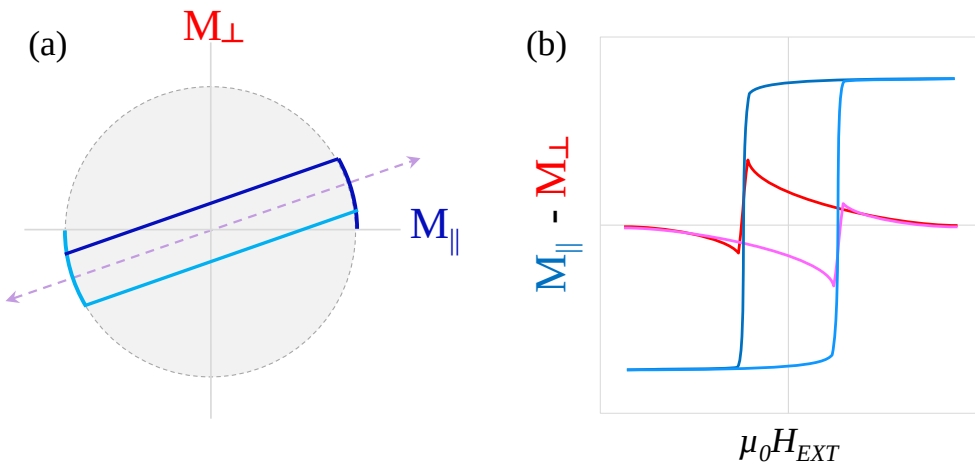


Figure B.5: Complete polar plot (a), with the hysteresis loop (b) for reversal magnetization in model uniaxial system.

### B.4.3 Biaxial system 2-steps reversal

In this example a biaxial system is presented with field direction at approximately above 22.5° (inside the region where SW model predicts double transitions ). In figure B.6 we see the situation. Now that we have introduced the uniaxial case, following the biaxial is quite simple. The rotative regions now are the blue, the orange and the yellow arrow-arcs in sketch (a). The process is similar than in the previous case. From saturation, rotation takes place as the field is reduced to zero. At zero, the magnetization is sitting in the axis that crosses the first quadrant. Upon reversing the field, rotation continues until the region closer to the axis in the second quadrant becomes more favorable, and the jump happens (green arrow). From there, more rotation happens (orange arrow-arc) around this axis, until the field is negative enough as to make the vicinity of the axis in the third quadrant more favorable. Then another jump happens as the red arrow shows. From there, rotation happens now until the negative saturation is reached.

Sketches (b) and (c) show the magnetization components behavior. Now, during the first jump, the perpendicular component increases very much with respect to the parallel one. Rounded loops can be seen now, until the next jump happens, indicative of inter-jump rotative process. Sketch (d) shows the final vectorial hysteresis loops corresponding to this process.

The polar plot with both branches, not shown in figure B.6 to avoid excess of arrows, can be seen in figure B.7(a), with the hysteresis loop in (b).

The irreversible jumps are not very close to 90°. In nucleation and domain wall motion reversal processes, where at low fields the magnetic moments are mainly sit at anisotropy directions and the nucleation of reversed domains starts up much earlier than the point at which the switching process happens in the coherent rotation model, each jump corresponds to domain walls at 90° between reversed domains, and the jumps are much closer to this angle.

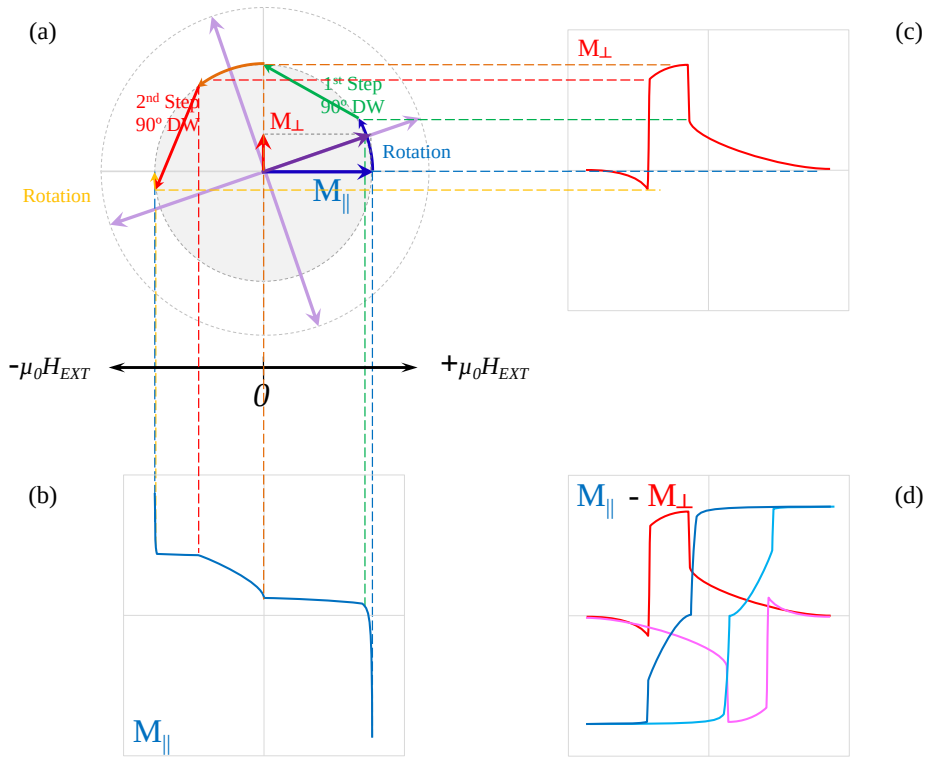


Figure B.6: A diagram of the reversal in a biaxial system with external field close to the first axis. In sketch (a), the magnetization vector follows the colored arc-arrows, rotating when reversible process takes place, and jumping in irreversible processes. Corresponding branches of the parallel and perpendicular magnetization components are depicted in (b) and (c) respectively. Composition of the forward and backward branches leads to the hysteresis loops of both components (blue and red respectively) in sketch (d). Here we find two jumps. Deeper explanation in main text.

### B.4.4 Angular evolution in SW uniaxial model system

Model angular vectorial hysteresis loops for a uniaxial coherent rotation ideal model system are illustrated in figure B.12 (at the end of the section), both in linear and polar plots, corresponding to external field directions from 0° to 360° every 15° degrees, with respect to the anisotropy axis. The loops have been obtained by using

the Stoner-Wohlfarth model through the simulation program (see appendix 1.6). For each angle, upper plots are the vectorial hysteresis loops, where parallel components are depicted in blue colors and perpendicular ones are depicted in red. Forward and backward branches are distinguished by using dark or soft tones of the associated colors, respectively. Open symbols have been used. Lower plots at each angle correspond to polar plot ($M_\perp v.s. M_\parallel$), and in this case forward branch is dark blue while backward branch is soft blue. The simulation has been carried out with magnetization set to unity, $M_S$=1, and for unity anisotropy constant $K_1/M_S$=1. Notice that easy axes plots have been highlighted with soft blue background, while hard axes plots have been highlighted with soft red. Each time any of the four characteristic axes are crossed, the perpendicular component changes its sign.

where $K_1$ is given in units of $M_S$.

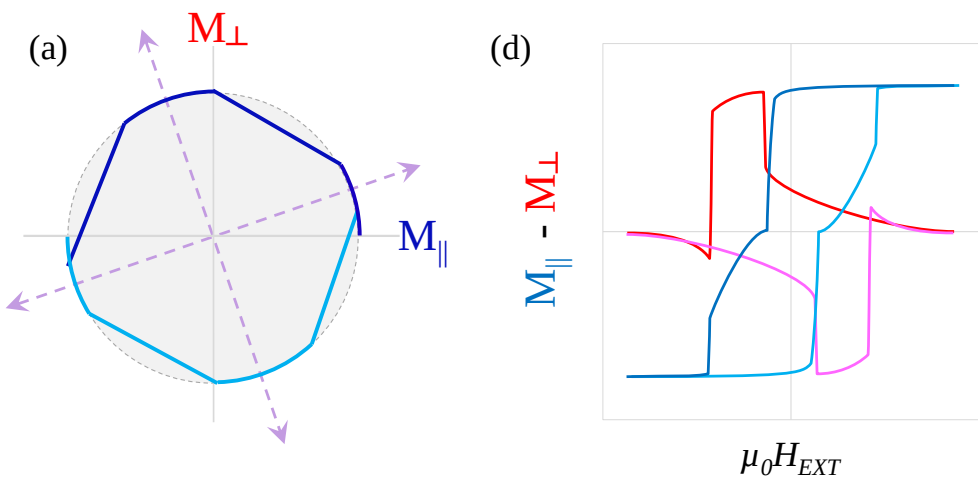


Figure B.7: Complete polar plot (a), with the hysteresis loop (b) for reversal magnetization in model biaxial system.

At easy axis directions, the magnetization parallel component is a squared loop, where $M_{S,\parallel}$ keeps constant and equals to the maximum magnetization value, $M_S$, all the time, changing only its sign at the transitions, i.e., from $+M_S$ to $-M_S$ and back to $+M_S$, at $-H_C$ in the forward branch and at $+H_C$ in the backward, respectively. The perpendicular component at this angle vanishes. The corresponding polar plot is similar to that of figure B.2.

The anisotropy constant can be derived for this ideal model as

$$K_1/M_S = H_C/2 \tag{B.1}$$

As the ratio in the left of this equation has the same dimensions as $H$ (and H is given here in mT, since it has implicitly incorporated $\mu_0$), it is also called the anisotropy field, $H_K$, given in mT.

As we move away from the easy axis, the parallel component is rounded and narrowed more and more and the loop is gradually closed. The perpendicular component begins to increase, and has the trigonometric-complementary behavior with respect to the parallel one, so that $M_{\parallel}^2 + M_{\perp}^2 = 1$. At 90°, the parallel component is a completely closed loop consisting in a straight slope, while the perpendicular one has balloon shape, consistent with a fully rotative process, that can be seen in the corresponding polar plot as a complete circle. Interestingly, notice that the perpendicular component changes its sign around both the easy and hard axes, as already explained. This is the expected behavior for single-particle like reversal process.

The angular evolution of $\mu_0 H_C$ and $\mu_0 H_S$ are depicted in figure B.8, in blue and red color respectively. Notice the position of the hard axis (blue dashed line) at 0° and 180°, and hard axes (red dashed lines) at 90° and 270°. The two-fold symmetry is clearly manifest as a repetition of the same pattern after 180° degrees.

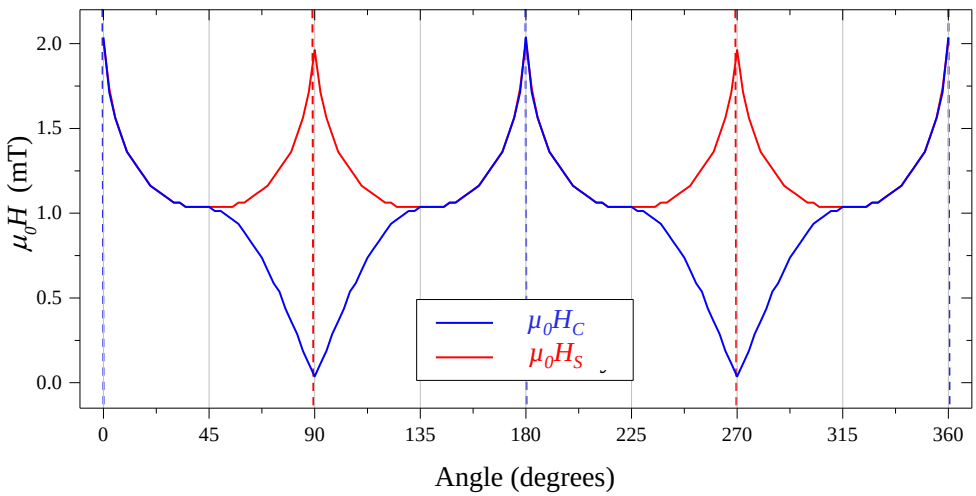


Figure B.8: Angular evolution of transition fields $\mu_0 H_C$ (blue) and $\mu_0 H_S$ (red) for single-particle like behavior (SW). Vertical dashed lines are set to mark axes positions, easy axes and hard axes (blue and red color respectively). The grid used for the simulation was 5° width.

Many of the features of this angular evolutions are discussed during this thesis. Some of them are mentioned also here. First, as can be seen in this figure, around easy axes both $\mu_0 H_C$ and $\mu_0 H_S$ coincides, while they separate at hard axes. Notice that at exact easy axes perpendicular component is zero and $H_S$ would be eventually impossible to compute, however if the field angle is set very close by a differential amount, the perpendicular component will detect the transition. Around hard axes, however, $H_C$ and $H_S$, split. As parallel component is becoming a closed loop, $H_C$ vanishes, while the perpendicular component becomes large and wide open. Even thought $H_C$ is vanishing at hard axes, the switching of the magnetization is still revealed by the perpendicular component. Second, the switching field expressed in

equation B.1 is valid using $H_S$ measured at hard axes, instead of $H_C$ at easy axis, and it is also valid at easy axis provided that we compute $H_S$ not at the exact easy axis (where it vanishes) but at an asymptotically close value, just away of it by a differential amount. In general, perpendicular component reveals more accurately the transitions.

The 3D plot of $M_{\parallel}$ is depicted in figure B.9. The upper plot is a perspective view where the easy squared loops at easy axes and closed loops at hard axes can be clearly identified. The lower plot is a top view. Notice the color patterns are perfectly duplicated every 180°, i.e. it presents a two-fold symmetry.

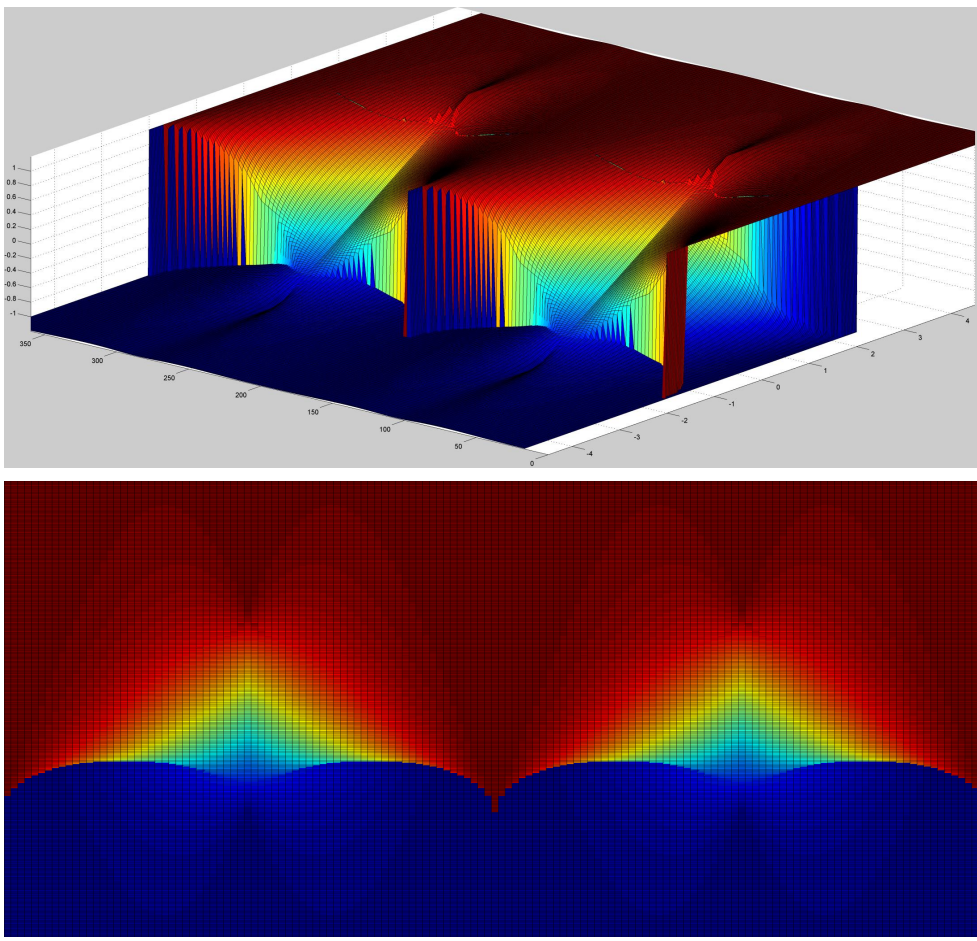

Figure B.9: 3D plots of the angular evolution of the magnetization parallel component (hystersis loop), in color map. The upper plot corresponds to a perspective view where easy and hard axes can be identified as the sections with squared loops at 0° and 180°, and those with a perfect straight slope at 90° and 270°, respectively. The lower plot is a top view. Notice that the color patterns are perfectly duplicated every 180°.

In figures B.10 linear plots of the the angular evolution of remanence is depicted for both parallel (blue) and perpendicular (red) components. Notice that they reproduce the same symmetry as the transition fields, with pattern repetition every 180°. It can be seen that the saturation magnetizations also follow the same two-fold symmetry for this system (not shown). In figure B.11, polar plots for transition fields (left) and remanence (right) are depicted, revealing clearly the symmetry.

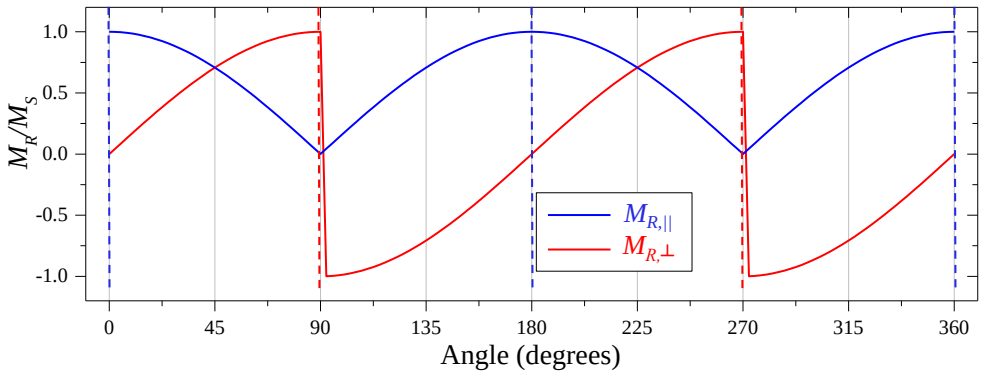


Figure B.10: Remanence evolution with angle for the ideal single-domain uniaxial system.

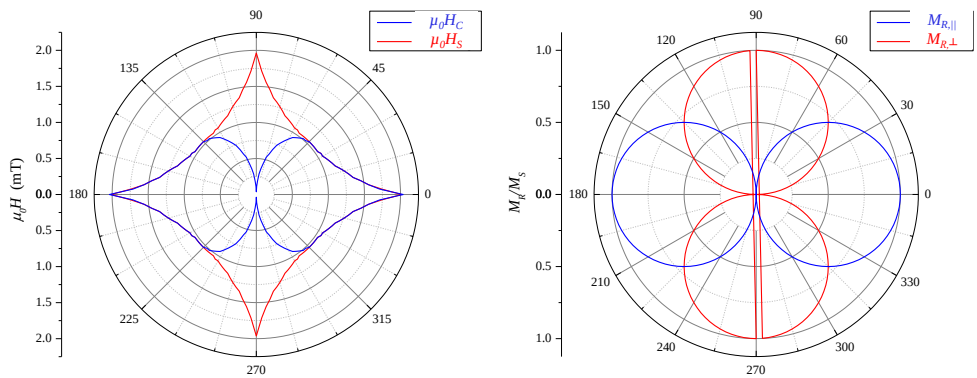


Figure B.11: Polar plots for the already exhibited figures B.8 (to the left) and B.10 (to the right). Note that in both cases, the two-fold symmetry is clearly identify.

We have used the simple uniaxial single-particle (SW) model system to introduce some of the features of the angular evolutions of transition fields and remanences, as well as some global ideas of the hysteresis loops evolutions.

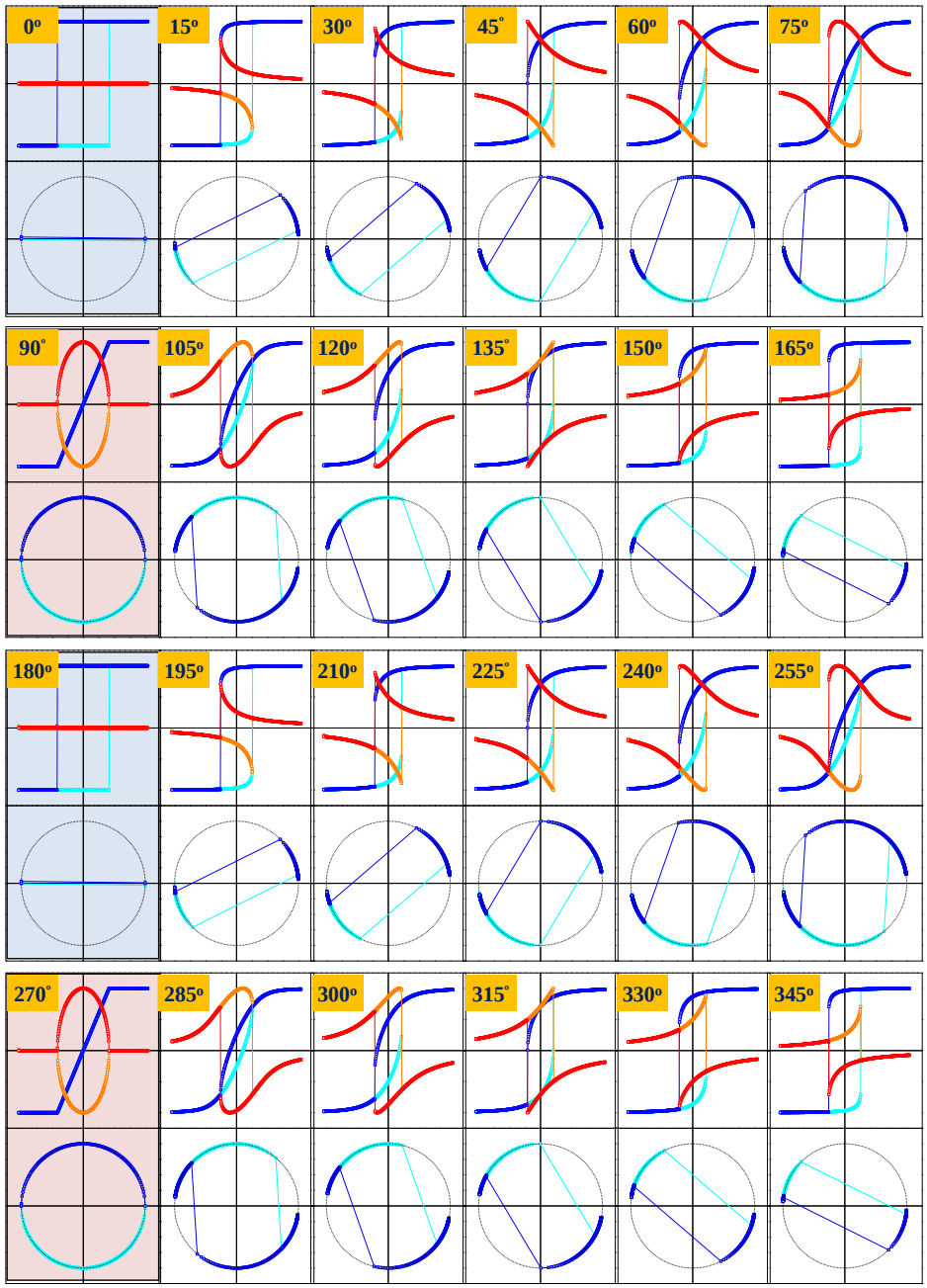


Figure B.12: Angular evolution of hysteresis loops for ideal coherent rotation (single-particle like) uniaxial system, see main text.

# C Meeting and departure points in hysteresis loops

In this appendix we stress on two characteristic points in the hysteresis loops that we have called meeting point and departure point. We define them for uniaxial system, but the validity could possibly be extended to other systems, with certain restrictions. In this context, these two points have been used as reference points for certain fitting procedures in this thesis. In particular, meeting point, defined at the parallel component of the magnetization, follows the switching field, which is only defined in the perpendicular one, so that the meeting point encodes in the parallel component information that usually requires the perpendicular one. Departure point, on the other hand, has its importance as a point that, together with the remanence and the saturation magnetization, allows to fully determine the rotative part of a reversal process. We launch the question on whether the ideas presented here are general or just a particular case of specific anisotropy symmetries.

## C.1 Switching field and meeting point

When comparing figure B.9 (bottom) with figure B.8 in appendix B section B.4.4, we immediately recognize in the former the curves followed by $H_C$ and $H_S$, as a color frontier. In fact, the frontier of the dark blue color with the reds and soft blues seams to be following the switching field, up side down. Moreover, the yellow fringe that makes frontier between greens and deep reds seams to follow the dip in the hard axes of the parallel coercive field, again up side down. The regions where the dark blue is in direct contact with the red (around $0^\circ$ and $180^\circ$), seams to be an asymptotic behavior for that yellow fringe, as if it were shrinking between red and blue.

In figure C.1 we have put together the top view of the 3D parallel component with angle (bottom color map in figure B.9) with the $H_C$ and $H_S$ curves of figure B.8, changed in sign, and rescaled to match the color map as explained above. The coincidence is absolute, and the question arises if this is just a matter of chance.

Looking again to the 3D plot of figure B.9, the meaning of the deep blue frontier is clear: it its the region in which the irreversible jump of the magnetization in the forward branch meets the backward branch. As the irreversible jump in the SW model is a sharp vertical line, this meeting point constitutes a corner, which is very acute near the easy axes, but it widens as we get closer and closer to the hard axes. So around the easy axes, the top view of the 3D plot exhibits a clear color jump, that becomes a softer color transition as we get closer to the hard axes.

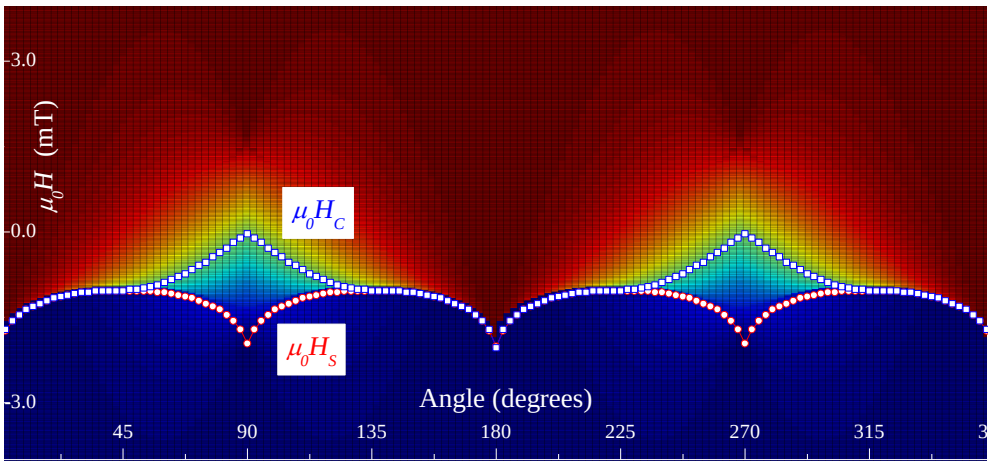


Figure C.1: Match between inverted $H_C$ and $H_S$ curves and the color frontiers in the top view of the 3D magnetization parallel component evolution with angle.

Now looking at figure B.12 in appendix B, we see that the switching field $H_S$ coincides with the aforementioned meeting point for all angles, while the coercive field $H_C$ is little by little moving apart as we go away from the easy axis, starting at around 22 degrees. Moreover, as the slope in $H_C$ from there is no longer a vertical line, but rather a sloppy curve, the color pattern in the 3D image gives up being an abrupt color change, but rather the soft color transition from blue to red going through the green and yellows. As in scale of colors of the 3D map the yellow corresponds to $M_{\parallel} = 0$, this yellow fringe represents $H_C$. The reason why everything is up side down is because from the top view of the 3D map, the forward branch hides the backward, and the transition fields in the forward branch have negative values, while we use to represent the absolute value, i.e., the positive one.

Starting from these ideas, we define a point in the hysteresis loops that will be called the *Meeting Point*, denoted by $H_M$. This point is the point in which the transition in the forward branch meets the backward branch, as a wall or a mountain slope meets the ground. When all the points are gather together, they create the curve of the switching field, and we end up with the conclusion that the parallel component encodes the switching field in this way, for this uniaxial case. The meeting point is illustrated in figure C.2.

## C.2 Departure point

Departure point is defined as the point at which the first irreversible transition begins. In figure C.3, the departure point is depicted for a single-domain (SW-like) hysteresis loop in a uniaxial system. The point has its associated field and magnetization values, named $H_D$ and $M_D$ respectively. This point can be sometimes difficult to locate in the magnetization parallel component. But if we look at the vectorial polar plot of $M_{\perp}$ as a function of $M_{\parallel}$ it will be easier, as is the point where the magnetization goes

out of the circle (see figure C.4). The point can also be identified in the perpendicular component, as can be easily seen in figure C.5(b), because there is a kink in the curve.

In the uniaxial ideal SW system there are angular regions where the three characteristic points $H_D$, $H_C$ and $H_M$ coincide. This is the case for hysteresis loops with irreversible transitions, i.e., abrupt vertical jumps in the cycles. At the angle where $H_C$ and $H_S$ split, $H_C$ turns out to be lower than $H_S$. In real experiments, many factors make all this features be slightly different, and defining the departure and meeting points may be difficult. In any case, the polar plot rapidly reveals both points.

The importance of the departure point is not the field at which it happens, but the value that the magnetization has at that point, $M_D$. In the following section this aspect will be justified.

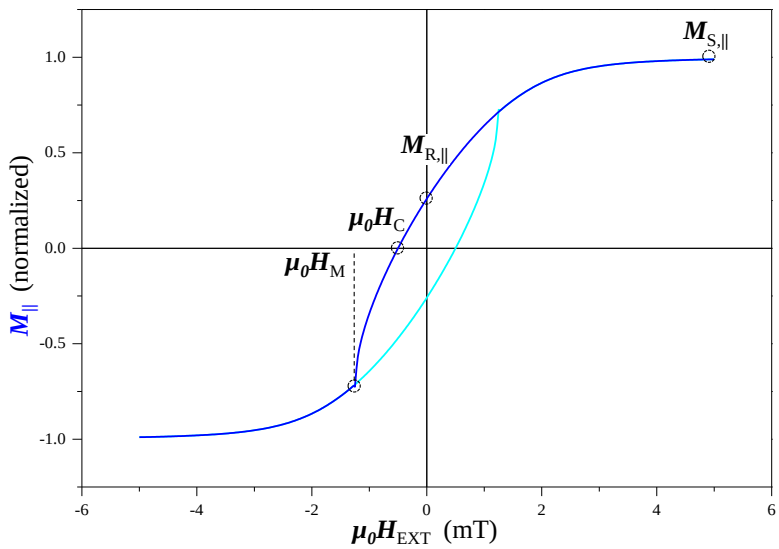


Figure C.2: A typical hysteresis loop with the quantitative parameters that can be obtained from it. The meeting point is here represented as $H_M$.

## C.3 Fitting reversible part in hysteresis

A way used in this thesis to quantify anisotropy constant is based on simulating hysteresis loops under the SW model, and finding what $K$ value predicts the rotative part of the experimental loops. Note that the rotative part of an experimental hysteresis loop might be shorter than that of the SW simulation, for instance this happens in nucleation and domain wall motion reversal mechanisms. This means that the irreversible jump happens at a smaller angular range.

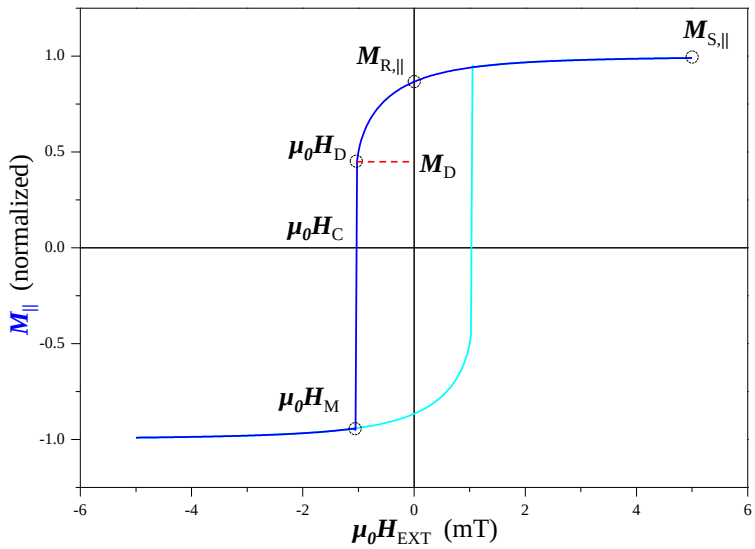


Figure C.3: A typical hysteresis loop with the quantitative parameters that can be obtained from it, as was shown in chapter 1.4, figure C.2. The departure point is here represented, together with the meeting point previously introduced.

This can be seen in figure C.4, where vectorial hysteresis loop taken at $-30°$ from anisotropy axis in a biaxial system is presented. Lines represent SW model simulation and symbols represent the experimental hysteresis loop. The experimental and SW hysteresis loops are depicted in (a), and their corresponding vectorial polar plots are depicted in (b). The symbols overlap the lines, i.e., follow the same rotation process, but the jump happens at an earlier angle. However, the rotative segment in the hysteresis loop must coincide when the simulated hysteresis has the correct anisotropy constant.

The magnetization value at the departure point in the hysteresis loops plays an important role to justify the procedure used in the fitting process. We explain this by using the biaxial system as an example. In figure C.5 a sequence of 5 vectorial hysteresis loops simulated with SW model for a pure biaxial system, with five different anisotropy constants $K_2/M_S$ from 1 to 5 mT, taken at 30° from the easy axis, have been depicted. $M_{\parallel}$ and $M_{\perp}$ are shown in plots (a) and (b) respectively, while in (c), a zoom-in of (a) has been done in the positive region of the loop. It can be seen that the curvature is different in each histeresys loop, but both $M_R$ and $M_D$ are fixed values for fixed angle of the field. This means that at a fixed angle, the departure point has the same parallel component, and hence the same perpendicular one. In other words, the maximum angle that the magnetization vector can reach during the rotative part of the loop before it switches, is the same for all anisotropy values, for a fixed angle of the external field.

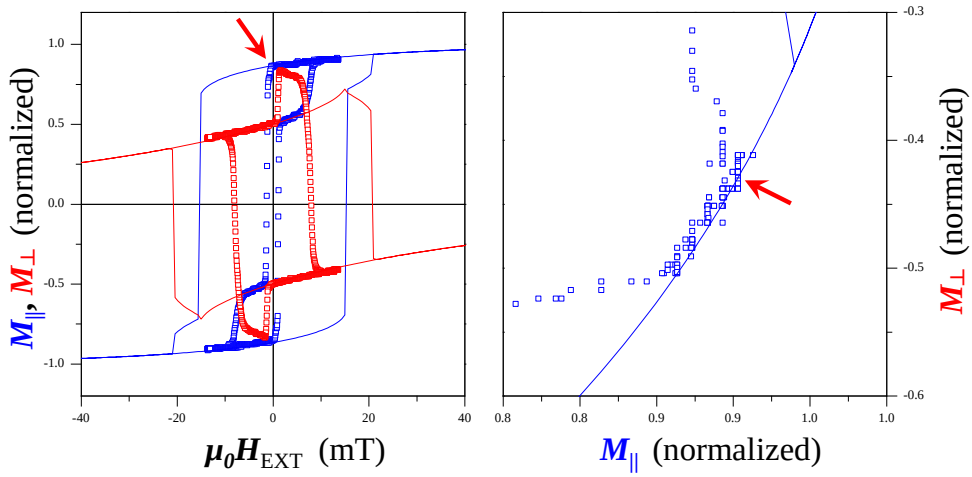


Figure C.4: Vectorial hysteresis loop taken at $-30°$ from anisotropy axis in a biaxial system. Lines represent SW model simulation and symbols represent the experimental hysteresis loop. The experimental and SW hysteresis loops are depicted in (a), and their corresponding vectorial polar plots are depicted in (b). Departure point, marked in red in (a) is easy to localized with the help of a vectorial polar plot (b) as the angle at which the points separate from the circle.

As the curvature of the parallel component is restricted by a trigonometric relation with the perpendicular one (and vice versa), it can be demonstrated that any SW simulated hysteresis loop at a fixed field angle will be the result of an horizontal rescaling of any other loop simulated at that same angle, provided that no change in the relative strength of anisotropy axis is done (this last thing is important in systems with multiple anisotropy contributions).

For instance, a loop with $K_2/M_S$=1, reproduces the loop with $K_2/M_S$ =5, simply if we multiply the component field axis by 5. This is like a scaling property of the rotative process upon changing the anisotropy constant value.

As fitting the rotative part consist on finding $K_2/M_S$ value that makes SW curvature of the rotative part overlap the experimental one, this is the same as making the SW simulation to pass through the departure and remanence points of the experimental curve (see figure C.4(a)). The first step is to check that the positions of $M_R/M_S$ in the SW simulation and in the experimental curve already matches. If this is not the case, either the angle considered in the SW simulation is not the correct, or the system is not pure biaxial, and other contributions should be considered in the simulation. Now, for the considerations previously done, we only need to correctly scale the normalized experimental magnetization, verify that SW and experimental $M_R/M_S$ values matches, and then rescale a $K_2/M_S$=1 SW simulated hysteresis until experimental departure point lies in the SW simulation. Then the curvature must be the same, and the scaling factor is the actual $K_2/M_S$ of our experimental biaxial

system. Naturally this method can be used with uniaxial systems as well.

This method of finding anisotropy constant through the rotative part of the hysteresis loop is exploited in the chapter devoted to systems with competing anisotropies. In that case, some assumptions are made to justify the consideration that the competing uniaxial anisotropy $K_1$ is negligible as far as its effects in the rotative part is concerned. This is a delicate question, however.

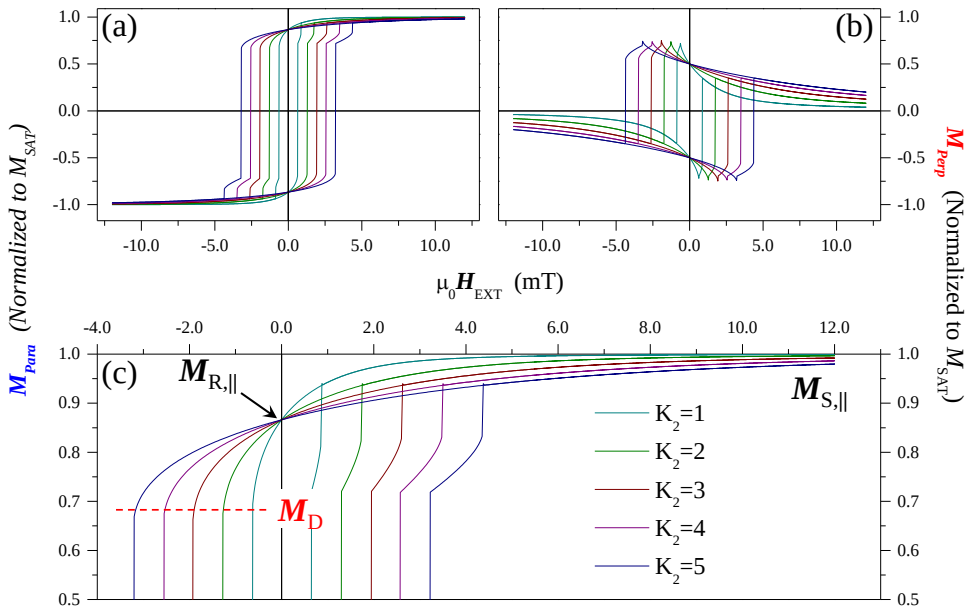


Figure C.5: The scaling effect is shown here for simulated SW loops of biaxial system at 30°. (a) parallel components of the magnetization for increasing values of $K_2/M_S$, from 1 to 5 mT appear in outward order (i.e. from lower $H_C$ value to higer). (b) The corresponding perpendicular components with the same criteria. (c) An enhancement of the departure points with dashed red lines indicating that all the points are at the same $M_D$ value (but different $H_D$ values). The effect of scaling with $K_2$ can be easily probed by multiplying the horizontal axis of $K_2 = 1$ by $K_2$ of any curve and noting that the resulting curve will overlap the curved simulated for that $K_2$ (not shown).

# D Thermal activated processes supplement

In this appendix we include some more details on thermal activated processes.

Thermal energy contributes to the probability of overcoming a barrier following a Boltzmann law, where the probability of success during a certain period of time, the attempt time $\tau_0$, is given by

$$exp(-\Delta\epsilon/k_bT) \tag{D.1}$$

It can be seen after doing some statistical arguments that $\tau_0 \simeq 10^{-10}$ s. For the duration $\tau$ of an experiment, the coercive field, (statistically defined as the field for which there is a 50% probability of switching) can be written as

$$H_C(T) = H_C(0)\left[1 - \sqrt{\frac{k_BT}{K}ln(\tau/\tau_0)}\right] \tag{D.2}$$

where $K$ is the anisotropy constant. As the logarithmic function is a slowly varying function of its arguments, effects of temperature on the coercive field are more patents than the effects of time scales. As a function of T, $H_C$ given in equation D.2 is a decreasing Arrhenius law of temperature.

This equation given in this way has some limitations, for instance does not take into account thermal dependences of anisotropy and magnetization, but is enough to illustrate the typical evolution with temperature expected for thermal activated reversal processes, and dynamical aspects of the reversal can be enclosed in it to a first approach.

A particular important aspect derived from this equation is that there is a temperature in which coercive field vanishes, the so called blocking temperature, $T_B$, which can be obtained solving equation D.2 for $H_C = 0$, giving

$$T_B(\tau) = \frac{K}{k_Bln(\tau/\tau_0)} \tag{D.3}$$

This temperature means that for a certain measurement time, below that temperature the magnetic moment does not fluctuate over that measuring time, called the blocked state, while above it the system fluctuates spontaneously averaging moment to zero, which is the so called superparamagnetic regime. For measuring times of the order of a second, $ln(\tau/\tau_0)$ is around 25, so that

$$T_B = \frac{K}{25k_B} \tag{D.4}$$

During this thesis we are not entering into the subject of superparamagnetism, and this couple of ideas have been set here just to make some emphasis on the importance of the dynamical effects in the magnetic parameters.

# E Theoretical models supplement

## E.1 Stohner-Wohlfarth model

The Stohner-Wohlfarth model is realized by minimization of the magnetic energy with respect to the magnetization vector angle, under the assumption that the magnitude of the magnetization vector is constant and equal to the saturation value all the time. The energy to be minimized contains the anisotropy energy contribution and the energy of the interaction between the magnetization and the external field (Zeeman energy). All the angles involved in the definition of the energy are set for a certain anisotropy symmetry, together with the angle of the external field (refer later in this section, figure E.12). A zero angle reference is usually taken to be one of the anisotropy axes (this will be discussed later). The minimization process is realized for each external field value in a sweep between negative to positive maximum values and back, obtaining the magnetization angle with respect to a reference direction, at each point. As the magnetization magnitude is constant, the vectorial components are calculated straightforward, and hence the vectorial hysteresis loop. During the minimization, for each field value, the energy curve is obtained as a function of the magnetization angle for all the range $0^\circ$ to $360^\circ$, and the minimum is localized. This process is repeated over the whole angular range of external field direction, yielding a full angular range vectorial hysteresis evolution. The evolution of the magnetization vector with the external field depends on magnetic history, influencing the minimization process. For this reason, the scan procedure for each angle of the field begins by first setting the field to its maximum sweep value, and finding the minimum position (angle) of the magnetization vector which is closer to the actual field direction (saturation condition). Both field direction and the minimum in this case should be inside the same valley, provided that the maximum field value is enough to almost saturate the system. This mean that the maximum field value must be greater than the anisotropy field which is double of the anisotropy constant. This first minimum is found, and then, its evolution as the field is swept is followed.

In figure E.1 example of a biaxial system with collinear uniaxial anisotropy is used to demonstrate the process, and how a vectorial hysteresis loop is born after it. Only the backward branch is depicted.

All we have to do is define the angles for the geometry, then let the computer do the minimization process over the external field swept to obtain the magnetization angle, from that we get the parallel and perpendicular components of the magnetization and we end up in the parallel and perpendicular hysteresis loops.

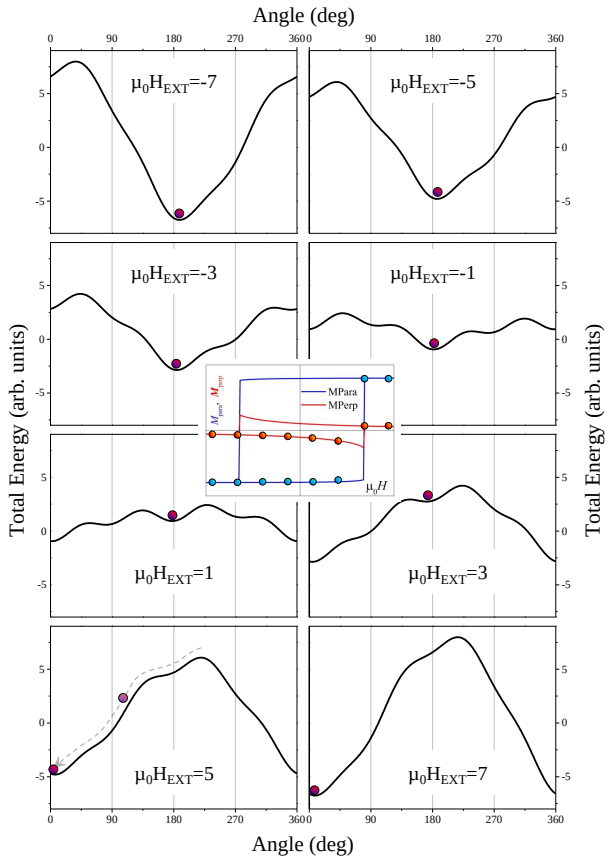


Figure E.1: Biaxial ($K_2/M_{SAT}$=1mT) with collinear uniaxial ($K_1/M_{SAT}$=1mT) system energy curves are presented here. Saturation magnetization is normalized, and athe external field has been set to 20° from uniaxial axis, varying from -7 to 7 mT (notes on units are given in the text). The simulation shows energy curves every 2 $H$ units, on the forward branch. Relevant on this graphs is the fact that full saturation on the external field direction is not reached for the maximum field values applied. Minimum of energy evolution is depicted by tracking the small ball movement. An abrupt jump happens somewhere in the vicinity of 5. Corresponding hysteresis loop for parallel and perpendicular are depicted in the inset at the center. Note that the $H$ variation grid ($\Delta = 2mT$) is very rough as to get some accuracy on loop.

### E.1.1 Energy terms of the SW model

The energy of the Stoner-Wohlfarth are defined in the following for certain cases. As already mention it takes into account the anisotropy energy and the Zeeman energy.

The anisotropy terms associated with a certain magnetic symmetry axes can be expressed as proportional to square sine functions of the magnetization vector with re-

spect to the axes [9]. The proportion is defined as the anisotropy constant, represented by K. Different K appear in each different anisotropy terms. The angle inside the sine function is multiplied by an integer factor so that the correct periodicity is reproduced. For instance, if the angle appears single, the square sine function will present two minimums at opposite directions (180°), representing a uniaxial anisotropy, and if the angle appears doubled, there will be four minimums separated by 90°, and this will represent a biaxial anisotropy with four equivalent directions, and so on. At zero field (Zeeman energy equals zero) energy minimum is governed by anisotropy and magnetization will prefer to be sitting at those minimums. In this context, the angle $\phi$ for the magnetization appearing in the sine functions, is referred to one of the anisotropy axis belonging to that energy term. When more than one anisotropy terms are present, with axis in a non collinear configuration, relative rotation of the anisotropy contributions will be referred with an additional angle, $\rho_{K_i}$, explained later in figure E.2.

The Zeeman energy is represented by the product of the magnetization, the external field magnitude, and the cosine of the angle between the magnetization and the external field.

The angle between the external field and the magnetization is designated by $\theta$. In figure E.2 the geometry of the different angles can be seen. For example the energy for an anisotropy scheme based on a uniaxial anisotropy collinear to a biaxial one can be expressed as

$$E = K_1 sin^2\phi + \frac{K_2}{4} sin^2 2\phi - MHcos(\theta) \tag{E.1}$$

In practical application of this equation, when full angular range simulation is performed, the angle between the external field and the anisotropy axes, or correspondingly that of the sample itself with respect to the external field will enter as the difference between $\theta$ and $\phi$ (and eventually, $\rho_K$ enters in the formula as well if the axis is not aligned in a sample reference direction, but at this point this is not important).

In equation E.1, $K_1$ is used to represent the anisotropy constant of the uniaxial anisotropy and $K_2$ for the biaxial one. The reference direction here is set as the $K_1$ anisotropy axis direction, used as well as the zero direction for the external field angle. $\theta$ is the angle for which we do the minimization process, i.e., that of magnetization vector and external field. The division by 4 in the $K_2$ anisotropy constant accounts for the multiplicity of the axis.

If the system were non collinear, we would only need to introduce the offset angle between the uniaxial axis and one of the biaxial's inside the square sine function for the corresponding shifted anisotropy. This is done with the help of the $\rho_K$ angle. There will be one such angle for each different anisotropy term. In a simple case in which uniaxial and biaxial are collinear and both are parallel to one of the samples edges, the angles $\rho_{K_1}$ and $\rho_{K_2}$ would be both set to zero.

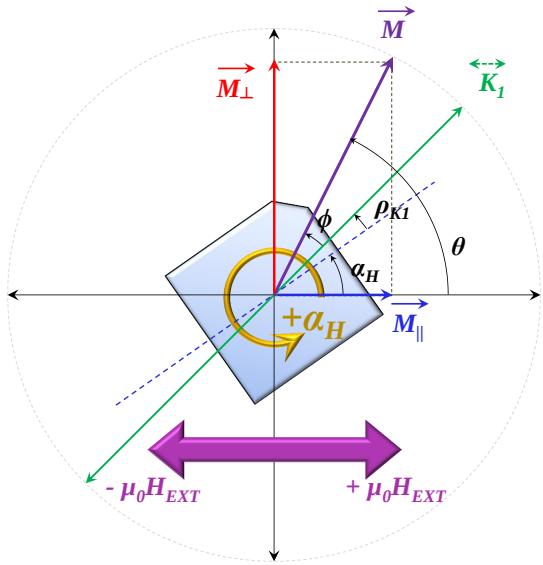


Figure E.2: Angle geometry for the magnetization and the external field for the Stohner-Wohlfarth model. A uniaxial anisotropy is depicted as an illustration. Magnetization components are taken with respect to the external field direction, which is fixed (double violet 3D arrow). The external field angle with respect to the sample axis is given by $\alpha_H$. Notice that a special angle $\rho_{K_1}$ has been defined to relate the anisotropy axis (green double arrow) to one of the sample's characteristic cutting direction (dashed blue line). When cutting direction coincides with characteristic magnetic axis, this angle is zero. Normally, as sample shape is not important for simulations, if only one anisotropy scheme is to be used in the simulation software, this angle is zero. But if a combination of various anisotropies are present, this angle helps to adjust their relative positions. $\phi$ appears here as the angle between the magnetization and an anisotropy axis. $M_{\parallel}$ appears in blue, and $M_{\perp}$ in red.

In figure E.3 the anisotropy energy terms for this example are presented in polar plot to the left, and the total energy of equation E.1 is presented in linear plot to the right, so that the minimum to be scanned as a function of $\theta$ are clearly identified. The plots in this figure are just an example to qualitatively understand the mechanics of the procedure: the evolution of the magnetization as the external field is swept between two positive and negative maximum values is such that it always tries to keep sitting at the minimum of the energy thus expressed. Minimization of the energy as a function of the magnetization angle $\theta$ gives the evolution of the magnetization during the reversal. This are the basics of the Stoner-Wohlfarth model in brief. To follow the minimization process as the magnetic field is swept implies to draw many curves like those in the figure to the right of figure E.3, one for each different field value, and track the minimum position. Later in this chapter this process will be shown with the help of a real simulations (figure E.4)

The simulation software developed during this thesis is capable of accounting for several anisotropies, such as uniaxial, biaxial, trigonal, unidirectional (for Exchange Biased systems), several angles between them, and even more, up to two combinations of each kind. This means that we can combine up to 8 anisotropies. For this reason we use an abstract reference direction, that we have already introduced implicitly some paragraphs before, and referred all the anisotropy axis and the external field direction to that reference. In doing so, each anisotropy axes configuration are related to that direction by means of angle $\rho_K$ associated.

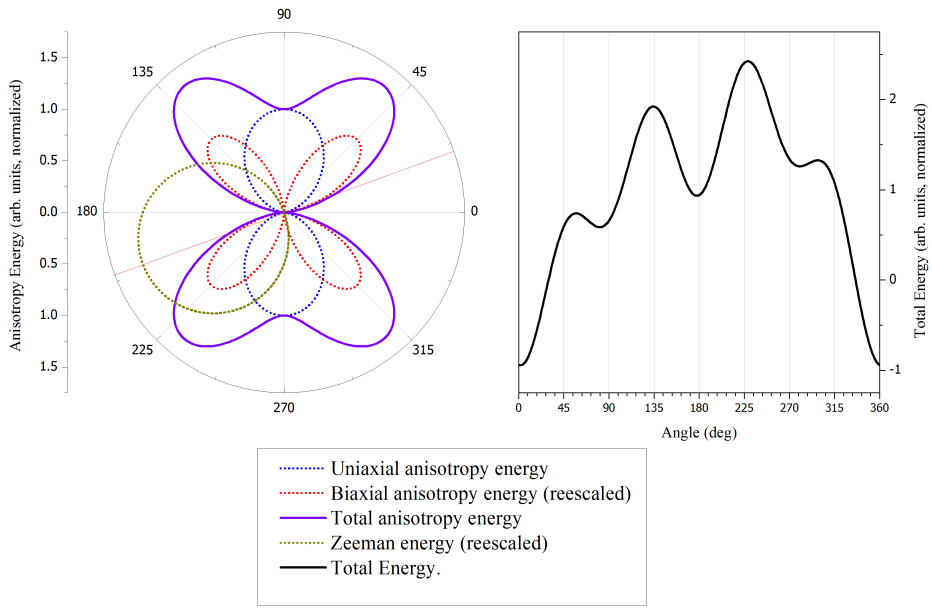


Figure E.3: Energy terms depicted in polar plot (to the left), and the corresponding total energy in linear plot (to the right). The polar plot allows to easily see the symmetries of the two anisotropies involved (blue and red, lobe shaped, dot lines). The minimums of these curves correspond to the anisotropy axis, as depicted in figure E.2. Total anisotropy energy is represented in the polar plot as a violet curve, where the combination of both anisotropies gives rise to minimums with different depth, the deepest one corresponds to the uniaxial axis, that adds up to the biaxial axis lying at that same angle. With green dots line appears the Zeeman energy term. This is an eccentric circle touching the zero point at an angle corresponding to $\theta$. The final total energy is the black curve in the linear plot to the right. Evolution of a similar curve with the magnitude of the external field is shown in figure E.1 to track minimums over a hysteresis loop.

For example, to simulate biaxial with uniaxial at 45° from each other, we could

set $\rho_{K_2}$ to 0 and $\rho_{K_1}$ to 45°. The zero angle reference direction for $\alpha_H$, i.e., the angle of the sample with respect to the external field, coincides with the biaxial axis. If we wanted to simulated what happens when the uniaxial axis is parallel to the external field, we then could use $\alpha_H$=45° for the field direction. Fixing the external field to 0° would then mean to put it parallel to one of the biaxial axes, and putting it to 135° will set it in between the biaxial axes and perpendicular to the uniaxial one.

Generalized expressions for the energy of each anisotropy is then like this:

$$E_{K_1} = K_1 sin^2\phi \tag{E.2}$$

$$E_{K_2} = \frac{K_2}{4} sin^2 2\phi \tag{E.3}$$

$$E_{K_3} = \frac{K_3}{6} sin^2 3\phi \tag{E.4}$$

$$E_{K_E} = K_E sin\phi \tag{E.5}$$

As already mentioned, the model can simulate two different anisotropies of each kind, so there are a couple of equations for each equation E.2 to E.5, each one with its corresponding anisotropy constants and angles with respect to reference directions.

In the context of the simulation software, the Zeeman energy is expressed as

$$E_Z = -Hcos(\theta) \tag{E.6}$$

Note that in this equation $\mu_0 M$ does not appear. This means that anisotropy constants $K_i$ in equations E.2 to E.5 are normalized to $M$, and H is given in mT, as well as $K_i$. Whenever we refer to anisotropy constants in the context of the SW or (later) Cowburn model, either they will be explicitly presented as divided by $M$, or it will be assumed to be so divided even if we do not express it. Notice as well that for simplicity, we use $M$=1, so the magnetization depicted in simulated hysteresis loops is normalized. All this aspects simplify very much the process of comparing with experimental data, since the hysteresis loops are also normalize and field is expressed in mT.

A real simulation (minimization process) can be seen in figure E.4. In this figure the energy curves evolution with $H_{EXT}$ can be seen, together with the tracks followed by the minimum position during the reversal, and the corresponding hysteresis loop thus generated. The example corresponds to a collinear biaxial-uniaxial system with $K_1$=0.2 mT and K2=1 mT, with an external field set at -27° of the uniaxial axis. We have scanned $H_{EXT}$ between -3.2 mT and 3.2 mT. To allow for easier understanding, we have used a very rough grid to scan $H_{EXT}$, so that the energy curves are well separated. The extreme values set for $H_{EXT}$ are chosen as a fraction of the grid step, so that the grid positions explored in the forward branch of the field swept are different than in the backward branch. With this trick, in figure (a) both forward and backward energy curves for the different $H_{EXT}$ values are visible, otherwise both branches would coincide and only one of then would be visible, due to overlapping. The blue energy curves correspond to forward branch ($H_{EXT}$ going from $+H_{MAX}$ to $H_{MAX}$) and the red ones to backward branch ($H$ going the other way around). Blue line and points are used to follow the forward minimum positions, and red ones for the backward track.

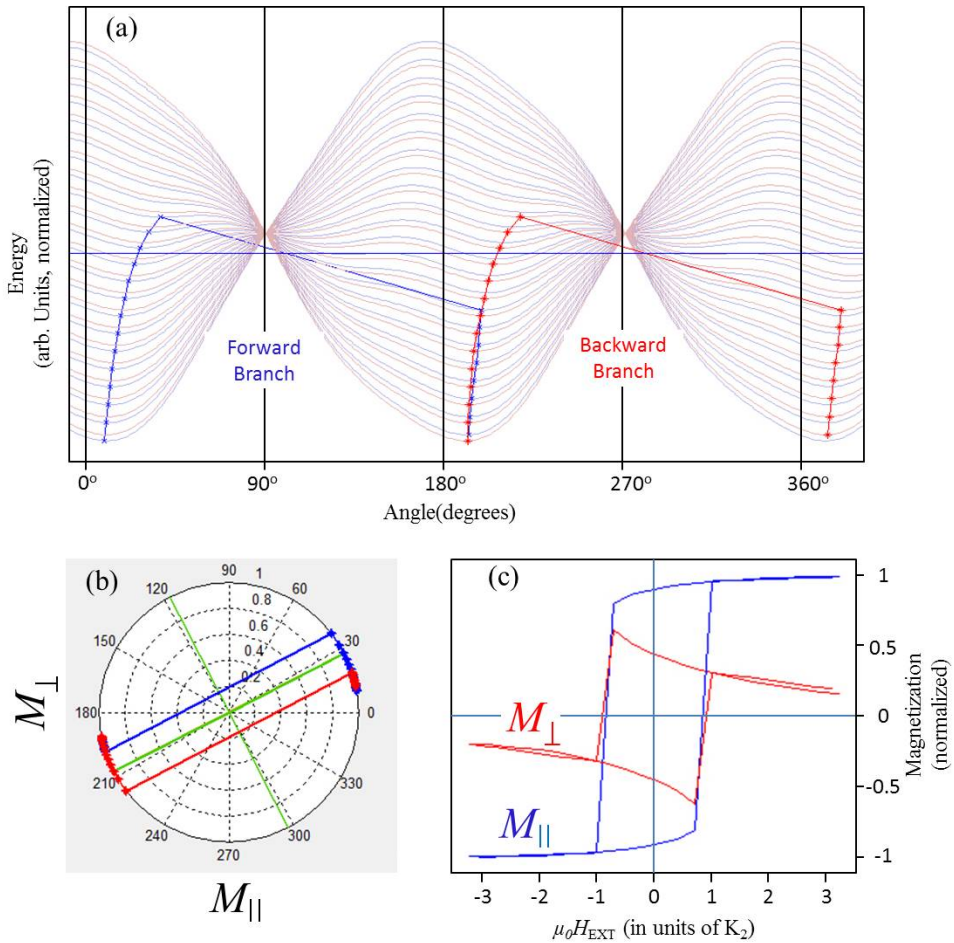


Figure E.4: (a) Family of energy curves for different $H$ values. Blue curves correspond to the forward branch, from $+H_{MAX}$ to -$H_{MAX}$, being $+H_{MAX}$ the one correspondinig to the beginning of the blue track of points. Red ones correspond to backward branch, form -$H_{MAX}$ to $+H_{MAX}$. The continuation of the blue track by the red points track marks the first red curve of the backward branch. This tracks give the magnetization angle $\theta$ for the energy minimum during the field swept. From this angle and the magnetization magnitude, set to unity for normalization, the parallel component to the external field, and the perpendicular one, can be obtained as a function of the field magnitude. (b) Polar plot obtained when $M_\perp$ is represented versus $M_\parallel$. Green lines represent the anisotropy axes as the sample is rotated 27° CCW. Blue points corresponds to the forward branch, and red points to the backward branch. (c) Hysteresis loops for Mpara (blue loop) and Mperp (red loop) obtained from $\theta$ directly by trigonometry (equations E.7 and E.8).

In the polar plot (b), the same color pattern is used to mark the corresponding

angles that follows the minimum of the energy. As the applied field is along -27° direction, the anisotropy axes appear rotated 27 degrees counter-clockwise from the field direction, set to zero ° (this is a convention to match experimental criteria, where the sample is moved in that direction while keeping the magnet fixed). It can be seen that the sample is not fully saturated by the external Field, as the starting minimum position does not correspond to 0°, but rather to something around 10°. From there, normalized magnetization follows the circle perimeter, indicative of rotation, until an abrupt jump flips it to the opposite direction. In figure (c) the corresponding hysteresis loops for the parallel and perpendicular components of M are depicted in blue and red color respectively. They are straightforward obtained by using the $\theta$ that minimizes energy, by simply trigonometry (with $M$=1):

$$M_{\parallel} = cos\theta \tag{E.7}$$

$$M_{\perp} = sin\theta \tag{E.8}$$

Unlike in figure E.1 where the loops have been approximated by hand using the little balls that followed the energy minimums, the hysteresis loops depicted in E.4 are real simulated loops directly obtained by the software developed in this thesis, with a non very dense grid for the external field, for didactic purposes.

The $H_{EXT,MAX}$ value used here is set having in mind the normalized usage of K that we are doing. It must be set to a value such that the transitions always lie in between the extreme values for any angle of $H_{EXT}$. In other words, we have to ensure that $H_C$ will always lie inside the range of $H_{EXT}$ for any angle. Otherwise the model would not show the transitions, and the loops would be incomplete. In the case we are using as example, in E.4, this means to set $H_{EXT}$ is around at least double the sum of $K_1$ and $K_2$. The reason is that $H_C$ at an easy axis in SW model corresponds to double the anisotropy constant divided by $M$. Our anisotropy constants are divided by $M$, as explained earlier, and the easiest axis correspond to that of the uniaxial axis, where one of the biaxial is also present (parallel). When using simulation software, a good value for $H_{EXT,MAX}$ should be tested at characteristic axes before trying to explore any other external field angle in a complete angular run.

We have explained that we use $M$=1 in the simulations. Now we add a comment on this respect. In addition to what has been already explained, putting $M$=1 brings another benefit, since the experimental v-MOKE technique used in this thesis (explained in sections 1.7, F and chapter 2) does not account for absolute values of it, so it is customary to keep it normalize. We take as unity the magnetization found at an easy axis, where the system is fully saturated, and this is why we are using $M$=$M_{SAT}$ in previous explanations. This assumption allows simplifying considerably the problems of units. If we needed to have the real $M$ value, we should complement our v-MOKE experiments with a suitable technique for that purpose (for example, VSM). Only relative values are obtained in experiments using v-MOKE, so the simulations will be done using the same criteria.

### E.1.2 The simulation software

The simulation software has been developed using MatLab, both the programmatic environment and the GUI (Graphical User Interface) environment, so as to make a

user friendly generalist application. The software has two main individual GUI modules, with a set of program modules called as routines responding to the GUI events, allowing the interaction with the user and performing the simulation tasks. They are:

```
exe_SW_GUI_Energy
exe_SW_GUI
```

The first one, entitled Energy Module, is used to plot the energy curves and the track that follows the minimum of energy, as the hysteresis loop is done, i.e., as the external field is swept. The aim of this module is to allow the user to get an idea of how the minimization process is carried out by the application, in order to check maximum external field values suitable for the full angular range simulation. This application can be used as well to detect any irregularity in the process, for checking the $H$ grid or for debugging procedures during development of any improvement in the software. In addition, is very useful for didactic purposes.

The application allows to

1. Plot the energy curves, the minimum position evolution (the track that configures the angle between $M$ and the reference direction allowing to decompose components along the external field direction.

2. Plot the hysteresis loops as they are created during the tracking of the minimum position.

3. Plot in polar coordinates the evolution of the magnetization vector.

Some additional options such as scale control, options to plot only the parallel or the perpendicular components, controls to change the angle of the external field in incremental steps by pressing single button, as well as a map of the anisotropy configuration, are implemented to make life easier.

The second one is the main SW simulation software entitled Hysteresis Module. It allows scanning a full or limited angular range for the external field direction, performing for each direction all the field sweep process to obtain the hysteresis loops and extract from them the magnetic parameters such as remanence and transition fields for each component of the magnetization. For each angle it creates the hysteresis loop in an internal matrix that is translated later to a text file stored in the computer disk, and additional angular tables that can be imported by other graphing software. Once the simulation is started, the application runs all the scans selected, under the anisotropy configuration previously set. After finishing, the hysteresis loops can be displayed in many ways, such as all at once, angle by angle, with selection of the components to be displayed. The angular plots of the different magnetic properties, such as transition fields and remanences can be also displayed, as well as 3D graphs of the angular evolution of the hysteresis loops. Magnetoresistance and the magnetic torque are also included in the software.

In fig. E.5 a screenshot of the `exe_SW_GUI_Energy` module can be seen, corresponding to the simulation exhibited in figure E.4. Figure E.6 shows a screenshot of the `exe_SW_GUI` module with a scan of hysteresis loops every 5° between 0° and 40° for a biaxial system with $K_2$=1. Hysteresis loops are stacked in the plot. In figure E.7

the options "M Rem. L" and "M Rem. P" have been marked to make appear the angular evolution of the parallel and perpendicular remanences, seen in the linear and polar plots of the screen. Figure E.8 shows the 35° hysteresis loop in biaxial system, with characteristic double transitions.

In figure E.9 a full angular 3D plot of the parallel component of the magnetization (hysteresis loops) for the same anisotropy configuration can be seen, where easy axes appear as a square tunnel that is constrained as angle approaches hard axes, and in figure E.10 perpendicular component 3D plot is shown, that looks a bit more intricate. As the transition jumps make the 3D plot change abruptly the color pattern, the 3D plots reveals the angular evolutions of transition fields, when seen from above, as drastic changes of color pattern. Different cuts in the 3D maps can provide additional information (not explored here).

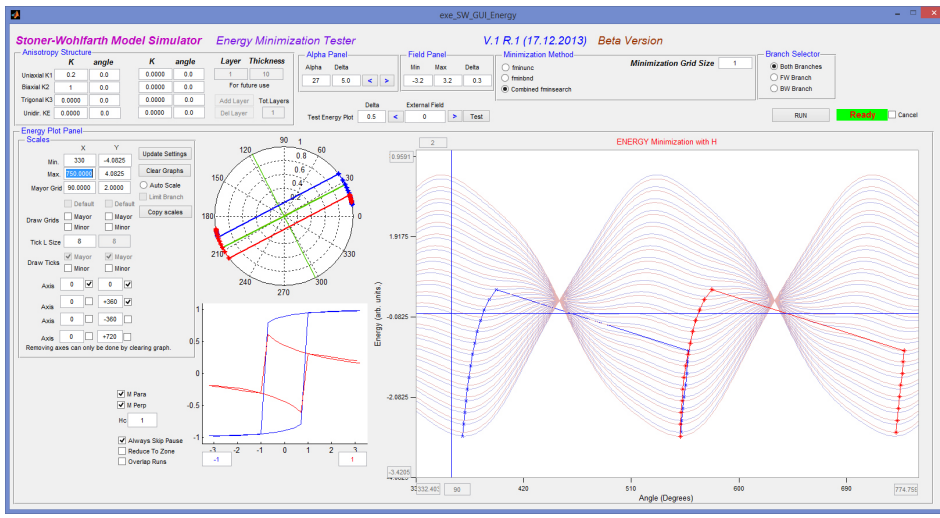


Figure E.5: Screenshot of the energy module `exe_SW_GUI_Energy`. Top panels are used to set the anisotropy parameters, the field parameters, and some aspects concerning the minimization process, and left panel contains the scaling parameters for the graphs. Top left graph is the $M_{\parallel}$ v.s. $M_{\parallel}$ polar plot of the hysteresis, that is depicted bottom left. The bigger graph to the right corresponds to the total energy family of curves as the external field magnitude is varyed by the simulation, and the $\phi$ magnetization angle minimum position tracks (superimpossed in blue and red).

The magnetic anisotropies are labeled in the following way:

1. Uniaxial, referred as $K_1$.
2. Biaxial, referred as $K_2$.
3. Trigonal, referred as $K_3$.
4. Unidirectional, referred as $K_E$.

Up to two independent anisotropies of each kind can be configured, in strength and angle with respect to the reference direction. The anisotropy configuration panel used in both GUI application can be seen in figure E.11. An additional set of parameters have been left ready for future implementation of multilayer configurations.

In order to allow more massive studies, a Multi-Scan option has been included, that permits scanning a range of values on each anisotropy, both in the $K$ value and in the angle. For example, we could perform a scan over $K_1$ angle with respect to $K_2$ in a biaxial with a uniaxial anisotropy superimposed, together with a scan on the $K_1/K_2$ ratio. We could for instance configure $K_2$ angle as 0°, and scan on $K_1$ angle from 0° to 45° every 2.5°, and for each angle, scan on $K_1$ value from 0.1 to 0.5 every 0.1, leaving $K_2$ set to unity. Multi-scan combinations are very difficult to program under a generalist way in the GUI interface. Instead, the program loops are pre-programmed, and can be easily changed in the code. Once a sequence of scans are written, the values for the scan and the interval can be varied without re-programming the loops, by using an external file. This file supports all the possible parameters that could be pre-programmed for scanning. This kind of scans is very useful for fitting procedures, as will be seen in later chapters. For example, if we want to check the collinearity in a biaxial with uniaxial anisotropy, we can do scans to fit the experimental angular evolutions.

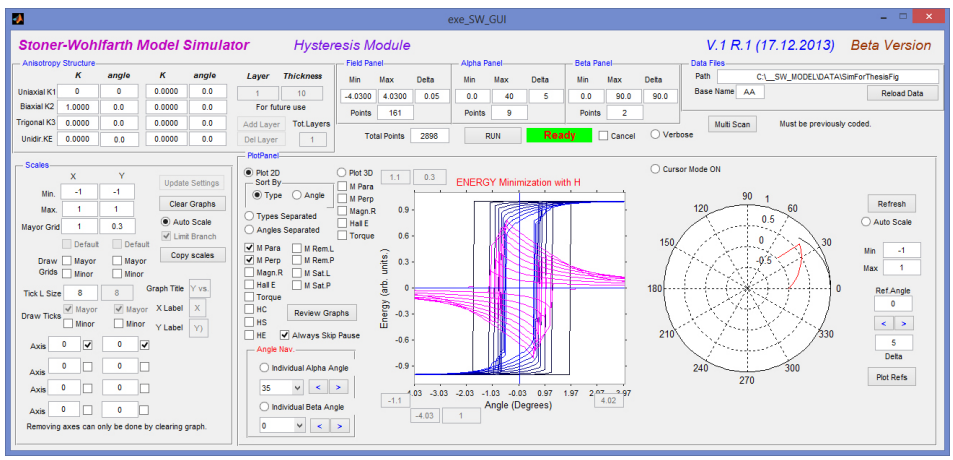


Figure E.6: Screenshot of the hysteresis module `exe_SW_GUI`. Top panels are used to set the anisotropy parameters, the field parameters, and the angular scan ranges for the external field direction, $\theta$, referred here as "alpha panel", and the current direction "beta panel" (this last one is for the magnetoresistance simulation'). Left panel contains the scaling parameters for the graphs. The graphs panel contains two graphs layouts, one is linear (square layout) and the other one is polar (circular layout). On the left side of the linear plot the different contents for each plot can be selected. In this case, a simulation with $K_2$=1 has been run, and the linear plot exhibits some hysteresis loops, while the polar plot shows a small part of the parallel and perpendicular remanence evolution with external field angle.

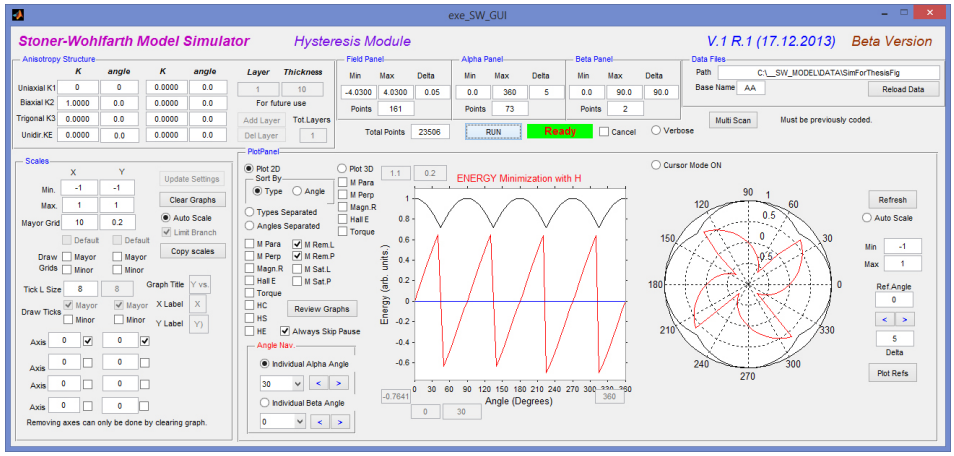


Figure E.7: Screenshot of the hysteresis module `exe_SW_GUI` as in figure E.6, showing parallel and perpendicular remanences for the full angular range, both in linear and polar plot.

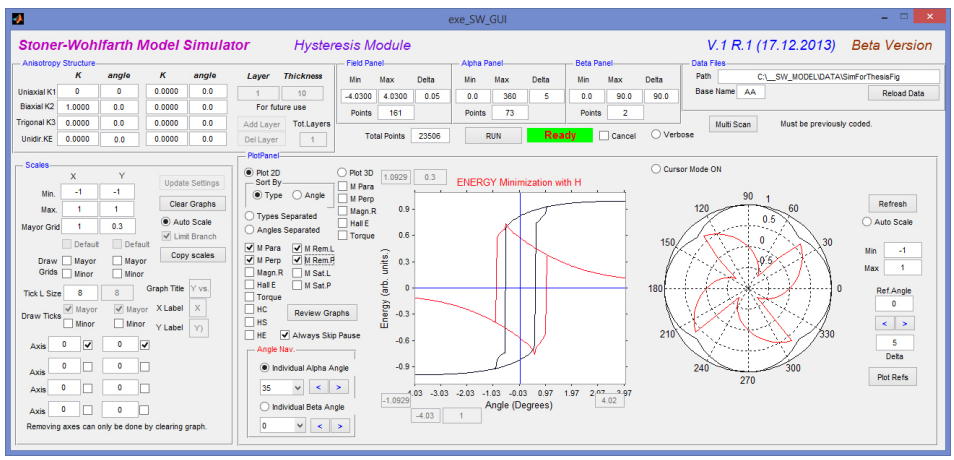


Figure E.8: Screenshot of the hysteresis module `exe_SW_GUI` as in figure E.6, showing parallel and perpendicular single hysteresis loops at 35°, with the polar plot of the remanence components.

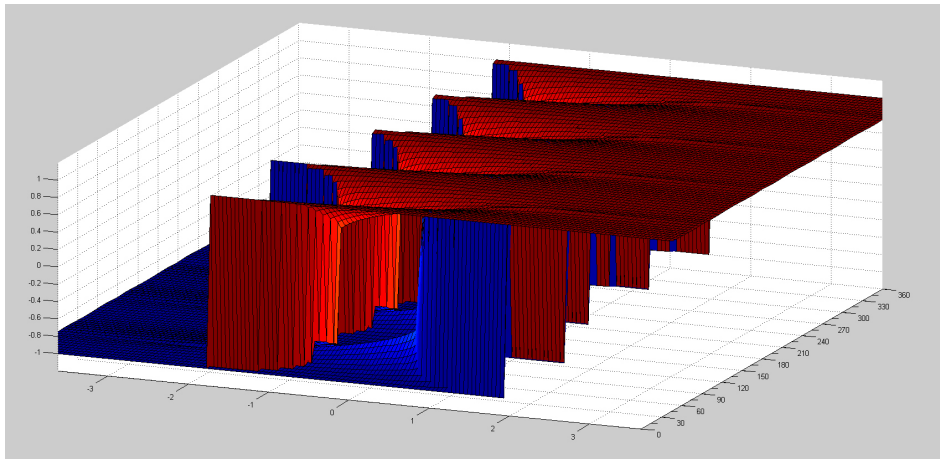

Figure E.9: 3D plot of the parallel component hysteresis loop with angle. As this kind of 3D plots can be rotated in MatLab, they are useful to get an idea of the angular evolution.

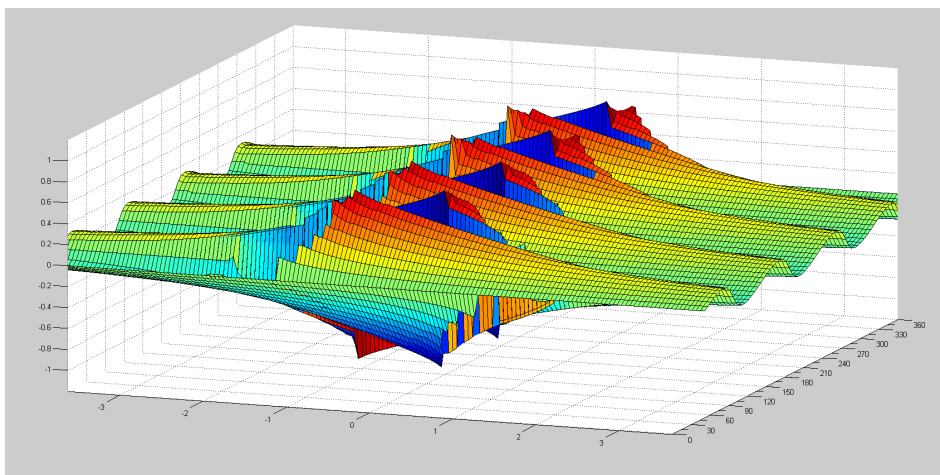

Figure E.10: 3D plot of the perpendicular component hysteresis loop with angle.

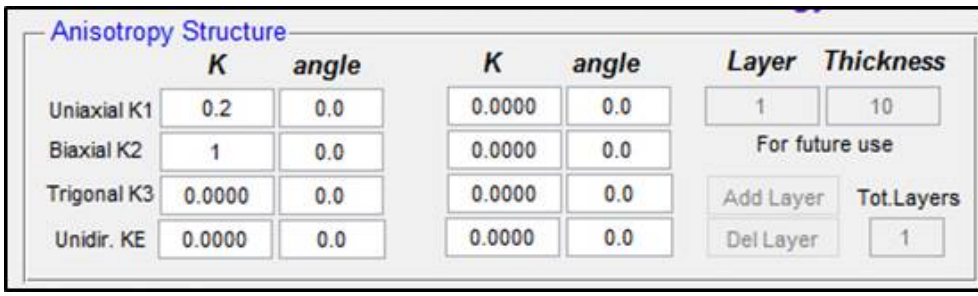


Figure E.11: The anisotropy panel, where the different configurations can be set.

## E.2 Cowburn model

In this appendix we give details on how Cowburn model proceeds to obtain transition fields. Notice that in the following, Cowburn model talks about transition field $H_{C,1}$ and $H_{C,2}$, where these two quantities are the position of the jumps in the parallel components of the hysteresis loop (eventually, a third jump can happen in 3-transition reversals). In the hysteresis loops analyzed in this thesis, we use the same criteria. However, it is interesting to mention here that the second jump in a parallel component for a 2-jumps reversal, corresponds to the transition field in the perpendicular component, i.e., is the switching field $H_S$.

### E.2.1 Mathematical formulation of the Cowburn model for collinear uniaxial-biaxial system

For a collinear uniaxial-biaxial system, the starting point in Cowburn model is equation E.1 in section 1.6 for the SW model energy (however beware of a change in angle notation, explained later). Consider a system with biaxial anisotropy directions oriented in [100] and [010], and a collinear uniaxial anisotropy oriented in the [100] direction. This last one direction is called the super easy axis or e.a. I because the anisotropy here is greater than that of the perpendicular direction, which only has the biaxial axis. We are going to consider the reference zero direction as the e.a.I, and use the notation $\theta$ for the magnetization angle with respect to that direction, and $\phi$ for the external field with respect to the same reference direction. Notice that these angle definitions are not the same as the notation used in SW model, and the geometrical diagram can be seen in figure E.12. The reason for that change of notation is to make it easier to understand the jump diagrams that will be used in the following development. The writing of the SW energy terms is straightforward. With this change of notation, equation E.1 reads

$$E = K_1 sin^2\theta + \frac{K_2}{4} sin^2 2\theta - MHcos(\theta - \phi) \tag{E.9}$$

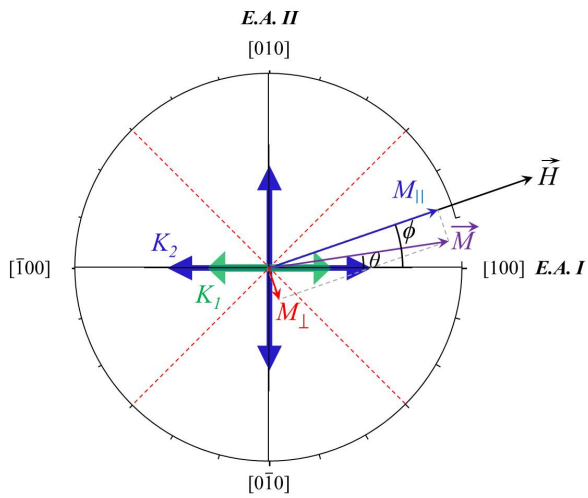


Figure E.12: Axis configuration and crystalline directions for the collinear uniaxial-biaxial system. Blue arrows correspond to the biaxial anisotropy axes, and red arrow corresponds to the uniaxial one. 0° and 180° are the super easy axis direction, while 90° and 270° are the normal biaxial axes. In dashed red the hard axes for the biaxial alone are depicted. (Do not confuse these red dashed lines with the true hard axes for this anisotropy configuration: while easy axis remains at 90° in a collinear uniaxial-biaxial anisotropy, hard axes do not).

At low fields the minimums of equation E.9 will lay on the angles where the anisotropies are located, i.e., aproximately at 0°, 90°, 180° and 270°. Single domain states at these angles have energies that are obtained after substitution of the corresponding $\theta$ angles in equation E.1:

$$E_{[\bar{1}00]} = MHcos\phi \tag{E.10}$$

$$E_{[100]} = -MHcos\phi \tag{E.11}$$

$$E_{[0\bar{1}0]} = K_1 + MHsin\phi \tag{E.12}$$

$$E_{[010]} = K_1 - MHsin\phi \tag{E.13}$$

When we consider the external field applied at an angle between 0° and 45°, the single domain closer to that direction is at [100], so we are dealing with reversal of the magnetization from [$\bar{1}$00] direction to [100]. In figure E.13 we have depicted the scheme for the configuration and the different routes that could be considered. The direct jump would go from [$\bar{1}$00] to [100], with expansion of DW at 180°, represented by a blue arrow in the figure. The 2-steps route would go from [$\bar{1}$00] to [010] in the first step, and from [010] to [100] in the second step, with DW at 90° in both steps, and is represented by green arrows. Due to the angular range for the external field considered, a 3-steps route like the one marked with red arrows on figure E.13 is not possible (demonstration of this impossibility is not shown). However it was

shown experimentally that above 45°, where the closest local minima to the external field directions would rather be on the ⟨010⟩ directions, a 3-steps route could happen. In figure E.14 such possibility is depicted together with a possible competing 2-steps route (in red and green arrows respectively) for this external field angular range, where the closer minima is at $[0\bar{1}0]$. This 3-steps route would follow the single domains states from $[0\bar{1}0]$ to $[\bar{1}00]$ in the first step, from there to [100] in the second step, and last from [100] to [010] in the third step. DW in this 3-step route are 90° for the first step, 180° for the second one and 90° for the third.

The possible routes available for a reversal will compete in between, in terms of the energy cost of each jump. The analysis of the energies involved and the coercive fields derived from them will tell the conditions that must be fulfilled to get the true route that the reversal will take.

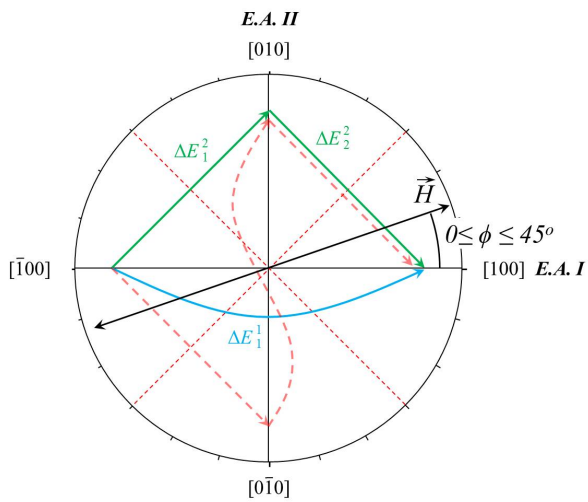


Figure E.13: Diagram of the possible reversal routes for angles between 0° and 45°. At this angles of the external field, the departure direction for the reversal is $[\bar{1}00]$, reversing towards [100]. A single jump route is depicted with waving blue arrow. A 2-steps route is depicted using green arrows. A 3-step route, not analyzed for this angles, is depicted in red dashed straight and waving arrows. The jumps are marked with the same nomenclature as in the equations for the corresponding energy increments. As superindex the total number of steps in the route is marked, and as subindex it is marked the jump number inside that route.

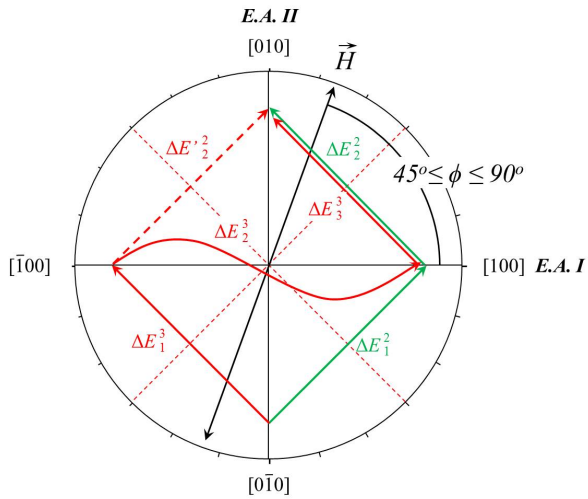


Figure E.14: Diagram of the possible reversal routes for angles between 45° and 90°. At this angles of the external field, the departure direction for the reversal is [0$\bar{1}$0], reversing towards [010]. A 2-steps route is depicted using green arrows. A 3-step route is depicted in red straight and waving arrows. The second jump of this 3-step route competes with a jump depicted in red dashed arrow. The jumps are marked with the same nomenclature as in the equations for the corresponding energy increments. As superindex the total number of steps in the route is marked, and as subindex it is marked the jump number inside that route. For the dashed jump, that is not part of the 2-steps and 3-steps routes depicted, a prime has been added.

To write the energy required for each jump, we have enumerated each jump in figures E.13 and E.14 by using a superindex that indicates the number of steps for the reversal, and as subindex the jump index. For instance, $\Delta E_1^2 = E_{[\bar{1}00]} - E_{[010]}$ corresponds to the first jump of a 2-steps route.

We assume that when two possible jumps compete in between to decide the reversal route, the one that happens at the lower coercive field will be the one observed. For example for angles between 0° and 45°, the direct jump competes with the first jump of the 2-steps route.eps route, as depicted in figure E.13.

In order to get the lower coercive field associated to each jump, we use one of the key points of the model: at the coercive field, the energy difference between the single domain configurations is the depinning energy of the corresponding DW involved (either 90° or 180°). We use the symbols $\epsilon_{90^\circ}$ and $\epsilon_{90^\circ}$ for the corresponding energies. This means that on each energy equation for each jump, when we substitute $H$ by the coercive field $H_C$ for the corresponding jump, the resultant energy is the DW energy for the corresponding DW angle, i.e., we have to substitute $\Delta$E by the corresponding $\epsilon$, i.e., by $\epsilon_{90^\circ}$ or $\epsilon_{180^\circ}$ depending on the orientations between spins of the departure single domain state and the arrival one.

For simplicity we are going to deal first with the competition between 1-step route and 2-steps route as in figure E.13. Let us consider the angular range $0° \leq \phi \leq 45°$.

The jumps involved for the 1-step reversal and the 2-steps reversal are:

$$\Delta E_1^1 = E_{[\bar{1}00]} - E_{[100]} = 2MHcos\phi \tag{E.14}$$

for the single jump of the 1-step route, and

$$\Delta E_1^2 = E_{[\bar{1}00]} - E_{[010]} = MH(cos\phi + sin\phi) - K_1 \tag{E.15}$$

$$\Delta E_2^2 = E_{[010]} - E_{[100]} = MH(cos\phi - sin\phi) + K_1 \tag{E.16}$$

Now, at the coercive field for each jump, the corresponding energy is the DW energy of the associated spin reorientation. In equation E.14, at $H_C$, $\Delta E_1^1$ corresponds to the 180° DW, i.e., to $\epsilon_{180^\circ}$, while in equations E.15 and E.16, the intervening DW are 90° domain walls, so at $H_{C1}$, we have $\Delta E_1^2 = \epsilon_{90^\circ}$, and at $H_{C2}$ is $\Delta E_2^2 = \epsilon_{90^\circ}$. substituting we get the following equations for the corresponding coercive fields:

$$H_C = \frac{\epsilon_{180^\circ}}{2Mcos\phi} \tag{E.17}$$

$$H_{C1} = \frac{\epsilon_{90^\circ} + K_1}{M(sin\phi + cos\phi)} \tag{E.18}$$

$$H_{C2} = \frac{\epsilon_{90^\circ} - K_1}{M(sin\phi - cos\phi)} \tag{E.19}$$

It is easier to extend to all angles, and the results are summarized here
1-step route:

$$H_C = \begin{cases} H_C = \frac{\epsilon_{180^\circ}}{2M|cos\phi|} & -45^\circ \leq \phi \leq 45^\circ, 135^\circ \leq \phi \leq 225^\circ \\ H_C = \frac{\epsilon_{180^\circ}}{2M|sin\phi|} & 45^\circ \leq \phi \leq 135^\circ, 225^\circ \leq \phi \leq 315^\circ \end{cases} \tag{E.20}$$

2-steps route:

$$H_{C1,2} = \frac{\epsilon_{90^\circ} \pm K_1}{M(\pm cos\phi \pm sin\phi)} \tag{E.21}$$

where the signs for each $H_{C1}$ and $H_{C2}$ are given by table E.15

| Angular ranges (degrees) | | 1-step route | | 2-steps route | | | | | |
|---|---|---|---|---|---|---|---|---|---|
| | | HC | | HC1 | | | HC2 | | |
| From | To | cos Term | sin Term | Ku Term | cos Term | sin Term | Ku Term | cos Term | sin Term |
| 0 | 45 | 1 | 0 | 1 | 1 | 1 | -1 | 1 | -1 |
| 45 | 90 | 0 | 1 | -1 | 1 | 1 | 1 | -1 | 1 |
| 90 | 135 | 0 | 1 | -1 | -1 | 1 | 1 | 1 | 1 |
| 135 | 180 | 1 | 0 | 1 | -1 | 1 | -1 | -1 | -1 |
| 180 | 225 | 1 | 0 | 1 | -1 | -1 | -1 | -1 | 1 |
| 225 | 270 | 0 | 1 | -1 | -1 | -1 | 1 | 1 | -1 |
| 270 | 315 | 0 | 1 | -1 | 1 | -1 | 1 | -1 | -1 |
| 315 | 360 | 1 | 0 | 1 | 1 | -1 | -1 | 1 | 1 |

Figure E.15: Table of signs for the different terms as a function of the angle, for 1-step and 2-step route

Now we impose the condition that when two jumps are in competition, the jump that will take place is the one with the lower $H_C$ value. In the angular range $0° \leq \phi \leq 45°$ the jumps in competition are $[\bar{1}00] \rightarrow [100]$ (the single 1-step jump) and $[\bar{1}00] \rightarrow [010]$ (the first jump of the 2-steps route) . So if we want to get a 2-steps route for the reversal, we need to impose that $H_{C1}$ in equation E.18 be lower than $H_C$ in equation E.17. Comparing equations we get the conditions for the angular range of the 1-step route as:

$$\begin{array}{ll} tan\phi < 2\frac{\epsilon_{90°}+K_1}{\epsilon_{180°}} - 1 & 0° \leq \phi \leq 45° \\ cot\phi < 2\frac{\epsilon_{90°}-K_1}{\epsilon_{180°}} - 1 & 45° \leq \phi \leq 90° \end{array} \tag{E.22}$$

In addition, equations E.20 enable us to obtain the domain wall energies by measuring the experimental coercive fields at certain angles. When the field is along [100], $\phi$ is zero, so that the first expression in E.20 leads to the value of $\epsilon_{180°}$:

$$\epsilon_{180°} = 2MH_C^{[100]} \tag{E.23}$$

Looking at the direction [010], and using equation E.21 leads to the expresion for $\epsilon_{90°}$:

$$\epsilon_{90°} = \frac{1}{2}M(H_{C1}^{[010]} + H_{C2}^{[010]}) \tag{E.24}$$

as well as for the value of the uniaxial anisotropy:

$$K_1 = \frac{1}{2}M(H_{C2}^{[010]} - H_{C1}^{[010]}) \tag{E.25}$$

Observe that although the angular range used in the previous process was $0° \leq \phi \leq 45°$, the angular range conditions for each type of route and the coercive fields involved are general, extended over the whole angular range. In particular, it is clear that they preserve the symmetries of the problem.

Now we are going to examine the possibility of a 3-steps route. We expect this possibility to happen in the angular range $45° \leq \phi \leq 90°$, so that the jump's energies involved are as depicted in figure E.14:

for the 2-steps route:

$$\Delta E_1^2 = E_{[0\bar{1}0]} - E_{[100]} = MH(cos\phi + sin\phi) + K_1 \tag{E.26}$$

$$\Delta E_2^2 = E_{[100]} - E_{[010]} = MH(sin\phi - cos\phi) - K_1 \tag{E.27}$$

and for the 3-steps route:

$$\Delta E_1^3 = E_{[0\bar{1}0]} - E_{[\bar{1}00]} = MH(sin\phi - sin\phi) + K_1 \tag{E.28}$$

$$\Delta E_2^3 = E_{[\bar{1}00]} - E_{[100]} = 2MHcos\phi \tag{E.29}$$

$$\Delta E_3^3 = E_{[100]} - E_{[010]} = MH(sin\phi - cos\phi) - K_1 \tag{E.30}$$

in addition, we include the energy of the jump named as $\Delta E_2^{'2}$, corresponding to the dashed red arrow in figure E.14, because this possible jump enters into play if the fist jump of the 3-steps route is to happen, as will be seen very soon:

$$\Delta E_{2}^{`2} = E_{[\bar{1}00]} - E_{[010]} = MH(cos\phi - sin\phi) - K_1 \tag{E.31}$$

the jumps that are in competition in this case are the following:

- First, the jump from $[0\bar{1}0]$ to $[\bar{1}00]$ for the first jump in the 3-steps route has to compete with the jump from $[0\bar{1}0]$ to $[100]$ for the first jump in a 2-steps route. The energies in competition are given by equations E.28 and E.26 respectively.

- If it success to do this jump, then the second jump of the 3-steps route, from $[\bar{1}00]$ to $[100]$ will have to compete with the jump from $[\bar{1}00]$ to $[010]$ for the second jump of a (different to the first) 2-steps route. The energies in competition are given by equations E.29 and E.31 respectively.

Observe that for the third jump in the 3-steps route there is no competition at all, and the corresponding coercive field should (and in fact will) be equal to the coercive field of the second jump in the corresponding 2-steps route.

With a little algebra, we get from each equations the corresponding conditions for the triple jump to happen:

$$\frac{\epsilon_{90^o} - K_1}{sin\phi - cos\phi} \leq \frac{\epsilon_{90^o} - K_1}{sin\phi + cos\phi} \quad 45° \leq \phi \leq 90° \tag{E.32}$$

$$\frac{\epsilon_{180^o}}{2cos\phi} \leq \frac{\epsilon_{90^o} - K_1}{sin\phi + cos\phi} \quad 45° \leq \phi \leq 90° \tag{E.33}$$

the first condition is satisfied if $\epsilon_{90^o} \leq K_1$. For the second one, we use the approximated expression $\epsilon_{180^o} = 2\epsilon_{90^o}$ and solving for $\phi$ to get:

$$45^o < tan^{-1}(\frac{K_1}{\epsilon_{90^o}}) \tag{E.34}$$

If we now gather together all conditions for the different possible reversal routes, we can generate magnetic phase diagram as depicted in figure E.16.

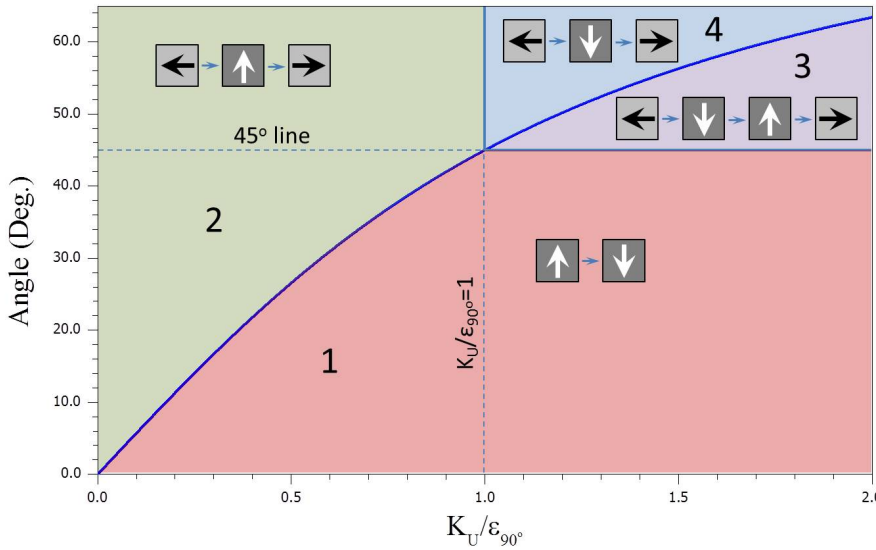


Figure E.16: A summary of the different routes are depicted here (following Cowburn et Al. in ref [21]). The curve blue curve separating the regions 1 and 3 from 2 and 4 corresponds to atan($\frac{K_1}{\epsilon_{90^o}}$). The other separating lines are marked in dashed lines. The horizontal one is located at angle 45°, and the vertical one is located at 1. The single domain orientations taking part in the reversals are depicted in small grey boxes with black or white arrows.

### E.2.2 Practical implementation of the model

For practical calculations, the model has been implemented (for simplicity reasons) directly by using a Microsoft EXCEL workbook where the angles have been spread in a column, and the coercive fields have been calculated in columns apart by direct application of the equations describe thus far taking into account the corresponding angular ranges of applicability. The Workbook has a similar aspect to the one shown in figure E.17. In the header of the workbook there is a box in which the phenomenological parameters are set, together with the $K_1/K_2 2$ ratio for which we want to do the simulation. The workbook includes a special sheet (not shown) in which data is trespassed in four single columns named Angle, $H_{C1}$, $H_{C2}$ and $H_{C3}$, where $H_{C1}$ refers either to $H_C$ in 1-step reversals and to $H_{C1}$ in multiple steps reversals, and $H_{C2}$ and $H_{C3}$ can be lefft unfilled in the cases where the do not apply. This 4-columns special sheet is suitable to export data to other software, such as Origin (demonstration graphs presented below have been done with Origin as is customary in this thesis).

Parameters of the model

| | $H_C$[100] | $H_{C1}$[010] | $H_{C2}$[010] | M | $K_U$ Simul | φ | $\varepsilon_{180}$ | $\varepsilon_{90}$ |
|---|---|---|---|---|---|---|---|---|
| Exp. Data | 0,678 | 0,229 | 1,084 | 1 | 0,8 | 0,0001 | 1,356 | 0,6565 |

3 jumps symmetric limits

| atan($K_u/\varepsilon_{90}$) = Ψ | 180-Ψ | 180+Ψ | 360-Ψ |
|---|---|---|---|
| 50,627 | 129,373 | 230,627 | 309,373 |

| Ku Calculado | 0,4275 |
|---|---|

| Angle | Range EQ | Sign table | | | | | | | | 1-Jump HC | 2-Jumps HC1 | 2-Jumps HC2 | 3-jumps Regions | 3-jumps HC1 | 3-jumps HC2 | 3-jumps HC3 |
|---|---|---|---|---|---|---|---|---|---|---|---|---|---|---|---|---|
| 30 | 5 | 1 | 0 | 1 | 1 | 1 | -1 | 1 | -1 | 0,783 | | | | | | |
| 32,5 | 5 | 1 | 0 | 1 | 1 | 1 | -1 | 1 | -1 | 0,804 | | | | | | |
| 35 | 5 | 1 | 0 | 1 | 1 | 1 | -1 | 1 | -1 | 0,828 | | | | | | |
| 37,5 | 5 | 1 | 0 | 1 | 1 | 1 | -1 | 1 | -1 | 0,855 | | | | | | |
| 40 | 5 | 1 | 0 | 1 | 1 | 1 | -1 | 1 | -1 | 0,885 | | | | | | |
| 42,5 | 5 | 1 | 0 | 1 | 1 | 1 | -1 | 1 | -1 | 0,920 | | | | | | |
| | | | | | | | | | | | | 5900896724,31 | | | | |
| 45 | 6 | 0 | 1 | -1 | 1 | 1 | 1 | -1 | 1 | | -0,101 | 3 | | | | |
| 47,5 | 6 | 0 | 1 | -1 | 1 | 1 | 1 | -1 | 1 | | -0,102 | 23,611 | 1,000 | -2,326 | 1,004 | 23,611 |
| 50 | 6 | 0 | 1 | -1 | 1 | 1 | 1 | -1 | 1 | | -0,102 | 11,817 | 1,000 | -1,164 | 1,055 | 11,817 |
| 52,5 | 6 | 0 | 1 | -1 | 1 | 1 | 1 | -1 | 1 | | -0,102 | 7,890 | | | | |
| 55 | 6 | 0 | 1 | -1 | 1 | 1 | 1 | -1 | 1 | | -0,103 | 5,931 | | | | |
| 57,5 | 6 | 0 | 1 | -1 | 1 | 1 | 1 | -1 | 1 | | -0,104 | 4,758 | | | | |
| 60 | 6 | 0 | 1 | -1 | 1 | 1 | 1 | -1 | 1 | | -0,105 | 3,979 | | | | |

Figure E.17: Calculation for Cowburn model have been implemented in Microsoft Excel, so that after setting the parameters in top left box, columns with corresponding $H_{C1}$,$H_{C2}$ and $H_{C3}$ are calculated. Data can be exported to other graphing software.

A normalization criterion has been used, dividing everything by M. This is carried out by simply setting M to unity. The anisotropy ratios are set by considering $K_2$ equal to unity, so that the ratio is directly the $K_1$ value. This is equivalent to normalize the anisotropy constants to $K_2$. A simulation for various ratios $K_1/K_2 2$ is presented in Fig. E.18.

In figure Fig. E.19 we show a simulated case where three transitions are observed. Note that the first jump of the 3-step route is at negative value. This means that the jump happens when the external field has not yet traversed the vertical axis, i.e., it happens before the external field has been reversed.

Some important observations must be done. First of all, $K_2$ is absent in all the formulas in the Cowburn model. The reason for that is very simple: because when substituting $\theta$=0°,90°,180° and 270° the sine function of double these angles is zero. Another way to think about it is by noting that the biaxial contribution is always the same for those angles where the single state domain happens. So even if it were not zero, it would be the same for all the four axis directions, adding a constant term to the total energy. Only the relative value of $K_1$ with respect to $K_2$ would be relevant.

If the uniaxial anisotropy where non collinear, all the calculations previously done would be more complex. Another thing to note is that without uniaxial anisotropy, Cowburn model would not predict 3-route transitions at all.

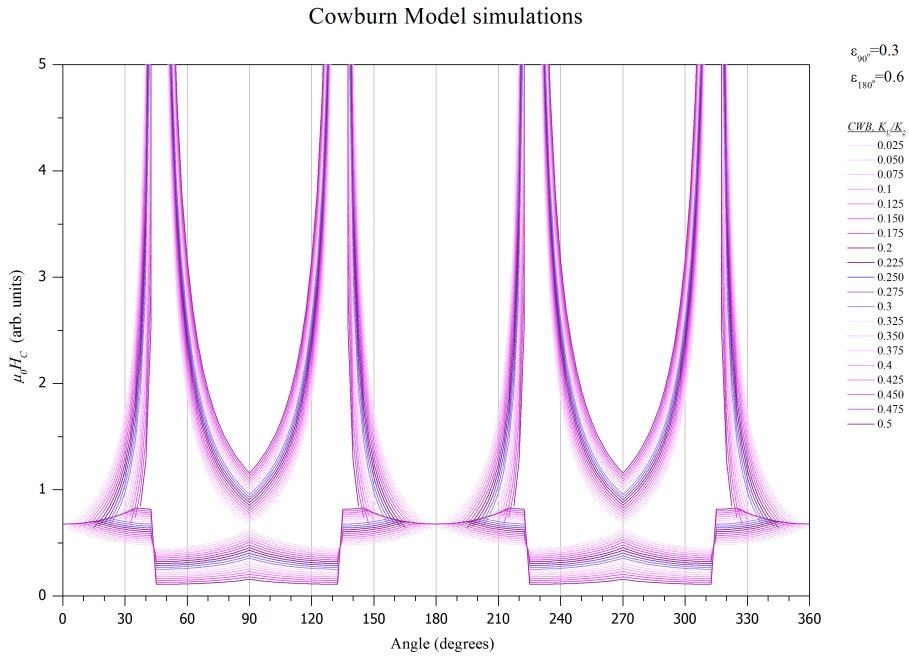


Figure E.18: Family of curves with $K_1/K_2$ from 0.025 up to 0.3 in a collinear biaxial-uniaxial system simulated with CW. For each $K_1/K_2$ ratio two branches can be distinguished: the branch running below unity corresponds to $H_{C1}$, while the branch above it corresponds to $H_{C2}$. Note that $H_{C1}$ is not always present, and there are regions with single step reversals, and regions with 2-steps reversals. As there are many curves represented here, color patterns are not easy to set. For simplicity, note that lowest $H_{C1}$ curves are associated to higher $H_{C2}$ curves. This is just for qualitative illustration. Note as well that no 3-steps reversals are present for the parameters used in this simulation ($\epsilon_{90°}$ is 0.6. for this simulation)

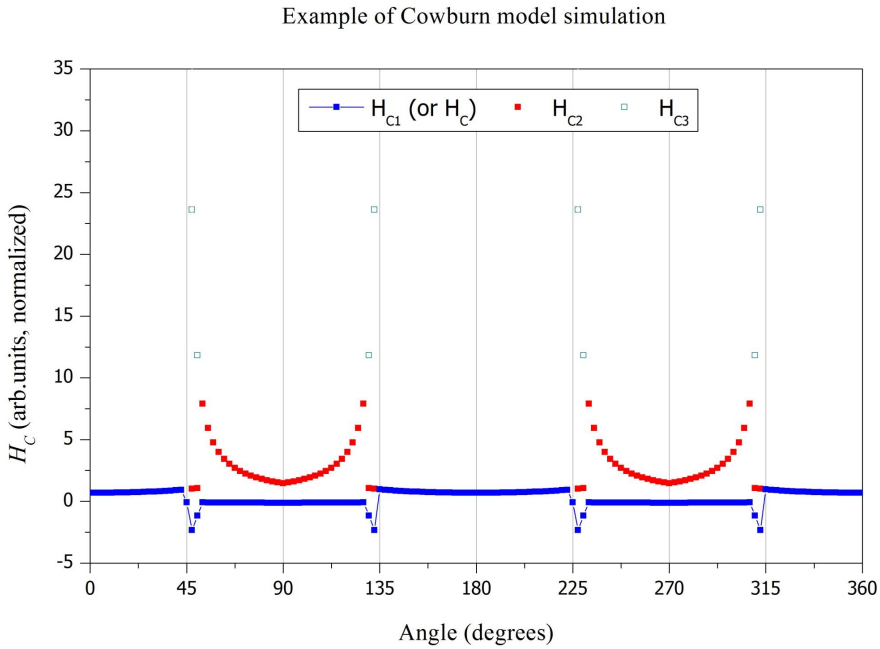


Figure E.19: Simulation of Cowburn model with 3-step reversals. Observe the evolution of the blue curve, for $H_{C1}$. At small angles above 45°, below 135°, above 225° and below 315°, the natural evolution of $H_{C1}$ splits: there is a drop in $H_{C1}$ to negative values, and the $H_{C2}$ values appear now in the original $H_{C1}$ position. The third jump appear as green open squares, following what otherwise would have been the normal $H_{C2}$ evolution of a 2-steps route. Observe that the first transition of a 3-step route appears at negative values, indicative that is happening before the external field changes its sign.

# F Magneto-Optical Kerr Effect formalism

## F.1 Origin of magneto-optic effects

The first phenomenological proposal to explain the magneto-optic effect came from Maxwell, who proposed that linearly polarized light could be expressed as a superposition of two circularly (left and right) polarization states (or circular modes), having different velocities arising at differences in the corresponding dielectric tensor constants. A first account from quantum mechanical point of view for the interaction of light with magnetized matter, came after Hulme in 1932 [8], but was unsatisfactory. He proposed a spin-dependent dielectric constant arising at the spin-orbit interaction which couples the electron spin to its motion. The spin-orbit interaction is expressed as

$$H_{SO} \sim (\nabla V \times \vec{p}) \cdot \vec{s} = \vec{p} \cdot (\vec{s} \times \nabla V) \tag{F.1}$$

where $\nabla V$ is the electric field through which the electron is moving, $\vec{p}$ is the electron's momentum and $\vec{s}$ its spin. The effect of a magnetic field on the electron motion is described by

$$H_{int} \sim -(e/mc)\vec{p} \cdot \vec{A} \tag{F.2}$$

with $\vec{A}$ the vector potential. So that the spin-orbit interaction can be viewed as an effective magnetic field vector potential acting on the electron's motion, given by

$$\vec{(}A) \sim \vec{s} \times \nabla V \tag{F.3}$$

This interaction manifest in the energy splitting from which Hulme calculated the refractive indexes of the two circularly polarized components, but neglecting the change in the wave function due to the spin-orbit interaction. His theory, however, failed due to the quenching of the orbital angular momentum in transition metals, that removed the energy splitting. Kittel demonstrated that the change of the wavefunction due to spin-orbit interaction was capable of giving the correct order of magnitude in the refractive index difference [9]. An improvement came after Argyres by using perturbation theory to provide a full description of the magneto-optic effect in ferromagnets.

The approach that we shall follow here is the macroscopic dielectric formalism of the magneto-optic Kerr effect, that rests on the analysis of the dielectric tensor [78, 180, 81]. This is a 3x3 (second rank) tensor represented by $\epsilon_{ij}$, the indexes running from 1 to 3. Any tensor can be decomposed in a symmetric and an antisymmetric part, denoted by S and A superscript respectively:

$$\begin{aligned} \epsilon_{ij} &= \epsilon_{ij}^S + \epsilon_{ij}^A \\ \epsilon_{ij}^S &= (\epsilon_{ij} + \epsilon_{ji})/2 \\ \epsilon_{ij}^A &= (\epsilon_{ij} - \epsilon_{ji})/2 \end{aligned} \tag{F.4}$$

The symmetric part can be diagonalized, so that only $\epsilon_{ii}$ elements are non null. If all of them have the same value $\epsilon$, then the symmetric part of the dielectric tensor is isotropic. On the other hand if this is not the case, it is anisotropic. However, its associated normal modes are linearly polarized, so they do not give rise to polarization rotation (at most they can cancel each other, extinguishing the wave, if the media allows for a $180^o$ phase shift).

On the other hand, the antisymmetric part of the dielectric tensor can always be written as

$$\epsilon^A = \begin{pmatrix} 1 & iQ_z & -iQ_y \\ -iQ_z & 1 & iQ_x \\ iQ_y & -iQ_x & 1 \end{pmatrix} \tag{F.5}$$

This matrix is fully determined by the three values $Q_x$, $Q_y$ and $Q_z$, and thus it is customary to use this off-diagonal elements in what is called its reduced representation, based on Voigt notation, i.e., the matrix is represented by the Voigt vector $\vec{Q} = (Q_x, Q_y, Q_z$ [11,12 from Bader]. This vector represents the off-diagonal elements of the dielectric tensor, and the refractive indexes of the two corresponding normal modes of the matrix are given by the following left and right circularly polarized components:

$$n_L = n(1 - \vec{Q} \cdot \hat{k}) \tag{F.6}$$

$$n_R = n(1 + \vec{Q} \cdot \hat{k}) \tag{F.7}$$

were n=$\sqrt{\epsilon}$ is the average refracting index. This expressions are the reason why Kerr effect are said to arise from the off-diagonals of the antisymmetric part of the dielectric tensor.

Arguments based on time reversal symmetry leads to the result that antisymmetric part of $\epsilon_{ij}$ could be generated by any quantity that breaks time reversal symmetry. In fact, magnetic field breaks time reversal symmetry, as it changes sign upon time reversal, and in consequence, it is encoded in the antisymmetric part of the dielectric tensor.

For practical calculations, we need to find first the reflection matrix of a magnetic material, with the proper boundary conditions applied to the Maxwell's equations. Using the so called boundary matrix method of Qiu et al. [78, 180, 81] we multiply the medium boundary ($\mathbf{A}_i$) and medium propagation matrices ($\mathbf{D}_j$) to obtain the matrix $\mathbf{M}$ defined by:

$$\mathbf{M} = \mathbf{A}_i^{-1} \Pi_{m=1}^N (\mathbf{A}_m \mathbf{D}_m \mathbf{A}_m^{-1}) \mathbf{A}_f \equiv \begin{pmatrix} \mathbf{G} & \mathbf{H} \\ \mathbf{I} & \mathbf{J} \end{pmatrix} \tag{F.8}$$

where the Fresnel reflection and transmission coefficients are defined as

$$\mathbf{G}^{-1} = \begin{pmatrix} t_{ss} & t_{sp} \\ t_{ps} & t_{pp} \end{pmatrix}; \ \mathbf{I}\mathbf{G}^{-1} = \begin{pmatrix} r_{ss} & r_{sp} \\ r_{ps} & r_{pp} \end{pmatrix} \tag{F.9}$$

In case of a thin magnetic film of thickness $d$ (the thickness small compared to the wavelength $\lambda$) on top of a semi-infinite sample, the reflection coefficient can be approximated as

$$\begin{aligned}
r_{ss} &= \frac{1}{\left(n_{\mathrm{i}}\cos\theta_{\mathrm{i}}+n_{\mathrm{f}}\cos\theta_{\mathrm{f}}\right)^2}\Big[n_{\mathrm{i}}^2\cos^2\theta_{\mathrm{i}}-n_{\mathrm{f}}^2\cos^2\theta_{\mathrm{f}}+ \\
&\quad +4\pi\mathrm{i}\frac{d}{\lambda}n_{\mathrm{i}}\cos\theta_{\mathrm{i}}\left(n_{\mathrm{m}}^2\cos^2\theta_{\mathrm{m}}-n_{\mathrm{f}}^2\cos^2\theta_{\mathrm{f}}\right)\Big] \\
r_{sp} &= -\frac{4\pi d}{\lambda}\frac{n_{\mathrm{f}}^2\sin\theta_{\mathrm{f}}m_y+n_{\mathrm{m}}^2\cos\theta_{\mathrm{f}}m_z}{\left(n_{\mathrm{i}}\cos\theta_{\mathrm{i}}+n_{\mathrm{f}}\cos\theta_{\mathrm{f}}\right)\left(n_{\mathrm{f}}\cos\theta_{\mathrm{i}}+n_{\mathrm{i}}\cos\theta_{\mathrm{f}}\right)}\times \\
&\quad \times n_{\mathrm{i}}\cos\theta_{\mathrm{i}}Q \\
r_{ps} &= +\frac{4\pi d}{\lambda}\frac{n_{\mathrm{f}}^2\sin\theta_{\mathrm{f}}m_y-n_{\mathrm{m}}^2\cos\theta_{\mathrm{f}}m_z}{\left(n_{\mathrm{i}}\cos\theta_{\mathrm{i}}+n_{\mathrm{f}}\cos\theta_{\mathrm{f}}\right)\left(n_{\mathrm{f}}\cos\theta_{\mathrm{i}}+n_{\mathrm{i}}\cos\theta_{\mathrm{f}}\right)}\times \\
&\quad \times n_{\mathrm{i}}\cos\theta_{\mathrm{i}}Q \\
r_{pp} &= \frac{1}{\left(n_{\mathrm{f}}\cos\theta_{\mathrm{i}}+n_{\mathrm{i}}\cos\theta_{\mathrm{f}}\right)^2}\left\{n_{\mathrm{f}}^2\cos^2\theta_{\mathrm{i}}-n_{\mathrm{i}}^2\cos^2\theta_{\mathrm{f}}-\right. \\
&\quad -4\pi\frac{d}{\lambda}\left[\mathrm{i}\left(n_{\mathrm{m}}^2\cos^2\theta_{\mathrm{f}}-n_{\mathrm{f}}^2\cos^2\theta_{\mathrm{m}}\right)+\right. \\
&\quad \left.\left.+\ n_{\mathrm{f}}^2\sin 2\theta_{\mathrm{f}}m_xQ\right]n_{\mathrm{i}}\cos\theta_{\mathrm{i}}\right\}
\end{aligned} \tag{F.10}$$

where $n_i$, $n_f$ and $n_m$ indexes of refraction of the initial, the final, and the magnetic medium. The incident angle is $\theta_{\mathrm{i}}$, while $\theta_{\mathrm{m}}$ and $\theta_{\mathrm{f}}$ are the (complex) angles of propagation in the magnetic layer and the substrate, respectively. The magneto-optic effect also depends on the material constant $Q$—the Voigt constant—that accounts for the off diagonal elements in the dielectric tensor, as already said.

It is found that in the first order the matrix is of the form

$$\mathbf{r}=\begin{pmatrix} r_{ss} & r_{sp} \\ r_{ps} & r_{pp}\end{pmatrix}\approx\begin{pmatrix} a & b_1m_x+b_2m_z \\ -b_1m_x+b_2m_z & c+dm_y\end{pmatrix} \tag{F.11}$$

For the sake of simplicity we use the frame of reference shown in figure 1.13 of section 1.7 (in the introduction of the thesis). The $x$ and $y$ directions are lying within the film plane, the surface normal is the $z$ direction, and the incident angle $\theta_i$ is contained in the $xz$ reflection plane. All calculations presented here are performed using the Jones formalism [181]. It is important to note that $r_{ss}$ is independent of magnetization. The components $r_{sp}$ and $r_{ps}$ are proportional while $r_{pp}$ contains an additional constant term. Upon reflection on the surface of the magnetic sample the electric field vector $\vec{E}$ of the incident light is reflected and results in $\vec{E}'$ as

$$\vec{E}'=\mathbf{r}\vec{E} \tag{F.12}$$

Naturally, the final measurement procedure consists of measuring the intensity, i.e., $I=\vec{E}'\cdot(\vec{E}')^*$ where the asterisk denotes the complex conjugate. It is easily seen that the intensity of the reflected $s'$-polarized light due to incoming $p$-polarized light (or vise versa) results in a signal that is quadratic in $m$. Consequently, such a measurement does not give proper information on the magnetic state of the sample. However,

the measurement of the reflected $p'$-polarization of incoming $p$-polarized light gives

$$\begin{aligned} I_p = E'_p(E'_p)^* &= cc^* + 2\mathrm{Re}[cd^*]m_y + dd^* m_y^2 \\ &\approx cc^* + 2\mathrm{Re}[cd^*]m_y + \mathcal{O}(m_y^2), \end{aligned} \tag{F.13}$$

assuming the typical case where $\mathrm{Re}[cd^*] \gg dd^*$. Hence, the constant term in $r_{pp}$ allows for easy measurement of $m_y$ in a transverse Kerr setup.

The presented setup is based on the idea of introducing an additional constant term in the $E_s$ component, therefore generating a linear term in the corresponding intensity. This is achieved by introducing a $\lambda/2$-retarder $\mathbf{L}_2$, rotated by $\pi/8$ off the optical axes, and by reading the two orthogonal components of the reflected light. In general, the reflected signal has the form

$$\begin{aligned} \begin{pmatrix} E''_s \\ E''_p \end{pmatrix} &= \mathbf{L_2 r} \begin{pmatrix} E_s \\ E_p \end{pmatrix} \\ &= \frac{\mathrm{i}}{\sqrt{2}} \begin{pmatrix} 1 & 1 \\ 1 & -1 \end{pmatrix} \begin{pmatrix} r_{ss} & r_{sp} \\ r_{ps} & r_{pp} \end{pmatrix} \begin{pmatrix} E_s \\ E_p \end{pmatrix}. \end{aligned} \tag{F.14}$$

For simplification let us assume only in-plane magnetization, i.e. $m_z = 0$, and incoming pure $p$-polarized light. The electric field vector after passing the retarder then has the form

$$\begin{pmatrix} E''_s \\ E''_p \end{pmatrix} = E_p \begin{pmatrix} b_1 m_x + c + d m_y \\ b_1 m_x - c - d m_y \end{pmatrix} \tag{F.15}$$

and the intensities read

$$\begin{aligned} I_s &= \frac{I_0}{2} \left\{ |c|^2 + |b_1|^2 m_x^2 + |d|^2 m_y^2 + 2\mathrm{Re}[b_1 d^*] m_x m_y + \right. \\ &\quad \left. + 2\mathrm{Re}[b_1 c^*] m_x + 2\mathrm{Re}[dc^*] m_y \right\} \\ I_p &= \frac{I_0}{2} \left\{ |c|^2 + |b_1|^2 m_x^2 + |d|^2 m_y^2 - 2\mathrm{Re}[b_1 d^*] m_x m_y - \right. \\ &\quad \left. - 2\mathrm{Re}[b_1 c^*] m_x + 2\mathrm{Re}[dc^*] m_y \right\}, \end{aligned} \tag{F.16}$$

where $I_0$ is the intensity of the incident beam. Adding and subtracting the two intensities gives

$$\begin{aligned} I_\Delta = I_s - I_p &= 2I_0 \left\{ \mathrm{Re}[b_1 c^*] m_x + \mathrm{Re}[b_1 d^*] m_x m_y \right\} \\ &\approx 2I_0 \mathrm{Re}[b_1 c^*] m_x + \mathcal{O}(m_x m_y) \\ I_\Sigma = I_s + I_p &= I_0 \left\{ |c|^2 + |b_1|^2 m_x^2 + |d|^2 m_y^2 + \right. \\ &\quad \left. + 2\mathrm{Re}[b_1 d^*] m_x m_y + 2\mathrm{Re}[dc^*] m_y \right\} \\ &\approx I_0 \left\{ |c|^2 + 2\mathrm{Re}[dc^*] m_y \right\} + \\ &\quad + \mathcal{O}(m_x^2, m_y^2, m_x m_y) \end{aligned} \tag{F.17}$$

As a result the difference signal is proportional to $m_x$, whereas the sum is linear in $m_y$, but has an additional DC-component, i.e. $I_\Sigma^{\mathrm{DC}} = |c|^2 = |r_{pp}^{\mathrm{DC}}|^2$. Note that due to

this DC component one finally gets

$$\frac{I_\Delta}{I_\Sigma^{\mathrm{DC}}} = \frac{2\mathrm{Re}[r_{sp}\left(r_{pp}^{\mathrm{DC}}\right)^*]}{|r_{pp}^{\mathrm{DC}}|^2} = \frac{2\mathrm{Re}[\frac{r_{sp}}{r_{pp}^{\mathrm{DC}}} r_{pp}^{\mathrm{DC}}\left(r_{pp}^{\mathrm{DC}}\right)^*]}{|r_{pp}^{\mathrm{DC}}|^2}$$
$$= 2\mathrm{Re}[\frac{r_{sp}}{r_{pp}^{\mathrm{DC}}}] \approx 2\theta_{\mathrm{K}}^p \propto m_x, \tag{F.18}$$
$$\frac{I_\Sigma^{\mathrm{AC}}}{I_\Sigma^{\mathrm{DC}}} = 2\mathrm{Re}[\frac{r_{pp}^{\mathrm{AC}}}{r_{pp}^{\mathrm{DC}}}] \propto m_y \tag{F.19}$$

which are the Kerr rotation and reflectivity change, which are proportional to the two in-plane components of the magnetization $m_x$ and $m_y$, respectively.

Similarly for incoming $s$-polarized light one obtains for the difference and the sum terms

$$\frac{I_\Delta}{I_\Sigma^{\mathrm{DC}}} = 2\mathrm{Re}[\frac{r_{ps}}{r_{pp}^{\mathrm{DC}}}] \approx 2\theta_{\mathrm{K}}^s \propto m_x, \tag{F.20}$$
$$\frac{I_\Sigma}{I_0} = \frac{I_\Sigma^{\mathrm{DC}}}{I_0} = R_{ss}, \tag{F.21}$$

the Kerr angle and a constant term, respectively. In this case, the sum $I_\Sigma$, does not contain useful information other than $R_{ss} = |r_{ss}|^2$, as $I_\Sigma \propto R_{ss} + \mathcal{O}(m_y^2)$. Consequently, there is no $I_\Sigma^{\mathrm{AC}}$ in the first order.

Therefore, the combination of $p$-polarized light and the detection of the two orthogonal components of the reflected light at the same time allows the determination of both in-plane magnetization components simultaneously. Notice that this is accomplished independently of the MOKE geometry. In this sense, we define the in-plane magnetization components parallel $M_\parallel$ and perpendicular $M_\perp$ with respect to the external magnetic field direction. In correspondence with figure 1.13 of section 1.7 (in the introduction of the thesis), for longitudinal MOKE geometry, i.e., $B_x$, the in-plane magnetization components can be derived from

$$M_\parallel = m_x \propto 2\theta_{\mathrm{K}}^p \approx \frac{I_\Delta}{I_\Sigma^{\mathrm{DC}}} \tag{F.22}$$
$$M_\perp = m_y \propto \frac{I_\Sigma^{\mathrm{AC}}}{I_\Sigma^{\mathrm{DC}}}, \tag{F.23}$$

whereas for transversal MOKE geometry, i.e., $B_y$,

$$M_\parallel = m_y \propto \frac{I_\Sigma^{\mathrm{AC}}}{I_\Sigma^{\mathrm{DC}}} \tag{F.24}$$
$$M_\perp = m_x \propto 2\theta_{\mathrm{K}}^p \approx \frac{I_\Delta}{I_\Sigma^{\mathrm{DC}}}. \tag{F.25}$$

Notice that each in-plane magnetization component can be derived independently from Kerr rotations or reflectivity changes, depending of the MOKE geometry. This will be used to determine experimentally the scale factor between both Kerr effects to obtain quantitative information of the in-plane resolved hysteresis loops. This is further discussed in Sec IV.

### F.1.1 Errors due to misaligned optical components

In the previous paragraph the ideal case has been discussed. In experiment, however, one must assume small angular errors in the optical components, i.e. polarizer, $\lambda/2$-retarder, and analyzer. Let us assume that these components have angular errors of $\alpha_1$, $\alpha_2$, and $\alpha_3$. In the following errors of the order $\alpha_i\alpha_j$ $(i,j=1,2,3)$ as well as $\alpha_i m_\xi m_\zeta$ $(\xi,\zeta = x,y,z)$ are neglected. In this approximation the final intensities including errors have the form

$$\begin{aligned} I_\Delta \quad \propto \quad & I_\Delta^{(1)} + 2\mathrm{Re}[b_1 d^*]m_x m_y + 2\mathrm{Re}[b_2 d^*]m_z m_y + \\ & +2\alpha_1\left(\mathrm{Re}[ac^*] + \mathrm{Re}[ad^*]m_y\right) + \\ & +2(2\alpha_2 - \alpha_3)I_\Sigma^{(1)} \end{aligned} \tag{F.26}$$

and

$$\begin{aligned} I_\Sigma \quad \propto \quad & I_\Sigma^{(1)} + |d|^2 m_x^2 + |b_1|^2 m_y^2 + |b_2|^2 m_z^2 + \\ & +2\mathrm{Re}[b_1 b_2^*]m_x m_z + \\ & +2\alpha_1\left(\mathrm{Re}[a^*b_1 - b_1 c^*]m_x + \mathrm{Re}[a^*b_2 + b_2 c^*]m_z\right) - \\ & -\alpha_3 I_\Delta^{(1)}. \end{aligned} \tag{F.27}$$

where $I_\Delta^{(1)}$ and $I_\Sigma^{(1)}$ are the error free first order approximations of the signals. Furthermore, the summation and subtraction, resulting in $I_\Sigma$ and $I_\Delta$, are assumed to be without error. Note that $\alpha_2$ does not effect $I_\Sigma$ as its effect cancels out in the sum, but mixes $I_\Sigma$ into $I_\Delta$. Moreover, $\alpha_3$ intermixes $I_\Delta$ and $I_\Sigma$; however, due to the adding and subtracting of the signals, $I_\Delta$ is doubly affected. Furthermore, one must keep in mind that the measured intensities, at both diodes, are dominated by the term $I_{p,s} \approx I_0/2|c|^2$. This term defines the photon noise. Assuming a Poisson statistic the resulting photon noise in each channel is proportional to $|c|$. Hence, the linear approximation becomes better with increasing $c$ and the relative photon noise decreases with $|c|^{-1}$.

To minimize the errors of $\alpha_1$ and $\alpha_3$ one first omits the retarder plate and introduces a non-magnetic reflecting material, i.e., without off-diagonal elements. Assuming that one wishes incoming $s$-polarized light, the according intensity is at the lowest order approximation of the form

$$I_p \propto (r_{pp}\alpha_1 - r_{ss}\alpha_3)^2 \tag{F.28}$$

This equation, however, has infinite solutions. Therefore, the optimizing process consists in three steps. First one of the polarizers is repeatedly rotated by 180°, such that the beam is entering from the opposite site. This operation transforms the according angle into its negative and the intensity will remain unchange only if the angle is 0. In the second step the intensity in the $p$-channel must be minimized for the second polarizer. As the minimum is quadratic, a precise adjustment can be difficult. This can be avoided by finding two opposite angles with identical intensity, such that the minimum will be at the average of these two angles. This procedure is applied when incoming $p$-polarized light is required. Finally the retarder is reintroduced. The retarder position is then optimized by making the intensities in the $I_s$ and $I_p$ channel identical, thereby minimizing $I_\Delta$.

### F.1.2 Optional $\lambda/4$-retarder

In the previous section, the theoretical description of the setup has shown that the detection of the two orthogonal light reflected components using incoming $p$-polarized light can provide, at first order, the simultaneous determination of the Kerr rotation angle and reflectivity variation, which are related to the two in-plane magnetization components. For instance, for longitudinal MOKE geometry, $m_x$ is provided by the Kerr angle whereas the change of reflectivity gives $m_y$.

In principle, the polarization rotation of a linearly polarized incident light when reflected by a magnetic material can be quantified by the Kerr rotation angle $\theta_{\mathrm{K}}$, as shown above, and by the Kerr ellipticity $\varepsilon$. In order to deal with the later, an additional quarter wave-plate ($\lambda/4$-retarder) before the Wollaston prism can be introduced in the setup, since it produces a $\pi/2$ phase difference between the $p'$- and $s'$- reflected components and interchanges Kerr angle and ellipticity. [78] Within the Jones formalism, the additional $\lambda/4$-retarder has the form

$$\frac{\mathrm{i}}{\sqrt{2}}\begin{pmatrix} 1+\mathrm{i} & 0 \\ 0 & 1-\mathrm{i} \end{pmatrix}. \tag{F.29}$$

It is easy to find that the sum is not affected by the $\lambda/4$-retarder, such that the result is identical to Eq. 9 and Eq. 11 for incoming $p$ and $s$ polarized light, respectively. For the difference, one finally gets

$$\left.\frac{I_\Delta}{\Sigma^{\mathrm{DC}}}\right|_{\lambda/4,p} = 2\mathrm{Im}[\frac{r_{sp}}{r_{pp}^{\mathrm{DC}}}] \approx 2\varepsilon_{\mathrm{K}}^{p} \propto m_x, \tag{F.30}$$

$$\left.\frac{I_\Delta}{\Sigma^{\mathrm{DC}}}\right|_{\lambda/4,s} = 2\mathrm{Im}[\frac{r_{ps}}{r_{pp}^{\mathrm{DC}}}] \approx 2\varepsilon_{\mathrm{K}}^{s} \propto m_x, \tag{F.31}$$

for incoming $p$ and $s$ polarized light, respectively. In both cases the difference is proportional to the Kerr ellipticity.

# G Notes on the compensation of dynamical effects for the study of transition fields

Depending on the coercive field of the system under study, the external field range must be adapted so that we get reasonably resolution to measure the hysteresis loops. As $H_C$ is expected to increase with decreasing temperature (for thermal activated reversal processes), there is sometimes no possibility to carry out full temperature range measurements without changing the applied field at some point, otherwise we could be measuring minor loops.

For this reasons, sometimes we are forced to split the temperature ramps into two regions, with a change in the external field range in between. If the field range is changed, without changing the frequency, the sweep rate will become different, and as a result dynamical effects can alter the coercive field upon field range change creating a kink between the two temperature regions. In order to avoid this, the same ratio dH/dt should be used by adjusting frequency correspondingly with the field range. When this is not possible due to technical problems (signal ripples or similar effects), a matching point should be used to connect the two resulting $H_C$ branches.

Notice that the coercive field values are higher as we increase the field rate of change (see for instant the chapter dedicated to dynamics), but the rotative part of the hysteresis loops is not affected. As a consequence, when matching the coercive fields, we should not re-scaling the whole hysteresis loop, but instead we should make a cut-off. Otherwise, the rotative part of the loops would be useless to obtain anisotropy constants via fit with SW.

As an example, loops in figure 5.12, corresponding to e.a. and h.a. and their $\pm$ 5° at 20 K, comes from an angular measurement carried out at 15 K with a coil that provides 36 mT per Ampere, at 4 Hz. This gives a field ratio of dH/dt=1T/s. On the other side, loops exibited in figure 5.12 correspond to temperature ramps taken by using a coil that provides 1.4 mT per Ampere, at 4 Hz as well. In this cases, the field rate of change is dH/dt=30mT/s. The dynamical effects are present, and we have to compensate them.

The compensation in this case is to remap $H_C$ for the loops acquired at a higher dynamical rate by using a scale factor of 0.667. As far as loops are concerned, however, this scale factor is not applicable, since we do not want to change the curvature of the rotative parts of the loops.

In general during this thesis, this kind of effects have been avoided by correctly tuning field rate (i.e., field range and frequency), and whenever it has been not possible, the compensation has been done in this way (a very delicate thing anyway).

# Conclusions

**The material presented in this thesis have covered selected aspects relating dynamical behavior of magnetic materials with specific magnetic characteristics and potential practical uses. The studies constitute specific probes of the relevance that dynamical effects have in the fundamental research aimed at technological applications. The importance of the reversal processes and magnetic anisotropy for this technology program is demonstrated, together with the capacity of tuning the reversal mechanism, through dynamical effects either thermally activated or field rate driven. Specific model systems have been selected to cover the different dynamical aspects, and the analysis have relied on phenomenological models for reversal of the magnetization. Necessary for the investigation has been the development of a new and unique instrument called TRISTAN**

This work has been developed in three frameworks, first, the technical aspects required to perform the investigations, second, the measurement process and data analysis, and third, the comparison with theoretical models to disentangle dynamical aspects of the reversal process and to quantify (to the extent that has been possible) the magnetic parameters derived from the analysis.

From the technical point of view, we remark the following aspects:

1. A new set-up called TRISTAN has been developed and built to suit the needs of this work: variable temperature full angular range vectorial MOKE magnetometer with time resolve capacity.

2. Standard v-MOKE magnetometers have been improved as well during this thesis.

3. Experiments can be carried out in an automated way, without the need to intervene on the measurement process at any moment. This converts the new instrument in a unique device.

4. Trainings in other techniques have also been done, such as XAS, XMCD, VSM, SEM and Kerr Microscopy, among others, that have contribute to throw some additional light on the experimental data.

From the point of view of the different model systems and phenomenology studied, the following must be pinpointed.

First, field rate driven dynamical effects have been addressed in $Co/Si(001)$ model system:

1. We have explained how field rate allows to change the reversal mechanism from propagative to nucleative in extended systems, observing the emergence of the Stoner-Wohlfarth astroid as field rate is increased over some decades.

2. The field rate for the onset of dynamical effects has been quantified.

3. It has also been addressed that under certain circumstances, the same dynamical aspects can be obtained even at quasi-static regimes, for extended systems.

Second, thermal driven spin reorientation at the Verwey transition has been studied for $Fe_3O_4/SrTO$ model system:

1. Room temperature anisotropy axes orientation have been confirmed to be rotated by 45° with respect to orientation already reported in the literature for other systems. In particular, the four-fold anisotropy axes are parallel to $< 100 >$ crystal directions, while below the Verwey transition they are aligned parallel to $< 110 >$.

2. Different features of the temperature evolution of magnetic parameters have been addressed in detail.

Third, thermal effects have been explored for a system with competing anisotropies, Fe/MgO(001), where the competition between magnetocrystalline four-fold magnetic anisotropy and the two-fold originated due to dipolar effects at the surface can be disentangled by looking at the different temperature evolutions. Remarkably we address the following important aspects:

1. We demonstrate that v-MOKE technique and, in special TRISTAN set-up, are fundamental tools for the purpose, allowing to disentangle the anisotropy landscape.

2. Upon acquisition of the temperature evolution of each magnetic anisotropy contributions, we confirm the different origins by checking the theory, and quantify the anisotropy constants.

3. We make use of two phenomenological models for that, and address a method to complement both models in the search of magnetic symmetries.

Third, thermal effects and field effects have been addressed in exchange bias system $Co/MnF_2$ of FM/AFM, with Néel temperature of 67 K. Heterostrutures of this kind have been long investigated and still today constitute hot topics for technological applications. On this respect, the following aspects have been covered:

1. We have addressed standard exchange bias behavior upon field cooling.

2. We have observed a negative (i.e., antiparallel) exchange coupling at the interface of the FM and AFM.

3. Different unidirectional anisotropies can be imprinted in the system by field cooling processes carried out at specific directions, that are related to the underlying trigonal structure of the antiferromagnetic layer, the $MnF_2$.

4. Unprecedentedly we report field induced exchange bias phenomena on $Co/MnF_2$ at temperatures well above the Néel temperature, where different behavior than the standard for increasing field magnitude is observed, with a reduction of the coercive field, as field amplitude is increased. Positive exchange bias can be field-induced above RT by using asymmetric fields. This effect had not been yet reported.

In the framework of theoretical models, new software has been developed on purpose for this thesis, covering the Stoner-Wohlfarth model with many options and flexibility, and the pinning models, in special Cowburn model for competing uniaxial and biaxial anisotropies. Important to address here is

1. Graphical user interface for easy to use environment, both for single simulations and massive scans.

2. Flexibility of the software, allowing may different configurations of anisotropies, from uniaxial to trigonal or unidirectional, with the possibility of intermixing at different angles.

3. Easy to use Cowburn simulation software.

4. Compatibility with our standard Origin-based software of analysis, allowing rapid comparison with experiments, and easy fitting procedures.

In summary, this thesis have covered new issues in fundamental physics of magnetic materials, in the framework of dynamical behavior and magnetic anisotropy, together with technical aspects, both in the context of experimental development and analysis procedures.

*In conclusion, with the investigations carried out, we set more basis for the development of future applications, and contribute to a higher level of understanding of reversal processes and the influence of dynamical and thermal effects. Results can be extended to other systems. In addition, the instrumental development and the analysis and interpretation techniques open new methods for the research in the field of nanomagnetism.*

# Conclusiones

**El material presentado en esta tesis ha cubierto aspectos selectos relacionados con el comportamiento dinámico de materiales magnéticos, con características específicas de gran potencialidad para usos prácticos. Los estudios realizados constituyen pruebas concretas de la relevancia que los efectos dinámicos tienen en la investigación fundamental orientada a las aplicaciones tecnológicas. La importancia de los procesos de inversión de imanación y las anisotropías magnéticas en el programa tecnológico han quedado demostradas, junto con la capacidad de ajustar dichos mecanismos, a través de efectos dinámicos activados térmicamente o inducidos por la velocidad de cambio del campo externo. Se han seleccionado sistemas modelo específicos para cubrir cada aspecto dinámico reseñado, y el análisis se ha basado en modelos fenomenológicos estudiados para la ocasión. Igualmente, para la investigación ha sido necesario la puesta en marcha de un nuevo instrumento, llamado TRISTAN, único en su clase.**

El trabajo se ha desarrollado, por tanto, en tres ámbitos, primero, en el técnico, requisito indispensable para la realización de la investigación, segundo en la medida y análisis de sistemas modelo específicamente seleccionados para los estudios de dinámica, y tercero, en la comparación con modelos teóricos, programados para la ocasión, para desenmarañar los efectos que los aspéctos dinámcos tienen en la inversión de imanación y cuantificar (en la medida de lo posible) los parámetros magnéticos involucrados.

Desde el punto de vista técnico, se remarcan los siguientes aspectos:

1. El desarrollo, pusta en marcha y explotación, durante esta tesis, de un nuevo instrumento denominado TRISTAN. Dicho instrumento consiste en un magnetómetro v-MOKE vectorial, de rango angular completo, capaz de trabajaar a temperatura variable controlada entre 5 K y 500 K, y capaz al mismo tiempo de realizar medidas de amplio rango dinámico (time resolved).

2. Se han mejorado al mismo tiempo los magnetmetros v-MOKE estandar que ya se disponan en el grupo de investigacin donde se ha desarrollado esta tesis.

3. Entre otras capacidades destacables, el nuevo instrumento se resume en un aparato capaz de realizar experimentos a temperatura variable, de modo automatizado, con todas las posibilidades de la técnica v-MOKE, es decir, magnetometría vecotiral de rango angular completo con acquisición simultanea de las dos componentes

de la magnetización in-plane, paralela y perpendicular, sin necesidad de realizar ninguna intervención en el aparato durante los barridos en ángulos y temperaturas. Esto convierte a TRISTAN en un instrumento único en su clase hasta la fecha.

4. Durante la tesis, además, también se han adquirido habilidades en otras técnicas, y en concreto cabe mencionar XAS, XMCD, VSM, SEM y microscopía Kerr entre otras. Además, el uso de estas técnicas ha contribuido a arrojar luz sobre algunos de los resultados experimentales obtenidos durante la tesis.

Desde el punto de vista científico, de los estudios de los diferentes sistemas modelo, hay que reseñar los siguientes aspectos.

En primer lugar, los efectos dinámicos inducidos por velocidad de campo se han abordado para el sistema modelo $Co/Si(001)$:

1. Hemos explicado cómo la velocidad de campo permite cambiar el mecanismo de inversión de imanación de propagativo a nucleativo, y se ha podido observar cómo emerge el denominado astroide de Stoner-Wohlfarth según se aumenta la velocidad de cambio del campo, indicativo del cambio de mecanismo de inversión antes mencionado.

2. La velocidad de campo a la que los efectos dinámicos comienzan a ser relevantes se ha cuantificado.

3. También se ha abordado el régimen quasi-sttático, en donde se ha mostrado cómo un sistema extendido puede incluso en régimen de baja velocidad de campo, desarrollar también procesos de inversión de imanación nucleativos que dominan sobre los propagativos.

En segundo lugar, se han estudiado efectos de reorientación de spin en la transición de Verwey para un sistema modelo de $Fe_3O_4/SrTO$, en el que cabe señalar los siguientes logros:

1. Se ha observado que la orientación de los ejes de anisotropía magnética a temperatura ambiente para este sistema no corresponden con los reportados en la literatura para otros sistemas de $Fe_3O_4$ sobre sustratos similales. De hecho, los ejes a temperatura ambiente son paralelos a las direcciones cristalinas $< 100 >$, y rotan $45°$ (a las direcciones $< 110 >$) al atravesar la temperatura de transición de Verwey.

2. En las evoluciones en temperatura se han observado características que permiten definir mejor cómo ocurre la transición.

En tercer lugar, se han explorado los efectos térmicos en el sistema modelo Fe/MgO(001) con competición de anisotropía, donde una anisotropía de orden cuatro de origen magnetocristalino compite con una de orden dos de origen dipolar. Estas anisotropías se muestran mezcladas, y se pueden desenmarañar mediante la investigación en temperatura, a través de las diferentes evoluciones que ambas poseen. Cabe destacar los siguientes resultados:

1. Este sistema ha permitido demostrar la potencia y versatilidad del instrumento TRISTAN como instrumento fundamental para la investigación en este campo.

2. La acquisición de la evolución en temperatura de los parámetros magnéticos permite desenmarañar las contribuciones individuales a la anisotropía magnética efectiva de este sistema, extensible a otros. Se ha confirmado el origen de estas anisotropías magnéticas y se han cuantificado.

3. Se han usado dos modelos fenomenológicos en el análisis, creando un método de estudio combinado que permite la búsqueda y entendimiento de las simetrías magnéticas.

En cuarto lugar, se han estudiado efectos dinámicos inducidos términcamente y por campo, en el sistema $Co/MnF_2$, ferro/antiferro con exchange bias, con temperarura de Néel de 67 K. Heterostructuras como esta se han investigado durante largo tiempo y todavía hoy en día constituyen tópcios relevantes para el desarrollo tecnológico. Los siguientes aspectos se han cubierto:

1. Se ha observado fenomenología de exchange bias estándar bajo procesos de enfriado bajo campo.

2. Se ha comprobado que el acoplo en la interfaz FM-AFM es de tipo antiparalelo.

3. Se ha podido inducir mediante el uso de procesos de enfriamiento bajo campo, distintas simetrías magnéticas por debajo de la temperatura de Néel, que reflejan la complejidad de la estructura magnética subyacente de la capa antiferromagnética de $MnF_2$.

4. Se reporta un efecto novedoso de exchange bias inducido por campo, por encima de la temperatura de Néel. Se observa una disminución del campo coercitivo conforme se sube el campo máximo aplicado, que es el comportamiento opuesto al reportado en la literatura para otros sistemas de exchange bias, y se ha inducido exchange bias positivo bajo aplicación de campos asimétricos. Este efecto está relacionado con el tipo de acoplo (antiparalelo) existente en la interfaz ferro/antiferro.

En el ámbito de los modelos teóricos, se ha desarrollado software propio durante la tesis, para cubrir los modelos de Stoner-wohlfarth y los de pinning, y en concreto, el de Cowburn. Algunos aspectos relevantes se detallan a continuación:

1. Se ha puesto énfasis especial en el interfaz gráfico de usuario, para permitir un uso fácil y flexible, tanto para simulaciones puntuales como para barrios angulares y de anisotropías amplios.

2. El software desarrollado admite multitud de configuraciones de anisotropía, desde la uniaxial a la trigonal o la unidireccional, con la posibilidad de mezclar todas en multitud de maneras.

3. Se ha hecho lo más compatible posible con el software de análisis de los ciclos de histéresis desarrollado en nuestro grupo de magnetismo (basado en Origin), y perfeccionado también durante la tesis. Esto ha permitido una fácil comparación de los datos experimentales con los teóricos y simulaciones, y un rápido ajuste de los mismos para así obtener valiosa información cualitativa y cuantitativa.

*En resumen, la tesis ha cubierto aspectos fundamentales de la física de materiales magnéticos de aplicación tecnológica, en el ámbito de los estudios de dinámica y efectos térmicos en la anisotropía magnética y los procesos de inverión de imanación, así como aspectos técnicos destacables, tanto en el contexto del desarrollo de instrumentación como en el del análisis de datos.*

# Publications

### Published


1. J.L.F. Cuñado, J. Pedrosa, F. Ajejas, P. Perna, R. Miranda, and J. Camarero
*Direct observation of temperature-driven magnetic symmetry transitions by vectorial resolved MOKE magnetometry*
J. Phys.: Condens. Matter in-press (2017).

2. J. Camarero, R. Miranda, J.L.F. Cuñado, and P. Perna
*Towards Spintronics Materials for Energy Saving: Advances in nanomagnetism via x-ray techniques*
IEEE EUROCON (2015)
DOI: 10.1109/EUROCON.2015.7313792

3. J.L..F. Cuñado, J. Pedrosa, F. Ajejas, A. Bollero, P. Perna, F. J. Teran, R. Miranda, and J. Camarero
*Vectorial-magneto optical Kerr effect technique combined with variable temperature and full angular range all in a single setup*
Rev. Sci. Instrum. **86**, 046109 (2015).

4. P. Perna, F. Ajejas, D. Maccariello, J.L.F. Cuñado, R. Guerrero, M. A. Niño, A. Bollero, R. Miranda, and J. Camarero
*Interfacial exchange coupling induced chiral symmetry-breaking of spin-orbit effects*
Phys. Rev. B Rapid Comm. **92**, 220422 (2015)

5. E. Jiménez, N. Mikuszeit, J.L.F. Cuñado, P. Perna, J. Pedrosa, D. Maccariello, C. Rodrigo, M. A. Niño, A. Bollero, J. Camarero and R. Miranda
*Vectorial Kerr magnetometer for simultaneous and quantitative measurements of the in-plane magnetization components*
Rev. Sci. Instrum. **85** , 053904 (2014).

6. P.Perna, D.Maccariello, C.Rodrigo, J.L. Cuñado, M. Muñoz, J.L. Prieto, M.A. Niño, A.Bollero, J. Camarero and R. Miranda
*Direct experimental determination of the anisotropic magnetoresistive effects*
Appl. Phys. Lett. **104**, 202407 (2014).

7. M. Monti, M. Sanz, M. Oujja, E. Rebollar, M. Castillejo, F. J. Pedrosa, A. Bollero, J.Camarero, J. L. F. Cuñado, N. M. Nemes, F. J Mompean, M. Garcia-Hernandez, S. Nie, K. McCarty, A. T N'Diaye, G. Chen, A. Schmid, and J. F. Marco
*Room temperature in-plane* $\langle 100 \rangle$ *magnetic easy axis for Fe3O4/SrTiO3(001) grown*

*by infrared pulsed laser deposition*
J. Appl. Phys. **114**, 223902 (2013).

8. P. Perna, C. Rodrigo, M. Muñoz, J. L. Prieto, A. Bollero, D. Maccariello, J. L. F. Cuñado, M. Romera, J. Akermann, E. Jiménez, N. Mikuszeit, V. Cros, J. Camarero, and R. Miranda
*Magnetization reversal signatures in the magnetoresistance of magnetic multilayers*
Phys. Rev. B **86**, 024421 (2012).

**In progress**

1. J.L.F. Cuñado, A. Bollero, T. Pérez-Castañeda, P. Perna, F. Ajejas, J. Pedrosa, A. Gudín, A. Maldonado, M. A. Niño, Rubén Guerrero, D. Cabrera, F. J. Teran, R. Miranda, and J. Camarero
*Emergence of the Stoner-Wohlfarth astroid in thin films at dynamic regime*
submitted to Nature Scientific Report (2017).

2. J.L.F. Cuñado, P. Perna, A. Bollero, N. S. Sokolov, S. Gastev, S. Suturi, A. Banshikof, V. Fedorov, D.Baranov, K. Koshmak, L. Pasquali, J. Nogués, R. Miranda, and J. Camarero
*Nature of the magnetic coupling in Co/MnF2 bilayers: negative vs. positive exchange bias*
in preparation (2017).

3. F.J. Pedrosa, J.L.F. Cuñado, M. Sanz, M. Oujja, E. Rebollar, J.F. Marco, J. de la Figuera, M. Monti, M. Castillejo, M. García-Hernández, F. Mompeán, J. Camarero, and A. Bollero
*Towards magnetic control of magnetite: a detailed study on the influence of substrate, orientation, and thickness of high quality stoichiometric films*
submitted to J. Appl. Phys (2017).

4. J.L.F. Cuñado, J.F. Pedrosa, J. Camarero, M. Sanz, M. Oujja, E. Rebollar, J.F. Marco, J. de la Figuera, M. Monti, M. Castillejo, M Garcia-Hernandez, F. Mompean, N.M. Nemes, T. Feher, B. Nafradi, L. Forro, and A. Bollero
*Spin reorientation in (001)-oriented magnetite films*
in preparation (2017).

**Contributions in other subjects**

1. P. Perna, F. Ajejas, D. Maccariello, J.L.F. Cuñado, R. Guerrero, M. A. Niño, M. Muñoz, J. L. Prieto, R. Miranda, and J. Camarero
*2D chiral asymmetry in unidirectional magnetic anisotropy structures*
AIP Advances **6**, 055819 (2016).

2. S. M. Ocampo, V. Rodriguez, L. De La Cueva, G. Salas, J. L. Carrascosa, M. J. Rodríguez, N. García-Romero, J.L.F. Cuñado, J. Camarero, R. Miranda, C. Belda-Iniesta, A. Ayuso-Sacido
*g-force induced giant efficiency of nanoparticles internalization into living cells*

3. Nature Scientific Reports **5**,15160 (2015). M Minniti, C Díaz, J L Fernández Cuñado, A Politano, D Maccariello, F Martín, D Farías, and R Miranda
*Helium, neon and argon diffraction from Ru(0001)*
J. Phys.: Condens. Matter **24**, 354002 (2012).

## Bibliography


[1] J. Stöhr and H. C. Siegmann, Springer-Verlag, Berlin (2006).

[2] S. D. Bader, Rev. Mod. Phys. **78**, 1 (2006).

[3] R. McCallum, L. Lewis, R. Skomski, M. Kramer, and I. Anderson, Annu. Rev. Mater. Res. **44**, 451 (2014).

[4] A. Fert, Rev. Mod. Phys. **80**, 1517 (2008).

[5] S. Parkin and S.-H. Yang, Nat. Nano. ***10***, 195 (2015).

[6] G. Bertotti, *Hysteresis in Magnetism* (Academic Press, New York, 1998).

[7] B. D. Cullity and C. D. Graham, Ed. John Wiley & Sons (2011).

[8] M. Johnson and R. H. Silsbee, Phys. Rev. Lett. ***55***, 1790 (1985).

[9] E. C. Stoner and E. P. Wohlfarth, Philos. Trans. R. Soc. London, Ser. A **240**, 599 (1948).

[10] A. Aharoni, Rev. Mod. Phys. **34**, 227 (1962).

[11] J. Vogel, J. Moritz, and O. Fruchart, C. R. Phys. **7**, 977 (2006).

[12] W. Wernsdorfer, Adv. Chem. Phys. **118**, 99 (2001).

[13] M. Jamet, W. Wernsdorfer, C. Thirion, D. Mailly, V. Dupuis, P. Mélinon, and A. Pérez, Phys. Rev. Lett. **86**, 4676 (2001).

[14] W. Wernsdorfer, B. Doudin, D. Mailly, K. Hasselbach, A. Benoit, J. Meier, J.-P. Ansermet, and B. Barbara, Phys. Rev. Lett. **77**, 1873 (1996).

[15] D. Givord, M. Rossignol, and D. Taylor, J. Phys. IV **2**, C3 (1992).

[16] R. P. Cowburn, S. J. Gray, J. Ferré, J. A. C. Bland, and J. Miltat, J. Apl. Phys. **78**, 7210 (1995).

[17] D. Ecija, E. Jiménez, N. Mikuszeit, N. Sacristán, J. Camarero, J. Gallego, J. Vogel, and R. Miranda, Phys. Rev. B **77**, 024426 (2008).

[18] P. Perna, L. Mechin, M. Saib, J. Camarero, and S. Flament, New Journal of Physics **12**, 103033.

[19] E. Jiménez, N. Mikuszeit, J. L. F. Cuñado, P. Perna, J. Pedrosa, D. Maccariello, C. Rodrigo, M. A. Niño, A. Bollero, J. Camarero, and R. Miranda, Rev. Sci. Instrum. **85** (2014).

[20] J. Cuñado, J. Pedrosa, F. Ajejas, A. Bollero, P. Perna, F. Teran, and J. Camarero, Rev. Sci. Instrum. **86**, 046109 (2015).

[21] R. P. Cowburn, S. J. Gray, and J. A. C. Bland, Phys. Rev. Lett. **79**, 4018 (1997).

[22] O. Fruchart, Institut Néel (CNRS and Universitá Grenoble) (2014).

[23] M. T. Johnson, P. J. H. Bloemenz, F. J. A. den Broeder, and J. J. de Vries, Rep. Prog. Phys. **59**, 14091458 (1996).

[24] M. Respaud, J. M. Broto, H. Rakoto, A. R. Fert, L. Thomas, B. Barbara, M. Verelst, E. Snoeck, P. Lecante, A. Mosset, J. Osuna, T. O. Ely, C. Amiens, and B. Chaudret, Phys. Rev. B **57**, 2925 (1998).

[25] S. M. F. Bdker and S. Linderoth, Phys. Rev. Lett. **72**, 282 (1994).

[26] U. Gradmann, J. Appl. Phys. **40**, 1182 (1969).

[27] D. Sander, J. Phys.:Condens. Matter **16**, R603 (2004).

[28] R. M. Bozorth, *Ferromagnetism* (Piscataway, NJ: IEEE, 1993).

[29] E. Kneller, *Ferromagnetismus* (Berlin: Springer, 1962).

[30] S. Chikazumi and S. H.Charap, *Physics of Magnetism* (Malabar, FL: Krieger, 1964).

[31] W. J. JrCarr, *Secondary Effects in Ferromagnetism* (Handbuch der Physik vol Band XVIII/2 Berlin: Springer, 1966).

[32] Blundell, *Magnetism in Condensed Matter* (Oxford: Oxford University Press, 2001).

[33] P. Bruno, *Magnetismus von Festkörpern und Grenzflächen Physical Origins and Theoretical Models of Magnetic Anisotropy* (Jülich: Forschungszentrum Jülich, pp 24.1-28, 1993).

[34] U. Gradmann, *Surfaces Interfaces and Ultrathin Films (Landolt-Börnstein Numerical Data and Functional* (Relationships in Science and Technology Group III, vol 19) (Berlin: Springer), 1988).

[35] U. Gradmann, *Magnetism in Ultrathin Transition Metal Films* (Handbook of Magnetic Materials vol 7) (Amsterdam: Elsevier Science) chapter 1, pp 1-96, 1993).

[36] U. Gradmann, *Magnetic Properties of Single Crystal Surfaces (Landolt-Börnstein Numerical Data and Functional* (Relationships in Science and Technology Group III, vol 24) (Berlin: Springer), 1994).

[37] J. A. C.Bland and B. Heinrich, (Ultrathin Magnetic Structures vol I (Berlin: Springer), 1994).

[38] J. A. C.Bland and B. Heinrich, (Ultrathin Magnetic Structures vol II (Berlin: Springer), 1994).

[39] K. Baberschke, M. Donath, and W. Nolting, *Band-Feromagnetism* ((Lecture Notes in Physics; Physics and Astronomy) (Berlin: Springer), 2001).

[40] P. Bruno and J.-P. Renard, Appl. Phys. A **49**, 1833 (1989).

[41] B. Heinrich, J. F. Cochran, A. S. Arott, S. T. Purcell, K. B. Urqhart, J. R. Dutcher, and W. F. JrEgelhoff, Phys. Rev. B **68**, 045416 (2003).

[42] H. C. Siegmann, J. Phys.: Condens. Matter **4**, 8395 (1992).

[43] G. A. Prinz, Ultramicroscopy, Topical Review R633 **47**, 346 (1992).

[44] W. J. M. de Jonge, P. J. H. Bloemen, and F. J. A. den Broeder, ((Ultrathin Magnetic Structures vol I) (Berlin: Springer), 1994).

[45] H. J. Elmers, J. Hauschild, H. Fritzsche, G. Liu, U. Gradmann, and U. Köhler, Phys. Rev. Lett. **75**, 2031 (1995).

[46] M. T. Johnson, P. J. H. Bloemen, F. J. A. den Broeder, and J. J. de Vries, Rep. Prog. Phys. **59**, 1409 (1996).

[47] M. Farle, Rep. Prog. Phys. **61**, 755 (1998).

[48] D. Sander, Rep. Prog. Phys. **62**, 809 (1999).

[49] D. Sander, S. Ouazi, A. Enders, Th.Gutjahr-Löser, V. S. Stepanyuk, D. I. Bazhanov, and J.Kirschner, J. Phys.: Condens. Matter **14**, 4165 (2002).

[50] J. F. Himpsel, J. E. Ortega, G. J.Mankey, and R. F. Willis, Adv. Phys. **47**, 511 (1998).

[51] R. Skomski, J. Phys.: Condens. Matter **15**, R841 (2003).

[52] N. Akulov, Z. Physic **100**, 197 (1936).

[53] R. Becker and W. Döring, *Ferromagnetismus* (Berlin, 1939).

[54] H. Callen and E. Callen, Phys. Rev **132**, 991 (1963).

[55] C. Zener, Phys. Rev. **96**, 1335 (1954).

[56] J. V. Vleck, Phys. Rev. **52**, 1178 (1937).

[57] J. H. van Vleck, Rev. Mod. Phys. **17**, 27 (1945).

[58] C. Kittel and J. V. Vleck, Phys. Rev. **118**, 1231 (1960).

[59] F. Keffer and T. Oguchi, Phys. Rev **100**, 1692 (1955).

[60] F. Keffer and T. Oguchi, Phys. Rev **117**, 718 (1960).

[61] R. Yanes, *Modeling of macroscopic anisotropies due to surface effects in magnetic thin films and nanoparticles* (Thesis at Universidad Autónoma de Madrid, 2011).

[62] W. H. Meiklejohn and C. P. Bean, Phys. Rev. **102**, 1413 (1956).

[63] V. Nikitenko, V. Gornakov, A. Shapiro, R. Shull, K. Liu, S. Zhou, and C. Chien, Phys. Rev. Lett. **84** (2000).

[64] M. Fitzsimmons, P. Yashar, C. Leighton, I. Schuller, J. Nogśs, C. Majkrzak, and J. Dura, Phys. Rev. Lett. **84** (2000).

[65] J. Nogués, D. Lederman, T. Moran, and I. Schuller, Phys. Rev. Lett. **76**, 4624 (1996).

[66] J. Nogués, D. Lederman, and I. Schuller, Phys. Rev. Lett. **61**, 1315 (2000).

[67] E. C. Stoner and E. P. Wohlfarth, IEEE Trans. Magn. **27**, 3475 (1991).

[68] M. Becker and M. Kersten, Phys. **64**, 660 (1930).

[69] B. Raquet, M. D. Ortega, M. Goiran, A. R. Fert, J. P. Redoules, R. Mamy, J. C. Ousset, A. Sdaq, and A. Khmou, J. Magn. Magn. Mater. **150**, L5 (1995).

[70] D. Jiles, *Introduction to Magnetism and Magnetic Materials* (CRC Press, 2015).

[71] D. Givord, P. Tenaud, and T.Viadieu, J. Magn. Magn. Mater. **72**, 247 (1988).

[72] R.-W. Gao and D.-H. Zhang, J. Appl. Phys. **35**, 4628 (1995).

[73] Q.-F. Zhan, S. Vandezande, K. Temst, and C. V. Haesendonck, Phys. Rev. B **80**, 094416 (2009).

[74] L. Néel, Ann. Geophys **5**, 99 (1949).

[75] P. Bruno, G. Bayreuther, P. Beauvillain, C. Chappert, G. Lugert, D. Renard, J. Renard, and J. Seiden, J. Appl. Phys **68**, 5759 (1990).

[76] G. Bayreuther, P. Bruno, G. Lugert, and C. Turtur, Phys. Rev. B **40**, 7399 (1989).

[77] J. Kerr, Phil. Mag. S. **3**, 024426 (1877).

[78] Z. Q. Qiu and S. D. Bader, J. Magn. Magn. Mater. **200**, 664 (1999).

[79] A. Hubert and R. Schäfer, *Magnetic Domains* (Springer-Verlag, Berlin, 2005).

[80] E. R. Moog and S. D. Bader, Superlatic. Microst. , 543 (1985).

[81] E. Jiménez, N. Mikuszeit, J. L. F. Cuñado, P. Perna, J. Pedrosa, D. Maccariello, C. Rodrigo, M. A. Niño, A. Bollero, J. Camarero, and R. Miranda, Rev. Sci. Instrum. **85**, 053904 (2014).

[82] J. Camarero, J. Sort, A. Hoffmann, J. M. García-Martín, B. Dieny, R. Miranda, and J. Nogués, Phys. Rev. Lett. **95**, 057204 (2005).

[83] T. Bobek, N. Mikuszeit, J. Camarero, S. Kyrsta, L. Yang, M. A. Niño, C. Hofer, L. Gridneva, D. Arvanitis, R. Miranda, J. J. de Miguel, C. Teichert, and H. Kurz, Adv. Mater. **19**, 4375 (2007).

[84] P. Prieto, K. R. Pirota, J. M. Sanz, E. Jiménez, F. Maccherozzi, and F. G. Panaccione, Appl. Phys. Lett. **90**, 032505 (2007).

[85] D. Ecija, E. Jiménez, N. Mikuszeit, N. Sacristán, J. Camarero, J. Gallego, J. Vogel, , and R. Miranda, Phys. Rev. B **77**, 024426 (2008).

[86] E. Jiménez, J. Camarero, J. Sort, J. Nogués, A. Hoffmann, N. Mikuszeit, J. M. García-Martín, B. Dieny, , and R. Miranda, Phys. Rev. B **80**, 014415 (2009).

[87] E. Jiménez, J. Camarero, J. Sort, J. Nogués, , A. Hoffmann, F. J. Teran, P. Perna, J. M. García-Martín, B. Dieny, , and R. Miranda, Appl. Phys. Lett. **95**, 122508 (2009).

[88] P. Perna, C. Rodrigo, E. Jiménez, N. Mikuszeit, F. J. Teran, L. Méchin, J. Camarero, and R. Miranda, J. Appl. Phys. **110**, 1391 (2011).

[89] J. M. Florczak and E. D. Dahlberg, J. Appl. Phys. **67**, 7520 (1990).

[90] c. Daboo, J. A. C. Bland, R. J. Hicken, A. J. R. Ives, M. J. Baird, , and M. J. Walker, Phys. Rev. B **47**, 11852 (1993).

[91] P. Vavassori, Appl. Phys. Lett. **77**, 1605 (2000).

[92] T. Kuschel, H. Bardenhagen, H. Wilkens, R. Schubert, J. Hamrle, J. Pistora, and J. Wollschläger, J. Phys. D: Appl. Phys. **44**, 265003 (2011).

[93] J. Cuñado, J. Pedrosa, F. Ajejas, A. Bollero, P. Perna, F. Teran, and J. Camarero, Rev. Sci. Instrum. **86**, 046109 (2015).

[94] E. H. Frei, S. Shtrikman, and D. Treves, Phys. Rev. **106**, 446 (1957).

[95] J. Miltat, G. Albuquerque, A. Thiaville, Hillebrands, and K. O. (Eds.), Topics in Appl. Phys. Springer-Verlag, Berlin **83** (2002).

[96] T. A. Moore and J. A. C. Bland, J. Phys.: Condens. Matter. **16**, R1369 (2004).

[97] P. Bruno, G. Bayreuther, C. Chappert, G. Lugert, D. Renard, and J. Seiden, J. Appl. Phys. **68**, 5759 (1990).

[98] T. A. Moore, J. Rothman, Y. B. Xu, and J. A. C. Bland, J. Appl.Phys. **89**, 7018 (2001).

[99] T. Moore, M. Walker, A. Middleton, and J. Bland, J. Appl. Phys. **97**, 053903 (2005).

[100] B. Raquet, R. Mamy, and J. C. Ousset, Phys. Rev. B **54**, 4128 (1996).

[101] J. Camarero, Y. Pennec, J. Vogel, M. Bonfim, S. Pizzini, M. Cartier, F. Ernult, F. Fettar, and B. Dieny, Phys. Rev. B **64**, 172402 (2001).

[102] J. Camarero, Y. Pennec, M. Bonfim, J. Vogel, S. Pizzini, A. Fontaine, M. Cartier, F. Fettar, and B. Dieny, J. Appl. Phys. **89**, 6585 (2001).

[103] F. García, J. Moritz, F. Ernult, S. Auffret, B. Rodmacq, J. C. B. Dieny, Y. Pennec, S. Pizzini, and J. Vogel, IEEE Transactions on Magnetics **38**, 2730 (2002).

[104] Y. Pennec, J. Camarero, J. C. Toussaint, S. Pizzini, M. Bonfim, F. Petroff, W. Kuch, F. Offi, K. Fukumoto, F. N. V. Dau, and J. Vogel, Phys. Rev. B **69**, 180402 (2004).

[105] T. A. Moore, G. Wastlbauer, and J. A. C. Bland, J. Phys.: Condens. Matter **15**, 407 (2003).

[106] S. Chikazumi, Oxford Science Publications, New York , pp. 118 (1997).

[107] D. Givord, P. Tanaud, and T. Viadieu, J. Magn. Magn. Mater. **72**, 247 (1988).

[108] J. Moritz, B. Dieny, J. P. Noziéres, Y. Pennec, J. Camarero, and S. Pizzini, Phys. Rev. B **71**, 100402 (2005).

[109] E. Jiménez, J. Camarero, P. Perna, N. Mikuszeit, F. Terán, J. Sort, J. Nogués, J. M. García-Martín, A. Hoffmann, B. Dieny, and R. Miranda, J. Appl. Phys. **109**, 07D730 (2011).

[110] P. Perna, F. Ajejas, D. Maccariello, J. Cuñado, R. Guerrero, M. Niño, A. Bollero, R. Miranda, and J. Camarero, Phys. Rev. B **92**, 220422 (2015).

[111] J. M. Colino, M. A. Arranz, A. J. Barbero, A. Bollero, and J. Camarero, J. Phys. D: Appl. Phys. **49**, 135002 (2016).

[112] R. Millar, J. Am. chem. Soc. **51**, 215 (1929).

[113] E. Verwey, Nature **44**, 327 (1939).

[114] C. Gleitzer, Eng. Mat. **125-126**, 355 (1997).

[115] A.Kozlowski, Z. Kakol, D. Kim, R. Zalecki, and J. Honig, Phys. Rev. B **54**, 12 093 (1996).

[116] F. Walz and H.Kronmüller, Phil. Mag. B **64**, 623 (1991).

[117] K. Belov, A. Goryaga, V. Pronin, and L. Skipetrova, JET P. Lett. **36**, 146 (1982).

[118] K. Belov, Physics-Uspekhi **36**, 380 (1993).

[119] L. Bickford, Phys. Rev. **76**, 137 (1949).

[120] L. Bickford, J. Brownlow, and R. Penoyer, Proc. I.E.E. **B104**, 238 (1957).

[121] K. Abe, Y. Miyamoto, and S. Chikazumi, J. Phys. Soc. Japan **41**, 1894 (1976).

[122] N. Tsuya, K. Arai, and K. Ohmori, Physica **86-88B**, 959 (1977).

[123] E. Aksenova, V. Gorbach, and V. Mamalui, Sov. Phys. Solid State **29**, 1149 (1987).

[124] R. Aragón, D. Buttrey, J. Shepherd, and J. Honig, Phys. Rev. B **31**, 430 (1985).

[125] R. Aragón, Phys. Rev. B **46**, 5328 (1992).

[126] J. Honig, J. Alloys Compounds **229**, 24 (1995).

[127] G. K. Rozenberg, G. Hearne, P. Pasternak, P. Metcalf, and J. Honig, Phys. Rev. B **53**, 6482 (1996).

[128] A. Muxworthy and E. McClelland, Geophys. J. Int. **140**, 101 (2000).

[129] E. Salje, Annu.Rev.Mater. Res **42**, 265 (2012).

[130] M. Yazdi, M. Major, A. Wildes, F. Wihlelm, A. Rogalev, W. Donner, and L. Alff, Phys. Rev. B **93**, 014439 (2016).

[131] D. Margulies, F. Parker, M. Rudee, F. Spada, J.N.Chapman, P. Aitchison, and A. Berkowitz, Phys. Rev. Letter **79**, 5162 (1997).

[132] M. Senn, J. Wright, and J. Attfield, Nature **481**, 173 (2012).

[133] J. Zuo, J. Spence, and W. Petuskey, Phys. Rev. B **42**, 8451 (1990).

[134] Y. Miyamoto and S. Chikazumi, J. Phys. Soc. Japan **57**, 2040 (1988).

[135] C. Medrano, M. Schlenker, J. Baruchel, J. Espeso, and Y. Miyamoto, Phys. Rev. B **59**, 1185 (1999).

[136] L. Skipetrova, PhD thesis, Moscow State University (1978).

[137] M. M. et al., J. Appl. Phys. **114**, 223902 (2013).

[138] J. Cuñado, J. Pedrosa, F. Ajejas, A. Bollero, P. Perna, F. Teran, and J. Camarero, Rev. Sci. Instrum **86**, 046109 (2015).

[139] L. Martí-García, A. Mascaraque, B. Pabón, R. Bliem, G. Parkinson, G.Chen, A. Schmid, and J. de la Figuera, Phys. Rev. B **93**, 134419 (2016).

[140] J. de la Figuera, Z. Novotny, M. Setvin, T. Liu, Z. Mao, G. Chen, A. NDiaye, M. Schmid, U. Diebold, A. Schmid, and G. Parkinson, Phys. Rev. B **88**, 161410 (2013).

[141] J. de la Figuera, L. Vergara, A. T. NDiaye, A. Quesada, and A. K. Schmid, Ultrmicroscopy **130**, 77 (2013).

[142] A. Hamie, Y.Dumont, E. Popova, A. Fouchet, B.Warot-Fonrose, C. Gatel, E. Chikoidze, J. Scola, B. Berini, and N. Keller, Thin Solid Films **525**, 115 (2012).

[143] F. Walz, J. Phys.:Condens. Matter **R285**, 14 (2002).

[144] K. Momma and F. Izumi, J. Appl. Crystallogr. **44**, 1272 (2011).

[145] P. Prieto, J. de la Figuera, L. Martín-García, J. Prieto, and J. Marco, J.Mat.Chem.C **4**, 7632 (2016).

[146] A. Pignocco and G. Pellissier, J. Selectrochem Soc. **112**, 1188 (1965).

[147] A. Pignocco and G. Pellissier, Surface Sci. **7**, 261 (1967).

[148] K. Molier and F. Portele, The Structure and Chemistry of Solid Surfaces, Wiley, New York **7**, 61 (1969).

[149] K. Moiler and P. Meischner, Private communication. .it .

[150] T. Kanaji, K. Asano, and S. Nagata, Vacuum **23**, 55 (1973).

[151] T. Urano and T. Kanaji, J. Phys. Soc. Jpn. **57**, 3043 (1980).

[152] C. Liu, Y. Park, , and S. D. Bader, J. Magn. Magn.Mater. **111**, L225 (1992).

[153] H. Fuke, A. Sawabe, and T. Mizoguchi, Jpn. J. Appl. Phys. **32**, L1137 (1993).

[154] U. Gradmann, Handb. Mag. Mat. **7**, 1 (1993).

[155] K. Honda and S. Kaya, Sci. Reports Tohoku Univ. **15**, 721 (1926).

[156] S. Blugel, Magnetische Anisotropie und Magnetostriktion .

[157] T. Bose, R. Cuadrado, R. Evans, R. Chepulskii, D. Apalkov, and R. Chantrell, J. Phys.:Condens. Matter **28** (2016).

[158] G. Bihlmayer, Private Communications, IFF, Julich .

[159] Y. Park, E. A. Fullerton, and S. B. Bader, Appl. Phys. Lett. **66**, 2140 (1995).

[160] Q.-F. Zhan, C. V. Haesendonck, S. Vandezande, , and K. Temst, Appl. Phys. Lett. **94**, 042504 (2009).

[161] R. K. Kawakami, E. J. Escorcia-Aparicio, and Z. Q. Qiu, Phys.Rev.Lett. **77**, 2570 (1996).

[162] J. Costa-Kramer, J. Menendez, A. Cebollada, F. Briones, D. Garcia, and A. Hernando, Journal of Magnetism and Magnetic Materials **210**, 348 (2000).

[163] F. Bisio, R. Moroni, F. B. de Mongeot, M. Canepa, and L. Mattera, Phys. Rev.Lett. **96**, 057204 (2006).

[164] E. Carpene, E. Mancini, C. Dallera, E. Puppin, and S. D. Silvestri, J. Appl. Phys. **108**, 063919 (2010).

[165] F. Radu and H. Zabel, Springer Tracts in Modern Physics **227**, 97 (2007).

[166] F. Garcia, J. Moritz, F. Ernult, S. Aufret, B. Rodmacq, B. Dieny, J. Camarero, Y. Pennec, S. Pizzini, , and J. Vogel, IEEE Trans. Magn. **38**, 2730 (2002).

[167] H. Ohldag, A. Scholl, F. Nolting, E. Arenholz, S. Maat, A. T. Young, M. Carey, and J. Stöhr, Phys. Rev. Lett. **91**, 017203 (2003).

[168] J. Camarero, Y. Pennec, J. Vogel, S. Pizzini, M. Cartier, F. Fettar, F. Ernult, A. Tagliaferri, and N. B. Brookes, Phys. Rev. B **67**, 020413 (2003).

[169] J. Camarero, J. Miguel, J. Goedkoop, J. Vogel, F. García, F. Romanens, S. Pizzini, N. B. Brookes, J. Sort, , and B. Dieny, Appl. Phys. Lett. **89**, 232507 (2006).

[170] S. M. Suturin, V. Fedorov, A. Banshchikov, D. Baranov, K. Koshmak, P. Torelli, J. Fujii, G. Panaccione, K. Amemiya, M. Sakamaki, T. Nakamura, M. Tabuchi, L. Pasquali, and N. Sokolov, J. Phys.: Condens. Matter **25**, 046002 (2013).

[171] G. Vérstey and I. Tomás, J. Appl. Phys. **77**, 6426 (1995).

[172] M. Kiwi, J. Mejía-López, R. Portugal, and R. Ramírez, Sol. Stat. Comm. **116**, 315319 (2000).

[173] O. Idigoras, A. K. Suszka, P. Vavassori, P. Landeros, J. M. Porro, and A. Berger, Phys. Rev. B , 132403 (2011).

[174] O. Idigoras, A. K. Suszka, P. Vavassori, B. Obry, B. Hillebrands, P. Landeros, and A. Berger, J. Appl. Phys. , 083912 (2014)).

[175] C. Kittel, *Introduction to Solid State Physics* ((New York: Wiley), 1963).

[176] H. Brooks, Phys. Rev. **58**, 909 (1940).

[177] J. Franse, Jour. de Phys. **32**, 186 (1971).

[178] N. L. Brukhatov and L. Kirensky, Physik. Z. Sowjectunion **12**, 602 (1937).

[179] J. Liu, E. Fullerton, O. Gutfleisch, and D. Sellmyer, *Nanoscale Magnetic MAterials and Applications* (Springer, 2009).

[180] Z. Q. Qiu and S. D. Bader, Rev. Sci. Instrum. **71**, 1243 (2000).

[181] R. Azzam and N. Bashara, North Holland, Amsterdam (1977).